MANY-BODY THEORY OF ELECTRICAL, THERMAL AND OPTICAL RESPONSE OF MOLECULAR HETEROJUNCTIONS

by

Justin Philip Bergfield

A Dissertation Submitted to the Faculty of the

COLLEGE OF OPTICAL SCIENCES

In Partial Fulfillment of the Requirements
For the Degree of

DOCTOR OF PHILOSOPHY

In the Graduate College

THE UNIVERSITY OF ARIZONA

2010

THE UNIVERSITY OF ARIZONA
GRADUATE COLLEGE

As members of the Dissertation Committee, we certify that we have read the dissertation prepared by Justin Philip Bergfield
entitled *Many-body theory of electrical, thermal and optical response of molecular heterojunctions*
and recommend that it be accepted as fulfilling the dissertation requirement for the Degree of Doctor of Philosophy.

Charles Stafford — Date: 24 May 2010

Philippe Jacquod — Date: 24 May 2010

Sumitendra Mazumdar — Date: 24 May 2010

Final approval and acceptance of this dissertation is contingent upon the candidate's submission of the final copies of the dissertation to the Graduate College.
I hereby certify that I have read this dissertation prepared under my direction and recommend that it be accepted as fulfilling the dissertation requirement.

Dissertation Director: Charles Stafford — Date: 24 May 2010

STATEMENT BY AUTHOR

This dissertation has been submitted in partial fulfillment of requirements for an advanced degree at the University of Arizona and is deposited in the University Library to be made available to borrowers under rules of the Library.

Brief quotations from this dissertation are allowable without special permission, provided that accurate acknowledgment of source is made. Requests for permission for extended quotation from or reproduction of this manuscript in whole or in part may be granted by the head of the major department or the Dean of the Graduate College when in his or her judgment the proposed use of the material is in the interests of scholarship. In all other instances, however, permission must be obtained from the author.

SIGNED: Justin Philip Bergfield

ACKNOWLEDGEMENTS

This work is the culmination of years of work and was only made possible with the support and guidance of my family, friends and teachers. At this time, I'd like to acknowledge a few of these contributions:

First, I would like to thank my wife Kaitlin, without whose love, patience, advice and companionship this would not have been possible. I would also like to acknowledge M. F. B. for your infectious positive attitude and uncanny ability to put everything in perspective. I must also thank my parents and brother for your constant interest in and support of me and my research, even when I decided to pursue a somewhat esoteric field of study. Lastly, I do not want to forget my friends with whom I have enjoyed many a free pizza lunch and after-work drink. Thank you all from the bottom of my heart.

Academically, I am honored to have worked under the supervision of Prof. C. Stafford. I am grateful for our frequent lunchtime physics conversations, your profound insight and also your patience in training an engineer and optical science student to appreciate the intricacies of many-body physics. I can only hope that some of your intuition has rubbed off!

I am thankful for discussions with and the guidance of Profs S. Mazumdar and P. Jacquod in the Department of Physics and Profs. E. Wright, P. Jessen, M. Mansuripur, F. Kueppers, and Dr. N. H. Kwong in the College of Optical Science. I would also like to extend the warmest thanks to all the staff members who have helped over the years. I am indebted to each of you for helping me in numerous ways over the years.

I would also like to thank Profs. R. Shoemaker, C. Maes, and Dr. R. Haar for giving me the opportunity to teach many more times than I was officially allowed to during my tenure as a doctoral student. Finally, I would like to thank the scores of students I have had over the years. You not only challenged and inspired me but also helped to make my time at the university fulfilling.

For my family

TABLE OF CONTENTS

TABLE OF CONTENTS – *Continued*

LIST OF FIGURES

LIST OF FIGURES – *Continued*

LIST OF TABLES

ABSTRACT

In this work, we develop a many-body theory of electronic transport through single molecule junctions based on nonequilibrium Green's functions (NEGFs). The central quantity of this theory is the Coulomb self-energy matrix of the junction Σ_{C}. Σ_{C} is evaluated exactly in the sequential-tunneling limit, and the correction due to finite lead-molecule tunneling is evaluated using a conserving approximation based on diagrammatic perturbation theory on the Keldysh contour. In this way, tunneling processes are included to infinite order, meaning that any approximation utilized is a truncation in the physical processes considered rather than in the order of those processes. Our theory reproduces the key features of both the Coulomb blockade and coherent transport regimes simultaneously in a single unified theory. Nonperturbative effects of intramolecular correlations are included, which are necessary to accurately describe the highest occupied molecular orbital (HOMO)-lowest unoccupied molecular orbital (LUMO) gap, essential for a quantitative theory of transport.

This work covers four major topics related to transport in single-molecule junctions. First, we use our many-body theory to calculate the nonlinear electrical response of the archetypal Au-1,4-benzenedithiol-Au junction and find irregularly shaped 'molecular diamonds' which have been experimentally observed in some larger molecules but which are inaccessible to existing theoretical approaches. Next, we extend our theory to include heat transport and develop an exact expression for the heat current in an interacting nanostructure. Using this result, we discover that quantum coherence can strongly enhance the thermoelectric response of a device, a result with a number of technological applications. We then develop the formalism to include multi-orbital lead-molecule contacts and multi-channel leads, both of which strongly affect the observable transport. Lastly, we include a dynamic screening correction to Σ_{C} and investigate the optoelectric response of several molecular junctions.

CHAPTER 1

Introduction

Molecular electronics is an exciting, rapidly growing field which draws upon the expertise of a wide range of disciplines including chemistry, electrical engineering, physics, material science and optics. Central to this work is the study of the flow of electrons, which carry heat, spin and charge, in single-molecule junctions (SMJs) composed of at least two macroscopic conducting leads coupled to a microscopic single molecule. Although chemists have worked with many of the molecules used in molecular electronics for over a century, the notion of designing a single-molecule-based electronic device first appeared in 1974 when Aviram and Ratner proposed a single-molecule rectifying diode [12]. Since then experimentalists have made remarkable progress, physically realizing SMJs using a variety of techniques to study a number of interesting phenomena such as current rectification [47, 126, 53], Coulomb blockade [149, 101, 150, 145, 208, 175], the Kondo effect [115, 116], vibrational effects [102, 78], optical response [200] and thermoelectric response [15, 152]. This open quantum system is of interest both as a fundamental tool to study nonequilibrium transport in an interacting nanostructure, and for designing devices which might derive new utility and enhanced performance by using the electronic properties of molecules.

At the length scale of a single molecule, typically only several Angstroms across, the Drude-Sommerfeld theory of electronic transport often used by electrical engineers breaks down and the coherent nature of the electron plays an important role. At this scale, it becomes appropriate to utilize an alternative approach put forward by Landauer that "conductance is transmission" [107], in which transport through a small conductor is thought of as scattering into an electronic waveguide where each mode has a certain transmission probability. The theoretical problem posed by a single-molecule junction is then: How can we predict transmission probabilities,

which are directly related to the observable conductance, from a microscopic quantum theory? When leads are attached to a single molecule the few-body electronic problem of that isolated molecule becomes a many-body problem of the junction, involving a macroscopic number of electrons. In general, the many-body problem is too difficult to be solved exactly, requiring the invocation of certain approximations.

Presently, most theoretical studies of electronic transport in SMJs utilize *ab initio* approaches based on implementations of density functional theory (DFT), a theory which aims to solve the *ground state* many-body problem variationally without resorting to any phenomenological factors [187, 46, 183, 77, 54, 190, 120]. These approaches are attractive because with them transport calculations scale linearly in the size of the system, unlike the exponential scaling exhibited by a full many-body calculation, making an atomistic model of a molecular junction feasible. However, DFT itself is only exact for the ground state electronic configuration, making its applicability to nonequilibrium problems like transport in a SMJ which require an accurate description of excited states uncertain *a priori* [136, 87, 37]. Moreover, even in equilibrium non-perturbative effects like the quantization of charge are not properly described by existing implementations of DFT [137, 188, 27, 63]. Motivated by these issues, we sought to develop a theory of transport capable of predicting existing experimental data.

A main goal of this work is to develop a many-body theory of quantum transport capable of predicting the response of an open quantum system, namely a single-molecule junction. To this end, we utilize nonequilibrium Green's functions (NEGF) as a framework for our transport theory, drawing upon the intuitive nature of diagrammatic perturbation theory to find a physically motivated approximation to the full many-body solution. We phrase our many-body theory in terms of the interacting molecular Green's function, simultaneously including both Coulomb-blockade and resonant tunneling phenomena in one unified theory.

In this chapter we give a brief overview of some of the experimental techniques used to fabricate a single-molecule junction and discuss the nature of transport at the quantum level. We also outline many of the most important aspects of the

NEGF formalism and of diagrammatic perturbation theory. In chapters 2 and 3, we develop the electrical and thermal theories of transport, respectively, presenting many striking examples along the way. In chapter 4, we extend our formalism for the lead-molecule interface and investigate multi-orbital lead-molecule contacts and multi-channel leads, both of which strongly affect the observable transport. We also consider the density-of-states of the macroscopic leads as a possible probe of the bonded molecule's state. In the final chapter of this thesis, we include dynamic correlation corrections in our perturbative expansion and investigate the photovoltaic effect in several single-molecule junctions.

1.1 Single-molecule junctions

A single-molecule junction is a device composed of at least two macroscopic conducting leads coupled to a single molecule. Most often single-molecule junctions are made using gold electrodes, as gold is a good conductor, is malleable, and binds well with thiolated molecules (i.e. molecules with -SH functional end-groups). Recently, transport studies have been performed using the archetypal benzene (C_6H_6) molecule directly bonded to two platinum electrodes [90]. Irrespective of the methods involved in constructing a molecular junction, of principal interest is the nonequilibrium electronic response, i.e. how the current or conductance is affected by the application of a bias voltage or large temperature gradient. As motivation for the theoretical discussion which constitutes the bulk of this work, let us first briefly review some of the experimental methods used in molecular electronics.

1.1.1 Break junctions

In a mechanically controlled break junction (MCBJ) a piezo-element is used to cause a macroscopic metallic wire to fracture, thereby producing a nanoscale gap between two clean, atomically sharp metal contacts. For a molecular junction, molecules are then deposited in between the two contacts to make an electrical circuit. The three-point bending configuration often utilized in break junctions is shown schematically

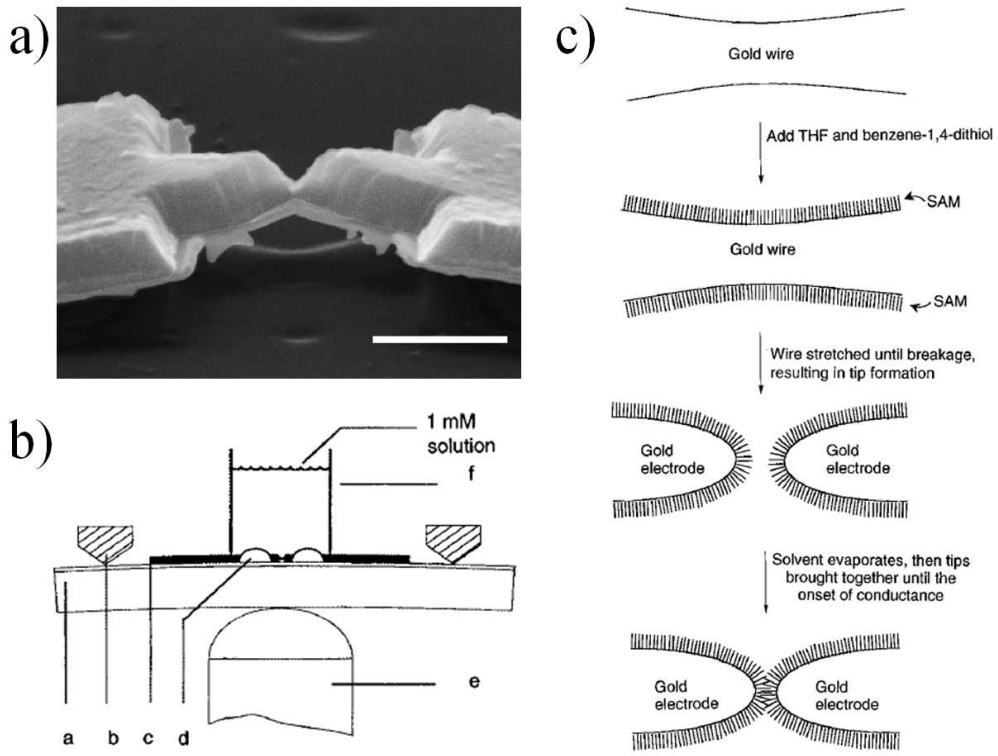

Figure 1.1: Mechanically controlled break junction (MCBJ) technique. (a) A scanning electron microscope (SEM) image of a lithographically fabricated gold MCBJ. The contact at the narrowest part is formed in a thin 20 nm gold layer. Taken from Ref. 2. (b) A schematic of the MCBJ device used in an experiment by Reed et al. [153] indicating 'a' the bending beam, 'b' the contour supports, 'c' the notched gold wire, 'd' the glue contacts, 'e' the piezoelectric element, and 'f' the glass tube with molecular solution. (c) A schematic representation of the formation of a molecular junction from Ref. 153.

in Fig. 1.1. By monitoring the current at a fixed bias through a MCBJ as the strain is applied, the point of fracture can be ascertained. One then reduces the strain until a non-zero conductance is observed. The advantages of this technique are that it is repeatable, can be done at low temperature in vacuum, and is quite insensitive to vibrations [3]. However, from a device perspective the involvement of mechanical parts is not desirable.

In their landmark experiment, Reed and colleagues [153] measured the electrical response of a single 1,4-benzenedithiol molecule bound to two gold leads using a

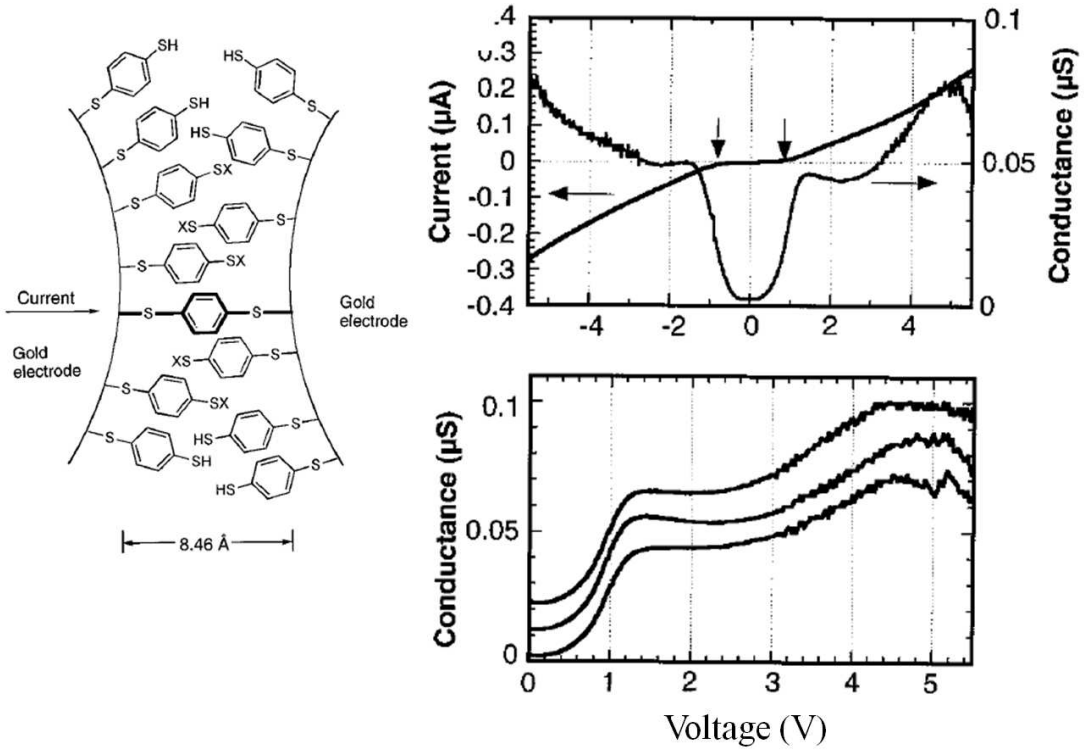

Figure 1.2: The molecular MCBJ experiment of Reed and coworkers [153]. Left: A schematic diagram of the researchers vision of their Au-1,4-benzenedithiol-Au junction. Right: The nonlinear electrical response of the junction. The traces in the lower figure illustrate the repeatable nature of the measurement and are offset for clarity.

MCBJ. The current and conductance they measured as a function of voltage bias is shown in Fig. 1.2. Their spectra exhibit distinct steps at certain voltages in both forward and reverse biases, a result which is consistent with a resonant tunneling process.

The thiol end-groups attached to benzene bond strongly with the gold surface, assuring good electric coupling between the molecule and the contact. A drawback with thiol end-groups, and with end-groups in general is that they generally act as an additional tunnel barrier for junction transport. In a recent experiment Kiguchi and colleagues [90] succeeded in forming MCBJs in which a single benzene molecule bonds directly to two platinum electrodes. Using a computer controlled loop thou-

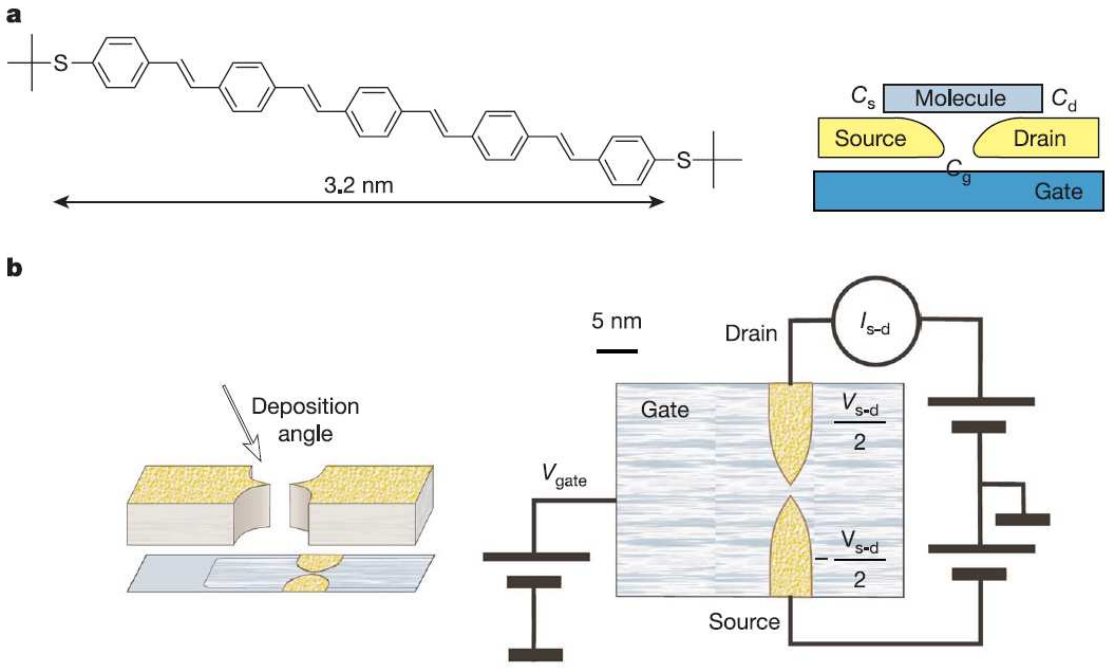

Figure 1.3: Schematic indicating various aspects of the experiment by Kutbakin et al. [101]. (a) A diagram of the OPV5 molecule used in this experiment. (b) A representation of the angled deposition technique and the final junction with source, drain and gating electrodes. Images are from Ref. 101.

sands of junctions were formed, indicating that benzene can form very strong bonds with the metallic surface directly.

1.1.2 Fixed-gap junctions

Most fixed-gap junctions are produced using a method known as electromigration, where a momentum transfer between the electrons and the ions of the metallic nanowire causes a sub-nanoscale breakage forming a small junction [144]. Unlike break junctions, the width of a fixed-nanogap junction cannot be adjusted arbitrarily, although there has been effort [112] to fine-tune the size of the gap using electrodeposition and etching. Once a nanogap is constructed, a molecular junction is formed when a molecule bridges the gap between the two electrodes, allowing current to flow.

Because of the irreversibility of the electromigration process the yield of work-

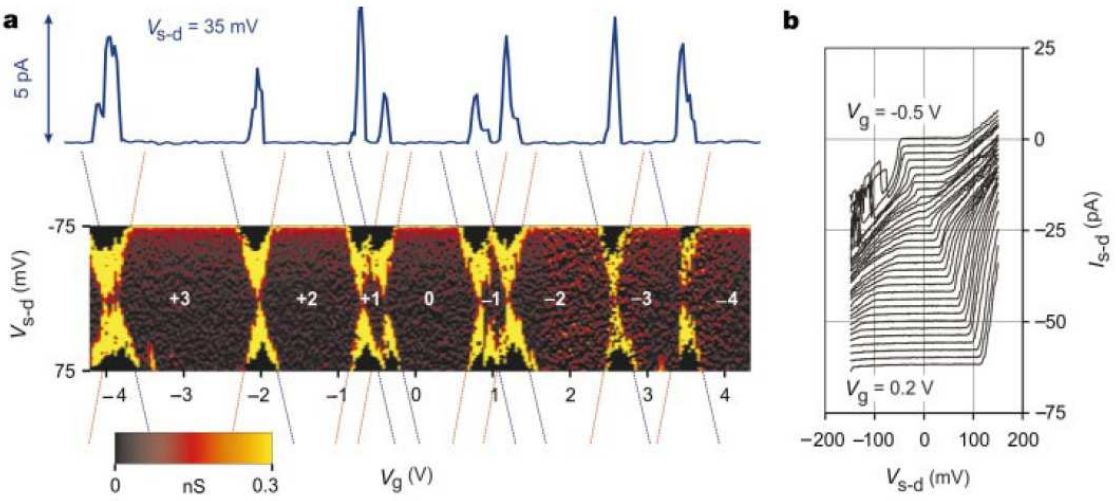

Figure 1.4: Experimentally resolved Coulomb blockade diamonds and nonlinear current for a single-OPV5 molecular junction at 4.2K. (a) The differential conductance as a function of gate voltage (horizontal axis) and bias voltage (vertical axis). (b) Traces of several nonlinear currents. Image is from Ref. 101.

ing devices is often quite low. Moreover, electromigration is a complex process with many associated difficulties, making it an experimentally challenging technique [119]. With that in mind, many of the most spectacular single-molecule transport experiments have been done using fixed-gap devices [149, 101, 145, 115, 116].

In a particularly remarkable experiment, Kubatkin and colleagues [101] utilized electromigration techniques to fabricate a fixed-gap three terminal junction, with the ability to adjust both the bias and gate voltage of the molecule. On top of the aluminium gate electrode the group lithographically patterned gold electrodes by adjusting the angle of the mask with reference to the deposition beam, shown schematically in Fig. 1.3. Once a 2nm gap was prepared the junction was warmed slightly, oligophenylenevynylene (OPV5) molecules were deposited and the gap was monitored until the conductance changed. Once a working device was fabricated, the group investigated the transport as a function of bias voltage and gate voltage. The resulting spectra, shown in Fig. 1.4, were all collected at liquid helium temperatures ($\sim$4.2K) and exhibit the Coulomb blockade diamonds associated with multiple charge states of the molecule. Coulomb blockade cannot be explained with an ef-

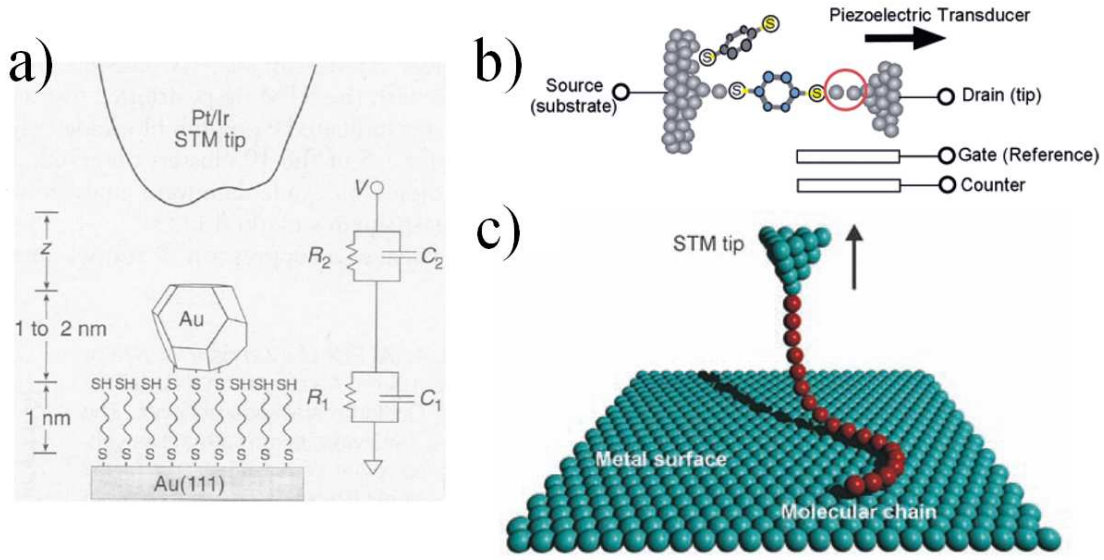

Figure 1.5: Image of various scanning-tunneling microscope (STM)-based single-molecule measurement methods. (a) From Ref. 8, a gold nanograin is used to contact a molecular self-assembled monolayer (SAM). (b) From Ref. 203, a gold STM tip collides with and is then extracted from a conducting surface with evaporated molecules forming thousands of break junctions. The measured current traces are used to generate conductance histograms for a single molecule. (c) From Ref. 105, the charge transport as a function of length is measured for a single poly-fluorene wire by binding it to an STM tip and subsequently adjusting the height of the tip relative to a conducting surface, effectively changing the length of the wire in the process.

fective single-particle theory since charge quantization is non-perturbative. This remarkable result is also motivation for the development of our many-body theory of electronic transport.

Very recently, Song and colleagues observed gating in molecular junctions composed of molecules as small as 1,4-benzenedithiol [175]. Although they were not able to consider such a molecule in the 'meta' configuration, their work does represent a major step toward the realization of a single-molecule transistor [29].

1.1.3 STM junctions

The first successful investigations of the electrical response of single molecules were performed using a scanning-tunneling microscope (STM) [25]. The device consists

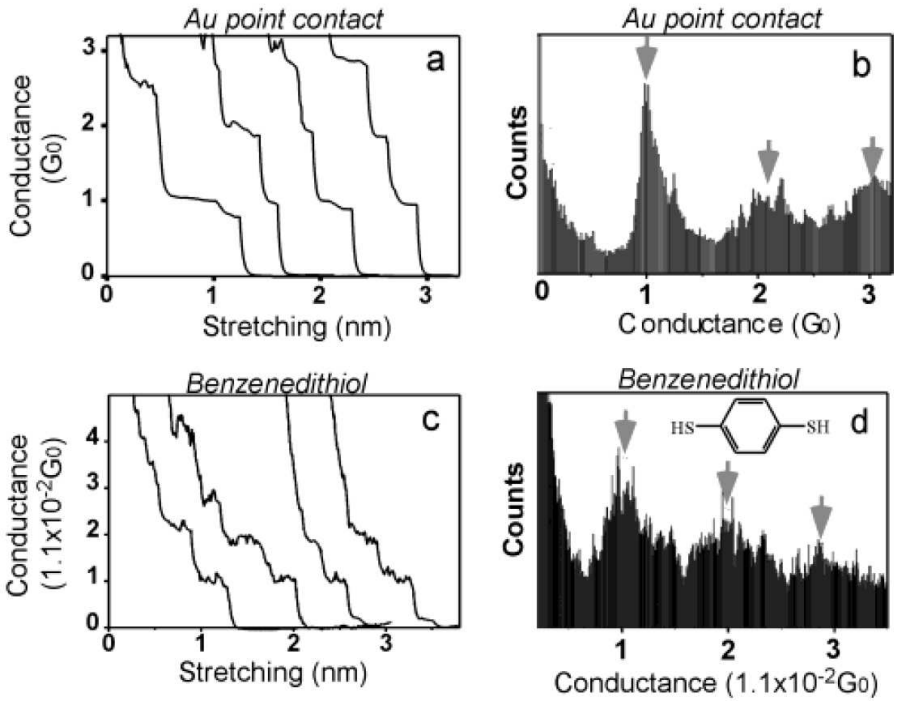

Figure 1.6: Measurements by Xiao et al. of the electronic response of gold and benzenedithiol using the contact-method with an STM. By repeatedly contacting the gold tip with a gold surface covered with molecules many thousands of molecular junctions were formed and measured. Using the current vs. distance traces conductance histograms were then constructed showing quantized conductance. For example, the conductance of benzenedithiol $\sim .011 G_0$. Similar experiments were performed by Venkataraman et al. using amine (nitrogen atom with lone pair) end-groups rather than thiols (sulfur-hydrogen) . Image is from Ref. 203.

of a conducting surface upon which a molecule is deposited and an atomically sharp tip which can be moved in space using piezo-elements. Over the past few decades, the STM has been used extensively for 'imaging' molecules on the surface of metals [201]. The image, of course, is actually a map of the electronic transmission which, as we will see in chapter 4, may relate to the molecular surface in a complex way.

Modified STM devices have also been used to form molecular junctions by a number of methods, several of which are shown schematically in Fig. 1.5. Because of their widespread usage in the molecular electronics community [203, 15, 195, 152, 204], we'll focus on the so-called contact method. As the name suggests, in the

contact method the STM is operated as an automated break junction where, using a computer controlled feedback loop, the conducting tip is pushed into *contact* with the conducting substrate immersed in a solution of molecules. Under fixed bias the tip is then extruded and the current is recorded. As shown in Fig. 1.6c, the current vs. distance traces have discrete plateaus corresponding to integral numbers of molecules in the junction. Since the STM tip is held at fixed bias the current can be used to generate conductance histograms, shown in panels (b) and (d) of the same figure. Like the break junction, this technique has the advantage of giving reproducible data that can be accumulated for longer times to lower statistical variations. In addition, the temperatures of both the substrate and the STM tip can be accurately controlled via joule heating, allowing both thermal and electronic measurements to be performed simultaneously in a single-molecule junction [15, 152].

For thiols on gold, the force required to break the Au-S bond is larger than that for the Au-Au bond, leading to grain migration, pitting of electrodes, and metal island formation that may complicate the interpretation of single-molecule measurements using this STM method. For this reason, several groups have investigated alternative chemical methods for binding molecules to the gold surface [35, 195].

1.2 Quantum transport

Quantum transport investigates the flow of conserved 'stuff' – mass, energy, particle number, charge, momentum – at the quantum scale. In the context of molecular junctions, the flowing stuff is most often the charge and heat of electrons. Because the term 'quantum scale' is quite vague and encompasses a large range in the physical dimensions of a system let us consider several important length scales involved in electronic transport:

- **The de Broglie wavelength λ**

  In his 1924 PhD thesis, Louis de Broglie postulated that the momentum-wavelength relation for a photon may also be true for material particles as well.

Many experiments since have validated his matter wave hypothesis which may be expressed mathematically as

$$\lambda = \frac{h}{p}, \tag{1.1}$$

where p is the momentum of the massive object and h=4.1356×10^{-15}eV · s is Planck's constant. For a Fermi gas p_{F}=$\sqrt{2m_{\mathrm{e}}E_{\mathrm{F}}}$, where m_{e}=9.109×10^{-31}kg is the electron mass and E_{F} is the Fermi energy. The experimentally measured Fermi surface of Gold is very nearly spherical, meaning that it is well modeled as a Fermi gas. With a Fermi energy of 5.5eV

$$\lambda_{\mathrm{Au}} = .52\mathrm{nm}, \tag{1.2}$$

- **The mean free path L_{m}**

  The mean free path L_{m} is the characteristic distance a particle travels between momentum altering collisions with impurities and is defined as

$$L_{\mathrm{m}} = v\tau_{\mathrm{m}}, \tag{1.3}$$

  where v is the particle's velocity and τ_m is the 'transport relaxation time'. The mean free path is not generally equal to the mean distance between collisions since the effectiveness of a collision at destroying the initial momentum state of a particle is rarely unity [42]. Taking the particle to be an electron at the Fermi-surface of a large piece of gold

$$L_{\mathrm{m}} = v_{\mathrm{F}}\tau_m = \sqrt{\frac{2E_{\mathrm{F}}}{m_e}}\tau_{\mathrm{m}} \approx 50nm, \tag{1.4}$$

  where τ_{m} ∼0.35fs [9, 95].

- **The phase-relaxation length L_ϕ**

  The phase-relaxation length L_ϕ is analogous to the coherence length in optics. Coherence is a measure of interferability which in the electronic case is related to the phase of the wavefunction. Consider the Aharonov-Bohm ring shown schematically in Fig. 1.7, in which an electron is split along two arms of a

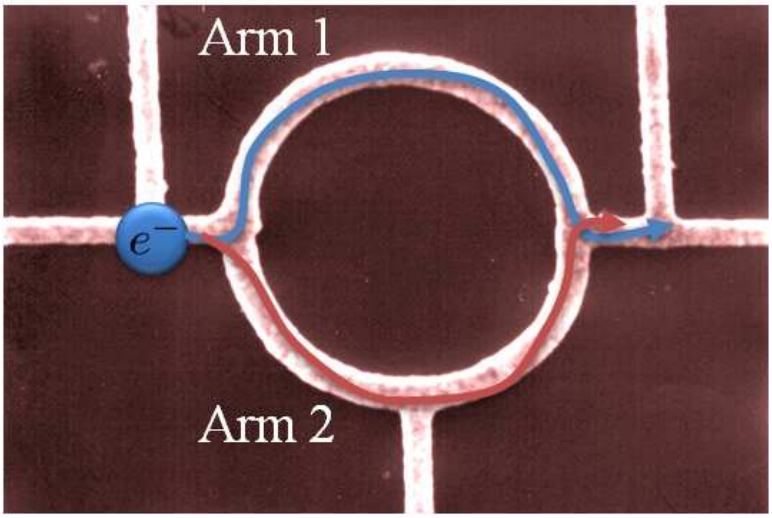

Figure 1.7: A SEM image of a microfabricated gold ring for Aharonov-Bohm type experiments. The two arms of the interferometer are labeled 'Arm 1' and 'Arm 2', respectively. Near the second arm is an additional lead used to adjust the phase relationship between the two arms. The ring is 70nm wide, 20nm thick with a diameter of 800nm. Image is modified from Ref. 184.

conducting ring. If we introduce static impurities into the arms the system still obeys time-reversal symmetry and although the phase relationship between the two arms will have changed, it still exists. Instead, if a dynamic source of phase randomization is present, for example caused by electron-electron scattering in either (or both) arms of the ring, then the phase in the two arms will be less correlated. The phase-relaxation length may be defined as

$$L_\phi = v\tau_\phi, \tag{1.5}$$

where v is the velocity and τ_ϕ is the characteristic time that a particle maintains a phase relation with itself.

In an Ohmic conductor, the electrical conductance G is related to the dimensions of a particular sample by a material dependent, but dimensionally independent, conductivity σ. For a two-dimensional conductor [42]

$$G = \sigma\frac{W}{L}, \tag{1.6}$$

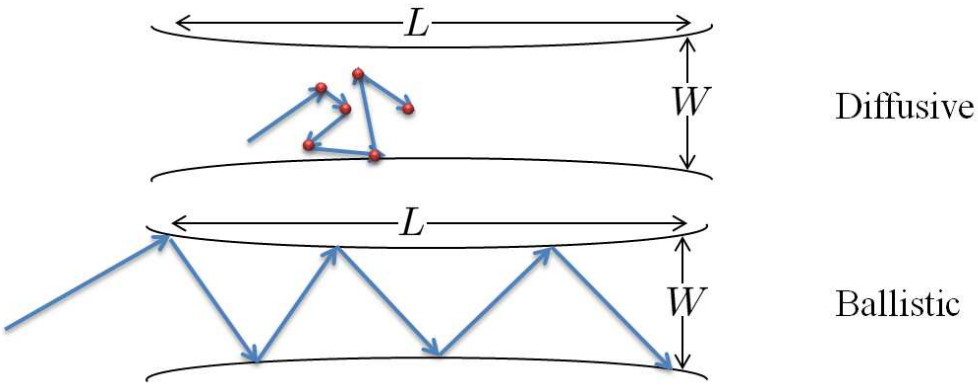

Figure 1.8: A schematic representation of the diffusive and ballistic transport regimes. In the former, the mean free path of the electron is much shorter than either the width W or length L of the conductor with the red dots indicating electron-electron scattering events. In the ballistic regime the mean free path of the electron is larger than the dimensions of the conductor.

where W and L are the width and length of the conductor, respectively. The transport in macroscopic conductors is diffusive, meaning that on average electrons scatter many times as they move across the sample, i.e. $L_{\mathrm{m}}, L_{\phi} < L$. As the dimensions of the conductor are reduced we expect that Eq. (1.6) will eventually break down because the sample will be smaller than the mean free path or phase-relaxation length. This is the so-called *ballistic transport regime* where electrons don't scatter in the conductor, shown schematically in Fig. 1.8. In this regime the wave nature of the electron appears prominently and the junction can be thought of as an electronic waveguide. The molecules often used in molecular junctions are usually on the order of several angstroms in size, meaning that their transport is predominantly ballistic in nature. In the next section, we briefly review main concepts of ballistic transport which will appear throughout this thesis.

1.2.1 Ballistic transport: The Landauer-Büttiker approach

Consider a two-terminal junction, molecular or otherwise, like that represented in the lower half portion of Fig. (1.8) with a central constriction with a length L and width W such that $L \gg W$. Here, we assume that the spatial confinement of

the constriction is absolute so that the electrons do not exceed the boundaries of the confinement, i.e. the transverse eigenfunctions are $\sin(\pi ny/W)$, where y is the transverse spatial coordinate.

If the chemical potential of the left-hand reservoir μ_{Left} is greater than that of the right-hand reservoir μ_{Right}, then the current carried by channel n is given by

$$I_n = ev_n N_n \equiv ev_n \frac{\partial N_n}{\partial E}(\mu_{\text{Left}} - \mu_{\text{Right}}), \tag{1.7}$$

where e is the electron's charge, v_n is the longitudinal velocity of the electron, N_n is the particle density in mode n, and $\frac{\partial N_n}{\partial E}$ is the density of states (DOS) in mode n. In one-dimension

$$\frac{\partial N_n}{\partial k} = \frac{1}{\Lambda}\frac{\Lambda}{2\pi} = \frac{1}{2\pi}, \tag{1.8}$$

where the spacing between k-states given by $2\pi/\Lambda$ and Λ is the period used in the periodic boundary conditions. The velocity is related to the electronic dispersion as

$$v_n = \frac{1}{\hbar}\frac{\partial E}{\partial k} \tag{1.9}$$

such that the current becomes

$$I_n = \frac{e}{\hbar}\frac{\partial E}{\partial k}\frac{\partial N_n}{\partial E}(\mu_{\text{Left}} - \mu_{\text{Right}}) = \frac{e}{2\pi\hbar}(\mu_{\text{Left}} - \mu_{\text{Right}}). \tag{1.10}$$

Equation (1.10) shows that the left-hand reservoir supplies all channels with the same current irrespective of the carrier velocities. Physically, this means that in terms of the current an abundance of slow carriers is equivalent to a relative dearth of fast carriers. Assuming that the coupling to the electrodes is weak we can relate the chemical potential's of the leads to the potential difference and find the conductance of a single-channel conductor, namely

$$G = \frac{I}{V} = \frac{\frac{e}{2\pi\hbar}(\mu_{\text{Left}} - \mu_{\text{Right}})}{(\mu_{\text{Left}} - \mu_{\text{Right}})/e} = \frac{e^2}{h} \equiv G_0, \tag{1.11}$$

where $\hbar$=$h/2\pi$ and h is Planck's constant. Including spin, the conductance quantum G_0=$2e^2/h$ $\sim$1/12.9kΩ. The first experimental experimental measurement of quantized electrical conductance is shown in Fig. 1.9. Their data exhibit characteristic plateaus of conductance corresponding to the opening of new transport

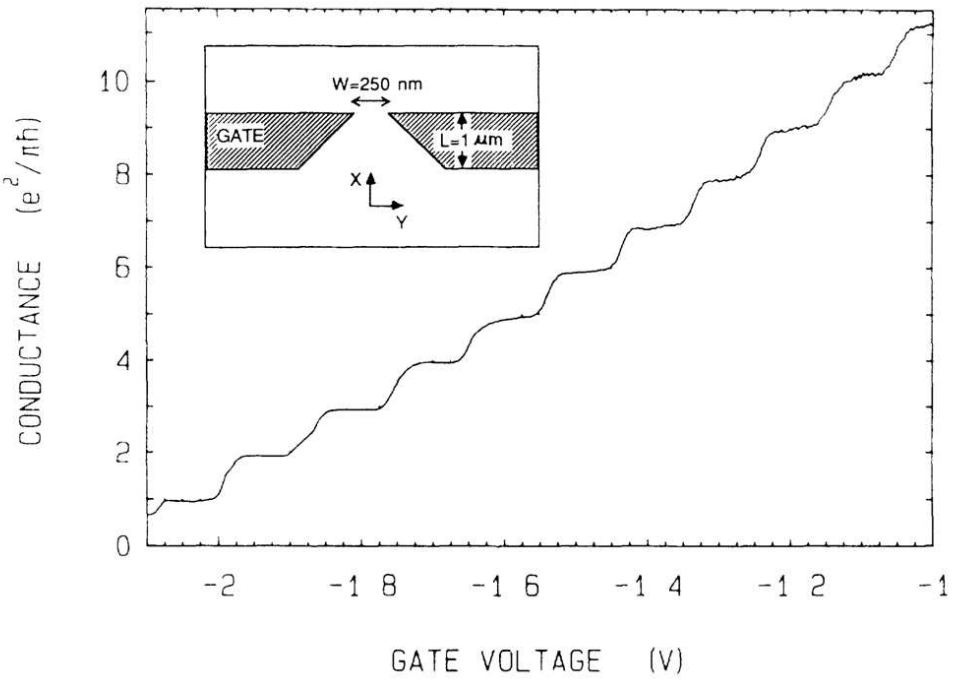

Figure 1.9: The conductance for a quantum point contact formed by gating the two-dimensional electron gas formed at the GaAs-AlGaAs interface. The characteristic plateaus correspond to the opening of new transport channels. Modified from Ref. 194.

channels in strong support of Landauer's statement "conductance is transmission". The conductance of a disordered metal in contact with two electron reservoirs is given by the Landauer formula

$$G = \frac{2e^2}{h} \sum_n \tau_n, \tag{1.12}$$

where τ_n is the transmission probability for the mode n of the conductor.

Motivated by the confusion of how to interpret the two- or four-probe conductance measurement results of mesoscopic electronic systems of 1985, Büttiker found an elegant solution which has since become the standard method of tackling this type of conductance problem [28]. The key concept Büttiker realized was to treat the current probes and voltage probes on an equal footing, i.e. making no qualitative distinction between current and voltage leads. Each probe is treated as a reservoir having its own chemical potential. The current flowing into lead m in a

multi-terminal junction is then found in a natural way where

$$I_m = \sum_{n=1}^{P} G_{mn}\mu_n, \tag{1.13}$$

where P is the total number of probes in a junction and

$$G_{mn} = \frac{e^2}{h}\sum_{ij} T_{ij}^{mn} \tag{1.14}$$

is the conductance between probes n and m. Here T_{ij}^{mn} is the transmission probability from channel j in lead n to mode i in lead n.

Now that we have enunciated the basic formulation of quantum transport, let us continue by discussing how to determine the transmission probability for a physical system. In the next section, we'll review several aspects of Green's function theory as it applies to the many-body problem of electrons. The modulus squared of the quantum Green's function is proportional to the transmission probability and is therefore an important part of our theoretical treatment of transport.

1.3 Green's functions

Green's functions, named after their self-taught mathematician inventor George Green, have found a host of applications in almost every scientific field. Originally, Green's functions were developed to solve inhomogeneous differential equations with specific boundary conditions. For an equation of the form

$$\mathcal{L}u(r) = f(r), \tag{1.15}$$

where $\mathcal{L}$ is a differential operator, f is the source term and r indicates an ordered set of coordinates, the Green's function is defined as the 'impulse response' or 'influence function' of $\mathcal{L}$ whereby

$$\mathcal{L}\mathcal{G}(r, r') = \delta(r - r'). \tag{1.16}$$

The great power of $\mathcal{G}$ lies in the fact that the solution $u(r)$ can be expressed as a sum (integral) of these impulse responses weighted by the source term

$$\int dr'\mathcal{G}(r, r')f(r') = u(r). \tag{1.17}$$

As we shall see in the chapters that follow, transport is conveniently phrased in terms of correlation functions. Although these correlation functions do not have the same mathematical form as the Green's function we have just discussed, they do share a philosophical verisimilitude. In a many-particle system, one is often interested in perturbing a configuration of particles by adding an additional particle at some position and time, waiting for a period of time and then asking what the probability is that a particle could be removed from some other position. Similarly, we are also often interested in the response of a system to the injection of a particle vacancy or hole.

Mathematically, there are a number of ways to express this response. Perhaps the most common is the time-ordered Green's function [124, 55]

$$G^{\mathrm{T}}_{\alpha\beta}(t_1,t_2) = -i\left\langle T\left(d_\alpha(t_1)d^\dagger_\beta(t_2)\right)\right\rangle \tag{1.18}$$

where $\langle\cdots\rangle$ indicates an average over all accessible equilibrium states and $d(t)$ and $d^\dagger(t)$ are Fermionic annihilation and creation operators in Heisenberg form, respectively. The Dyson time-ordering operator T orders operators such that later terms appear to the left of earlier ones as

$$T\left(d_\alpha(t_1)d^\dagger_\beta(t_2)\right) = \theta(t_1-t_2)d_\alpha(t_1)d^\dagger_\beta(t_2) - \theta(t_2-t_1)d^\dagger_\beta(t_2)d_\alpha(t_1), \tag{1.19}$$

where $\theta(t)$ is the Heaviside step function and the minus sign in the second term arises because $\{d_\alpha, d^\dagger_\beta\}=\delta_{\alpha\beta}$. Equation (1.18) may also be expressed as

$$G^{\mathrm{T}}_{\alpha\beta}(t_1,t_2) = \begin{cases} G^<_{\alpha\beta}(t_1,t_2) = i\langle d^\dagger_\beta(t_2)d_\alpha(t_1)\rangle & \text{if } t_2 > t_1 \\ G^>_{\alpha\beta}(t_1,t_2) = -i\langle d_\alpha(t_1)d^\dagger_\beta(t_2)\rangle & \text{if } t_2 < t_1, \end{cases} \tag{1.20}$$

where the G-lesser $G^<$ and G-greater $G^>$ functions are important in nonequilibrium problems. The time-ordering operation is of critical importance in the perturbation expansion that follows. In all discussions $\hbar$=1.

In the Heisenberg representation the time dependence of an operator is given by

$$\mathcal{O}_{\mathrm{H}} = e^{iHt}\mathcal{O}(0)e^{-iHt}, \tag{1.21}$$

where $\mathcal{O}(0)$ is a time-independent (Schrödinger) operator. Since the many-body problem is not generally integrable, we separate the Hamiltonian into two parts in the following way

$$H = H_0 + V(t), \tag{1.22}$$

where we assume that the 'free' term H_0 is time-independent, while the interaction term $V(t)$ *may* be time-dependent. Usually, H_0 is chosen as a Hamiltonian which is exactly solvable. As we shall see, a major advantage of phrasing the problem in this way is that the diagrammatic many-body perturbation theory that follows is an expansion in processes considered rather than process order, meaning that a finite number of physical processes can be included to infinite order.

Although the time-ordered Green's function is extremely useful as a mathematical tool, the retarded Green's function is more useful intuitively. As we shall see, however, the two are related and the choice of which to use is often a matter of taste and the problem at hand.

1.3.1 The retarded Green's function

The retarded Green's function is defined as follows

$$G^{\mathrm{R}}_{\alpha\beta}(t_1, t_2) = -i\theta(t_1 - t_2) \left\langle \left\{ d_\alpha(t_1), d^\dagger_\beta(t_2) \right\} \right\rangle, \tag{1.23}$$

where t_1 and t_2 are times, θ is the Heaviside step function, d ($d^\dagger$) are Fermionic annihilation (creation) operators in Heisenberg form, $\{\cdots\}$ indicates an anti-commutation operation and $\langle\cdots\rangle$ represents the statistical and quantum-mechanical average. The term retarded refers to the fact that the correlation is between the addition and removal of particles where the latter occurs a time $t_1 - t_2$ later than the former and is therefore temporally *retarded* in comparison. As this is the most often used Green's function in our work, we will drop the retarded label and assume that G refers to the retarded Green's function unless indicated otherwise. However, our choice of Green's function is a matter of convenience since the lesser, time-ordered and retarded Green's functions are each related to one another by

$$G^{\mathrm{R}} = G^{\mathrm{T}} - G^{<}. \tag{1.24}$$

For all Green's functions, the α and β indices are specific to the problem being considered, but in the case of molecular electronics they most often label the atomic orbitals of the molecule.

If the perturbation $V(t)$=0, then Eq. (1.23) may be evaluated explicitly using Eq. (1.21). Since the eigenvalues of H_0 are known exactly then, similarly, the retarded Green's function of this *free particle* is also known exactly. Before considering the case of $V(t) \neq 0$, it is instructive to examine the Green's function of a free-particle in some detail.

Free-particle Green's function

In order to simplify the present discussion we'll consider the zero-temperature Green's function, where the thermal average over states reduces to an evaluation of just the ground state. The more realistic case of non-zero temperature can then be evaluated by considering the thermal distribution of these Green's functions. Using Eq. (1.21), the retarded Green's function (1.23)

$$\begin{aligned} G^{(0)}_{\alpha\beta}(t_1,t_2) &= -i\theta(t_1-t_2)\left\langle \phi_0 \left| \left\{ e^{iH_0t_1} d_\alpha e^{-iH_0t_1}, e^{iH_0t_2} d^\dagger_\beta e^{iH_0t_2} \right\} \right| \phi_0 \right\rangle \\ &= -i\theta(t_1-t_2)\Big\{ \left\langle \phi_0 \left| d_\alpha e^{-iH_0t_1} e^{iH_0t_2} d^\dagger_\beta \right| \phi_0 \right\rangle + \\ &\qquad \left\langle \phi_0 \left| d^\dagger_\beta e^{iH_0t_2} e^{iH_0t_1} d_\alpha \right| \phi_0 \right\rangle \Big\} \\ &= -i\theta(t_1-t_2) e^{i(\varepsilon_\beta t_2 - \varepsilon_\alpha t_1)} \left\{ d_\alpha, d^\dagger_\beta \right\} \\ &= -i\theta(t_1-t_2) e^{i\varepsilon_\alpha(t_2-t_1)} \delta_{\alpha\beta} \end{aligned} \tag{1.25}$$

where ϕ_0 is the ground state of free-particle Hamiltonian $H_0 = \sum_n \varepsilon_n d^\dagger_n d_n$ and we have assumed that $H_0 \left|0\right\rangle = 0$ while $H_0 d_\alpha \left|0\right\rangle = -\varepsilon_\alpha d_\alpha \left|0\right\rangle$ and $H_0 d^\dagger_\alpha \left|0\right\rangle = +\varepsilon_\alpha d^\dagger_\alpha \left|0\right\rangle$ and the Fermionic anti-commutation relation $\left\{ d_\alpha, d^\dagger_\beta \right\} = \delta_{\alpha\beta}$. As a quantum Green's function, G may be interpreted as the probability amplitude of finding the system at time t_1 with a particle in energy eigenstate α given that a particle was added in the energy eigenstate β at time t_2. Equation (1.25) indicates that for all $t_1 > t_2$ the probability is unity since $\left| G^{(0)}_{\alpha\beta} \right|^2 = 1$, so long as $\alpha = \beta$. Physically, this result is a reflection of the infinite lifetime of the free-particle and is quite intuitive, since

without any outside influences we would expect a particle initially in an energy eigenstate to remain in that eigenstate.

It is interesting to consider Eq. (1.25) in the Fourier domain

$$\begin{aligned} G^{(0)}_{\alpha\beta}(E) &= \mathscr{F}\Big\{G^{(0)}_{\alpha\beta}(t_1-t_2)\Big\} = \int_{-\infty}^{\infty} dt'\; G^{(0)}_{\alpha\beta}(t')e^{iEt'} \\ &= -i\delta_{\alpha\beta}\int_{-\infty}^{\infty} dt'\theta(t')e^{iEt'}e^{-i\varepsilon_\alpha t'} \equiv -i\delta_{\alpha\beta}\int_{-\infty}^{\infty} dt'\theta(t')e^{iEt'}e^{-i(\varepsilon_\alpha+i\eta)t'} \\ &= -\frac{e^{i(E-\varepsilon_\alpha+i\eta)t'}}{E-\varepsilon_\alpha}\bigg|_{t'=0}^{\infty} = \delta_{\alpha\beta}\lim_{\eta\to 0^+}\left[\frac{1}{E-\varepsilon_\alpha+i\eta}-\frac{e^{i(E-\varepsilon_\alpha+i\eta)\infty}}{E-\varepsilon_\alpha+i\eta}\right] \\ &= \frac{\delta_{\alpha\beta}}{E-\varepsilon_\alpha+i0^+}, \end{aligned} \tag{1.26}$$

where we have assumed that G is time-shift invariant. δ is a positive infinitesimal used to evaluated the exponential at ∞, where whenever t' is finite $\eta\times t'=0$ and when t' is infinite $\eta\times t'=\infty$. In this work, we often use the notation $i0^+$ as a shorthand for introducing a factor $i\eta$ in the exponential and taking the limit in which the variable approaches zero from the right at the end of the calculation.

Equation (1.26) is an important result directly linking the eigenvalues of the Hamiltonian to the pole structure of the Green's function. In order to highlight this point we rewrite Eq. (1.26) in matrix form as

$$G^{(0)}(E) = \left(\mathbf{1}E - H_0 + i0^+\right)^{-1}, \tag{1.27}$$

where $\mathbf{1}$ is the identity matrix. Equation (1.27) is quite general and holds for any Hamiltonian H_0 which is bilinear in creation and annihilation operators, namely where $H_0{=}\sum_{n,m} h_{nm}d_n^\dagger d_m$. In chapter 2, we develop a many-body theory of quantum transport using a molecular Hamiltonian to construct $G^{(0)}$ which includes two-body interaction terms quartic in field operators. As we'll see, these Green's functions can't generally be expressed as in Eq. (1.27). However, if the two-body term is factorized, as in the Hartree-Fock approximation, then Eq. (1.27) still holds.

Before moving on to interacting particles let us relate the Green's function to a macroscopic observable, the density of states (DOS). We begin by introducing the spectral function

$$A_{\alpha\beta}(E) = i\left[G_{\alpha\beta}(E) - G^\dagger_{\alpha\beta}(E)\right] = -2\,\mathrm{Im}\left\{G_{\alpha\beta}(E)\right\} \tag{1.28}$$

which is closely related to the DOS

$$\rho(E) = \frac{1}{2\pi} \mathrm{Tr}\{A_{\alpha\beta}\}. \tag{1.29}$$

We mention in passing that the spectral function obeys a sum rule, namely $\int A_{\alpha\beta}(E)/2\pi = \delta_{\alpha\beta}$, which holds true even in the interacting system. Using the free particle Green's function given by Eq. (1.26), the spectral function for the free-particle is

$$\begin{aligned} A_{\alpha\beta} &= -2\delta_{\alpha\beta} \,\mathrm{Im}\left\{\frac{1}{E - \varepsilon_\alpha + i0^+}\right\} \\ &= +2\pi\delta_{\alpha\beta}\delta(E - \varepsilon_\alpha), \end{aligned} \tag{1.30}$$

and the corresponding DOS is given by

$$\rho(E) = \sum_\alpha \delta(E - \varepsilon_\alpha), \tag{1.31}$$

where we have used the Sokhatsky-Weierstrass theorem (or 'Dirac identity') in deriving Eq. (1.30)

$$\lim_{\eta\to 0^+} \frac{1}{x + i\eta} = P\left\{\frac{1}{x}\right\} - i\pi\delta(x). \tag{1.32}$$

If the particle is not free but has a long lifetime τ such that $\tau^{-1} \ll \varepsilon_\alpha$, then the spectral function becomes a Lorentzian with height $2/\tau$ and a half-width at half-maximum of τ^{-1}. In the next section, we will add the interactions back into the system and develop a diagrammatic method to express the perturbation theory that follows.

1.3.2 Diagrammatic perturbation theory

As we have seen, without interactions the Green's function is both intuitive and mathematically straightforward to calculate. But what happens when interactions are turned on? Physically, we no longer expect the stationary states of the free-particle to be the stationary states of the interacting system; instead the new *quasi*-particle excitation of the system will be imbued with finite lifetimes and new energies. This complex cacophony of particle interactions occurs in addition to the

intrinsic fluctuations of a quantum system. Together these facts mean that the full quantum many-body problem is generally a very difficult problem to solve.

Fortunately, this problem has been studied extensively since the inception of quantum mechanics over 100 years ago. Although no analytic solution is known, various perturbative methods have been developed to find approximate solutions to the problem. In this section, we'll outline the salient aspects of a diagrammatic approach which we use extensively in later chapters.

In order to formulate a many-body perturbation theory in terms of Green's functions, it is advantageous to consider quantum mechanics in the *interaction representation*, where operators and states both depend on time in the following way

$$\mathcal{O}(t) = e^{iH_0 t}\mathcal{O}(0)e^{-iH_0 t} \tag{1.33}$$

and

$$|\psi(t)\rangle = e^{-iH_0 t}e^{-iH(t)t}\,|\psi(0)\rangle \tag{1.34}$$

where $\mathcal{O}(0) \equiv \mathcal{O}_S$ is a Schrödinger (time-independent) operator. Recalling that $H(t) = H_0 + V(t)$ and that, in general, $[H_0, V(t)] \neq 0$ and consequently that $e^{H_0}e^{V(t)} \neq e^{H(t)}$, it is evident that that the exponent in Eq. (1.34) is *not* simply $e^{-iV(t)t}$.

Consider the evolution of the state vector $|\psi(t)\rangle$ given by Eq. (1.34) over an infinitesimal time interval δt. Over such a short time interval we know

$$\begin{aligned}
\frac{\partial}{\partial t}\,|\psi(t)\rangle &= -iV(t)\,|\psi(t)\rangle \\
\lim_{\delta t\to 0}\frac{|\psi(t+\delta t)\rangle - |\psi(t)\rangle}{\delta t} &= -iV(t)\,|\psi(t)\rangle \\
\Rightarrow |\psi(t+\delta t)\rangle &\cong [1 - i\delta t V(t)]\,|\psi(t)\rangle \cong e^{-iV(t)\delta t}\,|\psi(t)\rangle
\end{aligned} \tag{1.35}$$

where the exponential of an operator is interpreted in the usual way as a Taylor expansion

$$e^{\mathcal{O}} = \mathbf{1} + \mathcal{O} + \frac{1}{2!}\mathcal{O}^2 + \ldots + \frac{1}{n!}\mathcal{O}^n + \ldots \tag{1.36}$$

In general the Hamiltonian is the generator of time evolution and, as Eq. (1.35) indicates, in the interaction representation over an infinitesimal time interval the state evolves according to $V(t)$.

The S-matrix

At this point we introduce the S-matrix $S(t, t_0)$ which evolves a state from time t_0 to t [202, 51]. By repeated application of the infinitesimal evolution given in Eq. (1.35) we find

$$\begin{aligned} S(t,t_0) &= \lim_{\delta t\to 0} e^{-iV(t_0)\delta t}e^{-iV(t_0+\delta t)\delta t}\times\cdots\times e^{-iV(t-\delta t)\delta t}e^{-iV(t)\delta t} \\ &= T\left[\exp\left(-i\int_{t_0}^{t}dt'V(t')\right)\right] \\ &= \sum_{n=0}^{\infty}\left(-\frac{i}{\hbar}\right)^n\frac{1}{n!}\int_{t_0}^{t}dt_1\cdots\int_{t_0}^{t_{n-1}}dt_nT\left[V(t_1)\cdots V(t_n)\right]. \end{aligned} \tag{1.37}$$

It is straightforward to show that the S-matrix operator is unitary and may be concatenated as[1]

$$S(t,t_0) = S(t,t')S(t',t_0). \tag{1.38}$$

Equation (1.37) is deceptively simple. If $V(t)$ at different times commute, then the T operation reduces to the identity operator and we recover the result we would expect for a product of exponentials. In general however $[V(t), V(t')] \neq 0$, meaning that evaluation of the time-ordering operation T is an involved process which gives rise to many high-order operator products. In fact, the evaluation of non-equal time commutation relations lies at the very heart of the many-body problem and is the goal of Green's function theory!

So what point is there in just rephrasing the same intractable problem? Before we answer that, consider the expectation value of the operator $\mathcal{O}(t)$

$$\langle\mathcal{O}(t)\rangle = \frac{\langle\psi(t)|\,\mathcal{O}(t)\,|\psi(t)\rangle}{\langle\psi(t)|\psi(t)\rangle}. \tag{1.39}$$

Next, we imagine that in the distant past there were no interactions and that the interactions were 'turned on' adiabatically so that we can begin in some known ground state of H_0 and evolve the system to include interactions. At zero-temperature, the

[1]Eq. (1.34) may also be expressed using the time-ordering notation as $|\psi(t)\rangle = S(t,0)\,|\psi(0)\rangle$.

relationship between the ground state of H_0 and the ground state of the interacting case is established by the Gell-Mann Low theorem which states that: a system in a nondegenerate stationary state cannot make a transition into another state under the action of an infinitely slow perturbation [62, 124, 55]. Mathematically, this statement may be expressed as follows

$$|\psi(t)\rangle = S(t,-\infty)\,|\phi_0\rangle \tag{1.40}$$

such that

$$\begin{aligned}\langle\mathcal{O}(t)\rangle &= \frac{\langle\phi_0|\,S(-\infty,t)\mathcal{O}(t)S(t,-\infty)\,|\phi_0\rangle}{\langle\phi_0|\,S(-\infty,t)S(t,-\infty)\,|\phi_0\rangle} \\ &\equiv \frac{\langle\phi_0|\,T\left[\mathcal{O}(t)S\right]|\phi_0\rangle}{\langle\phi_0|\,S\,|\phi_0\rangle}\end{aligned} \tag{1.41}$$

where $|\phi_0\rangle$ is the ground state of H_0 and in the second step we have assumed *time-reversal symmetry* of the system such that

$$S(-\infty,t) = S(\infty,t). \tag{1.42}$$

We have also defined $S \equiv S(\infty,-\infty)$ recognizing that by Eq. (1.38) $S(\infty,-\infty)$=$S(\infty,t')S(t',-\infty)$. Physically, $\langle\phi_0|\,S\,|\phi_0\rangle$ corresponds to a sum over *vacuum polarization graphs* [124, 127, 55] which correspond to the infinite number of ways quantum fluctuations can perturb a vacuum state and return to a vacuum state. The time-ordered product may be written explicitly as

$$T\left[\mathcal{O}(t)S\right] = \sum_{n=0}^{\infty}\left(-\frac{i}{\hbar}\right)^n\frac{1}{n!}\int_{-\infty}^{\infty}dt_1\cdots\int_{-\infty}^{\infty}dt_n T\left[\mathcal{O}(t)V(t_1)\cdots V(t_n)\right]. \tag{1.43}$$

As we have already seen, Green's functions are expectation values of operators. Equation (1.43) shows us that the exact expression for the expectation value of an operator is a sum of terms in which the interaction Hamiltonian acts n times, where $n \geq 0$. This is very exciting, since we have already derived an analytic expression for the $n = 0$ term of the Green's function $G^{(0)}$. Ideally, we would like to express the expectation value as a series in $G^{(0)}$ and something related to $V(t)$. In order to do that, however, we need a systematic way of dealing with the time-ordered products of the form $T(ABCD\cdots XYZ)$ where A,B, etc. are creation and annihilation operators.

Wick's theorem

A powerful method useful in evaluating expressions like Eq. (1.43) is Wick's theorem, [55, 124, 1] which states that a time-ordered product of operators may be decomposed into a sum over normal products involving zero or more contractions. Symbolically, Wick's theorem may be expressed as [1]

$$\begin{aligned} T(ABCD\cdots XYZ) &= N(ABC\cdots XYZ) \\ &+ N(\overbrace{AB}C\cdots XYZ) + N(\overbrace{ABC\cdots XY}Z) + \cdots \\ &+ N(\overbrace{AB}\overbrace{C\cdots XY}Z) + N(\overbrace{A\overbrace{BC}\cdots XY}Z) + \cdots \\ &+ \cdots \\ &+ N(\overbrace{AB}\overbrace{C\cdots XY}\overbrace{Z}) + N(\overbrace{A\overbrace{BC}\cdots XY}\overbrace{Z}) + \cdots \end{aligned} \tag{1.44}$$

where the operator N normal orders an operator product such that creation operators appear to the left of the annihilation operators and the 'pairing' or 'contraction' operator

$$\overbrace{AB} = T(AB) - N(AB). \tag{1.45}$$

The trick of Wick's theorem is that the average over the ground state of a normal-ordered product vanishes such that

$$\langle\phi_0|\,\overbrace{AB}\,|\phi_0\rangle = \langle\phi_0|\,T(AB)\,|\phi_0\rangle \tag{1.46}$$

and for Eq. (1.44)

$$\begin{aligned} \langle T(ABCD\cdots XYZ)\rangle &= \langle T(AB)\rangle\langle T(CD)\rangle\cdots\langle T(YZ)\rangle \\ &\quad -\langle T(AC)\rangle\langle T(BD)\rangle\cdots\langle T(YZ)\rangle - \cdots, \end{aligned} \tag{1.47}$$

where the average in each case is over the ground state. This is an important formal result: the time-ordering operation acting on a product of many operators can be factorized into an operation on product pairs. In our present context the operators are Fermionic creation and annihilation operators and the pairs are expressible as Green's functions.

In order to make this point more concrete let us follow the example of Ref. 124 and evaluate

$$\begin{aligned}\langle\phi_0|\, T[d_\alpha(t)d^\dagger_\beta(t_1)d_\gamma(t_2)d^\dagger_\delta(t')]\,|\phi_0\rangle \\ &= \langle\phi_0|\, T[d_\alpha(t)d_\beta(t_1)^\dagger]\,|\phi_0\rangle\,\langle\phi_0|\, T[d_\gamma(t_2)d^\dagger_\delta(t')]\,|\phi_0\rangle \\ &\quad - \langle\phi_0|\, T[d_\alpha(t)d^\dagger_\delta(t')]\,|\phi_0\rangle\,\langle\phi_0|\, T[d_\gamma(t_2)d_\beta(t_1)^\dagger]\,|\phi_0\rangle\,, \end{aligned} \tag{1.48}$$

where we have enumerated all non-zero two operator pairings, and the minus sign in the second term arises from the three operator exchanges required to form the bracket. Notice that each term in the right-hand side of Eq. (1.48) is a time-ordered Green's function averaged over the ground state allowing us to write the expectation value in terms of Green's functions

$$\begin{aligned}\langle\phi_0|\, T[d_\alpha(t)d^\dagger_\beta(t_1)d_\gamma(t_2)d^\dagger_\delta(t')]\,|\phi_0\rangle \\ &= (i)^2 G_0^{\mathrm{T}}(\alpha,\beta;t,t_1)G_0^{\mathrm{T}}(\gamma,\delta;t_2,t') \\ &\quad - (i)^2 G_0^{\mathrm{T}}(\alpha,\delta;t,t')G_0^{\mathrm{T}}(\gamma,\beta;t_2,t_1),, \end{aligned} \tag{1.49}$$

where in analogy with our notation for the retarded Green's function, the time-ordered Green's function for a free particle is given by

$$G_0^{\mathrm{T}}\left(\alpha,\beta;t_1,t_2\right) = -i\,\langle\phi_0|\, T[d_\alpha(t_1)d^\dagger_\beta(t_2)]\,|\phi_0\rangle\,. \tag{1.50}$$

Thus far, we have outlined a many-body perturbation theory for evaluating expectation values which requires the evaluation of a sum of time-ordered products for an arbitrarily large number of operators. Wick's theorem states that many of the terms in this sum vanish and the evaluation of a time-ordered product can be expanded into all possible pairings which, in turn, may be expressed as Green's functions.

Feynman diagrams and Dyson's equation

It was Feynman who introduced a pictorial way of expressing the contractions in terms like Eq. (1.49) [56], several of which are shown in Fig. (1.10). His diagrams

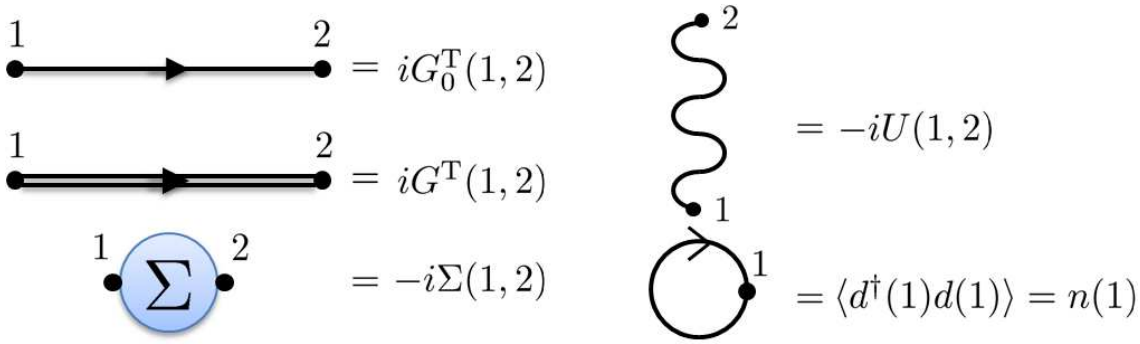

Figure 1.10: A Feynman diagram 'dictionary' showing the diagrams and equivalent mathematical expressions for several important terms. The label numbers are meant to indicate spatial and temporal indices appropriate to the problem. U is a bare interaction term and $n(1) \equiv G^{\mathrm{T}}_{\alpha\alpha}(t_1, t_1)$ is the occupancy at coordinate $1 \equiv (\alpha, t_1)$.

are actually mathematical graphs with elements that are topologically connected via edges which intersect at vertices since, according to the linked cluster theorem, all 'disconnected' graphs in the numerator of Eq. (1.41) are canceled by the same terms in the denominator [1, 124, 52]. With this in mind, we write the time-ordered Green's function in the energy domain as [124]

$$\begin{aligned} G^{\mathrm{T}}_{\alpha\beta}(E) &= -i\sum_{n=0}^{\infty}(-i)^n \int_{-\infty}^{\infty} d(t-t')e^{iE(t-t')} \int_{-\infty}^{\infty} dt_1 \cdots \int_{-\infty}^{\infty} dt_n \\ &\quad \times \langle\phi_0| \quad \underbrace{T[d_\alpha(t)d^\dagger_\beta(t')V(t_1)\cdots V(t_n)}_{\text{over all different, connected graphs}} \quad]\,|\phi_0\rangle\,, \end{aligned} \tag{1.51}$$

where we have assumed that G^{T} is time-shift invariant. Equation (1.51) may be equivalently expressed in matrix form as

$$\begin{aligned} G^{\mathrm{T}}(E) &= G^{\mathrm{T}}_0(E) + G^{\mathrm{T}}_0(E)\Sigma(E)G^{\mathrm{T}}_0(E) \\ &\quad + G^{\mathrm{T}}_0(E)\Sigma(E)G^{\mathrm{T}}_0(E)\Sigma(E)G^{\mathrm{T}}_0(E) + \cdots \\ &= G^{\mathrm{T}}_0(E)\left[\mathbf{1} + \Sigma(E)G^{\mathrm{T}}(E)\right], \end{aligned} \tag{1.52}$$

where $\Sigma(E)$ is known as the *self-energy* matrix and is related to the interaction terms $V(t)$. Equation (1.52) may be further simplified by recognizing that the recursion is a geometric series so that

$$G^{\mathrm{T}}(E) = \left[(G^{\mathrm{T}}_0(E))^{-1} - \Sigma(E)\right]^{-1}, \tag{1.53}$$

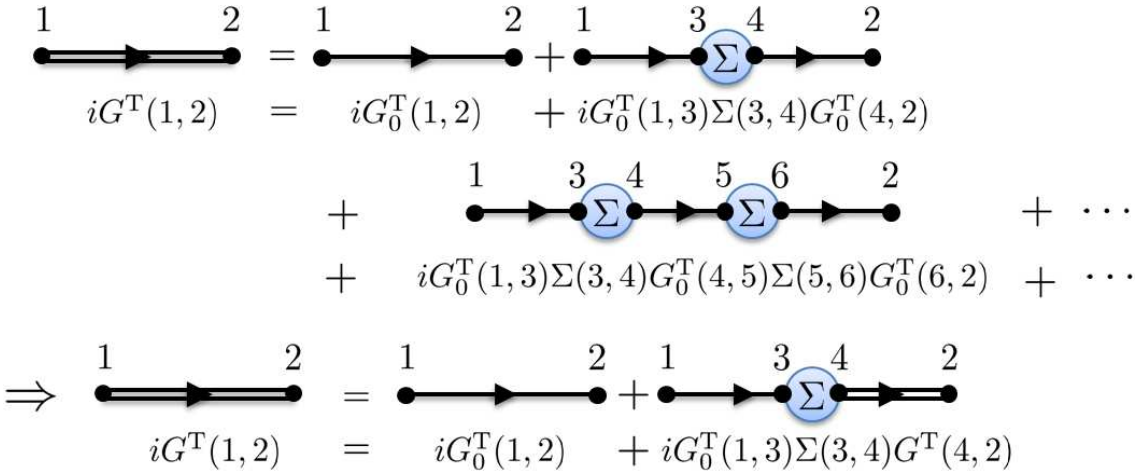

Figure 1.11: Dyson's equation expressed diagrammatically and mathematically.

a general relation commonly referred to as Dyson's equation after its inventor, Freeman Dyson [51]. Dyson's equation may also be written diagrammatically as shown in Fig. 1.11, where we have used the Feynman 'dictionary' shown in Fig. 1.10. The self-energy Σ is so-called because it encapsulates the effect of interactions on the 'self' G_0, shifting and broadening the free particle's pole structure. This effect is also called 'dressing', so it is often stated that the effect of Σ is to dress the bare particle's states. Although we have expressed Dyson's equation in terms of the time-ordered Green's function it holds equally true for the retarded Green's function [124].

A large amount of theoretical groundwork has been presented in this section so let us review what's been covered. Without interactions, the exact solution to the unperturbed Hamiltonian is assumed known, meaning that the exact Green's function is also known. When interactions are included we found that time-dependent perturbations gave rise to an infinite series of higher-order Green's functions that, with the help of Wick's theorem, may be recast in terms of the unperturbed Green's function and a self-energy which encapsulates the effect of interactions. Both these mathematical objects may be drawn pictorially using Feynman diagrams where the nature of the physics involved is phrased intuitively. Finally, a formal closed form expression for the full Green's function, including interactions, is found using Dyson's

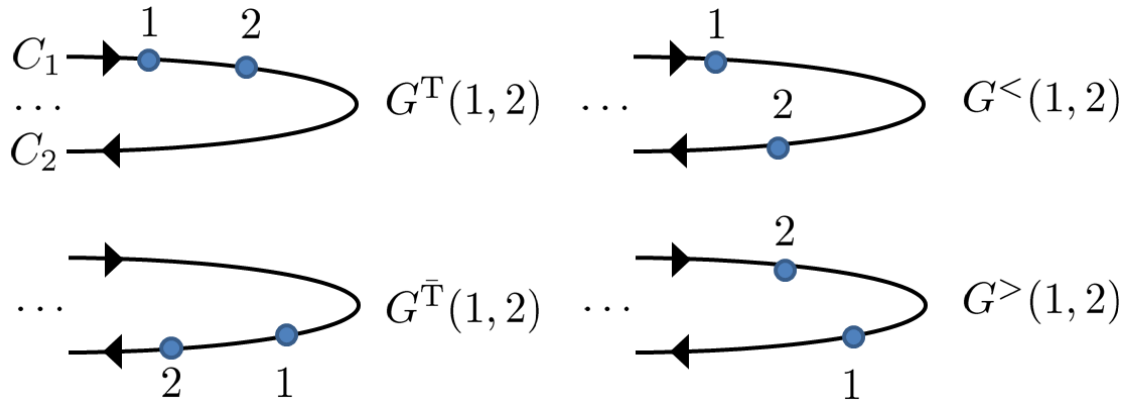

Figure 1.12: On the Keldysh contour there are two temporal branches, C_1 and C_2, which require four types of Green's functions to be considered in the S-matrix contour-time integral. The "lesser" and "greater" terms correspond to Green's functions which cross from C_1 to C_2 and C_2 to C_1, respectively.

equation where the physical processes embodied in the self-energy are included to infinite order. Although the diagrammatic approach does not 'solve' the many-body problem, it is still a very powerful technique since the approximations invoked can be understood physically and are not just mathematical truncations of the perturbative series.

The only assumption we have made up to this point is that the system is time-reversal invariant, meaning that the system is in the same state in the distant future as it was in the distant past. In equilibrium, we argued that this was a valid assumption. However, in this work we are concerned with nonequilibrium phenomena, for example the flow of current through a molecular junction where the number of electrons in a given lead reservoir never returns to its original state. In the next section, we briefly review a method introduced by Schwinger [164] to study nonequilibrium problems using many of the elements from the equilibrium perturbation theory.

1.3.3 Non-equilibruim systems: the Keldysh contour

Schwinger's idea was to consider the time integrals present in the S-matrix on a time-contour rather than a time-line. Schwinger's contour loop has two branches:

the first C_1 extends from the distant past to some contour 'time' τ while the other C_2 closes the loop returning from τ back to the distant past. Often $\tau \to \infty$. Out of equilibrium Gell-Mann and Low's theorem does not hold, making the use of Schwinger's contour a necessity. However, even for equilibrium systems Schwinger's contour loop is conceptually appealing since there is no longer the need to relate the state of the system in the distant past to that of the distant future.

Keldysh [89], Craig [38], Kadanoff, and Baym [83] further developed Schwinger's ideas and applied them to condensed matter applications. Their approach was to develop the S-matrix perturbation theory in the increased basis mandated by the two contours, whereby the time-ordered products are interpreted as contour ordered products. For example, Eq. (1.43) becomes

$$T_{\mathrm{C}}\left[\mathcal{O}(t)S\right] = \sum_{n=0}^{\infty}\left(-\frac{i}{\hbar}\right)^{n}\frac{1}{n!}\int_{-\infty}^{\infty}dt_1\cdots\int_{-\infty}^{\infty}dt_n T_{\mathrm{C}}\left[\mathcal{O}(t)V(t_1)\cdots V(t_n)\right], \quad (1.54)$$

where T_{C} is the contour-ordering operator and the enumeration of possible time-orderings must account for the fact that each time integral produces one set of terms for the C_1 contour and another for the C_2 contour. The n^{th} term of the S-matrix therefore produces 2^n arrangements. As indicated in Fig. 1.12, there are four Green's functions to consider when evaluating contour-ordered products. Rather than consider all of these Green's functions at each step it is advantageous to define a contour-time-ordered Green's function

$$G^{\mathrm{C}}_{\alpha\beta}(\tau_1,\tau_2) = -i\left\langle T_{\mathrm{C}}\left(d_\alpha(\tau_1)d^\dagger_\beta(\tau_2)\right)\right\rangle \equiv \begin{cases} G^{<}_{\alpha\beta}(t_1,t_2) & t_1\in C_1, t_2\in C_2 \\ G^{>}_{\alpha\beta}(t_1,t_2) & t_1\in C_2, t_2\in C_1 \\ G^{\mathrm{T}}_{\alpha\beta}(t_1,t_2) & t_1,t_2\in \mathrm{C}_1 \\ G^{\bar{\mathrm{T}}}_{\alpha\beta}(t_1,t_2) & t_1,t_2\in \mathrm{C}_2 \end{cases}, \quad (1.55)$$

where τ_1 and τ_2 are contour-time coordinates. Using this Green's function we can apply the diagrammatic perturbation theory as in the equilibrium case and convert to real-time coordinates at the end of the calculation using the conversion rules of Langreth [108] given in Table 1.1. Their nonequilibrium Green's function (NEGF) technique has been used extensively in a variety of materials and devices. Since

Contour	Real axis
$C = \int_C AB$	$C^< (t_1, t_2) = \int_t \left[A^{\rm R} B^< + A^< B^{\rm A} \right]$ $C^{\rm R} = \int_t A^{\rm R} B^{\rm R}$
$D = \int_C ABC$	$D^< = \int_t \left[A^{\rm R} B^{\rm R} C^< + A^{\rm R} B^< C^{\rm A} + A^< B^{\rm A} C^{\rm A} \right]$ $D^{\rm R} = \int_t A^{\rm R} B^{\rm R} C^{\rm R}$
$C(\tau, \tau') = A(\tau, \tau') B(\tau, \tau')$	$C^<(t,t') = A^<(t,t') B^<(t,t')$ $C^{\rm R}(t,t') = A^<(t,t') B^{\rm R}(t,t') + A^{\rm R}(t,t') B^<(t,t') +$ $+ A^{\rm R}(t,t') B^{\rm R}(t,t')$
$D(\tau, \tau') = A(\tau, \tau') B(\tau', \tau)$	$D^<(t,t') = A^<(t,t') B^>(t',t)$ $D^{\rm R}(t,t') = A^<(t,t') B^{\rm A}(t',t) + A^{\rm R}(t,t') B^<(t',t)$

Table 1.1: The Langreth rules for analytic continuation. The superscript 'A' indicates the advanced form of the function; the conjugate of the retarded function. This table is from Ref. 71.

the Langreth rules are purely mathematical we'll complete our discussion with an example.

Example: Hartree-Fock diagrams

Let us derive the self-energies for a few diagrams which will be important in chapter 2, the direct (Hartree) and exchange (Fock) diagrams shown in Fig. 1.13. The numbers at each vertex represent space-time coordinates where time is measured on a Keldysh contour. We begin by applying the Feynman rules, which are shown schematically in Fig. 1.10 and restated here for clarity

- Open bare electron line is $iG_0^{\rm C}(1,2)$.
- Closed bare electron line is $n(1) \equiv G^{\rm C}_{\alpha\alpha}(\tau_1, \tau_1)$, where $1 \equiv (\alpha, \tau_1)$.
- A bare interaction line is $-iU(1,2)$.
- A self-energy is $-i\Sigma(1,2)$.
- Integration is over all internal vertices and other degrees of freedom (e.g. spin).

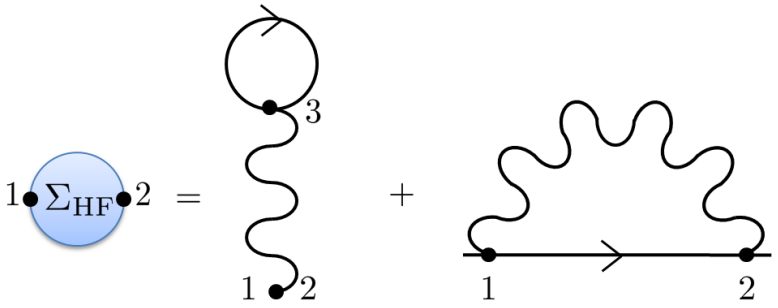

Figure 1.13: The Hartree and Fock (exchange) self-energy terms, comprising all first-order self-energy terms. The number at each vertex are coordinates in the appropriate space. For the nonequilibrium problem these are Keldysh contour times.

Reading from Fig. 1.13 directly we find

$$-i\Sigma_{\rm HF}(1,2) = \underbrace{\delta(1-2)\int d3(-iU(1,3))n(3)}_{\rm Hartree} + \underbrace{(-iU(1,2))G_0^{\rm C}(1,2)}_{\rm Fock}, \tag{1.56}$$

where the space-time coordinates are labeled such that $1 \equiv (\alpha,\tau_1)$, $2 \equiv (\beta,\tau_2)$ and $3 \equiv (\gamma,\tau_3)$, and spatial coordinates are discrete while the contour-times are continuous.

Transforming into relative coordinates, the Hartree self-energy may be expressed as

$$\left[\Sigma_{\rm H}(\tau_2-\tau_1)\right]_{\alpha\beta} = \delta(\tau_1-\tau_2)\int_{\rm C} d\tau_3 U_{\alpha\gamma}(\tau_3-\tau_1)n_\gamma(\tau_3). \tag{1.57}$$

Using the first Langreth rule given in Table 1.1, this expression in Keldysh-time can be in real-time as

$$\begin{aligned}
\left[\Sigma^{\rm R}_{\rm H}(t_2-t_1)\right]_{\alpha\beta} &= \delta(t_1-t_2)\delta_{\alpha\beta}\sum_{\gamma\neq\alpha}\int_{-\infty}^{\infty} dt_3 U^{\rm R}_{\alpha\gamma}(t_3-t_1)n^{\rm R}_\gamma(0) \\
&= \delta(t_1-t_2)\delta_{\alpha\beta}\sum_{\gamma\neq\alpha}\int_{-\infty}^{\infty} d(t_3-t_1)\left[\frac{1}{2\pi}\int_{-\infty}^{\infty} d\omega\, e^{i\omega(t_3-t_1)}U^{\rm R}_{\alpha\gamma}(\omega)\right] n^{\rm R}_\gamma(0) \\
&= \delta(t_1-t_2)\delta_{\alpha\beta}\sum_{\gamma\neq\alpha}\left[\frac{1}{2\pi}\int_{-\infty}^{\infty} d\omega U^{\rm R}_{\alpha\gamma}(\omega)\underbrace{\int_{-\infty}^{\infty} d(t_3-t_1)e^{i\omega(t_3-t_1)}}_{2\pi\delta(\omega)}\right] n^{\rm R}_\gamma(0) \\
&= \delta(t_1-t_2)\delta_{\alpha\beta}\sum_{\gamma\neq\alpha} U^{\rm R}_{\alpha\gamma}(\omega=0)n^{\rm R}_\gamma(0),
\end{aligned} \tag{1.58}$$

where in relative coordinates $n^{\rm R}(3) = n(3) = G^{\rm C}_{\gamma\gamma}(\tau_3 - \tau_3) = n_\gamma(0)$. The lesser term $[\Sigma^<_{\rm H}(t_2 - t_1)]_{\alpha\beta}$=0 since τ_1 and τ_2 must reside on different contours and Eq. (1.56) possesses a $\delta(1-2)$ function. In the Coulomb gauge, the bare interaction line is instantaneous [124] meaning that we could have equivalently let $-iU(1,3) \equiv -iU_{\alpha\gamma}(\tau_1,\tau_3)\delta(\tau_1-\tau_3)$. Equation (1.58) may be transformed into the Fourier domain where

$$\left[\Sigma^{\rm R}_{\rm H}(E)\right]_{\alpha\beta} = \delta_{\alpha\beta}\sum_{\gamma\neq\alpha} U^{\rm R}_{\alpha\gamma} n_\gamma. \tag{1.59}$$

Next, we evaluate the Fock contribution to the self-energy which may be written in relative coordinates in Keldysh-time coordinates as

$$[\Sigma_{\rm F}(\tau_2 - \tau_1)]_{\alpha\beta} = U_{\alpha\beta}(\tau_2 - \tau_1)\left[G^{\rm C}_0(\tau_2 - \tau_1)\right]_{\alpha\beta} \tag{1.60}$$

Noticing that this contour product resembles the $C(\tau,\tau')$ expression in Table 1.1, the Fock term may be translated into real-time coordinates giving

$$\begin{aligned}\left[\Sigma^{\rm R}_{\rm F}(t_2 - t_1)\right]_{\alpha\beta} &= iG^<_{\alpha\beta}(t_2-t_1)U^{\rm R}_{\alpha\beta}(t_2-t_1) + \\ &\quad iG^{\rm R}_{\alpha\beta}(t_2-t_1)U^<_{\alpha\beta}(t_2-t_1) + \\ &\quad iG^{\rm R}_{\alpha\beta}(t_2-t_1)U^{\rm R}_{\alpha\beta}(t_2-t_1),\end{aligned} \tag{1.61}$$

and the lesser term is given by

$$[\Sigma^<_{\rm F}(t_2 - t_1)]_{\alpha\beta} = iG^<_{\alpha\beta}(t_2-t_1)U^<_{\alpha\beta}(t_2-t_1), \tag{1.62}$$

where we have temporarily dropped the 0 and C indices in the contour-ordered Green's function for clarity. Recognizing that products in the time domain correspond to convolutions in the frequency domain, we again proceed by taking the Fourier transform

$$\begin{aligned}\left[\Sigma^{\rm R}_{\rm F}(E)\right]_{\alpha\beta} &= \frac{i}{2\pi}\int_{-\infty}^{\infty} dE' \left[G^<_{\alpha\beta}(E')U^{\rm R}_{\alpha\beta}(E-E') + \right. \\ &\quad G^{\rm R}_{\alpha\beta}(E')U^<_{\alpha\beta}(E-E') + \\ &\quad \left. G^{\rm R}_{\alpha\beta}(E')U^{\rm R}_{\alpha\beta}(E-E')\right],\end{aligned} \tag{1.63}$$

and

$$[\Sigma_{\rm F}^{<}(E)]_{\alpha\beta} = \frac{i}{2\pi}\int_{-\infty}^{\infty} dE' G_{\alpha\beta}^{<}(E') U_{\alpha\beta}^{<}(E-E'), \tag{1.64}$$

where the Fourier transform is defined as $\mathscr{F}\{f\}[E]=1/2\pi\int dt f(t)e^{iEt}$.

If the interaction lines are instantaneous then $U^{<}=0$ and $\Sigma_{\rm HF}^{<}=0$. The retarded term may also be simplified considerably, specifically

$$\begin{aligned}\left[\Sigma_{\rm HF}^{\rm R}(E)\right]_{\alpha\beta} &= \delta_{\alpha\beta}\sum_{\gamma\neq\alpha} U_{\alpha\gamma}^{\rm R} n_\gamma + U_{\alpha\beta}^{\rm R}\frac{i}{2\pi}\int_{-\infty}^{\infty} dE' \left[G_{\alpha\beta}^{<}(E') + \underbrace{G_{\alpha\beta}^{\rm R}(E')}_{=0}\right] \\ &\equiv \delta_{\alpha\beta}\sum_{\gamma\neq\alpha} U_{\alpha\gamma}^{\rm R} n_\gamma - U_{\alpha\beta}^{\rm R}\langle d_\beta^\dagger d_\alpha\rangle, \end{aligned} \tag{1.65}$$

where we have used the fact that the integral over all energy of the retarded Green's function is zero and that

$$\langle d_\beta^\dagger d_\alpha\rangle = \frac{-i}{2\pi}\int_{-\infty}^{\infty} dE\, G_{\alpha\beta}^{<}(E). \tag{1.66}$$

1.4 Summary

In this chapter, we have introduced the reader to the field of molecular electronics by first reviewing some common methods of fabricating single-molecule junctions. Based on the small size of the junctions, it was argued that the transport in these devices was primarily ballistic in nature. The theory of ballistic transport first proposed by Landauer takes the approach that "conductance is transmission" so that even in a conductor devoid of impurity scattering there is a finite conductivity. Moreover, the conductance was found to be quantized in units of $G_0=e^2/h$ ($\sim$1/25.81kΩ), a value expressed purely in terms of fundamental constants.

In Sec. 1.3 we laid the groundwork for the theory developed for charge transport in chapter 2 and heat transport in chapter 3 by reviewing the nonequilibrium Green's function (NEGF) approach to the many-body problem. With the help of Wick's theorem, the Green's function in the interacting system could be expressed in terms of the non-interacting Green's function and a self-energy which could be approximated using Feynman diagrams. We completed this section by deriving the Hartree-Fock self-energy which will be used in Sec. 2.1.4 of the next chapter.

CHAPTER 2

Electronic Transport in Single-Molecule Junctions

Electron transport in single-molecule junctions (SMJs) [143, 140, 182] is of fundamental interest both as an exemplar of a nanosystem operating out of equilibrium, and as a means to probe important chemical [103] and biological [162] processes, with myriad potential device applications [182, 29, 178]. Following the landmark experiment of Reed et al. [153], in which the differential conductance of a single 1,4-benzenedithiol (BDT) molecule was first repeatably measured, the nascent field of single-molecule electronics became an experimental reality. In spite of the profusion of experimental and theoretical works since Reed's experiment there has been, to our knowledge, no prior general theoretical framework to treat the many-body problem of a single molecule coupled to metallic electrodes.

Presently, the dominant paradigm in quantum chemistry consists of mean-field approaches based on density-functional theory (DFT) [187, 46, 183, 77, 54, 190, 120] which have been shown to have a number of serious shortcomings [136, 87, 37]. For example, mean-field approaches *cannot* properly account for important interaction effects like Coulomb blockade, where the coordination of individual charges gives rise to energetically well separated peaks in the differential conductance, because current implementations of DFT do not accurately describe charge quantization.

An alternative approach is to solve the few-body molecular Hamiltonian exactly, and treat electron hopping between molecule and electrodes as a perturbation. This approach has been used to describe molecular junction transport in the sequential-tunneling regime [76, 136, 18], but describing coherent quantum transport in this framework remains an open theoretical problem. Higher-order tunneling processes may be treated rigorously in the density-matrix formalism [98, 161] and the closely related superoperator Green's function approach [69, 60], but the expansion is typically truncated at second [60] or fourth order [98, 148], the calculation of higher-

order terms being prohibitively difficult. Furthermore, this approach has thus far been limited to very small molecules, and it is unclear what the prospects for larger and more complex molecules of interest for potential device applications.

In this chapter, we provide a detailed derivation of our many-body theory of molecular junction transport. Two useful approximate solutions for the nonequilibrium Coulomb self-energy are given and discussed in Sec. 2.1.4, and two important macroscopic observables, current and thermopower, are presented in Sec. 2.1.5. The details of the model used to describe a molecular heterojunction consisting of a π-conjugated molecule covalently bonded to metallic electrodes are presented in Sec. 2.2. The electric and thermoelectric response of a BDT-Au junction are calculated in Sec. 2.3, and compared to experimental results. In Sec. 2.4, several examples highlighting the necessity of properly accounting for electron-electron correlations in transport problems are discussed. Finally, a discussion and conclusions are presented in Sec. 2.5.

2.1 Nonequilibrium many-body transport theory

In this section, we develop a many-body theory of molecular junction transport based on nonequilibrium Green's functions [130, 72, 197] (NEGF), in order to utilize physically motivated approximations that sum terms of all orders. The junction Green's functions are calculated exactly in the sequential-tunneling limit, and the corrections to the electron self-energy due to finite tunneling width are included via Dyson-Keldysh equations. The *tunneling self-energy* is calculated exactly using the equations-of-motions method [131, 72], while the correction to the *Coulomb self-energy* is calculated using diagrammatic perturbation theory. In this way, tunneling processes are included to infinite order, meaning that any approximation utilized is a truncation in the physical processes considered rather than in the order of those processes.

Our approach reproduces the key features of both the Coulomb blockade and coherent transport regimes simultaneously in a single unified transport theory. Non-

perturbative effects of intramolecular correlations are included, which are necessary to accurately describe the highest occupied molecular orbital (HOMO)-lowest unoccupied molecular orbital (LUMO) gap, essential for a quantitative theory of transport.

2.1.1 Molecular junction Hamiltonian

The Hamiltonian of a junction consisting of a molecule coupled to several metallic electrodes may be written

$$H_{\text{junction}} = H_{\text{mol}} + H_{\text{leads}} + H_{\text{T}}. \tag{2.1}$$

The molecular Hamiltonian can be formally divided into one-body and two-body terms $H_{\text{mol}} = H^{(1)}_{\text{mol}} + H^{(2)}_{\text{mol}}$. In general, neglecting spin-orbit coupling, the one-body term can be written

$$H^{(1)}_{\text{mol}} = \sum_{n,m,\sigma} \left[H^{(1)}_{\text{mol}}\right]_{n\sigma,m\sigma} d^{\dagger}_{n\sigma} d_{m\sigma}, \tag{2.2}$$

where $d^{\dagger}_{n\sigma}$ creates an electron of spin σ on atomic orbital n of the molecule and $[H^{(1)}_{\text{mol}}]$ is a hermitian matrix. For simplicity, the atomic basis orbitals are taken to be orthonormal, so that the anticommutator $\{d^{\dagger}_{n\sigma}, d_{m\sigma'}\} = \delta_{nm}\delta_{\sigma\sigma'}$.

In a localized orthonormal basis, a general spin-rotation invariant two-body (e.g. Coulomb) interaction has the form

$$H^{(2)}_{\text{mol}} = \frac{1}{2} \sum_{n,m} U_{nm} \rho_n \rho_m, \tag{2.3}$$

where $\rho_n = \sum_\sigma d^{\dagger}_{n\sigma} d_{n\sigma}$. Values of U_{nm} for π-conjugated systems [33, 30] are discussed in Sec. 2.2.

Extending to a non-orthogonal basis is straightforward in principle: in a general basis $\{a_{k\sigma}\}$ is related to $\{d_{n\sigma}\}$ via $d_{n\sigma} = \sum_k A_{nk} a_{k\sigma}$. The Coulomb interaction therefore takes the form

$$H^{(2)}_{\text{mol}} = \sum_{\sigma,\sigma'} \sum_{i,j,k,\ell} V_{ijk\ell} a^{\dagger}_{i\sigma} a_{j\sigma} a^{\dagger}_{k\sigma'} a_{\ell\sigma'}, \tag{2.4}$$

where $V_{ijk\ell} \equiv \sum_{n,m} U_{nm} A^*_{ni} A_{nj} A^*_{mk} A_{m\ell}$. $H^{(2)}_{\rm mol}$ also takes the above form in a localized but non-orthogonal basis.

Because of their continuous and almost featureless density of states around the Fermi energy, the macroscopic metallic electrodes (labeled $\alpha \in [1, \ldots, M]$) may be modeled as non-interacting Fermi gases:

$$H_{\rm leads} = \sum_{\alpha=1}^{M} \sum_{\substack{k\in\alpha \\ \sigma}} \epsilon_{k\sigma} c^\dagger_{k\sigma} c_{k\sigma}, \tag{2.5}$$

where $c^\dagger_{k\sigma}$ creates an electron of energy $\epsilon_{k\sigma}$ in lead α. The electrostatic interaction of molecule and electrodes due to the electric dipoles formed at each molecule-electrode interface may be included in $H^{(1)}_{\rm mol}$, as discussed in Sec. 2.2. Tunneling of electrons between the molecule and the electrodes is described by the Hamiltonian

$$H_{\rm T} = \sum_{\alpha=1}^{M} \sum_{k\in\alpha} \sum_{n,\sigma} \left(V_{nk} d^\dagger_{n\sigma} c_{k\sigma} + \text{H.c.} \right). \tag{2.6}$$

2.1.2 Molecular junction Green's functions

The electronic system (2.1) of molecule plus electrodes has an infinite Hilbert space. A formal simplification of the problem is obtained through the use of the Green's functions [130, 72]

$$G_{n\sigma,m\sigma'}(t) = -\frac{i}{\hbar}\theta(t)\langle\{d_{n\sigma}(t), d^\dagger_{m\sigma'}(0)\}\rangle, \tag{2.7}$$

$$G^<_{n\sigma,m\sigma'}(t) = \frac{i}{\hbar}\langle d^\dagger_{m\sigma'}(0)\, d_{n\sigma}(t)\rangle, \tag{2.8}$$

known as the retarded and Keldysh "lesser" Green's functions, respectively. Steady-state physical observables in the molecular transport junction can be expressed in terms of G and $G^<$. Transient effects [181, 196, 191, 138] are not considered in this work, although they can be investigated using this theory. In this section, an exact Dyson equation for G is derived, along with a corresponding Keldysh equation for $G^<$.

Setting $\hbar = 1$, the retarded Green's function obeys the equation of motion [72]

$$i\frac{\partial}{\partial t} G_{n\sigma,m\sigma'}(t) = \delta(t)\delta_{nm}\delta_{\sigma\sigma'} - i\theta(t)\left\langle \left\{ \left[d_{n\sigma}(t), H_{\rm junction} \right], d^\dagger_{m\sigma'}(0) \right\} \right\rangle. \tag{2.9}$$

For the purposes of this discussion, only the spin-diagonal term $G_{n\sigma,m\sigma}$ is needed [cf. Eqs. (2.20)–(2.37)]. Evaluating the commutators $[d_{n\sigma}, H_{\rm mol}]$ and $[d_{n\sigma}, H_{\rm T}]$, and noting that $[d_{n\sigma}, H_{\rm leads}] = 0$, Eq. (2.9) becomes

$$\begin{aligned} i\frac{\partial}{\partial t}G_{n\sigma,m\sigma}(t) &= \delta(t)\delta_{nm} + \sum_{n'}\left[H^{(1)}_{\rm mol}\right]_{n\sigma,n'\sigma} G_{n'\sigma,m\sigma}(t) \\ &\quad + \sum_{\alpha}\sum_{k\in\alpha} V_{nk}\, g_{k\sigma,m\sigma}(t) + \sum_{n'} U_{nn'} G^{(2)}_{n',n\sigma m\sigma}(t), \end{aligned} \tag{2.10}$$

where

$$g_{k\sigma,m\sigma'}(t) = -i\theta(t)\left\langle\left\{c_{k\sigma}(t), d^{\dagger}_{m\sigma'}(0)\right\}\right\rangle \tag{2.11}$$

and

$$G^{(2)}_{n',n\sigma m\sigma'}(t) = -i\theta(t)\left\langle\left\{\rho_{n'}(t)d_{n\sigma}(t), d^{\dagger}_{m\sigma'}(0)\right\}\right\rangle. \tag{2.12}$$

The equation of motion for $g_{k\sigma,m\sigma}(t)$ is

$$i\frac{\partial}{\partial t}g_{k\sigma,m\sigma}(t) = -i\theta(t)\left\langle\left\{\left[c_{k\sigma}(t), H_{\rm junction}\right], d^{\dagger}_{m\sigma}(0)\right\}\right\rangle. \tag{2.13}$$

Evaluating the commutators $[c_{k\sigma}, H_{\rm T}]$ and $[c_{k\sigma}, H_{\rm leads}]$, and noting that $[c_{k\sigma}, H_{\rm mol}] = 0$, Eq. (2.13) becomes

$$i\frac{\partial}{\partial t}g_{k\sigma,m\sigma}(t) = \epsilon_{k\sigma}g_{k\sigma,m\sigma}(t) + \sum_{n'} V^{*}_{n'k} G_{\rm n'\sigma,m\sigma}(t). \tag{2.14}$$

Fourier transforming Eqs. (2.10) and (2.14) into the energy domain, and eliminating $g_{k\sigma,m\sigma}(E)$, one arrives at the following matrix equation for $G(E)$:

$$\left[\mathbf{1}E - H^{(1)}_{\rm mol} - \Sigma_{\rm T}(E)\right] G(E) = \mathbf{1} + UG^{(2)}(E), \tag{2.15}$$

where the retarded *tunneling self-energy* matrix is

$$\left[\Sigma_{\rm T}(E)\right]_{n\sigma,m\sigma'} = \delta_{\sigma\sigma'}\sum_{\alpha}\sum_{k\in\alpha}\frac{V_{nk}V^{*}_{mk}}{E - \epsilon_{k\sigma} + i0^{+}}. \tag{2.16}$$

Eq. (2.15) may be recast in the form of Dyson's equation

$$G(E) = \left[\mathbf{1}E - H^{(1)}_{\rm mol} - \Sigma_{\rm T}(E) - \Sigma_{\rm C}(E)\right]^{-1} \tag{2.17}$$

via the ansatz $UG^{(2)}(E) \equiv \Sigma_{\rm C}(E)G(E)$, which defines [124] the retarded *Coulomb self-energy* matrix $\Sigma_{\rm C}(E)$, the central quantity of the many-body theory, which must be determined via an appropriate approximation as discussed below. A prescription to compute $\Sigma_{\rm C}$ is given below in Secs. 2.1.3–2.1.4. Eq. (2.17) is a general formal result, independent of the choice of basis, and is the starting point for our analysis.

For nonequilibrium problems, the Keldysh "lesser" self-energy and Green's function are also needed. $G^<$ is determined by the Keldysh equation [72]

$$G^<(E) = G\,\Sigma^< G^\dagger + (1 + G\,\Sigma)G^<_{\rm mol}(1 + \Sigma^\dagger G^\dagger), \tag{2.18}$$

where $G^\dagger(E)$ and $\Sigma^\dagger(E)$ are the advanced Green's function and self-energy, respectively, $\Sigma^< = \Sigma^<_{\rm T} + \Sigma^<_{\rm C}$, and $G^<_{\rm mol} = \lim_{\Sigma_T \to 0} G^<$. The second term on the right-hand side of Eq. (2.18) is infinitesimal and can be neglected, provided all of the molecular resonances have a finite broadening due to the lead-molecule coupling. If the molecule has localized states which don't coupled to the lead reservoirs (e.g. due to symmetry) then the second term may not be negligible.

The "lesser" tunneling self-energy is

$$[\Sigma^<_{\rm T}(E)]_{n\sigma,m\sigma'} = i\sum_\alpha f_\alpha(E)\,[\Gamma^\alpha(E)]_{n\sigma,m\sigma'}\,, \tag{2.19}$$

where $f_\alpha(E) = \{1 + \exp[(E-\mu_\alpha)/k_BT_\alpha]\}^{-1}$ is the Fermi-Dirac distribution for lead α, and

$$[\Gamma^\alpha(E)]_{n\sigma,m\sigma'} = 2\pi\delta_{\sigma\sigma'}\sum_{k\in\alpha} V^*_{nk}V_{mk}\,\delta(E-\epsilon_{k\sigma}) \tag{2.20}$$

is the tunneling-width matrix for lead α.

2.1.3 Molecular Green's function

In the limit of infinitesimal lead-molecule coupling $\sum_\alpha \Gamma^\alpha/k_{\rm B}T \to 0$, coherent superpositions of different energy eigenstates of the molecule can be neglected, and the junction Green's function becomes

$$\lim_{\Sigma_{\rm T}\to 0}[G(E)]_{n\sigma,m\sigma} \equiv [G_{\rm mol}(E)]_{n\sigma,m\sigma} = \sum_{\nu,\nu'}[\mathcal{P}(\nu)+\mathcal{P}(\nu')]\,\frac{\langle\nu|d_{n\sigma}|\nu'\rangle\langle\nu'|d^\dagger_{m\sigma}|\nu\rangle}{E - E_{\nu'} + E_\nu + i0^+}, \tag{2.21}$$

where $|\nu\rangle$ and $|\nu'\rangle$ are many-body eigenstates of the isolated molecule satisfying $H_{\rm mol}|\nu\rangle = E_\nu|\nu\rangle$, $d_{n\sigma}$ ($d^\dagger_{n\sigma}$) annihilates (creates) an electron of spin σ on the $n^{\rm th}$ atomic orbital of the molecule and $\mathcal{P}(\nu)$ is the probability that ν is occupied.

Equation (2.21) can be derived from Eq. (2.7) by expanding the Green's function in terms of a complete basis (e.g. $\sum_\nu |\nu\rangle\langle\nu|$). In the time domain

$$\begin{aligned}
\left[G_{\rm mol}(t)\right]_{n\sigma,m\sigma} &= -i\theta(t)\langle\left\{d_{n\sigma}(t), d^\dagger_{m\sigma}\right\}\rangle \\
&= -i\theta(t)\langle e^{iHt}d_{n\sigma}e^{-iHt}d^\dagger_{m\sigma} + d^\dagger_{m\sigma}e^{iHt}d_{n\sigma}e^{-iHt}\rangle \qquad (2.22)
\end{aligned}$$

where $\langle\cdots\rangle \equiv {\rm Tr}\left\{\rho\cdots\right\}$ indicates an average over an ensemble of molecular states $|\nu\rangle$ weighted by a thermodynamic factor $\mathcal{P}(\nu)$ and we have converted between the Heisenberg time-dependent to Schrödinger time-independent operators using $d_n\left(t\right)\!=\!e^{iHt}d_ne^{-iHt}$. Transforming Eq. (2.22) into the Fourier domain we find

$$\begin{aligned}
\left[G_{\rm mol}(E)\right]_{n\sigma,m\sigma} &= \mathscr{F}\Big\{\left[G_{\rm mol}(t)\right]_{n\sigma,m\sigma}\Big\} = \int_{-\infty}^{\infty} dt\; e^{iEt}\left[G_{\rm mol}(t)\right]_{n\sigma,m\sigma} \\
&= -i\int_0^\infty dt\; e^{iEt}\sum_\nu \mathcal{P}(\nu)\big\{\langle\nu\left|e^{iHt}d_ne^{-iHt}d^\dagger_{m\sigma}\right|\nu\rangle \\
&\qquad\qquad + \langle\nu\left|d^\dagger_{m\sigma}e^{iHt}d_ne^{-iHt}\right|\nu\rangle\big\} \\
&= -i\sum_{\nu,\nu'}\mathcal{P}(\nu)\int_0^\infty dt\; e^{it(E-E_{\nu'}+E_\nu)}\langle\nu\left|d_{n\sigma}\right|\nu'\rangle\langle\nu'\left|d^\dagger_{m\sigma}\right|\nu\rangle \\
&\qquad\qquad + e^{it(E+E_{\nu'}-E_\nu)}\langle\nu\left|d^\dagger_{m\sigma}\right|\nu'\rangle\langle\nu'\left|d_{n\sigma}\right|\nu\rangle \\
&= \sum_{\nu,\nu'}\mathcal{P}(\nu)\frac{\langle\nu|d_{n\sigma}|\nu'\rangle\langle\nu'|d^\dagger_{m\sigma}|\nu\rangle}{E-E_{\nu'}+E_\nu+i0^+} + \mathcal{P}(\nu')\frac{\langle\nu|d^\dagger_{m\sigma}|\nu'\rangle\langle\nu'|d_{n\sigma}|\nu\rangle}{E-E_\nu+E_{\nu'}+i0^+},
\end{aligned} \qquad (2.23)$$

which is equivalent to Eq. (2.21). The 'lesser' molecular Green's function is given by

$$\begin{aligned}
\left[G^<_{\rm mol}(E)\right]_{n\sigma,m\sigma'} &= \mathscr{F}\left\{i\sum_{\nu,\nu'}\mathcal{P}(\nu)\langle\nu|d^\dagger_{m\sigma'}|\nu'\rangle\langle\nu'|e^{iH_{\rm mol}t}d_{n\sigma}e^{-iH_{\rm mol}t}|\nu\rangle\right\} \\
&= i\sum_{\nu,\nu'}\mathcal{P}(\nu)\langle\nu|d^\dagger_{m\sigma'}|\nu'\rangle\langle\nu'|d_{n\sigma}|\nu\rangle\int_{-\infty}^{\infty}dt e^{i(E_{\nu'}-E_\nu+E)t} \\
&= 2\pi i\sum_{\nu,\nu'}\mathcal{P}(\nu)\langle\nu|d^\dagger_{m\sigma'}|\nu'\rangle\langle\nu'|d_{n\sigma}|\nu\rangle\delta\left(E+E_{\nu'}-E_\nu\right). \qquad (2.24)
\end{aligned}$$

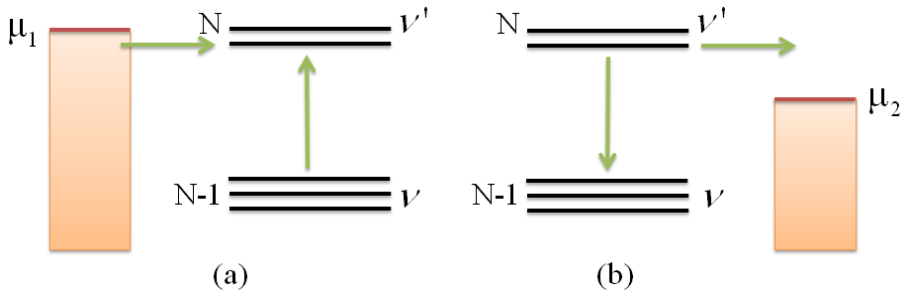

Figure 2.1: A schematic representation of detailed balance. The left-hand and right-hand sides of Eq. (2.25) are represented in (a) and (b), respectively.

The nonequilibrium probabilities $\mathcal{P}(\nu)$ can be determined by solving a system of semiclassical rate equations for sequential tunneling [17, 76, 136, 18]. For steady-state transport, they satisfy the principle of detailed balance (see Fig. 2.1):

$$\mathcal{P}(\nu)\sum_{\alpha}\tilde{\Gamma}_{\alpha}^{\nu\nu'}f_{\alpha}\left(E_{\nu'}-E_{\nu}\right)=\mathcal{P}(\nu')\sum_{\alpha}\tilde{\Gamma}_{\alpha}^{\nu\nu'}\left[1-f_{\alpha}\left(E_{\nu'}-E_{\nu}\right)\right]. \tag{2.25}$$

Here the rate constants are given by Fermi's Golden rule as

$$\tilde{\Gamma}_{\alpha}^{\nu\nu'}=\mathrm{Tr}\left\{\Gamma^{\alpha}(E_{\nu'}-E_{\nu})C^{\nu\nu'}\right\}, \tag{2.26}$$

where $\Gamma^{\alpha}(E)$ is given by Eq. (2.20) and

$$[C^{\nu\nu'}]_{n\sigma,m\sigma'}=\langle\nu|d_{n\sigma}|\nu'\rangle\langle\nu'|d_{m\sigma'}^{\dagger}|\nu\rangle \tag{2.27}$$

are many-body matrix elements [94, 177, 180]. From the normalization of the many-body wavefunctions, the total resonance width $\tilde{\Gamma}^{\nu\nu'}=\sum_{\alpha}\tilde{\Gamma}_{\alpha}^{\nu\nu'}$ scales as $\sim\sum_{\alpha}\mathrm{Tr}\{\Gamma^{\alpha}\}/N$, where N is the number of atomic orbitals in the molecule. For strongly-correlated systems, there is an additional exponential suppression of Eq. (2.27) as $N\to\infty$ due to the orthogonality catastrophe [180, 7].

Linear response transport is determined by the equilibrium Green's functions. In equilibrium, the solution of the set of Eqs. (2.25) reduces to

$$\mathcal{P}(\nu)=e^{-\beta(E_{\nu}-\mu N_{\nu})}/\mathcal{Z}, \tag{2.28}$$

where $\mathcal{Z}$ is the grand partition function of the molecule at inverse temperature β and chemical potential μ and N_{ν} is the occupancy of state ν.

Eq. (2.21) implicitly defines the Coulomb self-energy matrix $\Sigma_{\rm C}^{(0)}$ in the sequential tunneling limit via

$$G_{\rm mol}(E) = \left[\mathbf{1}E - H_{\rm mol}^{(1)} - \Sigma_{\rm C}^{(0)}(E)\right]^{-1}. \tag{2.29}$$

$\Sigma_{\rm C}^{(0)}$ is the high-temperature limit of the Coulomb self-energy (i.e., the limit $k_BT/\,{\rm Tr}\{\Gamma^\alpha\} \gg 1$), and describes intramolecular correlations and charge quantization effects (Coulomb blockade away from resonance). The nonperturbative treatment of intramolecular correlations provided by exact diagonalization of $H_{\rm mol}$ in Eq. (2.21) allows for an accurate description of the HOMO-LUMO gap, which is essential for a quantitative theory of transport.

2.1.4 The Coulomb self-energy $\Sigma_{\rm C}$

In general, the Coulomb self-energy matrix $\Sigma_{\rm C} = \Sigma_{\rm C}^{(0)} + \Delta\Sigma_{\rm C}$, where $\Delta\Sigma_{\rm C}$ describes the change of the Coulomb self-energy due to lead-molecule coherence emerging at temperatures $k_BT \lesssim {\rm Tr}\{\Gamma^\alpha\}$. Using this decomposition of the Coulomb self-energy, Dyson's equation (2.17) can be rewritten in the following useful form:

$$G^{-1}(E) = G_{\rm mol}^{-1}(E) - \Sigma_{\rm T} - \Delta\Sigma_{\rm C}, \tag{2.30}$$

where the self-energy terms $\Sigma_{\rm T} + \Delta\Sigma_{\rm C}$ describe the effects of finite tunneling width. $\Sigma_{\rm T}$ is given by Eq. (2.16). Here we point out that $\Delta\Sigma_{\rm C}$—unlike $\Sigma_{\rm C}^{(0)}$—can be evaluated perturbatively using diagrammatic techniques on the Keldysh time-contour (cf. Fig. 2.2). Such a perturbative approach is valid, in principle, at temperatures/bias voltages satisfying $\max\{T, eV/k_B\} > T_K$, where T_K is the Kondo temperature [151]—or when there is no unpaired electron on the molecule (such as within the HOMO-LUMO gap of conjugated organic molecules).

$\Sigma_{\rm T} + \Delta\Sigma_{\rm C}$ may be thought of as the response of the junction to turning on the tunneling coupling Γ^α. A subtlety in the perturbative evaluation of $\Delta\Sigma_{\rm C}$ is that the diagrams determining the Coulomb self-energy are typically formulated [124] in terms of the Green's functions of the noninteracting system, $G^{(0)}(E) = (\mathbf{1}E - H_{\rm mol}^{(1)} - \Sigma_{\rm T})^{-1}$ and $G_{\rm mol}^{(0)}(E) = (\mathbf{1}E - H_{\rm mol}^{(1)} + i0^+)^{-1}$, while the response of the

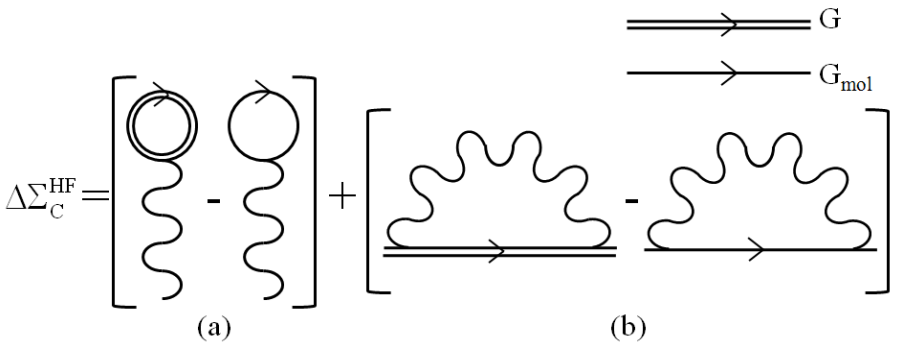

Figure 2.2: The correction to the Coulomb self-energy $\Delta\Sigma_{\rm C}$ is given in the self-consistent Hartree-Fock approximation by the sum of (a) the Hartree (direct) term and (b) the Fock (exchange) term. The wavy line represents the Coulomb interaction, which has the form $U_{nm}\delta(\tau-\tau')$ on the Keldysh time contour.

junction is determined by the full Green's function $G(E)$ [cf. Eq. (2.37)]. Evaluating diagrams using $G^{(0)}(E)$ and $G^{(0)}_{\rm mol}(E)$ would yield a correction to the Coulomb self-energy with a pole structure unrelated to that of $\Sigma^{(0)}_{\rm C}$, so that adding the two together would not yield a physically meaningful result. Our strategy is thus to calculate $\Delta\Sigma_{\rm C}$ by reformulating the terms in the perturbative expansion in terms of the full Green's function $G(E)$ via appropriate resummations. This procedure is in general nontrivial, but the result for the Hartree-Fock correction is given in Sec. 2.1.4 below, based on physical arguments. Higher-order self-energy diagrams can be included in a similar fashion and will be explored in some detail later in Chapter 5.

Electron-phonon coupling [132, 61, 147, 197, 45, 174] can also be included in the many-electron theory via the self-energy terms $\Sigma_{\rm e-ph}+\Delta\Sigma^{\rm e-ph}_{\rm C}$, where $\Sigma_{\rm e-ph}$ is given by the usual self-energy diagrams,[61, 147, 197, 45, 174] and $\Delta\Sigma^{\rm e-ph}_{\rm C}$ is the corresponding correction to the Coulomb self-energy.

The Elastic Cotunneling Approximation : $\Sigma_{\rm C}=\Sigma^{(0)}_{\rm C}$

Far from transmission resonances and for $T\gg T_K$, $\Delta\Sigma_{\rm C}$ can be neglected. This is the limit of *elastic cotunneling* [10, 66]. The Green's functions are given by Eqs. (2.17) and (2.18), with $\Sigma_{\rm C}=\Sigma^{(0)}_{\rm C}$. As mentioned previously, $[\Sigma^{(0)}_{\rm C}]^<$ does not make a finite contribution to the Keldysh equation Eq. (2.18) when $\Sigma_{\rm T}$ is finite. This

approximation is a *conserving approximation*—current is conserved [cf. Eq. (2.40)] and the spectral function $A(\omega)=i\,\mathrm{Tr}\left\{G(\omega)-G^\dagger(\omega)\right\}$ obeys the usual sum-rule

$$\int_{-\infty}^{\infty}\frac{d\omega}{2\pi}\,A(\omega)=1. \tag{2.31}$$

In order to understand the validity of this (zeroth-order) approximation to the Coulomb self-energy, we investigate the effect of the first-order Hartree-Fock correction on transport in the next section.

The self-consistent Hartree-Fock correction : $\Sigma_{\rm C}=\Sigma_{\rm C}^{(0)}+\Delta\Sigma_{\rm C}^{\rm HF}$

In the Hartree-Fock (HF) approximation, the retarded Coulomb self-energy matrix is real and is given by (cf. Sec. 1.3.3)

$$\left[\Sigma_{\rm C}^{\rm HF}\right]_{n\sigma,m\sigma'}=\delta_{\sigma\sigma'}\left[\delta_{nm}\sum_{n'}U_{nn'}\langle\rho_{n'}\rangle-U_{nm}\langle d_{m\sigma}^\dagger d_{n\sigma}\rangle\right], \tag{2.32}$$

and $\left[\Sigma_{\rm C}^{\rm HF}\right]^<=0$. In general,

$$\langle d_{n\sigma}^\dagger d_{m\sigma'}\rangle=-\frac{i}{2\pi}\int_{-\infty}^{\infty}dE\,[G^<(E)]_{m\sigma',n\sigma} \tag{2.33}$$

and

$$\lim_{\Sigma_{\rm T}\to 0}\langle d_{n\sigma}^\dagger d_{m\sigma'}\rangle=\sum_\nu\mathcal{P}(\nu)\langle\nu|d_{n\sigma}^\dagger d_{m\sigma'}|\nu\rangle. \tag{2.34}$$

The Hartree-Fock correction is then $\Delta\Sigma_{\rm C}^{\rm HF}\equiv\Sigma_{\rm C}^{\rm HF}-\Sigma_{\rm C}^{\rm HF}|_{\Sigma_{\rm T}\to 0}$. The Feynman diagrams representing this correction are shown in Fig. 2.2. A self-consistent solution of Eqs. (2.18), (2.30), and (2.32)–(2.34) yields a conserving approximation: charge, spin and energy are conserved, and the spectral weight obeys the usual sum rule.

The use of the interacting Green's functions G and $G_{\rm mol}$ in the evaluation of the Hartree self-energy is clearly justified on physical grounds, since this yields the classical electrostatic potential due to the actual nonequilibrium charge distribution on the molecule. The direct (Hartree) and exchange (Fock) contributions to $\Delta\Sigma_{\rm C}$ must be treated on an equal footing in order to cancel the unphysical self-interaction, justifying the use of the same interacting Green's functions in the evaluation of the

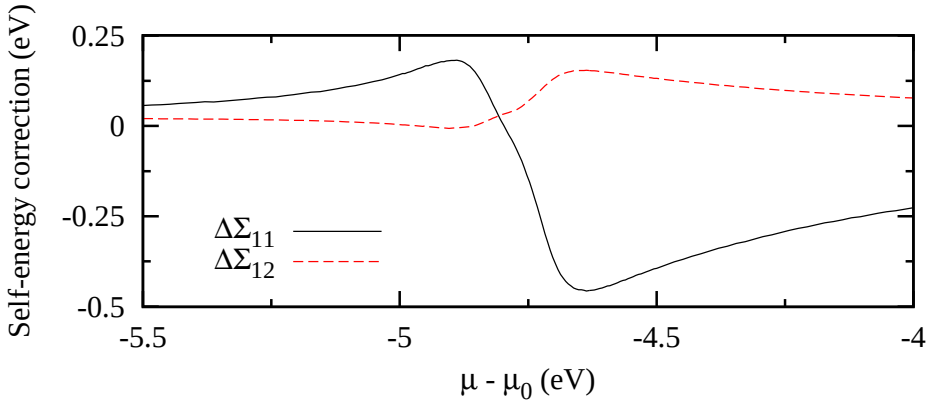

Figure 2.3: Self-consistent Hartree-Fock correction to the Coulomb self-energy matrix of a hypothetical C–C diatomic molecule versus lead chemical potential, shown in the vicinity of the HOMO resonance. Here $\mu_0 = (\varepsilon_{\rm HOMO} + \varepsilon_{\rm LUMO})/2$ is the chemical potential of the isolated molecule and $T = 300$K. The molecular junction parameters $U_{11} = U_{22} = 8.9$eV, $U_{12} = 4.4$eV, $t_{12} = 2.0$eV, and $\Gamma_1 = \Gamma_2 = 0.2$eV were used (see Sec. 2.2).

exchange self-energy. The diagrams of Fig. 2.2 would be quite complex if expressed in terms of noninteracting Green's functions, because both G and $G_{\rm mol}$ involve $\Sigma_{\rm C}^{(0)}$, which includes all possible combinations of Coulomb lines and intramolecular propagators.

The self-consistent Hartree-Fock correction for a diatomic molecule is shown in Fig. 2.3. The parameters were chosen so that the resonance width $\sim \sum_\alpha {\rm Tr}\{\Gamma^\alpha\}/N = 0.2$eV, where N is the number of atomic orbitals in the molecule. The elements of the matrix $\Delta\Sigma_{\rm C}^{\rm HF}$ are largest near a transmission resonance, but vanish on resonance. This behavior can be understood by considering the molecular correlation functions shown in Fig. 2.4. Inclusion of the tunneling self-energy without the corresponding correction to the Coulomb self-energy leads to a charge imbalance on the molecule near resonance. This in turn leads to a Hartree correction which tends to counteract the charge imbalance. A corresponding behavior is found for the exchange correction and off-diagonal correlation function. A non-self-consistent calculation would yield a much larger correction $\Delta\Sigma_{\rm C}^{\rm HF}$, indicating the important role of screening. It should be pointed out that a treatment of screening in linear response is not adequate near resonance.

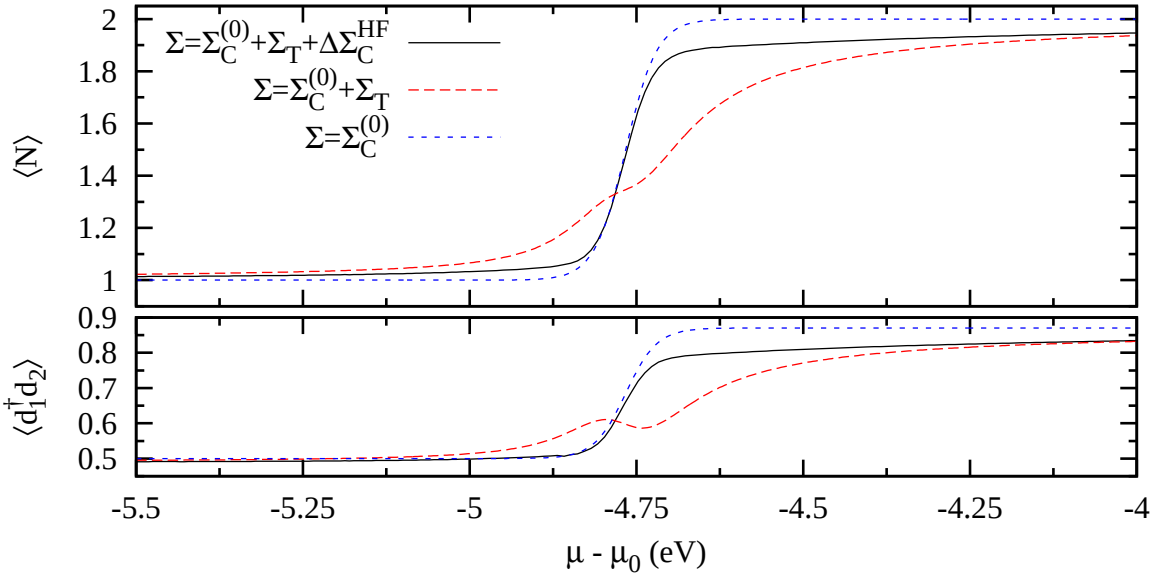

Figure 2.4: Equilibrium correlation functions near the HOMO resonance for a diatomic molecule (same parameters as in Fig. 2.3). Top: Total molecular charge $\langle N \rangle$ in three different approximations: $\Sigma = \Sigma_{\rm C}^{(0)}$ (isolated molecule in the grand canonical ensemble); $\Sigma = \Sigma_{\rm C}^{(0)} + \Sigma_{\rm T}$ (elastic cotunneling approximation); and $\Sigma = \Sigma_{\rm C}^{(0)} + \Sigma_{\rm T} + \Delta\Sigma_{\rm C}^{\rm HF}$ (self-consistent HF correction). The charging step is broadened in the elastic cotunneling approximation compared to that of the isolated molecule, and acquires a 'knee' near resonance. In the self-consistent HF approximation, the charge imbalance $\Delta N = \langle N \rangle - \langle N \rangle|_{\Sigma_{\rm T}\to 0}$ is strongly screened near resonance, leading to a charging step as steep as that of the isolated molecule, but asymptotically approaches the elastic cotunneling result away from resonance. Bottom: The correlation function $\langle d_{1\sigma}^\dagger d_{2\sigma} \rangle$ in the same three approximations.

The tendency toward charge quantization near resonance is significantly increased by the self-consistent HF correction, as shown in Fig. 2.4. The steepness of the self-consistent charging step is limited only by thermal broadening. This result is consistent with previous theoretical studies [64, 128, 65] of Coulomb blockade in metal islands and quantum dots, but inconsistent with the behavior of the Anderson model [151], where singular spin fluctuations modify this generic behavior.

The Friedel sum-rule [59, 108] relating the sum of the scattering phase shifts to the total charge on a nanostructure provides a stringent test of the accuracy of a many-body approximation. Like charge conservation, the Friedel sum-rule can be proven for any "Φ-derivable" self-energy [55, 73], but is not satisfied *a priori*

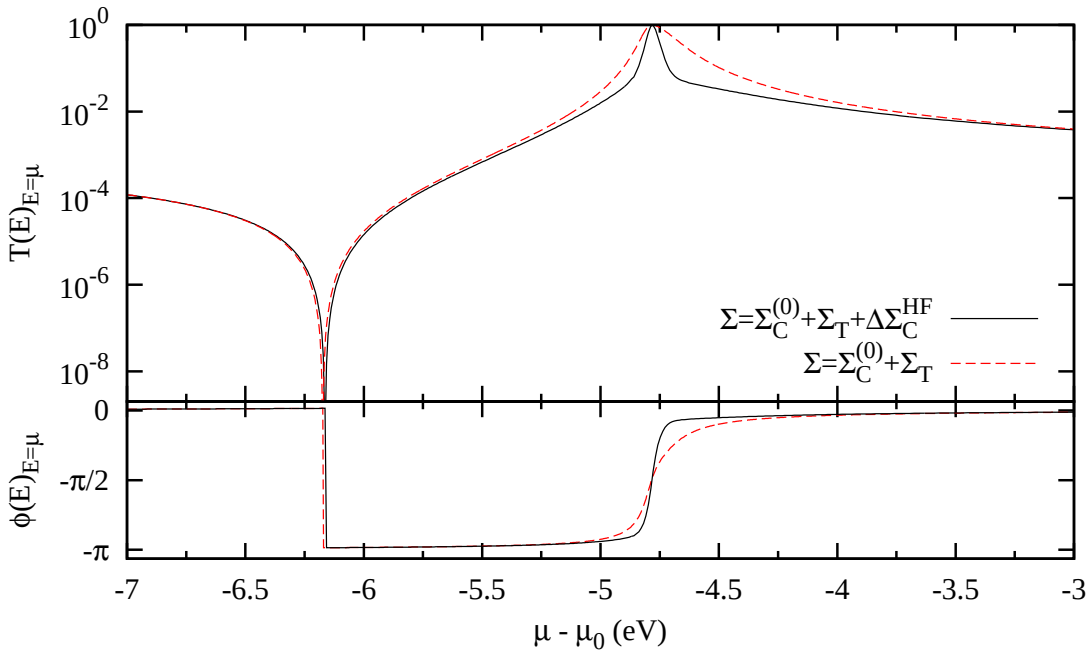

Figure 2.5: Transmission probability and phase calculated with and without the self-consistent HF correction. Note that the transmission peaks and nodes are not shifted by $\Delta\Sigma_C^{HF}$, but the width of the transmission resonance is reduced asymmetrically.

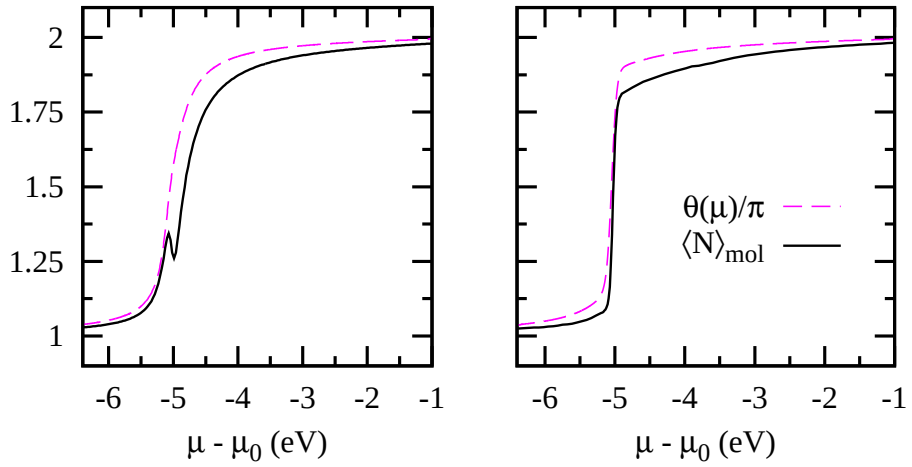

(a) $\Delta\Sigma_C = 0$ (b) $\Delta\Sigma_C = \Delta\Sigma_C^{HF}$

Figure 2.6: Transmission phase and total charge in the vicinity of the HOMO resonance of a diatomic junction at T = 300K. Agreement with the Friedel sum-rule is improved (b) by inclusion of the self-consistent Hartree- Fock correction. Note the sharpness of the charging step in (b), indicating a strong tendency toward charge quantization in SMJ.

in our nonperturbative approach. Figure 2.6 shows results for a diatomic junction, indicating that agreement with the Friedel sum-rule is improved significantly by inclusion of the self-consistent Hartree-Fock correction. Note that exact agreement is not expected at finite temperature. These results suggest that the Friedel sum-rule is indeed recovered as additional diagrammatic corrections are included in $\Sigma_{\rm C}$, in support of our diagrammatic perturbation theory.

As shown in Fig. 2.5, the transmission peaks and nodes are not shifted by the self-consistent HF correction, and the transmission phase is not changed significantly. Because of this, the elastic cotunneling approximation will be used in the majority of calculations presented in this work. Transport properties [cf. Eqs. (2.40) and (2.41)] are therefore qualitatively better described in the elastic cotunneling approximation than are the correlation functions, and the approximation is quantitatively accurate in the cotunneling regime $|\mu - \mu_{\rm res}| > \Gamma$, $\max\{T, eV/k_B\} > T_K$.

2.1.5 Macroscopic observables

Junction current

Once the Green's functions are known, relevant physical observables can be calculated. One important measurable quantity is the electrical current flowing into lead α, defined as

$$I_\alpha = -e\frac{d}{dt}\langle N_\alpha\rangle, \tag{2.35}$$

where $N_\alpha = \sum_{k\in\alpha,\sigma} c^\dagger_{k\sigma}c_{k\sigma}$ and $-e$ is the charge of the electron. The time derivatives on the right-hand side of Eq. (2.35) can be evaluated using standard quantum mechanics to obtain

$$\begin{aligned} I_\alpha &= \frac{ie}{\hbar}\langle[N_\alpha, H_{\rm junction}]\rangle \equiv \frac{ie}{\hbar}\langle[N_\alpha, H_{\rm T}]\rangle \\ &= \frac{ie}{\hbar}\sum_{k\in\alpha}\sum_{n,\sigma}\left\{V_{nk}\langle d^\dagger_{n\sigma}c_{k\sigma}\rangle - V^*_{nk}\langle c^\dagger_{k\sigma}d_{n\sigma}\rangle\right\}. \end{aligned} \tag{2.36}$$

The correlation functions in the second line of Eq. (2.36) may be formally expressed in terms of the junction's Green's functions, leading to the following general result

[130]

$$I_\alpha = \frac{ie}{h}\int dE\ \mathrm{Tr}\left\{\Gamma^\alpha(E)\left(G^<(E) + f_\alpha(E)\left[G(E) - G^\dagger(E)\right]\right)\right\}, \tag{2.37}$$

where f_α is the Fermi distribution for lead α and the tunneling-width matrix Γ is given by Eq. (2.20).[1] Using the following relation (derived from Dyson's equation)

$$i\left(G - G^\dagger\right) = iG\left(\Sigma_\mathrm{C} - \Sigma_\mathrm{C}^\dagger\right)G^\dagger + \sum_\beta G\Gamma^\beta G^\dagger \tag{2.38}$$

one can show that the current may be separated into elastic and inelastic contributions such that

$$I_\alpha = I_\alpha|_\mathrm{el} + I_\alpha|_\mathrm{in}, \tag{2.39}$$

where the elastic part reduces to the multi-terminal Büttiker formula [28]

$$I_\alpha|_\mathrm{el} = \frac{e}{h}\sum_{\beta=1}^{M}\int_{-\infty}^{\infty} dE\ T_{\alpha\beta}(E)\left[f_\beta(E) - f_\alpha(E)\right], \tag{2.40}$$

with the transmission function given by [43]

$$T_{\alpha\beta}(E) = \mathrm{Tr}\left\{\Gamma^\alpha(E)G(E)\Gamma^\beta(E)G^\dagger(E)\right\}. \tag{2.41}$$

The inelastic part is given by

$$I_\alpha|_\mathrm{in} = -\frac{ie}{h}\int_{-\infty}^{\infty} dE\ \mathrm{Tr}\left\{\Gamma^\alpha(E)G(E)\left[(1 - f_\alpha(E))\Sigma_\mathrm{C}^< + f_\alpha(E)\Sigma_\mathrm{C}^>\right]G^\dagger(E)\right\}. \tag{2.42}$$

Although the current cannot generally be expressed in terms of a transmission function, in the elastic cotunneling approximation with finite lead-molecule coupling $\Sigma_\mathrm{C}^< = [\Sigma_\mathrm{C}^{(0)}]^< \approx 0$ and $I_\alpha|_\mathrm{in}$ is negligible. In this approximation, the current through the junction be found using Eq. (2.40). More generally, $I_\alpha|_\mathrm{in}$ is zero whenever $\mathrm{Im}\,\Delta\Sigma_\mathrm{C} = 0$, since $\Delta\Sigma - \Delta\Sigma^\dagger = \Delta\Sigma^> - \Delta\Sigma^<$ implying $\Delta\Sigma^< = 0$ when $\mathrm{Im}\,\Delta\Sigma_\mathrm{C} = 0$. As we shall see in chapter 3, the derivation for the heat current in an interacting quantum system is very similar.

[1] Eq. (2.37) is a multi-terminal expression, where $\Sigma_\mathrm{T}^<$ (2.19) includes a sum over all leads.

Thermoelectric power

In 1822, Thomas Seebeck discovered that an electrical voltage developed between the hot and cold ends of a material [49]. This diffusive transport of charges continues until the electric field generated cancels the effect of the thermal gradient and equilibrium is reached. The thermoelectric power, or Seebeck coefficient, is a two-terminal, linear-response quantity generally associated with bulk materials which is defined as the coefficient relating the thermoelectric voltage to the temperature gradient

$$\nabla V = -S\nabla T. \tag{2.43}$$

We can derive an expression for S within our many-body theory by considering Eq. (2.40) in equilibrium

$$\begin{aligned} I_1 = 0 &= \frac{2e}{h}\int_{-\infty}^{\infty} dE\; T_{12}(E)\left[f_2(E) - f_1(E)\right] \\ &\cong \frac{2e}{h}\int_{-\infty}^{\infty} dE\; T_{12}(E)\left(-\frac{\partial f_0}{\partial E}\right)\left[\Delta\mu_2 - \Delta\mu_1 + \frac{(E-\mu)}{T}\left(\Delta T_2 - \Delta T_1\right)\right] \\ &= \frac{2e^2}{h}\left[\int_{-\infty}^{\infty} dE\; T_{12}(E)\left(-\frac{\partial f_0}{\partial E}\right)\right]\Delta V \\ &\qquad + \frac{2e^2}{h}\left[\frac{1}{Te}\int_{-\infty}^{\infty} dE\; T_{12}(E)(E-\mu)\left(-\frac{\partial f_0}{\partial E}\right)\right]\Delta T \end{aligned} \tag{2.44}$$

where ΔT=T_2-T_1, $\Delta\mu$=$-e\Delta V$=$-e(V_2 - V_1)$, and in linear response

$$f_\alpha(E) \cong f_0(E) + \left(-\frac{\partial f_0}{\partial E}\right)\left[\Delta\mu_\alpha + \frac{E-\mu}{T}\Delta T_\alpha\right], \tag{2.45}$$

with $f_0(E)$ as the equilibrium (zero-bias) Fermi-Dirac distribution at chemical potential μ_0 and temperature T_0, $\Delta\mu_\alpha = \mu_\alpha$-$\mu_0$ and $\Delta T = T_\alpha$ - T_0. Finally, the two terms in Eq. (2.44) can be rearranged as:

$$S(\mu, T) = -\frac{1}{\mathrm{eT}}\frac{\int_{-\infty}^{\infty} T_{12}(E)\left(-\frac{\partial f}{\partial E}\right)(E-\mu)\,dE}{\int_{-\infty}^{\infty} T_{12}(E)\left(-\frac{\partial f}{\partial E}\right)dE}. \tag{2.46}$$

2.2 π-conjugated molecular heterojunction model

In saturated hydrocarbons such as the alkanes, the valence electrons are bound in sp^3 hybridized covalent bonds. Such "σ-bonding electrons" have low mobility and exhibit an exponential decrease in electrical conductivity as a function of molecular length, making the conductance too small to measure for chains longer than 2-3nm [182, 204, 195]. The situation is completely different in π-conjugated molecules where the carbon atoms form sp^2 hybrid orbitals, leaving one valence electron per atom to occupy an unhybridized π-orbital. The itinerant electrons of this π-orbital have higher mobility than the σ-electrons, making π-conjugated molecules attractive for device applications [182, 29]. In addition, heterojunctions formed from π-conjugated molecules have extensive experimental characterization [143, 140, 182], making them an ideal test system for our many-body theory.

A semi-empirical π-electron Hamiltonian [33, 30, 29] can be used to model the electronic degrees of freedom most relevant for transport:

$$H_{\rm mol} = \sum_{n,\sigma} \varepsilon_n d^\dagger_{n\sigma} d_{n\sigma} - \sum_{n,m,\sigma} \left(t_{nm} d^\dagger_{n\sigma} d_{m\sigma} + \text{H.c.} \right) + \sum_{n,m} \frac{U_{nm}}{2} Q_n Q_m, \tag{2.47}$$

where $d^\dagger_{n\sigma}$ creates an electron of spin σ in the π-orbital of the nth carbon atom, ε_n is the atomic orbital energy, and t_{nm} is the hopping matrix element between orbitals n and m. Off-diagonal interaction terms arising from non-zero differential overlap of neighboring atomic orbitals are negligible in π-conjugated systems [14]. In the π-electron theory, the effect of different side-groups is included through shifts of the orbital energies ε_n. The effect of substituents (e.g., thiol groups) used to bond the leads to the molecule can be included [186, 142] in the tunneling matrix elements V_{nk} [cf. Eq. (2.6)].

The effective charge operator for orbital n is [180, 29]

$$Q_n = \sum_\sigma d^\dagger_{n\sigma} d_{n\sigma} - \sum_\alpha C_{n\alpha} \mathcal{V}_\alpha / e - 1, \tag{2.48}$$

where $C_{n\alpha}$ is the capacitive coupling between orbital n and lead α, e is the magnitude of the electron charge, and $\mathcal{V}_\alpha$ is the voltage on lead α. The lead-molecule

capacitances are elements of a full capacitance matrix C, which also includes the intra-molecular capacitances, determined by the relation $C_{nm} = e^2[U^{-1}]_{nm}$. The values $C_{n\alpha}$ are determined by the zero-sum rules required for gauge invariance [106]

$$\sum_m C_{nm} + \sum_{\alpha=1}^{M} C_{n\alpha} = 0, \tag{2.49}$$

and by the geometry of the junction (e.g. $C_{n\alpha}$ inversely proportional to lead-orbital distance).

The effective interaction energies for π-conjugated systems can be written [33, 30]

$$U_{nm} = \delta_{nm} U_0 + (1 - \delta_{nm}) \frac{U_0}{\epsilon \sqrt{1 + \alpha (R_{nm}/\text{Å})^2}}, \tag{2.50}$$

where U_0 is the on-site Coulomb repulsion, $\alpha = (U_0/14.397\text{eV})^2$, and R_{nm} is the distance between orbitals n and m. The phenomenological dielectric constant ϵ accounts for screening due to both the σ-electrons and any environmental considerations, such as non-evaporated solvent [30]. With an appropriate choice of the parameters t_{nm}, U_0, and ϵ, the *complete spectrum of electronic excitations* up to 8–10eV of the molecules benzene, biphenyl, and *trans*-stilbene in the gas phase can be reproduced with high accuracy [30] by exact diagonalization of Eq. (2.47). An accurate description of excited states is essential to model transport far from equilibrium. Larger conjugated organic molecules can also be modeled [33, 32] via Eqs. (2.47) and (2.50).

σ-orbitals can also be included in Eq. (2.47) as additional energy bands, and the resulting multi-band extended Hubbard model can be treated using the same NEGF formalism sketched above. Tunneling through the σ-orbitals may be important in small molecules [88, 172], especially in cases where quantum interference leads to a transmission node in the π-electron system.

The biggest uncertainty in modeling single-molecule heterojunctions is the lead-molecule coupling [86]. For this reason, we take the two most uncertain quantities characterizing lead-molecule coupling—the tunneling width Γ and the chemical potential offset $\Delta\mu$ of isolated molecule and metal electrodes—initially as phenomenological parameters to be determined by fitting to experiment. In the broad-band

limit [81] for the metallic electrodes, and assuming each electrode is covalently bonded to a single carbon atom of the molecule, the tunneling-width matrix reduces to a single constant: $\Gamma^{\alpha}_{nm}(E) = \Gamma_{\alpha}\delta_{na}\delta_{ma}$, where a is the orbital connected to electrode α. Typical estimates [135, 186, 142] indicate $\Gamma \lesssim 1$eV for organic molecules coupled to gold contacts via thiol groups.

2.3 The 1,4-benzenedithiol (BDT) molecular junction

As a first application of our many-body theory of molecular junction transport, we consider the benchmark system of benzene(1,4)dithiol (BDT) with two gold leads [153, 155, 203, 40, 99, 189, 152, 15]. The Hamiltonian parameters for benzene are [30] $U_0 = 8.9$eV, $\epsilon = 1.28$, $t_{nm} = 2.68$eV for n and m nearest neighbors, and $t_{nm} = 0$ otherwise. We consider a symmetric junction (symmetric capacitive couplings and $\Gamma_1 = \Gamma_2 \equiv \Gamma$) at room temperature (T=300K).

2.3.1 Linear electric and thermoelectric junction response

Thermoelectric effects [146, 152, 15] provide important insight into the transport mechanism in single-molecule junctions, but are particularly sensitive to correlations [31, 176], calling into question the applicability of effective single-particle theories. We have investigated thermoelectric effects in molecular heterojunctions for the first time using many-body theory. The thermopower S of a molecular junction is obtained by measuring the voltage $\Delta\mathcal{V} \equiv -S\Delta T$ created across an open junction in response to a temperature differential ΔT. In general, S can be calculated by taking the appropriate linear-response limit of Eq. (2.37), which includes both elastic and inelastic processes. As discussed in Sec. 2.1.5, however, for purely elastic transport [cf. also Secs. 2.1.4 and 2.1.4], Eq. (2.40) can be used to derive the well-known result [168, 193] given by Eq. (2.46).

Thermopower measurements [15, 152] provide a means to determine [146] the lead-molecule chemical potential mismatch $\Delta\mu$=$\mu_{\rm Au}$-μ_0, where μ_0=$(\varepsilon_{\rm HOMO} + \varepsilon_{\rm LUMO})/2$ and $\varepsilon_{\rm HOMO}$ ($\varepsilon_{\rm LUMO}$) is the HOMO (LUMO) energy level.

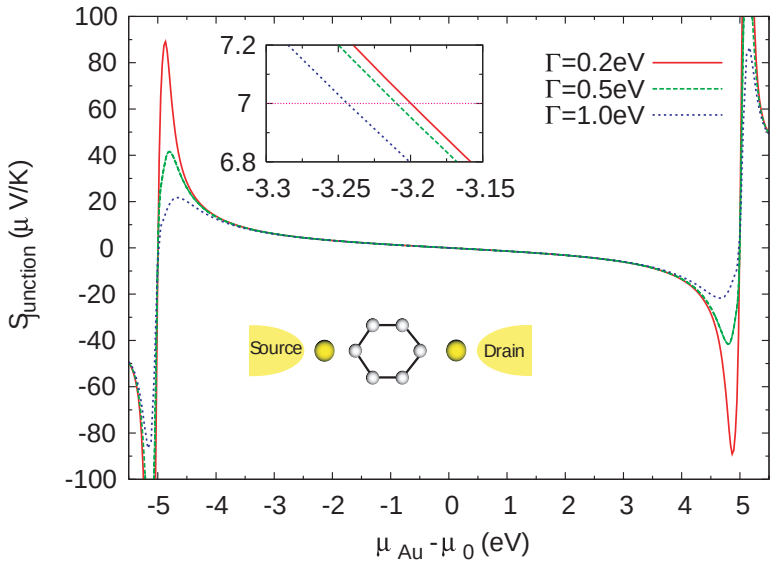

Figure 2.7: Thermoelectric power of a BDT-Au junction at $T = 300$K as a function of the lead-molecule chemical potential mismatch for three different tunneling widths. Comparison to the experimental value [15] $7.0 \pm 0.2\mu$V/K fixes $\mu_{\rm Au} = \mu_0 - (3.22 \pm 0.04)$eV (see inset showing closeup of experimentally relevant parameter range).

Figure 2.7 shows the thermopower of a BDT junction as a function of $\Delta\mu$, calculated from Eqs. (2.41) and (2.46) in the elastic cotunneling approximation. As pointed out by Paulsson and Datta [146], S is nearly independent of Γ away from the transmission resonances, allowing $\Delta\mu$ to be determined directly by comparison to experiment. The thermopower of a BDT-Au junction was recently measured by Baheti et al. [15], who obtained the result $S = (7.0 \pm 0.2)\mu$V/K. Equating this experimental value with the calculated thermopower shown in Fig. 2.7, we find that $-3.25\text{eV} \leq \mu_{\rm Au} - \mu_0 \leq -3.15\text{eV}$ over a broad range of Γ values. The Fermi level of gold thus lies about 1.8eV above the HOMO resonance, validating the notion that transport in these junctions is hole-dominated. Nonetheless, $\mu_{\rm Au} - \varepsilon_{\rm HOMO}$ is sufficiently large that the elastic cotunneling approximation is well justified.

The only other free parameter in the molecular junction model is the tunneling width Γ, which can be found by matching the linear-response conductance to experiment. Although there is a large range of experimental values [120], the

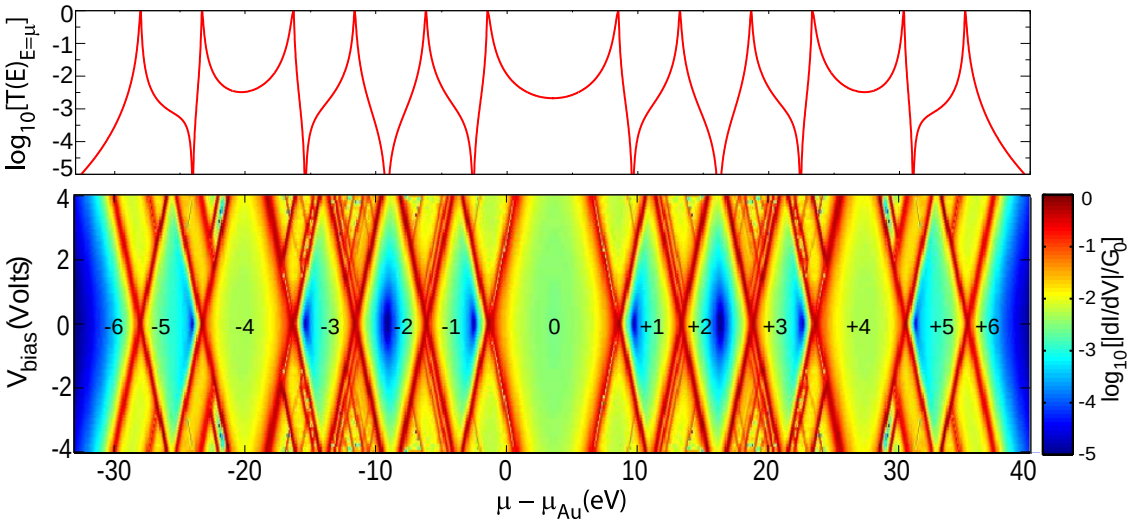

Figure 2.8: Linear-response conductance versus chemical potential (top panel) and differential conductance versus chemical potential and bias voltage (bottom panel) for a benzene(1,4)dithiol–Au junction. The calculation was carried out within the elastic cotunneling approximation using Eq. (2.40), with $\Gamma_1 = \Gamma_2 = 0.63$eV and $T = 300$K. Here $G_0 = 2e^2/h$ is the conductance quantum. Note the asymmetric Fano-like lineshapes and the transmission nodes (arising from destructive interference) in the top panel. The numbers within the central diamonds of the bottom panel indicate the quantized charge on the molecule (relative to neutral benzene). The full spectrum is shown for completeness.

most reproducible and lowest resistance contacts were obtained by Xiao, Xu and Tao [203], who report a single-molecule conductance value of $0.011\mathrm{G}_0$. This fixes $\Gamma = (0.63 \pm 0.02)$eV with $\mu_{\mathrm{Au}} - \mu_0 = -3.22 \pm 0.04$eV. This value of Γ is within the range predicted by other groups for similar molecules [135, 186, 142, 86]. With the final parameter in the model fixed, we can now use our many-body transport theory to predict the linear and nonlinear response of this molecular junction.

The transmission probability $T(E)|_{E=\mu}$ of the BDT junction is shown as a function of $\mu - \mu_{\mathrm{Au}}$ in the upper panel of Fig. 2.8. This is the linear-response conductance in units of the conductance quantum $G_0 = 2e^2/h$. The chemical potential μ is related to the gate voltage V_g in a three-terminal junction via the gate capacitance C_g. The transmission spectrum shown in Fig. 2.8 exhibits several striking features: a large but irregular peak spacing with an increased HOMO-LUMO gap; non-symmetric,

Fano-like resonance lineshapes; and transmission nodes due to destructive interference in the coherent quantum transport.

2.3.2 Nonlinear junction transport

We next calculate the differential conductance $\partial I/\partial V_{\rm bias}$ of the BDT-Au junction as a function of μ and $V_{\rm bias}$ (see Fig. 2.8, lower panel). The current was calculated in the elastic cotunneling approximation using Eqs. (2.40) and (2.41). This approximation accurately describes non-resonant transport, including the transmission nodes, as well as the positions and heights of the transmission resonances, as discussed in Sec. 2.1.4. The differential conductance spectrum of the junction exhibits clear signatures of excited-state transport [201, 44] and an irregular "molecular diamond" structure analogous to the regular Coulomb diamonds observed in quantum dot transport experiments [44]. The charge on the molecule is quantized within the central diamonds of Fig. 2.8, an important interaction effect inaccessible to so-called *ab initio* mean-field calculations. In Fig. 2.8, the full spectrum is shown for completeness, although the junction may not be stable over the entire range of bias and gate voltages shown.

Apart from the central HOMO-LUMO gap, the widths of the diamonds in Fig. 2.8 can be roughly explained via a capacitive model in which the molecule is characterized by a single capacitance $C_{\rm mol} = e^2/\langle U_{nm}\rangle$, where $\langle U_{nm}\rangle = 5.11$eV is the average over all molecular sites. The HOMO-LUMO gap of $\sim$10eV is significantly larger than this estimate of the charging energy, an indication of the significant deviations of our theory from a simple constant interaction model.

Charge quantization, also known as *Coulomb blockade*, has been observed in several different types of molecular heterojunctions [145, 116, 101, 149, 41], but has not yet been observed in BDT junctions due to the difficulty of gating such small molecules [114]. The unambiguous observation of Coulomb blockade in junctions involving larger molecules (with *smaller* charging energies) indicates that such interaction effects, lying outside the scope of mean-field approaches, are undoubtedly even more pronounced in small molecules like BDT. Important aspects of this phe-

nomenon remain to be understood in larger molecules, such as the anomalously low reported values of the charging energy [145, 116, 101, 149, 41].

A zero-bias cross section of the bottom panel of Fig. 2.8 reproduces the transmission spectrum shown in the top panel of the same figure. Increasing the bias voltage, we find that the resonances split into negatively sloped particle-like ($|e|dV/d\mu = -\left(C_1 + C_2 + C_g\right)/C_1$) lines and positively sloped hole-like ($|e|dV/d\mu = +\left(C_1 + C_2 + C_g\right)/C_2$) lines, where C_1 and C_2 are the mean lead-molecule capacitances, defined by $C_\alpha = \langle C_{n\alpha} \rangle$, $\alpha = 1, 2$. In the symmetric coupling case ($C_1 = C_2$ with $C_g/C_1 \ll 1$) the lines therefore have slopes of -2 and +2 for particle-like and hole-like lines, respectively. Within the V-shaped outline traced by the particle-like and hole-like lines, we find signatures of resonant tunneling through electronic excited states in the many narrow, nearly parallel resonance lines. While transport through electronic excited states has not yet been unambiguously identified in single-molecule heterojunctions, it has been observed in quantum dots [201, 44] and carbon nanotubes [160].

An accurate description of the HOMO-LUMO gap is essential for a quantitative theory of transport in molecular heterojunctions. The central HOMO-LUMO gap shown in Fig. 2.8 is significantly larger than that predicted [143] by density functional theory—which neglects charge-quantization effects—but is consistent with previous many-body calculations in the sequential tunneling regime [76, 136, 18]. It should be emphasized that the transport gap $\Delta\mu_{\rm tr}$ in a molecular junction exceeds the optical gap $\hbar\omega_{\rm min}$ of an isolated molecule. Roughly speaking, $\Delta\mu_{\rm tr} \simeq \hbar\omega_{\rm min} + e^2/C_{\rm mol} + E_x$, where $e^2/C_{\rm mol} \approx \langle U_{nm} \rangle$ is the charging energy of an effective capacitor (see discussion above) and $-E_x$ is the exciton binding energy.

Excitonic states of the BDT-Au junction can be identified in the differential conductance spectrum of Fig. 2.9 as the lowest-energy (i.e., smallest bias) excitations outside the central diamond of the HOMO-LUMO gap, from which it is apparent that $\Delta\mu_{\rm tr} \approx 2\hbar\omega_{\rm min}$ for a BDT-Au junction.

Our results reproduce the key features of both the coherent and Coulomb blockade transport regimes: Quantum interference effects, such as the transmission nodes

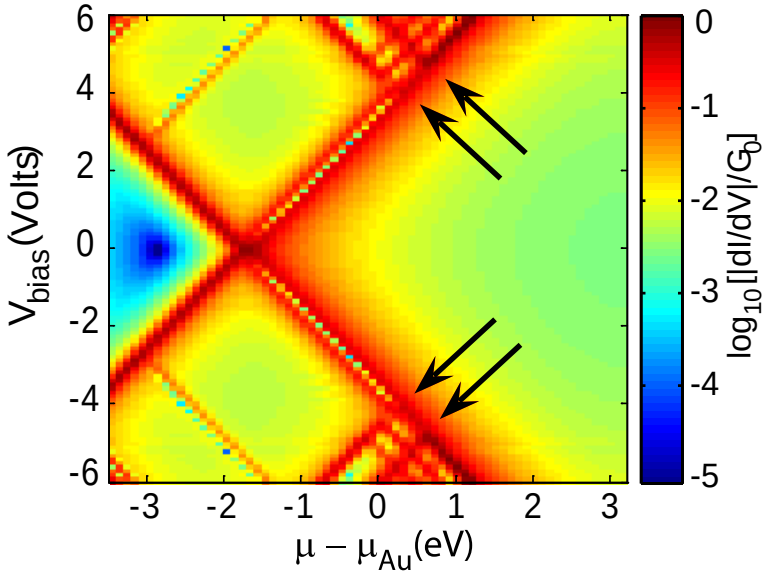

Figure 2.9: Differential conductance spectrum of a 1,4-benzenedithiol–Au junction (same parameters as in Fig. 2.8), focusing on the vicinity of the HOMO resonance. The arrows indicate features corresponding to resonant tunneling through excitonic states of the junction.

predicted within mean-field theory [29, 172, 171], are confirmed, while the differential conductance spectrum exhibits characteristic charge quantization "diamonds" [145, 116, 101, 149, 41]—an effect outside the scope of mean-field approaches based, for example, on density-functional theory. The HOMO-LUMO transport gap obtained is consistent with previous many-body treatments in the sequential tunneling limit [76, 136, 18].

2.4 The importance of many-body effects on transport

In general, mean-field approaches underestimate quantum and thermal fluctuations because they approximate the dynamic electron-electron correlations by a static single-body potential. Especially at the nanoscale, where the energetic cost of adding electrons is large, it seems likely that the details of the charge correlations would affect the transport. Surprisingly, within the molecular electronics community, many-body terms are often thought of as small corrections to the mean-field

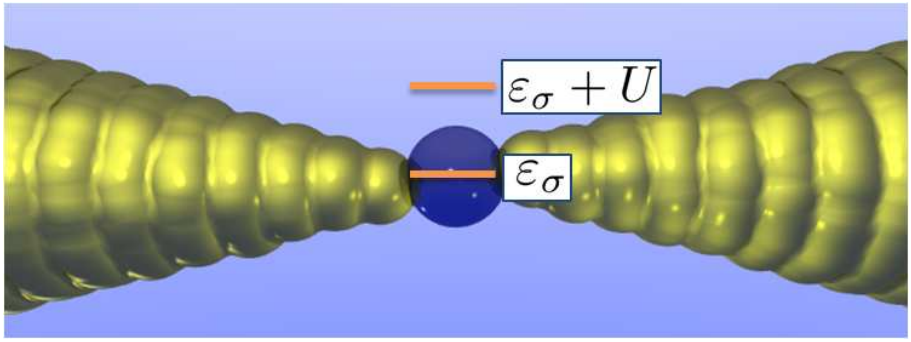

Figure 2.10: A schematic diagram of an 'Anderson molecule' junction composed of a single atomic level coupled to two metallic leads. The addition spectrum for spin σ has two electronic resonances: the first at ε_σ and another at $\varepsilon_\sigma+U$ corresponding to the transition from zero to one and one to two electrons on the molecule, respectively.

solution, with only a slight effect on transport.

In the first part of this section, we consider transport through an 'Anderson junction' composed of a single orbital tunnel-coupled to two metallic leads and find a large discrepancy between the junction currents predicted by many-body and mean-field theories. Next, we investigate quantum transport through a molecular radical, which maps onto an Anderson model at low energy, and discuss the inability of spin-unrestricted mean-field theory to reproduce even qualitative features of the transmission spectrum.

2.4.1 The 'Anderson' molecular junction

As a first example of the importance of including many-body correlations, consider a junction composed of two metallic leads coupled to a single 'Anderson molecule' described by the following Hamiltonian [6]

$$H_{\rm mol} = \varepsilon_\uparrow n_\uparrow + \varepsilon_\downarrow n_\downarrow + U n_\uparrow n_\downarrow, \tag{2.51}$$

where the number operator $n_\sigma{=}d_\sigma^\dagger d_\sigma$ for spin σ and the Coulomb integral $U{=}\int dr_1 dr_2 \left|\psi(r_1)\right|^2 \left(e^2/\left|r_1-r_2\right|\right) \left|\psi(r_2)\right|^2$. In our discussion here, we take $U{=}$8.9eV [30, 23].

The occupancy of the isolated molecule can vary between zero and two, so a

natural eigenbasis of Eq. (2.51) is the set of Fock states $\{|0\rangle, |\uparrow\rangle, |\downarrow\rangle, |\uparrow\downarrow\rangle\}$ with corresponding eigenenergies $\{0,\ \varepsilon_\uparrow,\ \varepsilon_\downarrow,\ \varepsilon_\uparrow+\varepsilon_\downarrow+U\}$. As indicated schematically in Fig. 2.10, the Anderson junction has two electronic addition resonances for each spin species σ: one at ε_σ and another at $\varepsilon_\sigma + U$.

The many-body molecular Green's function can be found from the Hamiltonian using Eq. (2.21):

$$\begin{aligned}
[G_{\mathrm{mol}}(E)]_{\sigma\sigma} &= \sum_{\nu,\nu'} [\mathcal{P}(\nu) + \mathcal{P}(\nu')] \frac{\langle\nu|d_\sigma|\nu'\rangle\langle\nu'|d_\sigma^\dagger|\nu\rangle}{E - E_{\nu'} + E_\nu + i0^+} \\
&= \frac{1 - \langle n_{\bar\sigma}\rangle}{E - \varepsilon_\sigma + i0^+} + \frac{\langle n_{\bar\sigma}\rangle}{E - \varepsilon_\sigma - U + i0^+},
\end{aligned} \tag{2.52}$$

where the bar on the spin index σ is meant to indicate the opposite spin and the thermodynamic factors $\mathcal{P}(\nu)$ and $\mathcal{P}(\nu')$ have been rewritten in terms of

$$1 - \langle n_{\bar\sigma}\rangle = \frac{1 + e^{-\beta(\varepsilon_\sigma - \mu)}}{\mathcal{Z}} \tag{2.53}$$

and

$$\langle n_{\bar\sigma}\rangle = \frac{e^{-\beta(\varepsilon_{\bar\sigma} - \mu)} + e^{-\beta(\varepsilon_{\bar\sigma} + \varepsilon_\sigma + U - 2\mu)}}{\mathcal{Z}} \tag{2.54}$$

with $\beta{=}1/k_{\mathrm{B}}T$ and the grand canonical partition function $\mathcal{Z}{=}\sum_\nu e^{-\beta(E_\nu - N_\nu\mu)}$. Note that in many-body theory, without any broken spin symmetry (i.e. with $\varepsilon_\uparrow{=}\varepsilon_\downarrow$) each spin species' molecular Green's function has two poles, a consequence of the fact that there are two non-zero matrix elements for the creation operator: $\langle\sigma|\, d_\sigma^\dagger\, |0\rangle$ and $\langle\uparrow\downarrow|\, d_\sigma^\dagger\, |\bar\sigma\rangle$.

In the spin-unrestricted Hartree-Fock (UHF) approximation, the spin symmetry of the mean-field potential is not enforced. In fact, the symmetry is usually deliberately broken so as to engineer a shift of electronic resonances into agreement with a known spectrum. In spite of the unphysical nature of this symmetry breaking spin-unrestricted methods are ubiquitous and appear in many of the methods used in molecular electronics (cf. most implementations of DFT, LDA+U, etc.) because their Hilbert spaces scale linearly in the size of the system and make the investigation of large molecules possible. In addition, because of the technological difficulties involved with gating a single molecule, the entire molecular spectrum is

not often considered to be as important as the HOMO and LUMO resonances. While engineering a spin potential capable of mimicking an entire spectrum may not be possible, the broken spin-symmetry necessary to fit two resonances using this scheme can always be found.

Within the UHF approximation the Hamiltonian of Eq. (2.51) becomes

$$H_{\mathrm{mol}}^{\mathrm{UHF}} = \sum_{\sigma\in\{\uparrow,\downarrow\}} E_\sigma n_\sigma, \tag{2.55}$$

where the energies $E_\sigma{=}\varepsilon_\sigma + U\langle n_{\bar{\sigma}}\rangle$ are found using first-order perturbation theory along with the factorization

$$\begin{aligned}\langle n_\uparrow n_\downarrow\rangle &= \langle d_\uparrow^\dagger d_\uparrow d_\downarrow^\dagger d_\downarrow\rangle \equiv \langle d_\uparrow^\dagger d_\uparrow\rangle\langle d_\downarrow^\dagger d_\downarrow\rangle - \underbrace{\langle d_\uparrow^\dagger d_\downarrow\rangle\langle d_\downarrow^\dagger d_\uparrow\rangle}_{=0,\text{nohopping}} \\ &= \langle n_\uparrow\rangle\langle n_\downarrow\rangle. \end{aligned}\tag{2.56}$$

The UHF Hamiltonian given by Eq. (2.55) is a sum of two Hamiltonians, one for each spin species, coupled to each other by their densities. There is no Fock (exchange) contribution because there is only a single site in the Anderson model. As the name suggests, in the mean-field approximation particles interact with the static potential arising from the average potential made by the other particles. In this light, Eq. (2.56) is quite intuitive since it implies that $n_\uparrow n_\downarrow \equiv \langle n_\uparrow\rangle n_\downarrow$, where the potential energy arising from the 'other particles' is $U\langle n_\uparrow\rangle$. Following the same prescription as before, the molecular Green's function for spin σ can be found from the Hamiltonian giving

$$\left[G_{\mathrm{mol}}^{\mathrm{UHF}}(E)\right]_{\sigma\sigma} = \frac{1}{E - H_{\mathrm{mol}}^{\mathrm{UHF}} + i0^+} = \frac{1}{E - (\varepsilon + U\langle n_{\bar{\sigma}}\rangle) + i0^+}, \tag{2.57}$$

which consists of only a single pole.

In a symmetric two-terminal junction the current is given in the elastic cotunneling limit by Eq. (2.40)

$$I = \frac{e}{h}\int_{-\infty}^{\infty} T\left(E\right)\left[f_2\left(E\right) - f_1\left(E\right)\right], \tag{2.58}$$

where the transmission probability $T\left(E\right){=}\Gamma^2\sum_\sigma \left|G_{\sigma\sigma}\left(E\right)\right|^2$ and $f_\alpha(E){=}\{1+\exp\left[\beta(E-\mu_\alpha)\right]\}^{-1}$ is the Fermi-Dirac distribution for lead α at

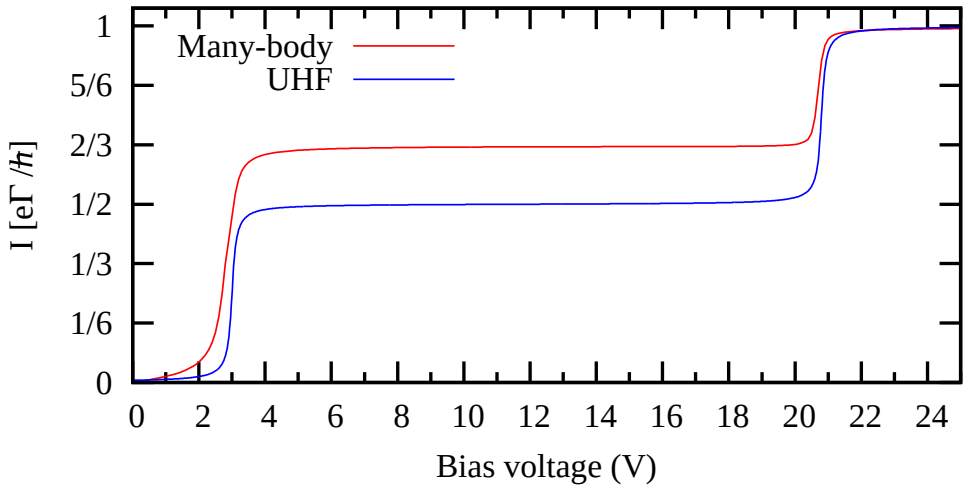

Figure 2.11: The current as a function of bias voltage for an Anderson junction using many-body and UHF theory. Each theory predicts steps in the current at the same voltages, although the heights of the two steps are different. For voltages between the two current steps, the many-body theory predicts a plateau height of 2/3 while the spin-unrestricted approach gives 1/2.

inverse temperature β=$1/k_{\mathrm{B}}T$. The tunneling-width matrix element Γ is taken as an energy independent constant for all the simulations discussed in this section.

The current in an Anderson junction is shown as a function of bias voltage in Fig. 2.11, using both many-body and UHF theories. The current has been normalized in units of $\lim_{V\to\infty} I = e\Gamma/\hbar$. The inability of mean-field theories to correctly describe the relative step heights in the current-voltage curve of a SMJ in the Coulomb blockade regime has been put forward as a "smoking gun" for the importance of many-body correlations [137].

A current step occurs at a voltage V where the leads' chemical potentials correspond to molecular addition energies, opening an additional transport channel of the junction. The equilibrium chemical potential μ_0=8eV so that the first step occurs at ΔV=3V and the second 2U away at ΔV=20.8V. In the many-body simulation there was no broken spin-symmetry: $\varepsilon_\uparrow$=$\varepsilon_\downarrow$=5eV. In the UHF simulation $\varepsilon_\uparrow$=5eV and $\varepsilon_\downarrow$=$\varepsilon_\uparrow$+U=13.9eV, so as to ensure the proper current step positions. As the figure shows, each theory predicts steps in the current at the same voltages, although the heights of the two steps are different. For voltages between the two current steps,

two charge states of the junction are energetically accessible, and the many-body theory predicts a plateau height of 2/3 while the spin-unrestricted approach gives 1/2.

In UHF theory, G_{mol} has only a single pole per spin species, meaning that the height of each step of the Coulomb staircase for the Anderson model is identical (1/2 in normalized units) since when ΔV=3V the spin-up-only channel opens and when ΔV=20.8V the spin-down-only channel opens. In contrast, the many-body G_{mol} has two poles per spin species so when ΔV=3V a charge channel opens transporting electrons of *both spins* but when ΔV=20.8 the step is reduced since, according to the Pauli-exclusion principle, only one spin-channel is available [210]. The first current step height is therefore twice as high as the second giving 2/3 and 1/3 in normalized units, respectively.

In UHF, the spin-rotation symmetry of the Hamiltonian is broken in order to mimic a charge gap. Transport, however, is not just a function of energy levels but also of matrix elements, which depend on symmetry. Consequently, even though the gap and energy levels of the molecular resonances were the identical in the many-body and UHF simulations, the broken spin symmetry in the latter approach means that the two spin species contributed unequally to the transport, giving rise to the discrepancy in the junction current. Physically, the spin symmetry can be broken by the Zeeman effect in an external magnetic field. The Zeeman splitting must satisfy $\mu_{\mathrm{B}}B/k_{\mathrm{B}}T \gg \max(T, T_K)$ to fully break spin-rotation invariance, where B is the magnetic field strength, μ_{B} is the Bohr magneton , T is the temperature, k_{B} is Boltzmann's constant and T_K is the Kondo temperature. In the case of the pentadienyl radical SMJ discussed in the next section, however, the magnetic field strength required to break spin symmetry to such an extent that the transmission spectrum resembles that of the spin-unrestricted calculation is greater than 10^4T.

2.4.2 Radical-based molecular junctions

In the previous section, we found that transport is not simply a matter of molecular energy levels but depends on the symmetry of the molecular states as well. Here we

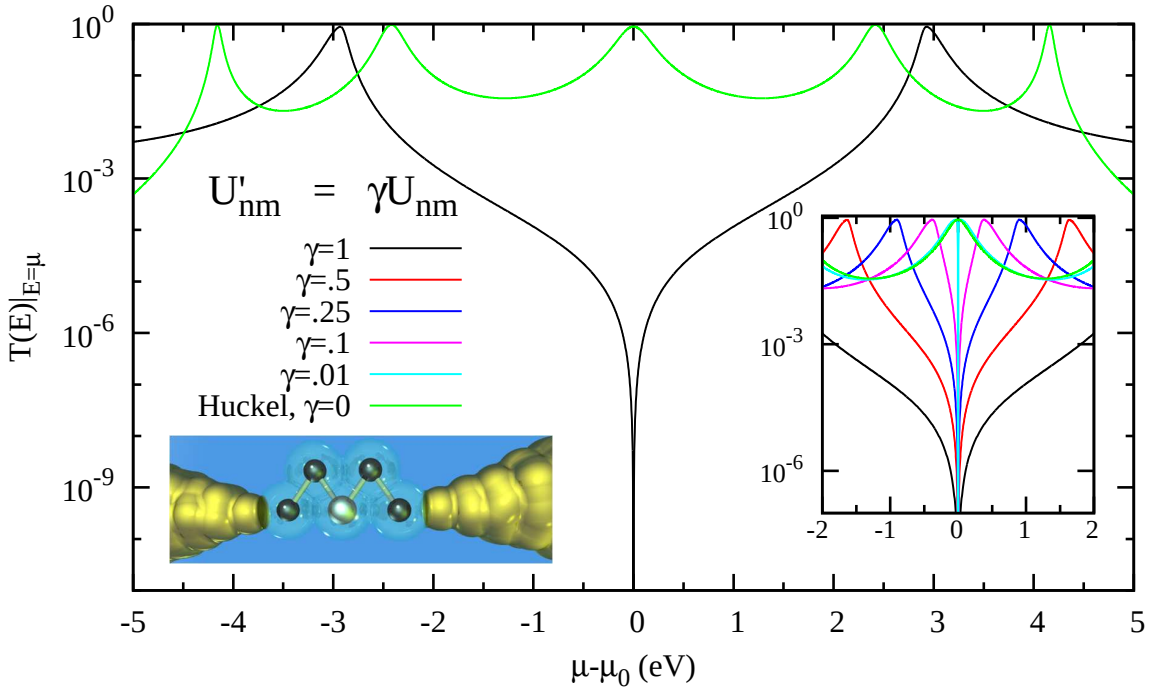

Figure 2.12: The room-temperature (T=300K) transmission function of a pentadienyl radical junction (sketched above) as a function of the intra-molecular interaction strength γ. As Coulomb interactions are turned on ($\gamma \neq 0$), a HOMO-LUMO gap forms, and the transmission resonance at the Fermi level becomes a node. The nearest neighbor hopping matrix element t_s=2.2 and t_d=2.6eV for single and double-bonds, respectively. U_{nm} is the interaction matrix element between sites n and m and follows the form outlined in Sec. 2.1.1. The on-site repulsion U_{nn}=8.9eV in this case.

explore the importance of these symmetries further by considering a radical-based junction, where the molecule possesses an unpaired electron. In this section we find that the broken spin symmetry required to mimic the correct charge gap in UHF gives rise to large qualitative errors in the transmission spectrum of radical-based junctions.

In the discussion that follows we consider transport in a pentadienyl radical junction, which is shown schematically in the bottom left-hand corner of Fig. 2.12. The π-electrons of the pentadienyl radical were modeled using the Hamiltonian discussed in Sec. (2.2) with intramolecular nearest-neighbor hopping matrix elements set to t_s=2.2eV and t_d=2.6eV for single and double-bonds, respectively. The lead-

molecule coupling was chosen to be symmetric and taken in the broad-band limit such that Γ=0.5eV.

The transmission probability spectra shown in the inset of Fig. 2.12 shows the emergence of a HOMO-LUMO 'Mott gap' as the Coulomb interaction strength γ is increased. When γ=0 electron-electron correlations are neglected and our many-body Green's functions are equivalent to those found using Hückel theory. As interactions are turned on the degeneracy of the HOMO and LUMO levels is lifted and the mid-gap transmission peak predicted by Hückel theory becomes a transmission node.

Transmission nodes are generic features of coherence in single-channel transport. In our formulation of transport, the transmission probability is equal to the modulus squared of the junction's Green's function, meaning that the transmission nodes must arise from terms in the Green's function. The structure of the molecular Green's function is generally complicated but the low-energy excitation spectrum of a molecular radical can be mapped onto the Anderson model, which has already been derived in Sec. 2.4.1.

In the Anderson model, all non-zero poles of the many-body molecular Green's function, neglecting the thermodynamic weighting factors, have a weight of one (cf. Eq. (2.52)). The mid-gap transmission node shown in Fig. 2.12 arises because the two poles of G_{mol} have equal matrix elements and contribute equally and oppositely when μ=μ_0. Consequently, $G_{\mathrm{mol}}(\mu_0)$=0 and $T(\mu_0) \propto |G_{\mathrm{mol}}(\mu_0)|^2$=0.

In UHF, however, the molecular Green's function of a single spin species has only a single pole. This type of transmission node therefore lies outside the scope of any mean-field theory because, even if a HOMO-LUMO gap is put in by hand by breaking spin symmetry, the separate poles for up and down spins would not interfere.

Presently, most modern transport calculations involve implementations of density functional theory (DFT); a theory which would give the exact electronic ground state, including all charge-charge coherences, if the exact exchange-correlation functional were known. A spin-unrestricted DFT calculation of the transmission through

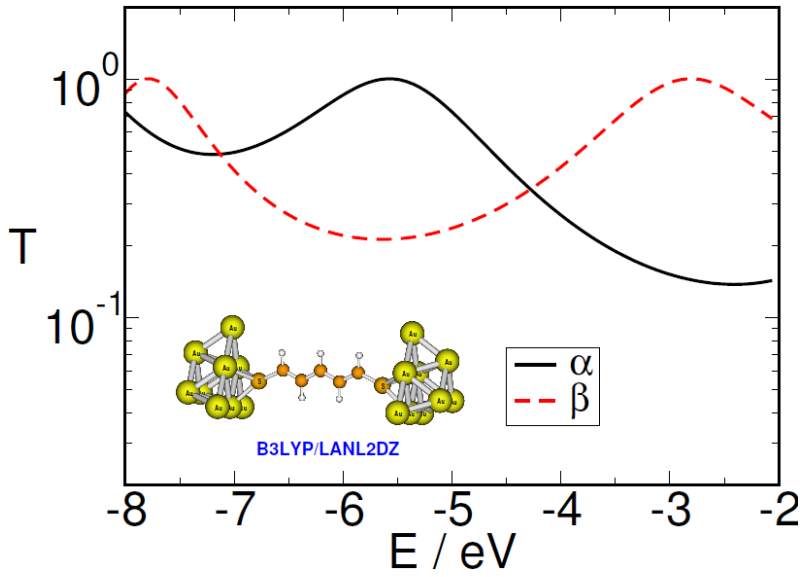

Figure 2.13: A state-of-the-art DFT calculation of the transmission probability spectrum for α and β spin species through a pentadienyl radical junction. This calculation exhibits no nodal features, in agreement with our understanding of the limitations of mean-field approaches. The simulation was performed by our collaborators G. Solomon and C. Herrmann.

a pentadienyl radical SMJ is shown in Fig. 2.13, where no transmission nodes are found near the Fermi energy of gold (≈-5.5eV). In spite of DFT's sophistication, existing implementations of the exchange-correlation functional don't properly describe the quantization of charge [188, 97, 136, 63] and consequently the resulting transport doesn't exhibit a Mott-node.

2.5 Summary

In this chapter, we presented a many-body theory of electron transport in single-molecule heterojunctions that treats coherent quantum effects and Coulomb interactions on an equal footing. As a first application of our theory, we have investigated the thermoelectric power and differential conductance of a prototypical single-molecule junction, benzenedithiol with gold electrodes.

The central object of the many-body theory is the Coulomb self-energy $\Sigma_{\rm C}$ of the junction, which may be expressed as $\Sigma_{\rm C} = \Sigma_{\rm C}^{(0)} + \Delta\Sigma_{\rm C}$, where $\Sigma_{\rm C}^{(0)}$ is the result in the

sequential-tunneling limit, and $\Delta\Sigma_{\mathrm{C}}$ is the correction due to a finite tunneling width Γ. In this chapter, $\Sigma_{\mathrm{C}}^{(0)}$ was evaluated exactly, thereby including intramolecular correlations at a nonperturbative level, while the direct and exchange contributions to $\Delta\Sigma_{\mathrm{C}}$ were evaluated self-consistently using a conserving approximation based on diagrammatic perturbation theory on the Keldysh contour. An important feature of our theory is that this approximation for $\Delta\Sigma_{\mathrm{C}}$ can be systematically improved by including additional processes diagrammatically. In this way, important effects such as dynamical screening, spin-flip scattering [151], and electron-phonon coupling [132, 61, 147, 197, 45, 174] can be included as natural extensions of the theory.

As a first application of our many-body transport theory, we investigated the benchmark system of 1,4-BDT with gold electrodes. Two key parameters determining the lead-molecule coupling—the tunneling width Γ and the chemical potential offset $\Delta\mu$—are fixed by comparison to linear-response measurements of the thermoelectric power [152, 15] and electrical conductance [203]. The nonlinear junction response is then calculated without any free parameters. The differential conductance spectrum of the junction exhibits an irregular "molecular diamond" structures analogous to the regular Coulomb diamonds [44] observed in quantum dot transport experiments, as well as clear signatures of coherent quantum transport—such as transmission nodes due to destructive interference—and of resonant tunneling through molecular excited states.

Lastly, we compared the transport predictions using UHF and our many-body theory for both an Anderson model and a radical-based junction and discovered significant qualitative and quantitative discrepancies between the two theories. Spin-unrestricted mean-field theories like UHF are ubiquitous, constituting the dominant theoretical paradigm in molecular electronics, and have already been applied to transport problems involving molecular radicals [75]. The large effect of an unphysical broken spin symmetry on the transport suggests that extraordinary care must be taken when interpreting the results of these studies.

CHAPTER 3

Thermoelectric Response of Single-Molecule Junctions

In chapter 2 we developed a many-body theory of electronic transport for junctions composed of an interacting quantum system coupled to macroscopic leads. Within that theory, we also derived an expression for the charge current flowing from one lead to another. In addition to charge, electrons also carry heat and in this chapter we use thermodynamics in conjunction with our many-body theory to develop an exact expression for the heat current flowing in a molecular junction. We then investigate the linear and nonlinear thermoelectric response of a number of molecular junctions and find several interesting results.

In single-molecule junctions (SMJs), it is often assumed that transport is dominated by elastic scattering processes. Since the phonon modes of the molecule and the Debye frequency of the leads are often far detuned from one another and, as we shall see in chapter 5, the electronic contribution to the inelastic transport is small, this is most likely a reasonable assumption. Presently, however, no experiments have been performed to verify this assumption because measuring the degree of transport coherence in molecular junctions is extremely difficult. In Sec. 3.2 we show that, in contrast to the electrical transport, *thermoelectric effects are dramatically enhanced* in the vicinity of a transmission node which can only arise from interference, thus providing a "smoking gun" for coherent transport that can be easily measured in experiments on single-molecule junctions.

In Sec. 3.3 we investigate the limits of the rule-of-thumb quantity ZT as a predictor of nonequilibrium thermodynamic device *performance* at the nanoscale. Lastly, in Sec. 3.4 we investigate transport in junctions exhibiting high-order transmission interferences, giant thermoelectric responses and large thermodynamic efficiencies.

3.1 Nonequilibrium heat transport theory

In order to investigate thermoelectric effects in SMJs, where Coulomb interactions play an essential role [23], we first derive an exact expression for the heat current in an interacting nanostructure. Using this result, together with the corresponding expression for the electrical current given by Eq. (2.37), we derive expressions for the linear thermoelectric response of the junction.

3.1.1 Derivation of the junction heat current

As in chapter 2, we begin by considering a junction consisting of a single molecule covalently bonded to M metallic electrodes (labeled $\alpha \in [1, \ldots, M]$). The Hamiltonian of the system may be written

$$H_{\text{junction}} = H_{\text{mol}} + \sum_{\alpha=1}^{M} \left[H_{\text{lead}}^{(\alpha)} + H_{\text{T}}^{(\alpha)} \right], \tag{3.1}$$

where H_{mol} is the molecular Hamiltonian. Each electrode is modeled as a non-interacting Fermi gas:

$$H_{\text{lead}}^{(\alpha)} = \sum_{\substack{k\in\alpha \\ \sigma}} \varepsilon_{k\sigma} c_{k\sigma}^{\dagger} c_{k\sigma}, \quad N_{\alpha} = \sum_{\substack{k\in\alpha \\ \sigma}} c_{k\sigma}^{\dagger} c_{k\sigma}, \tag{3.2}$$

where $c_{k\sigma}^{\dagger}$ creates an electron of energy $\varepsilon_{k\sigma}$ in lead α. Tunneling of electrons between the molecule and electrode α is described by the Hamiltonian

$$H_{\text{T}}^{(\alpha)} = \sum_{k\in\alpha} \sum_{n,\sigma} \left(V_{nk} d_{n\sigma}^{\dagger} c_{k\sigma} + \text{H.c.} \right), \tag{3.3}$$

where $d_{n\sigma}^{\dagger}$ creates an electron of spin σ on the nth atomic orbital of the molecule.

The starting point for our derivation of the heat current is the fundamental thermodynamic identity at constant volume, $TdS = dE - \mu dN$. Applying the identity to electrode α, one finds

$$I_{\alpha}^{Q} \equiv T_{\alpha} \frac{dS_{\alpha}}{dt} = \frac{d}{dt} \left\langle H_{\text{lead}}^{(\alpha)} \right\rangle - \mu_{\alpha} \frac{d}{dt} \left\langle N_{\alpha} \right\rangle, \tag{3.4}$$

where I_α^Q is the heat current flowing from the molecule into electrode α, and T_α and μ_α are the temperature and chemical potential, respectively, of electrode α. The time derivatives on the right-hand side of Eq. (3.4) may be evaluated using standard quantum mechanics to obtain

$$\begin{aligned} I_\alpha^Q &= -\frac{i}{\hbar}\left\{\left\langle\left[H_{\rm lead}^{(\alpha)}, H_{\rm junction}\right]\right\rangle - \mu_\alpha\langle[N_\alpha, H_{\rm junction}]\rangle\right\} \\ &= \frac{i}{\hbar}\sum_{k\in\alpha}\sum_{n,\sigma}(\varepsilon_{k\sigma}-\mu_\alpha)\left[V_{nk}\langle d_{n\sigma}^\dagger c_{k\sigma}\rangle - V_{nk}^*\langle c_{k\sigma}^\dagger d_{n\sigma}\rangle\right]. \end{aligned} \tag{3.5}$$

The second line of Eq. (3.5) is similar to the corresponding formula for the electrical current given by Eq. (2.36), except for the additional factor of $\varepsilon_{k\sigma}-\mu_\alpha$ inside the sum. The correlation functions in the second line of Eq. (3.5) may be formally expressed in terms of the junction's Green's functions using Dyson's equation, [24] leading to the general result:

$$\begin{aligned} I_\alpha^{(\nu)} &= -\frac{i}{h}\int_{-\infty}^{\infty} dE(E-\mu_\alpha)^\nu \times \\ &\quad {\rm Tr}\left\{\Gamma^\alpha(E)\left(G^<(E) + f_\alpha(E)\left[G(E) - G^\dagger(E)\right]\right)\right\}, \end{aligned} \tag{3.6}$$

where $\nu = 1$ gives the heat current and $\nu = 0$ the number current. Here $f_\alpha(E)$ and $\Gamma^\alpha(E)$ are the Fermi-Dirac distribution and tunneling-width matrix, respectively, for lead α. $G(E)$ and $G^<(E)$ are Fourier transforms of the retarded and Keldysh "lesser" Green's functions, respectively. Eq. (3.6) is an exact formal result,[1] and provides a complete framework for calculating heat transport and thermoelectric effects in interacting nanostructures. To the best of our knowledge, we are the first to derive such an expression for the heat current.

As we found in chapter 2, the junction's retarded Green's function obeys a molecular Dyson equation [23]

$$G^{-1}(E) = G_{\rm mol}^{-1}(E) - \Sigma_{\rm T} - \Delta\Sigma_{\rm C}, \tag{3.7}$$

where $G_{\rm mol}$ may be evaluated by exact diagonalization of $H_{\rm mol}$ in the sequential-tunneling limit, and the self-energy terms $\Sigma_{\rm T} + \Delta\Sigma_{\rm C}$ describe the effects of finite

[1] Eq. (3.6) is a multi-terminal expression, where $\Sigma_{\rm T}^<$ (2.19) includes a sum over all leads.

tunneling width. Here the tunneling self-energy matrix, given by Eq. (2.16), can be calculated exactly, while the tunneling correction $\Delta\Sigma_{\rm C}$ to the Coulomb self-energy can in general only be calculated approximately (cf. Sec. 2.1.4). However, in the middle of the highest occupied molecular orbital (HOMO)-lowest unoccupied molecular orbital (LUMO) gap—the region of principal interest for this discussion—it can be shown [23] that $\Delta\Sigma_{\rm C} \approx 0$. Both $G(E)$ and $G^<(E)$ arise from time-ordered Green's functions on the Keldysh time-contour [71], so any prescription for calculating $G(E)$ also yields $G^<(E)$ without further approximations.

3.1.2 The elastic cotunelling regime and linear-response observables

In many cases of interest in nanostructures, elastic processes dominate transport. This is the case if $\mathrm{Im}\,\Delta\Sigma_{\rm C} \approx 0$ and electron-phonon scattering is negligible. Then Eq. (3.6) may be simplified and cast in a form analogous to the multi-terminal Büttiker formula [24]

$$I_\alpha^{(\nu)} = \frac{1}{h}\sum_{\beta=1}^{M}\int_{-\infty}^{\infty} dE\,(E-\mu_\alpha)^\nu\, T_{\alpha\beta}(E)\,[f_\beta(E)-f_\alpha(E)]\,, \tag{3.8}$$

where the transmission function is given by Eq. (2.41).

In linear response, the set of equations (3.8) (with $\nu = 0, 1$) may be further simplified by considering the junction's response to leading order in temperature and chemical potential differences. In matrix form these equations may be written as

$$\begin{pmatrix} I_\alpha^{(0)} \\ I_\alpha^{(1)} \end{pmatrix} = \sum_\beta \begin{pmatrix} \mathcal{L}_{\alpha\beta}^{(0)} & \frac{1}{T}\mathcal{L}_{\alpha\beta}^{(1)} \\ \mathcal{L}_{\alpha\beta}^{(1)} & \frac{1}{T}\mathcal{L}_{\alpha\beta}^{(2)} \end{pmatrix} \begin{pmatrix} \mu_\beta - \mu_\alpha \\ T_\beta - T_\alpha \end{pmatrix}, \tag{3.9}$$

where

$$\mathcal{L}_{\alpha\beta}^{(\nu)}(\mu, T) = \frac{1}{h}\int dE \left(-\frac{\partial f}{\partial E}\right)(E-\mu)^\nu\, T_{\alpha\beta}(E). \tag{3.10}$$

Here $f(E)$ is the equilibrium (zero-bias) Fermi distribution with chemical potential μ and temperature T. We may then use the $\mathcal{L}$ functions to compactly encode a

number of important transport properties [57]:

$$G_{\alpha\beta}(\mu,T) = e^2\mathcal{L}^{(0)}_{\alpha\beta}(\mu,T) \tag{3.11}$$

$$S_{\alpha\beta}(\mu,T) = -\frac{1}{eT}\frac{\mathcal{L}^{(1)}_{\alpha\beta}(\mu,T)}{\mathcal{L}^{(0)}_{\alpha\beta}(\mu,T)} \tag{3.12}$$

$$\kappa_{\alpha\beta}(\mu,T) = \frac{1}{T}\left(\mathcal{L}^{(2)}_{\alpha\beta}(\mu,T) - \frac{\left[\mathcal{L}^{(1)}_{\alpha\beta}(\mu,T)\right]^2}{\mathcal{L}^{(0)}_{\alpha\beta}(\mu,T)}\right) \tag{3.13}$$

where G is the electrical conductance, S is the thermopower (Seebeck coefficient) derived in Sec. 2.1.5, and κ is the electronic contribution to the (two-terminal) thermal conductance. Another important linear response quantity $ZT{=}S^2GT/\kappa$ will be discussed in relation to thermodynamic performance in Secs. 3.3 and 3.4. The linear-response transport coefficients of an interacting system thus have a structure identical to that of a non-interacting system, except that $T_{\alpha\beta}(E)$ must be calculated using the interacting Green's functions. It should be emphasized that Eqs. (3.11)–(3.13) can also be derived directly from the full heat current expression of Eq. (3.6), provided $\lim_{\Delta\mu\to 0}(\mathrm{Im}\Delta\Sigma_{\mathrm{C}}/\Delta\mu) = 0$ and $\lim_{\Delta T\to 0}(\mathrm{Im}\Delta\Sigma_{\mathrm{C}}/\Delta T) = 0$ (with similar conditions on the electron-phonon self-energy).

3.2 Thermoelectric enhancement near transmission nodes

Electronic phase coherence underlies many of the unique and potentially revolutionary aspects of molecular device technology [29]. However, unequivocal experimental signatures of phase-coherent electron transport are difficult to obtain. Aharonov-Bohm interferometers have been used in quantum-dot [205, 163, 11] and carbon nanotube [13] studies to determine both the degree of coherence and to map the phase evolution of transmission by controlling the magnetic field and gate-voltage, respectively. Phase information can also be extracted from asymmetric Fano lineshapes arising from interference between resonant and non-resonant transport pathways; [36] the degree of asymmetry is related to the degree of phase coherence, so an experiment needs to distinguish between a symmetric Breit-Wigner lineshape and a

slightly asymmetric one in order to demonstrate phase coherence.

A characteristic feature of coherent transport is the existence of nodes in the transmission eigenvalue spectra [29, 170, 24, 22]. A transmission node can only arise from destructive quantum interference, and as such constitutes a clear signature of coherent quantum transport in any system. However, incoherent processes may also give rise to very low transmission probabilities whose effect on the electrical conductance may be experimentally indistinguishable [129] from that of a transmission node. In this section, we calculate both the thermopower S and the Lorenz number L for three representative molecular junctions and discover a large thermoelectric enhancement arising from quantum interference in the vicinity of a transmission node.

The calculated spectra for isoprene, 1,3-benzenedithiol, and [18]-annulene junctions are shown in Figs. 3.1a, 3.1b, and 3.1c, respectively. Each junction has a transmission node in the center of the HOMO-LUMO gap (see Fig. 3.1, upper panels). Both the thermopower S (middle panels) and the Lorenz number $L = \kappa/GT$ (lower panels) are strongly enhanced in the vicinity of the mid-gap nodes. Although transmission nodes are generic features of coherent transport, mid-gap nodes are experimentally advantageous for two reasons: (i) when the lead chemical potential is in the gap, the molecule is charge-neutral, and (ii) the mismatch between the metal leads' Fermi energies and the center of the HOMO-LUMO gap is typically small (a few eV or less), so available gating techniques [182] should be sufficient to tune across the node.

In Fig. 3.1, isoprene and benzenedithiol were modeled using the same semi-empirical π-electron Pariser-Parr-Pople (PPP) Hamiltonian discussed in Sec. 2.2, which has been shown to accurately describe Coulomb interactions and π-conjugation [33, 30, 29, 23]. [18]-annulene was modeled using Hückel molecular orbital theory ($\Sigma_{\rm C} = 0$). The interaction and hopping matrix elements were taken from Ref. 30. The tunneling-width matrix was taken in the broad-band limit [81] whereby $\Gamma^{\alpha}_{n\sigma,m\sigma'}(E) = \Gamma_{\alpha}\delta_{\sigma\sigma'}\delta_{na}\delta_{ma}$, where a is the π-orbital connected to lead α. The junctions were taken to be symmetric, with $\Gamma_1 = \Gamma_2 = 0.5$eV. It should be

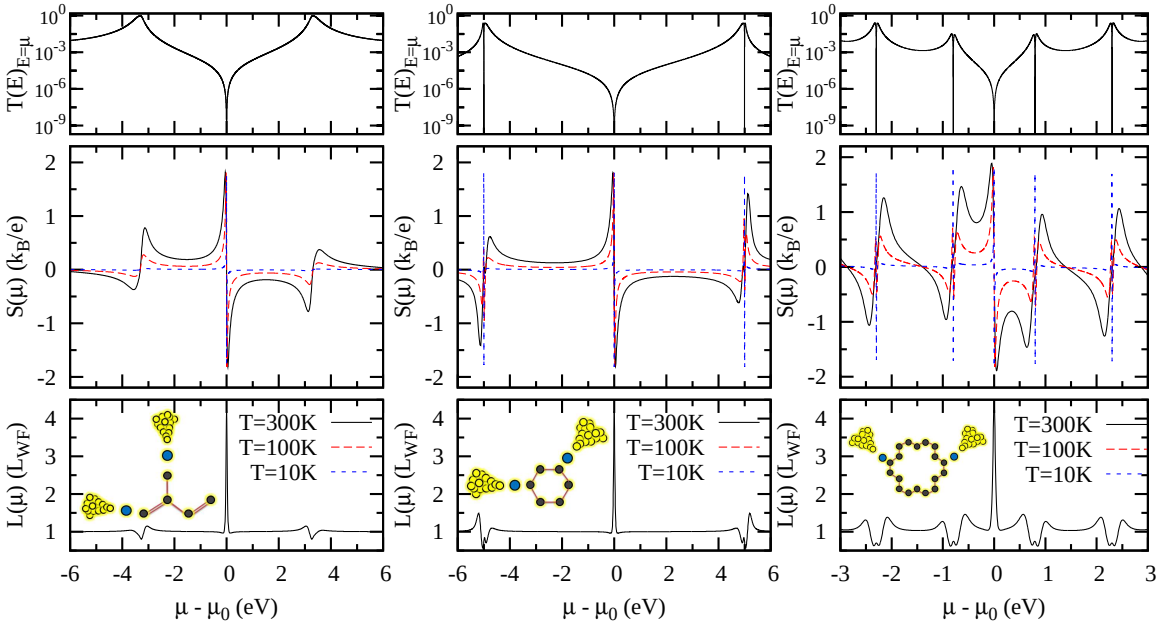

(a) isoprene (b) 1,3-benzenedithiol (c) 18-annulene

Figure 3.1: Transmission probability (upper panels, logarithmic scale), thermopower (middle panels), and Lorenz number (lower panels) as a function of lead chemical potential for three single-molecule junctions possessing transmission nodes at the center of the HOMO-LUMO gap, $\mu_0 \equiv (\varepsilon_{\mathrm{LUMO}} + \varepsilon_{\mathrm{HOMO}})/2$. Here $\Gamma_1 = \Gamma_2$=0.5eV for all three junctions. The thermopower spectrum $S(\mu)$ is calculated at three different temperatures, demonstrating the invariance of the peak value $S_{\max} = \pi k_B/\sqrt{3}e \approx 156\mu\mathrm{V/K}$ near the transmission node. The Lorenz number, given in units of $L_{\mathrm{WF}} = \frac{\pi^2}{3}(k_{\mathrm{B}}/e)^2$, peaks at a temperature-independent value of 21/5 at the transmission node.

emphasized, however, that the principal findings presented here depend only on the existence of transmission nodes, and not on the specific form of the molecular junction Hamiltonian.

The dramatic enhancement of thermoelectric effects predicted at a transmission node arises because entropy transport is less sensitive to quantum interference than is charge transport. The entropy current I^Q_α/T_α represents the flow of disorder, which quantum mechanically is related to the purity of a system's state where, for example, a pure state has zero entropy current. As such, the entropy current inherently involves incoherence and therefore cannot be completely blocked by destruc-

tive quantum interference, whereas the electrical current *can* be completely coherent and therefore *may* be completely blocked by destructive quantum interference. Since thermopower is the entropy per unit charge carried by an electrical current and the Lorenz number is the ratio of the entropy conductance to the electrical conductance, both are strongly enhanced at a transmission node.

Since the integrands in the numerator and denominator of Eq. (3.12) both include a thermal-averaging factor of $-\partial f/\partial E$, the thermopower does not diverge when the chemical potential is tuned across a transmission node, but instead approaches a finite value which is *independent* of temperature (see Fig. 3.1, middle panels). This latter point should be emphasized, since the thermopower also increases in magnitude and changes sign as the chemical potential crosses a transmission resonance [146]. In the case of a resonance, however, the peak value is dependent upon both the temperature and lead-molecule coupling [23]. From Eq. (3.12), it is evident that S is enhanced if $\mathcal{L}^{(1)}$ is large and $\mathcal{L}^{(0)}$ is finite (transmission resonance) or if $\mathcal{L}^{(0)}$ is small and $\mathcal{L}^{(1)}$ is finite (transmission node). Near a quadratic transmission node $T_{\alpha\beta}(E) \propto (E-\mu_0)^2$, it can be shown by direct evaluation of Eq. (3.12) that the thermopower reaches a universal maximum value [139] of $\pm S_{\max} = \pm\pi k_B/\sqrt{3}e \approx \pm 156\mu\mathrm{V/K}$, consistent with the numerical results shown in Fig. 3.1. $S_{\max}$ is over an order of magnitude larger than the values obtained in recent measurements of single-molecule junctions [152, 15].

The Lorenz number for each molecular junction is shown in the lower panels of Fig. 3.1, normalized by the value predicted by the Wiedemann-Franz (WF) law:

$$L_{\mathrm{WF}} = \frac{\kappa_0 h}{Te^2} \equiv \frac{\pi^2}{3}\left(\frac{k_{\mathrm{B}}}{e}\right)^2, \tag{3.14}$$

where $\kappa_0 = \frac{\pi^2}{3}\frac{k_{\mathrm{B}}^2 T}{h}$ is the thermal conductance quantum [154]. For each molecule considered, the Lorenz number varies by tens of percent from the WF law as the chemical potential crosses an electronic resonance. This variation is comparable to the variation among different metals [9]. At a quadratic transmission node, the

Lorenz number may be evaluated directly as

$$L_{\max} = \frac{1}{(eT)^2} \left. \frac{\mathcal{L}_{12}^{(2)}(\mu, T)}{\mathcal{L}_{12}^{(0)}(\mu, T)} \right|_{\mu=\mu_{\text{node}}} = \frac{7\pi^2}{5} \left(\frac{k_{\text{B}}}{e} \right)^2, \tag{3.15}$$

where we have assumed that the node is at least $k_{\text{B}}T$ away from any transmission peak. The peak Lorenz number is 420% larger than the WF value, several times greater than the variation near a transmission peak at low temperature. The peak Lorenz number is also universal, although the width of the peak depends on temperature.

3.2.1 Thermoelectrics as a measure of transport coherence

Recent mean-field simulations suggest that tunneling through σ-orbitals may wash out any exact transmission nodes in small conjugated molecules [88, 170]. We can include the effects of any such additional non-resonant channels—or incoherent processes outside the scope of Eq. (2.41)—phenomenologically by adding a small constant ϵ to the transmission probability

$$T'_{12}(E) = T_{12}(E) + \epsilon. \tag{3.16}$$

The dependence of the Lorenz number and thermopower on ϵ and temperature near the center of the HOMO-LUMO gap of an isoprene junction is shown in Fig. 3.2 and Fig. 3.3, respectively. Interestingly, we find that if a finite minimum transmission probability reduces the predicted enhancement of thermoelectric effects at low temperatures, the full effect is restored at sufficiently high temperatures (see Fig. 3.3). This behavior may be understood analytically by using $T'_{12}(E) = \gamma(E - \mu_0)^2 + \epsilon$ in Eq. (3.10), which gives

$$S_{\max} = \pm \frac{\pi k_B}{\sqrt{3}e} \left[1 + \left(\tilde{T}/T \right)^2 \right]^{-1/2} \tag{3.17}$$

and

$$\frac{L_{\max}}{L_{\text{WF}}} = \frac{21/5 + \left(\tilde{T}/T \right)^2}{1 + \left(\tilde{T}/T \right)^2}, \tag{3.18}$$

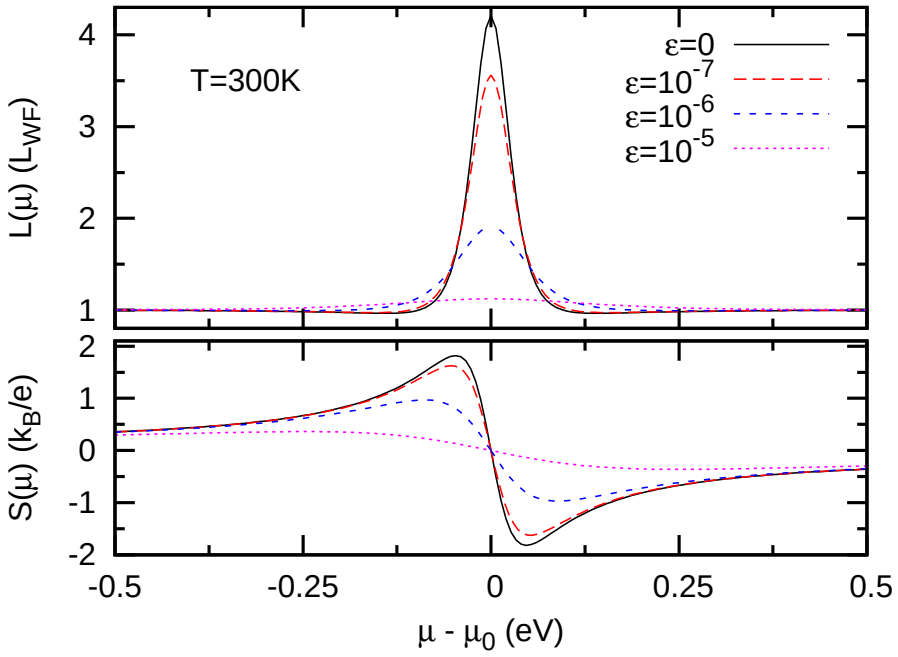

Figure 3.2: Lorenz number and Seebeck coefficient at $T = 300$K near the middle of the HOMO-LUMO gap of an isoprene junction, for various values of the minimum transmission probability ϵ. Here $\Gamma_1 = \Gamma_2$=0.5eV.

where the crossover temperature is defined by $k_B\tilde{T} = \sqrt{3\epsilon/\gamma\pi^2}$. Here γ is a constant related to the specific resonance structure of the molecule and the lead-molecule couplings. If only the LUMO and HOMO levels contribute appreciably to the transport, then $\gamma \simeq \Gamma_1\Gamma_2/2\Delta^4$, where $\Delta = (\varepsilon_{\rm LUMO} - \varepsilon_{\rm HOMO})/2$. Larger molecules, such as [18]-annulene where σ-tunneling is negligible, are thus good candidates for experimental observation of the predicted enhancement of thermoelectric effects if σ-tunneling washes out transmission nodes in small conjugated molecules.

Although we have focused on predictions of the linear thermoelectric response of single-molecule junctions in this chapter, it should be emphasized that Eq. (3.6) is an exact result valid for arbitrarily large bias and temperature gradients applied to an interacting nanostructure. To analyze the performance of a nanoscale thermoelectric device, it is necessary to go beyond linear response theory. For example, Eq. (3.6)

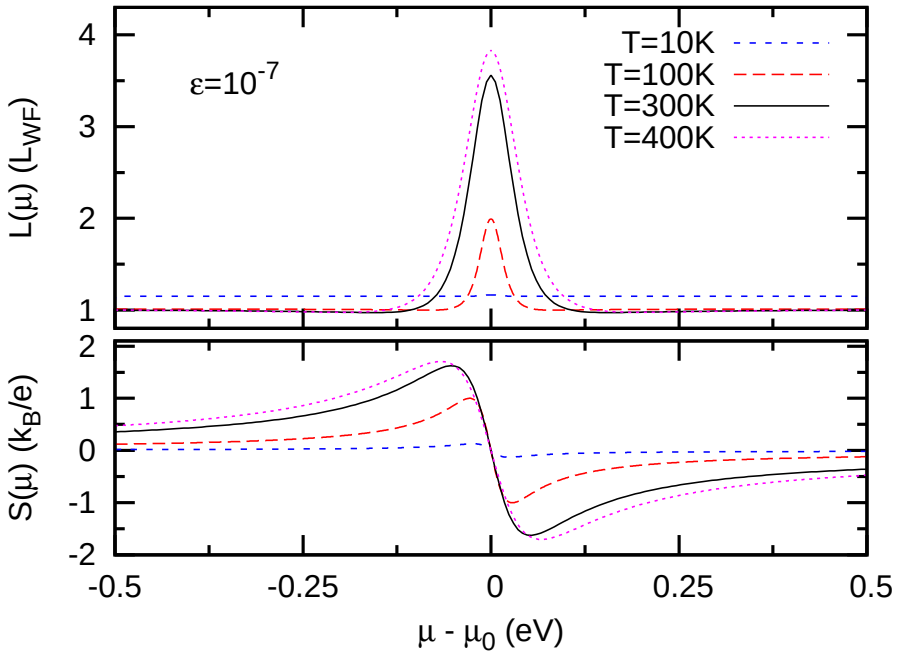

Figure 3.3: Lorenz number and Seebeck coefficient for an isoprene junction with $\epsilon = 10^{-7}$ for various temperatures. Here $\Gamma_1 = \Gamma_2$=0.5eV.

implies

$$\sum_\alpha I_\alpha^Q + \sum_\alpha \mu_\alpha I_\alpha^{(0)} = 0, \tag{3.19}$$

i.e., the total work done by the nanostructure against the external voltages equals the net heat flowing into the nanostructure. For a two-terminal heat engine with $T_2 > T_1$, the efficiency $\varepsilon = 1 - |I_1^Q|/|I_2^Q|$, and it is necessary to go beyond linear response theory to evaluate this expression.

3.3 Nonlinear thermoelectric response

As an engineering rule-of-thumb, ZT has been widely used to characterize the bulk thermoelectric response of materials [19, 49, 169]. At the nanoscale, however, the extent to which ZT is applicable is unclear, since bulk scaling relations for transport may break down due to quantum effects [43]. Moreover, ZT is a linear response metric, and cannot *a priori* predict nonequilibrium thermoelectric response.

In this section, we investigate the efficacy of ZT as a predictor of nonequilibrium device *performance* at the nanoscale by calculating the thermodynamic efficiency and power of an interacting quantum system using both nonequilibrium many-body [23] and Hückel theories. We discover that in both theories, variations of ZT and thermodynamic efficiency are in good qualitative agreement. However, large discrepancies between thermoelectric effects calculated within many-body and Hückel theory are found in the resonant tunneling regime, indicating the essential role of electron-electron interactions in nanoscale thermoelectricity. For a thermoelectric quantum tunneling device, we find that the power output can be changed significantly by varying an external parameter, such as a gate voltage, and that this variation is *not correlated* with the variation of ZT.

3.3.1 Thermodynamic efficiency vs. ZT

Neglecting inelastic processes, which are strongly suppressed at room temperature in SMJs, the current flowing into lead 1 of a two-terminal junction may be written as follows (3.8)

$$I_1^{(\nu)} = \frac{1}{h}\int_{-\infty}^{\infty} dE\,(E-\mu_1)^{\nu}\,T(E)\,[f_2(E)-f_1(E)]\,, \tag{3.20}$$

where $\nu = 0$ (ν=1) for the number (heat) current, $f_\alpha(E)$ is the Fermi function for lead α with chemical potential μ_α and inverse temperature β_α, and $T(E)$ is the transmission probability for an electron of energy E to tunnel across the junction.

In organic molecules such as those considered here, electron-phonon coupling is weak, allowing ZT to be expressed as follows:

$$ZT = ZT|_{el}\left(\frac{1}{1+\kappa^{ph}/\kappa^{el}}\right), \tag{3.21}$$

where [57]

$$ZT|_{el} = \left(\frac{\mathcal{L}^{(0)}\mathcal{L}^{(2)}}{\left[\mathcal{L}^{(1)}\right]^2}-1\right)^{-1} \tag{3.22}$$

and $\mathcal{L}^{(\nu)}$ is given by Eq. (3.10). Here f_0 is the equilibrium Fermi function and κ^{ph}=$\kappa_0 T^{ph}$ is the phonon thermal conductance, where κ_0=$(\pi^2/3)(k_{\rm B}^2 T/h)$ is the thermal conductance quantum [154] and T^{ph} is the phonon transmission probability.

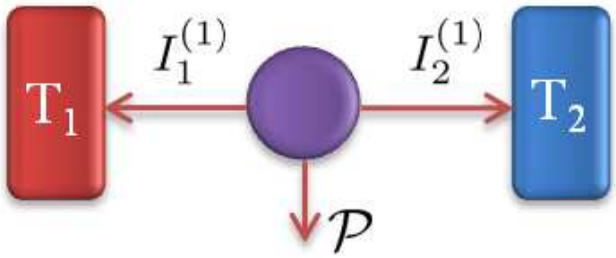

Figure 3.4: Schematic diagram of a thermoelectric device, where $I_\alpha^{(1)}$ is the heat current flowing into lead α, T_α is the temperature and $\mathcal{P}$ is the power output.

The phonon thermal conductance of the junction is typically limited by the lead-molecule interface [199]. Since the Debye frequency in the metal lead is typically smaller than the lowest vibrational mode of a small organic molecule, the spectral overlap of phonon modes between the two is small, implying $T^{ph} \ll 1$, so that $\kappa^{ph} \ll \kappa_0$. Nonetheless, it is claimed that κ^{ph} can reach values as large as 10^{-10}W/K for some SMJs [199, 165], so the correction to ZT due to phonon heat transport (*cf.* Eq. 3.21) must be taken into account for quantitative estimates of device performance [121]. We'll first consider purely electronic transport; the effect of phonons will be discussed in Sec. (3.4.1).

Thermodynamically, a system's response is characterized by the efficiency η with which heat can be converted into usable power $\mathcal{P}$ and by the amount of power that can be generated. Applying the first law of thermodynamics to the device shown in Fig. 3.4 gives:

$$\mathcal{P} = -I_1^{(1)} - I_2^{(1)} = I_1^{(0)}(\mu_1 - \mu_2), \tag{3.23}$$

where we mention that the power is equivalently phrased in terms of heat or electrical currents. The efficiency η is defined as the ratio of power output to input heat current:

$$\eta = \frac{\mathcal{P}}{\left|I_1^{(1)}\right|} = -\frac{I_1^{(1)} + I_2^{(1)}}{\left|I_1^{(1)}\right|}, \tag{3.24}$$

where we have assumed that $T_1 > T_2$. With these expressions for the power and efficiency, we can completely quantify the performance of a quantum device, both near to and far from equilibrium.

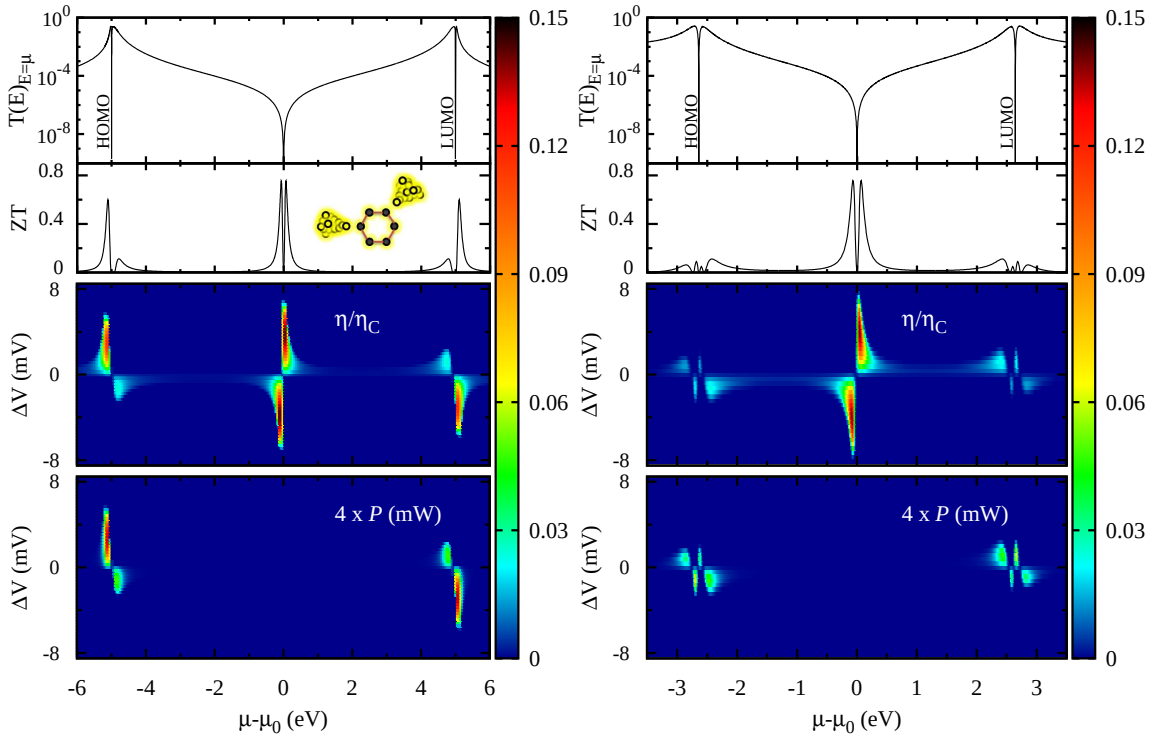

(a) many-body theory

(b) Hückel theory

Figure 3.5: The transmission probability $T(E)$, figure-of-merit ZT, Carnot-normalized efficiency η/η_C, and electrical power output $\mathcal{P}$ of a two terminal 1,3-benzene SMJ, with lead temperatures T_1=300K and T_2=250K, calculated using (a) many-body and (b) Hückel theory, highlighting the discrepancies near resonances and the similarities near the node in the two theories. As a function of μ, η and ZT are in excellent qualitative agreement while $\mathcal{P}$ is only peaked near resonance, suggesting that ZT is incomplete as a device performance metric. (a) Many-body calculations give $\mathcal{P}_{\text{peak}}$=33$\mu$W and $\eta_{\text{peak}}/\eta_C$=11.5% near resonance. (b) Hückel calculations give $\mathcal{P}_{\text{peak}}$=21$\mu$W and $\eta_{\text{peak}}/\eta_C$=2.7% near resonance. The mid-gap region is discussed in Fig. 3.6. Note that the peak ZT=0.75 is on par with currently available commercial thermoelectrics [169, 19]. Calculations were performed using the model and parameterization of benzene discussed in detail in Sec. 2.3 with Γ=0.63eV.

As a first example, we calculate the nonlinear thermodynamic response of a meta-connected Au-benzene-Au SMJ using many-body [23] and Hückel theory, shown in Fig. 3.5a and Fig. 3.5b, respectively. The transmission spectrum of this junction possesses a quadratic node within π-electron theory [24, 29], and will allow us to ascertain the importance of interactions on the thermoelectric response of a SMJ.

In the top panel of each figure is a section of the transmission spectrum, showing the HOMO and LUMO resonances and the quadratic node directly in between at μ=μ_0. Associated with this node is an enhancement in many linear-response metrics [24] including ZT, which is shown in the second panel from the top. The bottom two portions of each figure show the calculated efficiency η and power $\mathcal{P}$ when a junction with T_1=300K and T_2=250K is further pushed out of equilibrium via the application of a bias voltage ΔV. In all simulations presented here, the lead-molecule coupling is taken to be symmetric such that Γ^{α}_{nm}=$\Gamma\delta_{na}\delta_{ma}$, where n, m, and a are π-orbital labels and a is coupled to lead α. The efficiency is normalized with respect to the maximum allowed by the second law of thermodynamics, the Carnot efficiency $\eta_{\rm C} = \Delta T/T_1$, where ΔT=T_1-T_2.

The nonequilibrium thermodynamic response of a 1,3-benzene SMJ calculated using many-body theory is shown in Fig. 3.5a. The ZT and η spectra, shown in two middle panels of the same figure, exhibit peaks in the vicinity of both transmission nodes and resonances whereas the power $\mathcal{P}$, shown in the bottom panel, is only peaked near transmission resonances. Around either the HOMO or LUMO resonance, the peak power $\mathcal{P}_{\rm peak}$=33μW and peak efficiency $\eta_{\rm peak}/\eta_{\rm C}$=11.5% are only realized when the junction operates out of equilibrium at a bias voltage ΔV=3mV. With a chemical potential near the mid-gap node and ΔV=3.6mV, $\eta_{\rm peak}/\eta_{\rm C}$=14.9%, larger than near resonance but with a much lower peak power $\mathcal{P}_{\rm peak}$=.088nW.

In the vicinity of a resonance, there are both quantitative and qualitative differences in the linear and nonlinear thermodynamic response predicted by the two theories. By neglecting interactions, the Hückel theory fails to accurately predict both the degeneracy and position of electronic resonances. It also incorrectly determines the peak values of ZT, η and $\mathcal{P}$ in the vicinity of a resonance. As can be seen

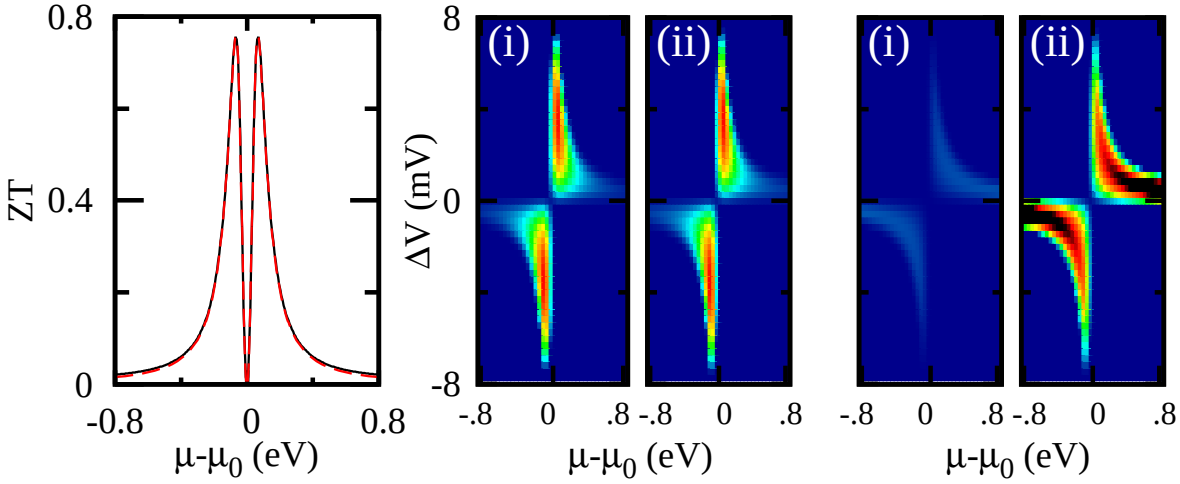

(a) ZT (b) η/η_C (c) $50\times\mathcal{P}$ (μW)

Figure 3.6: Calculations of ZT, η and $\mathcal{P}$ in the vicinity of the transmission node at μ=μ_0 of a meta-benzene SMJ using many-body (red line and panel i) and Hückel (black line and panel ii) theories. (a) and (b): ZT and η are found to be identical and independent of theory. (c) $\mathcal{P}$ is strongly affected by interactions where, at peak efficiency ($\eta_{\text{peak}}/\eta_C$=14.91%), many-body and Hückel calculations give $\mathcal{P}_{\text{max}}$=.088nW and $\mathcal{P}_{\text{max}}$=1.87nW, respectively. The simulation parameters and colorscale are the same as in Fig. 3.5.

near either (HOMO or LUMO) resonance in Fig. 3.5, the Hückel theory predicts a Carnot-normalized peak efficiency of 2.7% which is nearly five times less than the 11.5% predicted by the many-body theory. The peak power near a resonance also varies considerably between the two theories, where the Hückel calculations give $\mathcal{P}_{\text{peak}}$=21$\mu$W while many-body theory predicts $\mathcal{P}_{\text{peak}}$=33$\mu$W. These results indicate that interactions are required to accurately predict the thermoelectric response of devices operating in the resonant-tunneling regime. It is interesting to note, however, that in both models the linear-response metric ZT qualitatively captures the features of the nonlinear metric η.

Although interactions are *required* in order to ensure the invariance of transport quantities under a global voltage shift (i.e. gauge-invariance), near the particle-hole symmetric point the effect of interactions on the thermoelectric response should be small. In panels a-b of Fig. 3.6, a comparison of ZT and η using both many-body and Hückel theories is shown near μ_0 for a 1,3-benzene SMJ. Near this point, ZT and

η are independent of theory employed. In contrast, the power, shown in panel c of the same figure, exhibits an order of magnitude difference between the two theories. This observation can be understood by noticing that the calculated HOMO-LUMO gap is ≈10eV using many-body theory (panel c-i) whereas it is only ≈5.5eV when interactions are neglected in the Hückel theory (panel c-ii). Since the power is peaked near transmission resonances, whose widths are fixed by the lead-molecule coupling Γ, the larger gap found using many-body theory gives a correspondingly lower predicted power.

While the Hückel theory is not able to accurately characterize the thermoelectric response of a junction in the resonant-tunneling regime, it is sufficient for predicting η and ZT in the vicinity of the transmission node. Gating small molecules is a major technological challenge, meaning that we are often interested in transport near the particle-hole symmetric point where Hückel theory accurately predicts η and ZT. We shall use Hückel theory to simulate the larger molecules presented below.

3.4 Efficient nanoscale molecular thermoelectric devices

Thermoelectric (TE) devices are highly desirable since they can directly convert between thermal and electrical energy. Electrical power can be supplied to such a device to either heat or cool adjoining reservoirs (Peltier effect) or alternatively, the flow of heat (e.g. from a factory or car exhaust) can be converted into usable electrical power (Seebeck effect). Often, the efficiency of a TE device is characterized by the dimensionless figure-of-merit $ZT{=}S^2GT/\kappa$, constructed with the rationale that an efficient TE device should simultaneously: maximize the electrical conductance G so that current can flow without much Joule heating, minimize the thermal conductance κ in order to maintain a temperature gradient across the device, and maximize the Seebeck coefficient S to ensure that the coupling between the electronic and thermal currents is as large as possible [19, 49]. Generally, however, ZT is difficult to maximize because these properties are *highly correlated* with one another [79, 125, 169], a fact that becomes more pronounced at the nanoscale where

the number of degrees of freedom available is small.

If a TE material were found exhibiting $ZT \geq 4$ it would constitute a commercially viable solution for many heating and cooling problems at both the macro- and nano-scales, with no operational carbon footprint [49]. Currently, the best TE materials available in the laboratory exhibit $ZT \approx 3$, whereas for commercially available TE *devices* $ZT \approx 1$, owing to various packaging and fabrication challenges [19, 70].

In Sec. 3.2, enhanced thermoelectric effects were found in the vicinity of a transmission node of a quantum tunneling device. Generically, the transmission probability vanishes quadratically as a function of energy at such a transmission node [24]. Here we present results for a class of two-terminal single-molecule junctions (SMJ) with higher-order 'supernodes' in their transmission spectra. In the vicinity of a $2n^{\text{th}}$ order supernode:

$$T(E) \propto (E - \mu_{\text{node}})^{2n}, \tag{3.25}$$

where μ_{node} is the energy of the node. We find that junctions possessing such supernodes exhibit a scalable order-dependent quantum-enhanced thermoelectric response.

The transmission node in a meta-benzene junction can be understood in terms of destructive interference of electron waves traversing the ring at the Fermi energy [29]. According to Luttinger's theorem [108, 122], the Fermi volume is unaffected by the inclusion of electron-electron interactions. Consequently, in an aromatic ring such as benzene the Fermi wavevector $k_{\text{F}} = \pi/2d$ is conserved and is therefore sufficient to characterize quantum interference both with and without interactions near μ_0, since $\Delta\phi = k_{\text{F}}\Delta l$, where $\Delta\phi$ is the relative phase between transport paths with length difference Δl, and d is the inter-site distance.

This is an important result, since the energy of resonant levels will generally depend strongly on whether or not interactions are included. Since k_{F} is protected, however, the transmission node across a single phenyl group is not so much a coincidence of energy levels as a *wave phenomenon*, meaning that interference in molecules composed of multiple aromatic rings in series can be understood in terms of the inter-

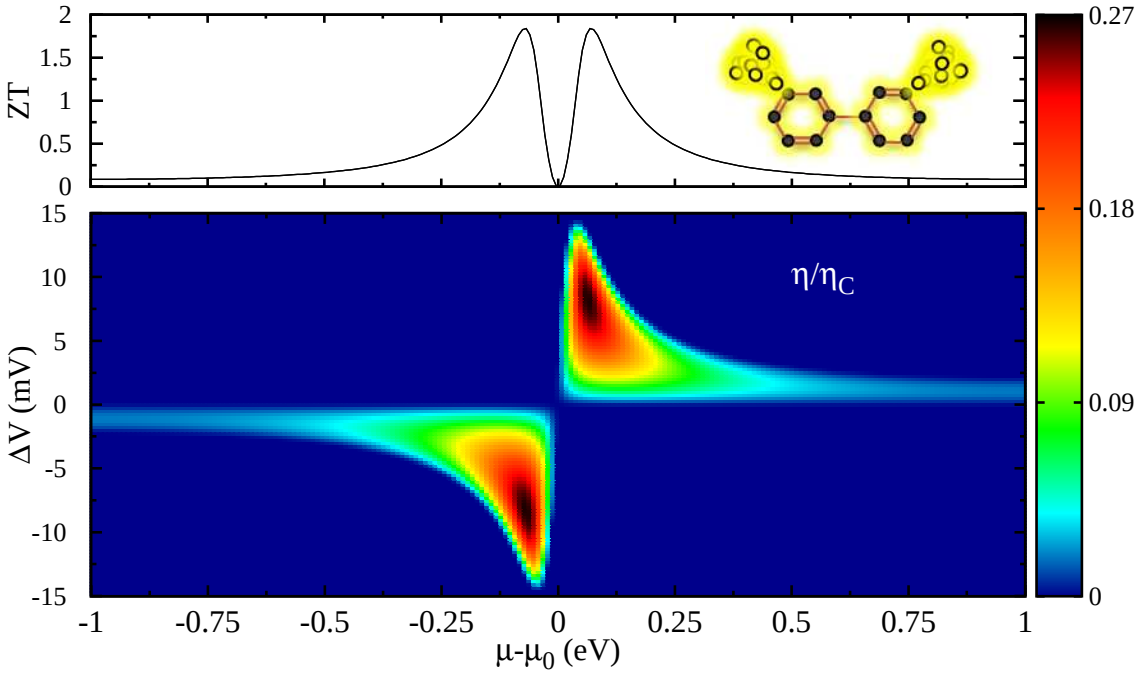

Figure 3.7: A closeup of ZT and η near the quartic supernode of a 3,3'-biphenyl SMJ showing ZT_{peak}=1.84 and $\eta_{\text{peak}}/\eta_{\text{C}}$=26.86% at a predicted power of 0.75pW. The junction geometry is shown schematically in the inset of the upper panel. Simulations were performed using Hückel theory with T_1=300K, T_2=250K and Γ=0.5eV.

ference within each subunit rather than the energy spectrum of the entire molecule. We find that such polycyclic molecules can exhibit higher-order *supernodes*, and that associated with a supernode is an order-dependent quantum enhancement of the junction's thermoelectric response. Additional transport channels (e.g. from σ-orbitals) or incoherent processes may lift the supernode. The effect on the thermoelectric response is small provided the processes are weak, as discussed in Sec. 3.2.1 [24].

The 3,3'-biphenyl junction, drawn schematically in the top panel of Fig. 3.7, can viewed as two meta-connected benzene rings in series. This junction geometry is similar to that studied by Mayor et al [129]. In agreement with the prediction that a biphenyl junction should possess a quartic supernode, the linear and nonlinear response shown in Fig. 3.7 exhibits peak values of efficiency (η/η_{C}=26.86%) and ZT (1.84) that are more than twice those of benzene. With $ZT\approx$2, the biphenyl

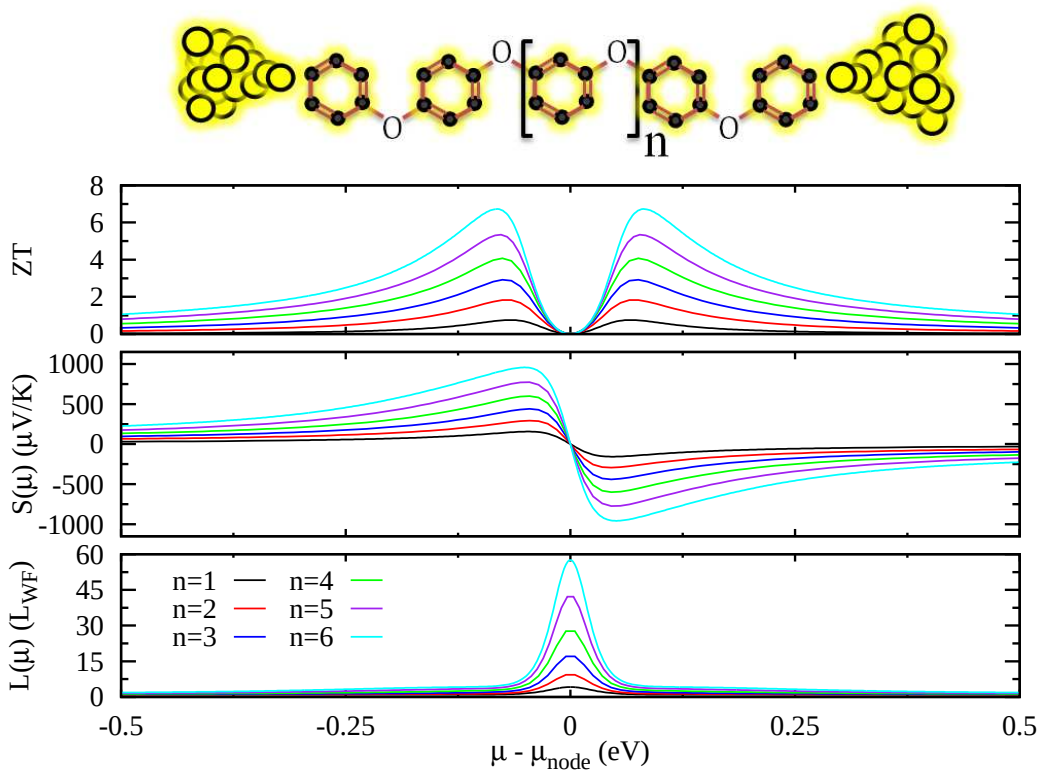

Figure 3.8: Supernode enhancement of ZT, thermopower S and Lorenz number L for polyphenyl ether (PPE) SMJs with n repeated phenyl groups, shown schematically above the top panel. As a function of n, ZT_{peak} scales super-linearly, exhibiting a peak value of 6.86 for n=6. The thermopower and Lorenz number are also enhanced with S_{peak}=957μV/K and L_{peak}=55.33L_{WF} at the same value of n. Simulations were performed using Hückel theory at room temperature (T=300K) with Γ=0.5eV. Inter-phenyl electronic hopping was set an order of magnitude below the intra-phenyl value of 2.64eV.

junction exhibits sufficient thermoelectric performance to be attractive for many commerical solid-state heating and cooling applications [19, 49, 169]. As we shall see, this is only the first in an entire class of supernode-possesing molecules which exhibit even larger values of η and ZT.

3.4.1 The effect of higher-order interferences

In larger molecules composed of n meta-connected phenyl groups in series, we expect that the transmission nodes should combine and give rise to a $2n^{\text{th}}$ order supernode.

Polyphenyl ether (PPE), shown schematically at the top of Fig. 3.8, consists of n phenyl rings connected in series with ether linkages. Based on our previous discussion, we predict that a PPE-based junction should exhibit a $2n^{th}$ order supernode. The figure-of-merit ZT, thermopower S and Lorenz number $L{=}\kappa/GT$ for PPE junctions are shown in the top, middle and bottom panels of Fig. 3.8, respectively, where the Lorenz number is normalized with respect to the Wiedemann–Franz (WF) value $\mathrm{L_{WF}}{=}(\pi^2/3)\,(k_\mathrm{B}/e)^2$.

The bottom panel of Fig. 3.8 shows an increasing peak Lorenz number L_peak with increasing n. In linear-response, L and S can be expressed in terms of Eq. (3.10) as

$$L|_{el} = \frac{1}{(eT)^2}\left(\frac{\mathcal{L}^{(2)}}{\mathcal{L}^{(0)}} - \left[\frac{\mathcal{L}^{(1)}}{\mathcal{L}^{(0)}}\right]^2\right), \tag{3.26}$$

and $S{=}-\frac{1}{eT}\frac{\mathcal{L}^{(1)}}{\mathcal{L}^{(0)}}$, where e is the magnitude of the electron's charge and T is the temperature. Using Eqs. (3.26) and (3.10) with the transmission function of Eq. (3.25) we find that:

$$\left.\frac{L_\mathrm{max}}{L_\mathrm{WF}}\right|_{el} = \left(\frac{3}{\pi^2}\right)\frac{\left[\partial_b^{2n+2} b\pi\,\mathrm{csc}(b\pi)\right]\big|_{b=0}}{\left[\partial_b^{2n} b\pi\,\mathrm{csc}(b\pi)\right]|_{b=0}}. \tag{3.27}$$

Setting $n{=}6$ in Eq. (3.27) gives $L_\mathrm{max}{=}55.33L_\mathrm{WF}$, corresponding exactly to the result of the full simulation shown in the bottom panel of Fig. 3.8. Similar agreement is found for the other values of n, confirming the presence of $2\mathrm{n}^{th}$ order supernodes in these junctions.

The above discussion considered purely electronic transport. According to Eq. (3.21), phonon heat transport may reduce ZT significantly [121], although it should be emphasized that the thermopower of the junction is unaffected provided the electron-phonon coupling is negligible. Figure 3.9 shows the effect of phonon heat transport on ZT of a 3,3'-biphenyl junction for several values of the phonon transmission probability T^{ph}. In the vicinity of the quartic transmission node, ZT is significantly reduced even for small values of T^{ph}. However, the large peaks of ZT found near the transmission resonances are largely insensitive to phonon heat transport due to the smaller ratio of κ^{ph}/κ^{el}. Practical supernode-based devices will

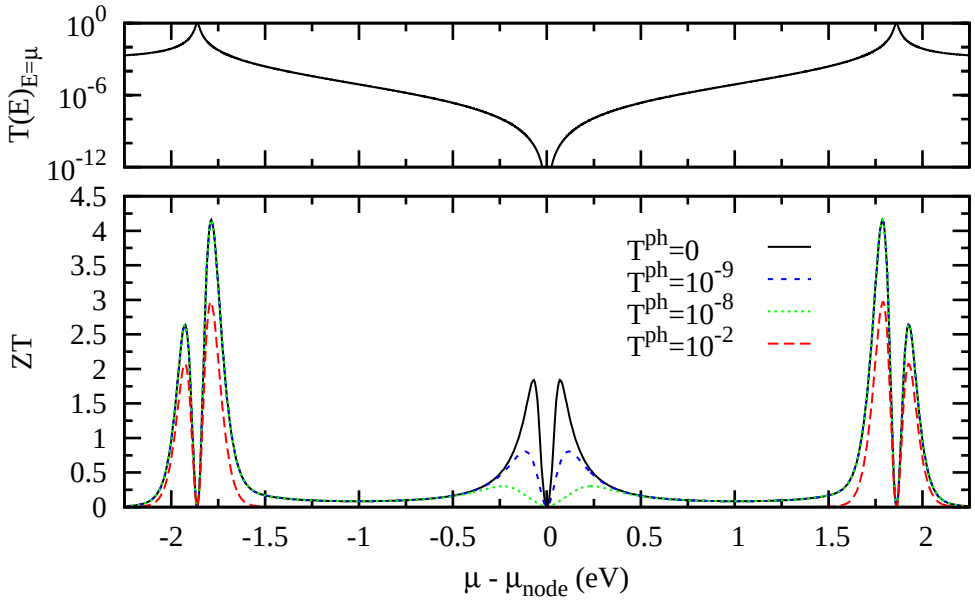

Figure 3.9: The transmission probability $T(E)$ and ZT for a 3,3'-biphenyl SMJ with several different phonon transmission values. Although phonon transport strongly reduces ZT near the supernode, the enhancement of ZT near the transmission peaks is fairly insensitive to moderate values of T^{ph}. Recall that $\kappa^{ph}=\kappa_0 T^{ph}$.

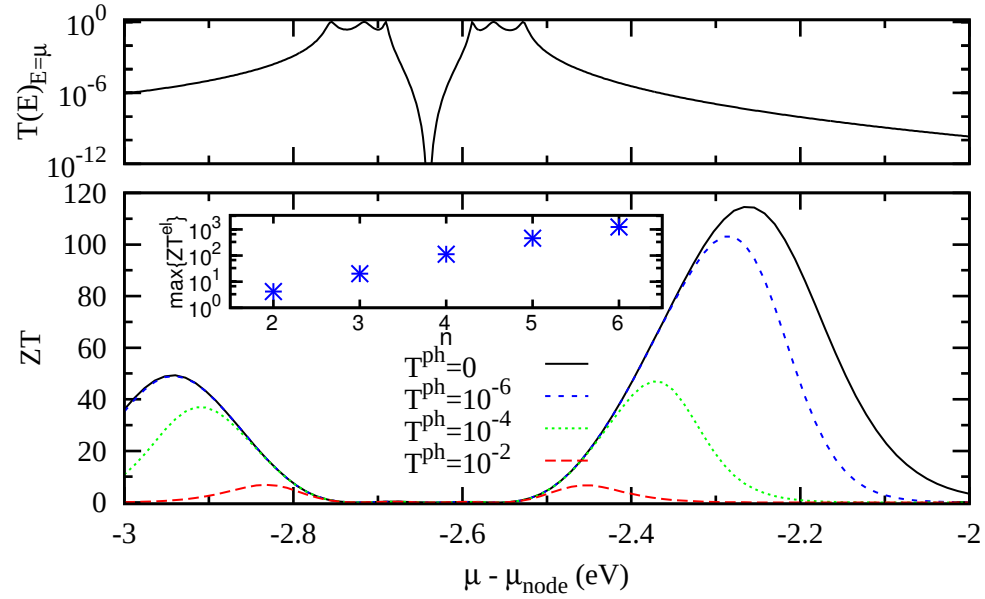

Figure 3.10: The transmission and ZT in the vicinity of a transmission peak for a tetraphenyl ether (n=4) molecule showing that ZT^{el} is enhanced in the vicinity of a higher-order peak. Inset: the maximal ZT^{el} value found near a $2n^{th}$ order transmission peak is shown on a log scale.

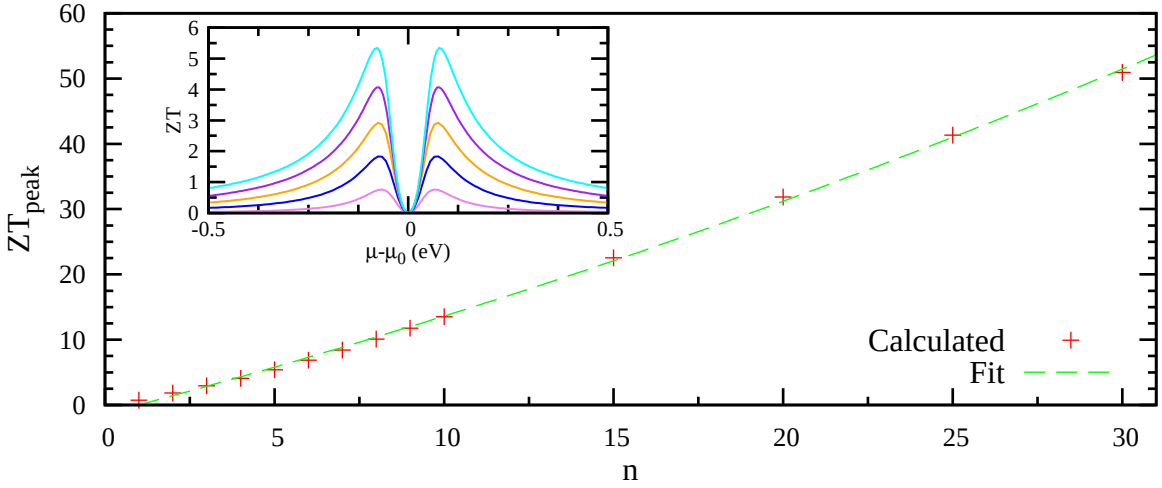

Figure 3.11: Near a $2n^{\text{th}}$ order *supernode* in a device's transmission spectrum, we find an order-dependent enhancement of the thermoelectric response which is limited only by the electronic coherence length. Calculations were performed for a polyphenyl ether (PPE) SMJ with n repeated phenyl groups at room temperature (T=300K) with Γ=0.5eV. Notice that the enhancement is super-linear in n. Inset: ZT as a function μ for n=1 . . . 5.

thus require careful engineering of phonon transport. For example, the inclusion of a vacuum tunneling gap in series with the junction would effectively block phonon transport.

Higher-order quantum interference effects can arise from both destructive and constructive interference. As evidenced by Fig. 3.9, thermoelectric devices based on constructive interference are far less sensitive to phonon effects. Figure 3.10 shows the transmission spectrum and ZT^{el} near the HOMO resonance of a tetraphenyl ether SMJ. The transmission resonance exhibits fine structure due to electronic standing waves along the molecular chain [85]. The interplay of the many closely spaced resonances gives rise to a dramatic enhancement of the thermopower in a regime of large electrical conductance, and hence a very large $ZT^{el} \sim 10^2$. The inset of Fig. 3.10 shows the exponential scaling of the peak ZT^{el} near the HOMO resonance of a polyphenyl ether SMJ as a function of the phenyl group number n. The predicted giant enhancement of ZT^{el} occurs over a broad energy range, in contrast to that expected from a narrow transmission resonance [57].

The peak value of ZT found near the particle-hole symmetric point $\mu_{\rm node}$ of a PPE junction is shown as a function of repeated phenyl unit number n in Fig. 3.11. As illustrated in the figure, $ZT_{\rm peak}$ scales super-linearly in n whereby $ZT_{\rm peak}$=4.1 in a junction composed of just four phenyl groups (n=4). Although in this thesis we focus primarily on molecular junctions, it should be stressed that our results are applicable to any device with transmission nodes arising from coherent electronic transport.

Thermoelectric devices based on individual SMJs are ideally suited for local cooling in integrated nanoscale circuit architectures. Supernode-based devices have a low transmission probability and thus a large electrical impedance capable of withstanding voltage surges. Moreover, high-power macroscopic devices could be constructed by growing layers of densely packed molecules. For example, a self-assembled monolayer with a surface density [209] of 4×10^{15}molecules/cm^2 would give 352kW/cm^2 at peak efficiency for a meta-benzene film. The efficiency of PPE-based devices increases with ring number and is only limited by the electronic coherence length, suggesting that highly efficient molecular-based thermoelectric devices may soon be realized.

3.5 Summary

In this chapter, we derived an expression for the heat current in an interacting quantum system using our many-body theory. Interestingly, we found that both the electrical and heat current formulae can be expressed in a similar form, allowing us to write the complete electronic response of an interacting quantum system in a single expression. When there are no inelastic contributions to the electron self-energy, we recover the well known Büttiker formula for the electric current in which transport can be phrased in terms of a transmission probability function, along with an analogous formula for the heat current.

As an initial application of our theory, we investigated the effect of a node in the transmission spectrum on the thermoelectric response of a molecular junction and

found that the thermopower reaches a temperature-independent maximum value of $\pm\pi k_B/\sqrt{3}e \approx \pm 156\mu$V/K, more than an order of magnitude larger than the values obtained in recent measurements [152, 15] of molecular junctions. Moreover, a 420% enhancement of the Lorenz number is also predicted at a transmission node. The dramatic enhancement of thermoelectric effects near a transmission node arises because the flow of entropy—an inherently incoherent quantity—is not blocked at non-zero temperature by destructive quantum interference. The thermopower therefore serves as a signature of coherent transport which can be easily measured with existing technology.

From an applications perspective, the thermoelectric response is only one aspect of a device's performance. A useful thermoelectric device must both efficiently convert between thermal and electronic energies and produce a reasonable amount of power. We calculated the full nonequilibrium spectrum of thermodynamic efficiency and found that it qualitatively resembles the spectrum of the popular performance metric ZT, suggesting that ZT encapsulates the salient physics related to efficiency even at the nanoscale. The usable power produced by a nanoscale device, however, was poorly characterized by ZT.

Technologically, a thermoelectric material with ZT>4 would be useful in myriad heating, cooling, and other power conversion applications. Even in the lab, the best materials exhibit ZT$\sim$3, with most commercially available products having ZT$\sim$1. Previously, we showed that in the vicinity of an electronic transmission node, a quantum device exhibits an enhanced thermoelectric response. Generically, these nodes have a quadratic energy dependence. In this chapter, we presented a class of single-molecule devices which exhibit $2n^{\text{th}}$ *supernodes*, leading to an order-dependent quantum enhanced thermoelectric response. The degree of enhancement in these systems scales superlinearly with n and is only limited by the electronic coherence length, making the realization of a ZT$\gg$4 junction feasible with a thin molecular film.

CHAPTER 4

The Lead-Molecule Interface

Transport through a single-molecule junction (SMJ) is a property of the junction as a whole, and is not a meaningful concept when applied to the leads or the molecule individually. From a theoretical perspective, the lead-molecule coupling is of vital importance since it transforms the few-body molecular problem into a many-body problem. The specific form of the lead-molecule coupling directly affects how we relate observable transport properties of the junction, such as the conductance or current, to the state of the molecule. Since we are interested in the electronic response of single molecules, a detailed understanding of the lead-molecule interface is therefore necessary.

In the first section of this chapter, we extend our many-body theory to allow multi-orbital bonding between the leads and the molecule. Such a junction could potentially be formed from a molecule lying flat on a metal or graphene surface, contacted from above by a scanning tunneling microscope (STM) tip. Both the transmission phase and probability are calculated for junctions with various contact symmetries. In 'flat' junctions where all the orbitals couple to a single channel of a lead, we find a dramatic suppression of the Coulomb blockade peaks caused by quantum interference [21]. It is postulated that such an effect may be visible in the apparent height of molecules adsorbed on a surface.

Next, we develop the framework to include multi-channel leads and simulate a multi-channel experiment involving two platinum leads directly bonded to benzene. Within the molecular electronics community, the term 'channels' is often used as a synonym for 'number of orbitals' when referring to a molecular junction [77, 173]. Although the number of orbitals certainly sets the upper bound on the number of channels, we find a better bound is given by the degeneracy of the most relevant molecular orbital. For the Pt-benzene-Pt junction we find two dominant channels,

owing to the orbital degeneracy of the ring structure. Finally, we consider multi-mode transport in a linear molecule and find only a single dominant channel.

As a final topic, we consider the molecular junction from an entirely different perspective. Instead of viewing the leads as a modification of the isolated molecule, we instead consider the molecule as a correction to the isolated leads. We then derive expressions for the Keldysh and retarded Green's functions of the lead and find that the Friedel oscillations caused by the molecule depend on the molecular state.

4.1 Transport with multi-orbital contact geometries

In this section, we consider junctions composed of small molecules coupled to two external single-channel leads. We extend our formalism to allow the molecule-lead coupling to occur either via single or multiple, spatially separated atomic orbitals. For single-orbital coupling we show that the presence of nodes in the junction's transmission spectrum depends critically upon the contact geometry of the junction. This is so because the connectivity determines the relative phase accumulated by an electron along different, interfering paths across the molecule. When multiple orbitals are coupled to a single-channel lead, the complex interplay of intramolecular interference manifests itself prominently in the junction's transport properties.

4.1.1 Multi-orbital formalism

As discussed previously in Sec. 2.1.2, the Green's function

$$G_{n\sigma,m\sigma'}(t) = -i\theta(t)\langle\{d_{n\sigma}(t), d^{\dagger}_{m\sigma'}(0)\}\rangle \tag{4.1}$$

of the junction may be transformed into the energy domain giving a molecular Dyson equation [23]

$$G(E) = \left[\mathbf{1}E - H^{(1)}_{\mathrm{mol}} - \Sigma_{\mathrm{T}}(E) - \Sigma_{\mathrm{C}}(E)\right]^{-1}, \tag{4.2}$$

where $H^{(1)}_{\mathrm{mol}}$ is the one-body part of the molecular Hamiltonian H_{mol}, Σ_{T} is the tunneling self-energy matrix and Σ_{C} is the Coulomb self-energy matrix. In this

chapter, $H_{\rm mol}$ is again modeled using the semi-empirical Hamiltonian discussed in Sec. 2.1.1 and $\Sigma_{\rm C}$=$\Sigma_{\rm C}^{(0)}$.

The tunneling self-energy $\Sigma_{\rm T}$=$\sum_{\alpha=1}^{2}\Sigma_{\rm T}^{\alpha}$ can be decomposed as the sum of contributions from the individual contacts, which we calculated exactly using an equations-of-motion method in Sec. 2.1.2

$$\begin{aligned}\left[\Sigma_{\rm T}^{\alpha}(E)\right]_{n\sigma,m\sigma'} &= \delta_{\sigma\sigma'}\sum_{k\in\alpha}\frac{V_{nk}V_{mk}^{*}}{E-\epsilon_{k\sigma}+i0^{+}} \\ &= -\frac{i}{2}\left[\Gamma^{\alpha}(E)\right]_{n\sigma,m\sigma'}+\int\frac{d\varepsilon}{2\pi}\frac{\left[\Gamma^{\alpha}(E)\right]_{n\sigma,m\sigma'}}{E-\varepsilon},\end{aligned} \tag{4.3}$$

where we have used the Sokhatsky-Weierstrass theorem $\frac{1}{x+i0^{+}}=P(\frac{1}{x})-i\pi\delta(x)$ and

$$\left[\Gamma^{\alpha}(E)\right]_{n\sigma,m\sigma'}=2\pi\delta_{\sigma\sigma'}\sum_{k\in\alpha}V_{nk}V_{mk}^{*}\,\delta(E-\epsilon_{k\sigma}). \tag{4.4}$$

Equation (4.3) may also be equivalently expressed in matrix form as follows

$$\Gamma^{\alpha}(E)=i\left(\Sigma_{\rm T}^{\alpha}(E)-\left[\Sigma_{\rm T}^{\alpha}(E)\right]^{\dagger}\right). \tag{4.5}$$

When $\Gamma(E)$ is an even function of energy the integral in Eq. (4.3) is zero and the imaginary part of the tunneling self-energy, which causes broadening of the molecular resonances, is the dominant contribution to $\Sigma_{\rm T}$. In the discussion that follows, we take the real part of the tunneling self-energy to be negligible as compared to the imaginary part. In the next section, we'll evaluate Eq. (4.3) using the dispersion relation for a tight-binding chain where the real part is not always negligible.

While the Green's function fully characterizes the molecular junction, the transmission phase is most readily defined in terms of the scattering matrix $S_{\alpha\beta}(E)$. For purely elastic quantum transport, the Green's function and scattering matrix are related as follows [58, 111]

$$S_{\alpha\beta}(E)=-\delta_{\alpha\beta}+i\gamma_{\alpha}(E)G(E)\gamma_{\beta}^{\dagger}(E). \tag{4.6}$$

The off-diagonal terms of S are the transmission amplitudes $\left[t_{\alpha\beta}(E)\right]_{nm}$ for scattering from mode m in lead β to mode n in lead α. The total transmission probability between leads α and β given by Eq. (2.41) may be equivalently expressed as

$$T_{\alpha\beta}(E)={\rm Tr}\left\{t_{\alpha\beta}(E)t_{\alpha\beta}^{\dagger}(E)\right\}, \tag{4.7}$$

where the trace is over all lead modes. The tunneling-width amplitude matrices $\gamma_\alpha(E)$ are related to the tunneling-width matrices $\Gamma^\alpha(E)$ as follows

$$\Gamma^\alpha(E) = \gamma_\alpha^\dagger(E)\gamma_\alpha(E). \tag{4.8}$$

In previous chapters, where $[\Gamma(E)]_{nm} = \Gamma(E)\delta_{nm}$, the effective γ matrix was actually a row vector with a single non-zero element $\sqrt{\Gamma(E)}$ at index n. With this coupling there is a single non-zero element of $t_{\alpha\beta}(E)$ which is proportional to $G_{nm}(E)$, allowing the phase of transmission to be easily calculated as $\theta(E)$=arg$[G_{nm}(E)]$. When multiple orbitals are coupled to a lead there are multiple non-zero elements of γ and the transmission phases are calculated by taking arguments of the eigenvalues of $t_{\alpha\beta}(E)$. In this section, we restrict our discussion to single-mode leads, where $t_{\alpha\beta}(E)$ is a rank one matrix with a single unique transmission eigenphase, with multi-mode leads left until the next section.

4.1.2 Coherent destruction of Coulomb blockade peaks

Coulomb blockade has been investigated in mesoscopic transport through metallic nanoparticles [198] and semiconductor quantum dots [5, 4], and more recently in molecular transport [149, 101, 23]. Because the distance between conductance peaks is set by the charging energy, one might naively think that transport in the Coulomb blockade regime is essentially incoherent. Recent interferometric experiments have shown, however, that electrons transferred through quantum dots retain memory of their phase [163, 11], a finding that has triggered intensive theoretical investigations on the transmission phase through interacting systems [109, 111, 167, 67, 166, 84].

Mesoscopic experiments access regimes where tunneling transport occurs either between two discrete channels (in lateral quantum dots) or two quasi-continua (in metallic nanoparticles) that are connected by a central quantum system with no particular symmetry. Consequently, interchannel coherence is either absent or washed out, and the spatial symmetry with which external terminals are connected to the central system matters little. The situation is fundamentally different in molecular transport, because molecules naturally possess symmetries that strongly affect

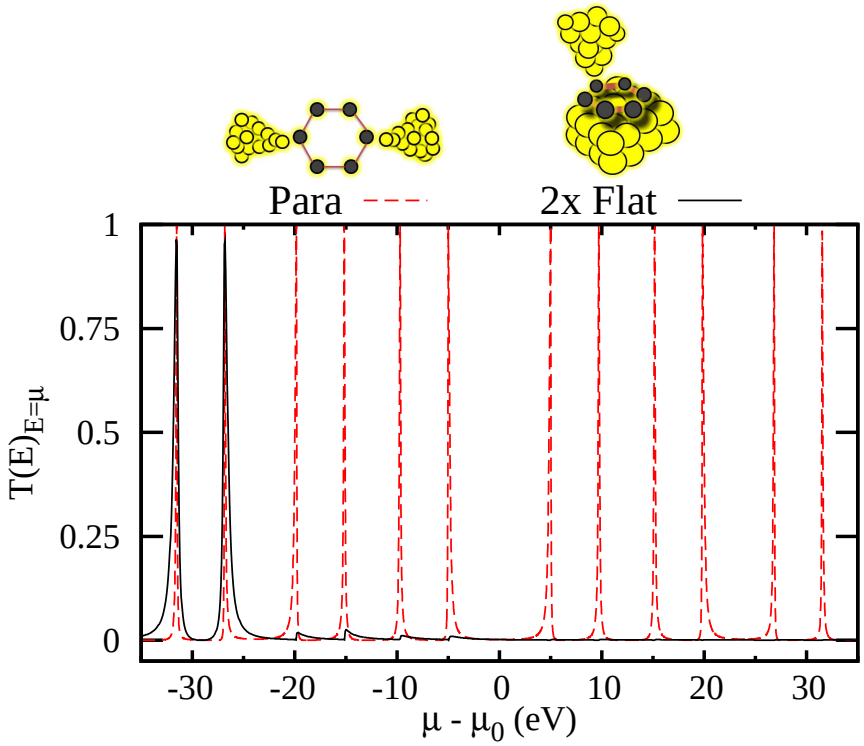

Figure 4.1: Top panel: Schematic diagrams of the para and the flat, multi-orbital coupling geometries for a benzene (C_6H_6) molecular junction. Main panel: Transmission probability through a benzene molecular junction as a function of the chemical potential of the molecule for the para (red curve) and flat geometries (black curve). For the black curve, the vertical axis has been rescaled by a factor of two to emphasize small remnants of Coulomb blockade peaks at -20eV and higher that would be invisible otherwise.

the phase-coherent transmission of electrons [29]. Moreover, molecular symmetries make it possible to tunnel-couple multiple orbitals to a single external electrode [91].

Presently, we consider molecular junctions which at a given chemical potential exhibit transmission nodes for certain connection geometries and no such nodes for other geometries. In general, the presence of a transmission node results in an additional π shift in the junction's transmission phase [109, 111]. This is of crucial importance for multi-orbital coupling, because this phase shift can turn constructive interferences into destructive ones, thereby suppressing the conductance. Accordingly, we find that Coulomb blockade peaks are strongly suppressed in molecular junctions where multiple atomic orbitals of the molecule couple to a single electrode.

As a graphic example of this effect, let us compare transport in the archety-

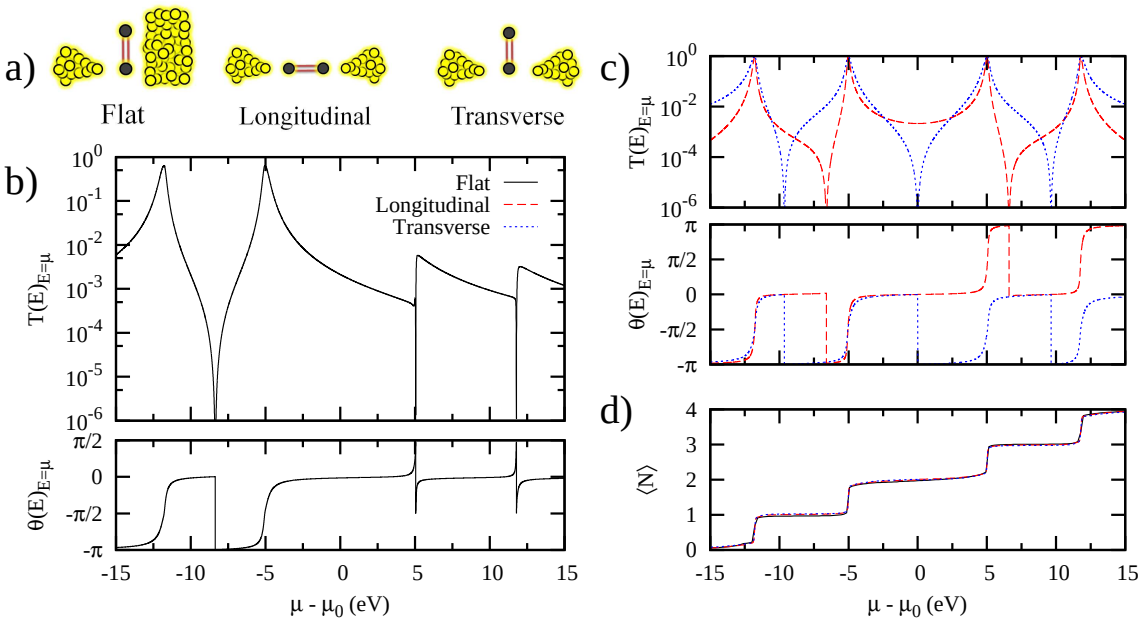

Figure 4.2: Numerically obtained transport results for flat, longitudinal and transverse ethylene (C_2H_4) junctions. (a) Schematic diagrams for each junction's geometry. (b) and (c) Transmission probabilities (top) and phases (bottom) for the flat (b) and transverse and longitudinal (c) connections. (d) Molecular π-orbital occupancy for all three geometries, showing that the destruction of the Coulomb peak does not affect the accumulation of charge on the molecule. Using the molecular Hamiltonian and parameterization of Sec. 2.1.1, the parameters for ethylene were: t=2.6eV, U_{11}=8.9eV, U_{12}=5.33eV and $\Gamma=\Gamma_I=\Gamma_{II}$=0.5eV in the longitudinal and transverse geometries while $[\gamma_{II}]_{nm}=\sqrt{\Gamma}/2$ in the flat geometry.

pal para-benzenedithol (BDT) junction to that of the 'flat' benzene junction, each shown schematically atop Fig. 4.1. In the main portion of that same figure, the transmission probability through a benzene molecule is plotted against its electrochemical potential μ. For single-orbital coupling one observes a standard Coulomb blockade sequence of twelve conductance peaks, corresponding to the filling of the six spin-degenerate electronic molecular states. The situation is altogether different in the flat configuration where one of the leads couples equally to all atomic orbitals, a geometry which can be realized if the molecule is deposited on a metallic surface [157, 156]. In this case, only the first two conductance peaks survive, while the remaining ten resonances are dramatically suppressed by destructive interference. In contrast, the molecular occupancy is almost the same in these two configurations.

In order to understand this behavior it is advantageous to first simplify our

present discussion and analysis by: (i) considering only two-terminal junctions, (ii) assuming each lead is characterized by a single-mode, and (iii) taking the broad-band limit [81] for the lead-molecule coupling, where $\Gamma^{\alpha}(E) \equiv \Gamma^{\alpha}$ becomes an energy-independent matrix of constants related to the tunneling rate. Together, the first two assumptions ensure the existence of a single well-defined transmission eigenphase $\theta(E) = \arg[t(E)]$ for the junction.

Although the investigation of coherent quantum transport in molecular junctions is not new [143], most theoretical studies limit their analyses to cases where Γ^{α} is diagonal, corresponding physically to the special case where single orbitals couple to single leads. Presently, we consider transport in a junction geometry we label 'flat,' where a single orbital connects to one lead while all atomci orbitals couple to a single channel (e.g., s-wave) of the surface electronic states in the other lead, a configuration which is already experimentally accessible [157, 156, 194].

In a flat junction with two leads, labeled I and II, the tunneling-amplitude matrices are $[\gamma_{\rm I}]_{nm} = \sqrt{\Gamma_{\rm I}}\delta_{na}\delta_{ma}$ and $[\gamma_{\rm II}]_{nm} = \sqrt{\Gamma_{\rm II}}$, where a is the orbital connected to lead I and all orbitals couple equally to lead II. $\Gamma_{\rm I}$ and $\Gamma_{\rm II}$ are constants characterizing the tunneling between the molecule and leads I and II, respectively. Following Eq. (4.6), the transmission amplitude becomes

$$t^{\rm Flat}_{\rm I,II}(E) = i\sqrt{\Gamma_{\rm I}\Gamma_{\rm II}}\sum_{j=1}^{N} G_{aj}(E), \tag{4.9}$$

where N is the total number of molecular orbitals. From Eq. (4.7), we see that the transmission probability will be composed of diagonal terms proportional to $\sum_j |G_{aj}|^2$ and cross terms proportional to $\sum_{j\neq k} G_{aj}G^{*}_{ak}$. We now show that interferences between various transmission amplitudes can cause these two terms to cancel, giving rise to a dramatic reduction of the transmission peaks.

For pedagogical reasons, we first consider several ethylene (C_2H_4) junctions, each shown schematically in Fig. 4.2a. The transmission probability and phase for the flat junction is shown in Fig. 4.2b, while the spectra for the transverse and longitudinal junctions are both shown in Fig. 4.2c. In all three geometries $\Gamma_{\rm I}$=0.5eV. In the longitudinal and transverse cases $\Gamma_{\rm II}$=0.5eV, while in the flat geometry $\Gamma_{\rm II}$=0.25eV

such that the total coupling $\tilde{\Gamma}_{\rm II}$=Tr $\left\{\Gamma^{\rm II}\right\}$=0.5eV.

For chemical potentials below the center of the highest occupied molecular orbital (HOMO) to lowest unoccupied molecular orbital (LUMO) gap (μ_0), the spectra of the three geometries are qualitatively very similar: for every peak in one geometry there is a corresponding peak in the others, and similarly for the nodes, although the exact location of the nodes varies. For $\mu > \mu_0$, however, there is a nearly 500× reduction of the Coulomb blockade peak height in the flat geometry as compared with either the longitudinal or transverse spectra.

The origin of this suppression can be understood by examining the transmission amplitudes in each geometry. In the longitudinal and transverse junctions we find

$$t^{\rm Long}_{\rm I,II}(E) = i\Gamma G_{12}(E) \tag{4.10}$$

and

$$t^{\rm Trans}_{\rm I,II}(E) = i\Gamma G_{11}(E), \tag{4.11}$$

respectively, where $\Gamma_{\rm I}$=$\Gamma_{\rm II}$=Γ. From Eq. (4.9), we see that the flat junction's amplitude

$$t^{\rm Flat}_{\rm I,II}(E) = i\Gamma/\sqrt{2}\,[G_{11}(E) + G_{12}(E)] \tag{4.12}$$

is proportional to the sum of the amplitudes from the other two configurations. From the longitudinal and transverse phase spectra, shown in the lower part of Fig. 4.2c, it is evident that the node in G_{11} when μ=μ_0 causes G_{11} and G_{12} to become π out of phase for all $\mu > \mu_0$. Exactly on resonance with $\mu > \mu_0$, $|G_{11}|$=$|G_{12}|$ and consequently, via total destructive interference, a transmission *peak* in the longitudinal (or transverse) spectrum becomes a transmission *node* in the flat junction's spectrum, with a concomitant lapse of the transmission phase in the latter. In the vicinity of a resonance, the two terms are not exactly equal but still interfere destructively giving rise to a pronounced reduction of the Coulomb blockade peaks instead of an exact cancellation.

Transmission peaks occur at energies where a system has a degeneracy between two charge states. Even though these Coulomb blockade peaks may be nearly destroyed by quantum interferences, as we just showed, the charge of the molecule

still changes by one as we cross each resonance. The π-orbital molecular occupancy is shown for all three junction geometries as a function of chemical potential in Fig. 4.2d and exhibits nearly the same spectra for all three geometries. Comparing the phase of transmission, shown in the bottom parts of Figs. (4.2b,4.2c) with the charge spectra, we see that for each step in the occupancy there is an associated increase in the transmission phase by π, in agreement with the Friedel-sum rule [59].

Since the suppression of transmission peaks in flat junctions is a manifestation of interference between multiple transport pathways, the effect should be more pronounced in larger molecules which possess a correspondingly larger number of transport pathways. To investigate this hypothesis, we consider the transmission spectrum for a flat benzene junction in which one electrode couples to just a single π-orbital of the benzene ring, while the second couples equally to all six π-orbitals. Such a junction could be experimentally realized by depositing a benzene molecule on a Pt or graphene surface and contacting it from above with an STM tip [157, 156].

The calculated spectrum of a flat-benzene junction is shown in Fig. 4.3 for several values of lead-molecule coupling. Except for the first two peaks, all the molecular resonances coincide with transmission nodes, a fact which is observable from the transmission probability or as π-slips in the transmission phase, shown in the bottom portion of the same figure. Owing to the molecular symmetry of benzene, there are only four non-degenerate terms in the flat junction's transmission amplitude. Using Eq. (4.9)

$$t_{\mathrm{I,II}}^{\mathrm{Flat}} = i\sqrt{\Gamma_{\mathrm{I}}\Gamma_{\mathrm{II}}}\left[t_{11} + \underbrace{t_{14}}_{\mathrm{Para}} + 2\underbrace{t_{12}}_{\mathrm{Ortho}} + 2\underbrace{t_{13}}_{\mathrm{Meta}}\right], \tag{4.13}$$

where the Ortho and Meta terms are doubly degenerate and the dependence on energy is implicit. The first two peaks correspond to resonant tunneling through the nodeless molecular ground state, for which no destructive interference is possible, so that all the terms in Eq. (4.13) are positive. For every other molecular resonance, three amplitudes are positive and three are negative such that by symmetry the total transmission amplitude vanishes exactly on resonance. Elsewhere in the spectrum, this *coordination of cancellation* is visible as a strong suppression

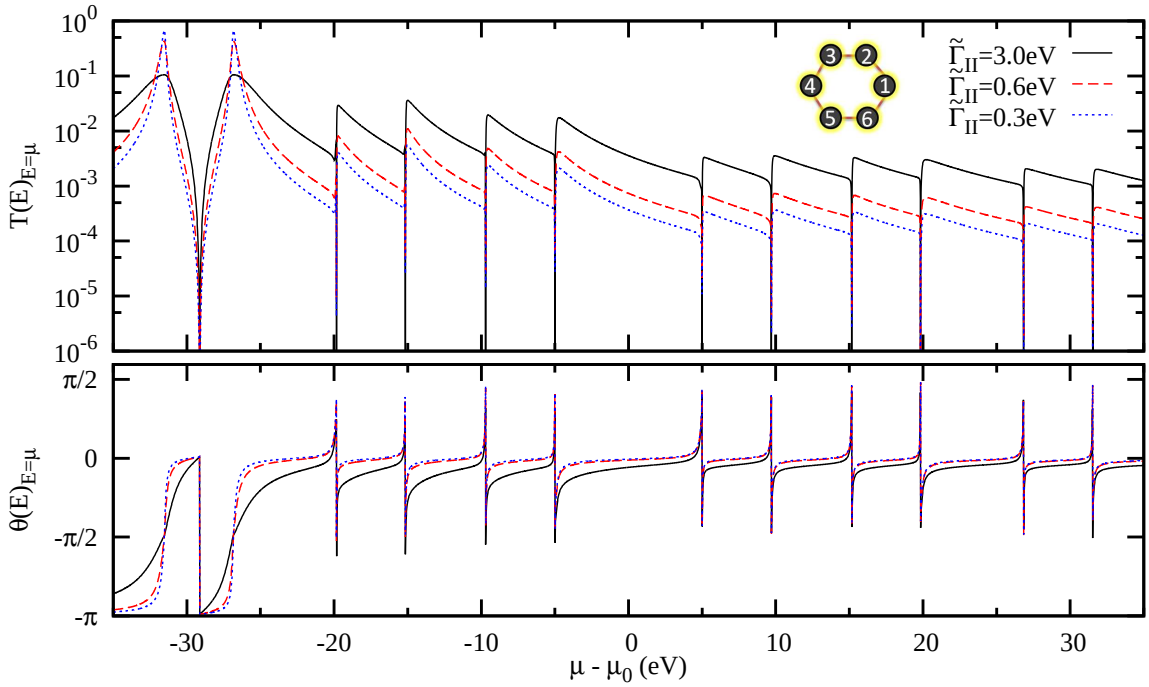

Figure 4.3: The transmission probability and phase for a flat, two-terminal benzene junction, exhibiting a maximal ∼3350× reduction in Coulomb blockade peak height for $\tilde{\Gamma}_{II}$=0.3eV. Reductions of ∼1050× and ∼50× were found for $\tilde{\Gamma}_{II}$=0.6eV and $\tilde{\Gamma}_{II}$=3.0eV, respectively. In all cases, lead I is coupled to a single orbital with Γ_I=0.6eV. The total coupling to the flat-contacted second lead $\tilde{\Gamma}_{II}$ was varied, where each orbital contributed $\tilde{\Gamma}_{II}/6$. Inset: A schematic showing the labeling of benzene's atomic orbitals. The model and parameterization used in these simulations are discussed in detail in Sec. 2.1.1].

of the molecular resonance peak heights. As the lead-molecule coupling is reduced the individual transmission amplitudes are only appreciable near a resonance, where destructive interference between amplitudes is most complete, resulting in enhanced peak suppression with *decreasing* lead-molecule coupling.

In summary, we find that quantum interference can effectively destroy Coulomb blockade peaks. The transmission probability of an electron tunneling through a flat junction, in which a single-channel lead couples to all molecular orbitals, is determined by considering the coherent superposition of transmission amplitudes from all possible junction connectivities. By virtue of the nodal structure of the many-body wavefunction, many of these amplitudes cancel or nearly cancel, strongly suppress-

ing the Coulomb blockade peak amplitudes but leaving the molecular charge state unaffected. Single-molecule junctions offer a novel and interesting physical system in which to investigate the effects of spatial symmetry and quantum-interference on transport.

4.2 Transport with multi-channel contacts

In this section, we investigate how transmission eigenvalue distributions of SMJs depend on the number of lead-molecule bonds and on molecular symmetry using a many-body theory of transport [23]. Specifically, we focus on junctions with benzene (C_6H_6) and butadiene (C_4H_6) bonded to two Pt leads (cf. Fig. (4.4)). Consistent with refs. 90 and 173, we find that the total number of *nonzero* transmission eigenvalues in a SMJ is limited only by the number of bonds to each electrode. However, increasing the number of bonds past a certain point leads to additional channels with very small transmission. The central finding of this section is that in SMJs with sufficient numbers of lead-molecule bonds *the number of dominant transmission channels is equal to the degeneracy of the molecular orbital closest to the metal Fermi level*. Additional transmission channels stemming from further off-resonant molecular states are strongly suppressed, but may still be experimentally resolvable [90] for very strong lead-molecule hybridization.

4.2.1 Multi-channel formalism and the lead-molecule coupling

In our many-body theory, the lead-molecule coupling is characterized by the tunneling matrix $\Gamma(E)$ which is directly related to the tunneling self-energy Σ_{T} which we found using an equation-of-motion method for the junction Green's function in Sec. 2.1.2. In the second and third chapters, we considered one specific instance of a single-channel lead: we took $[\Gamma(E)]_{nm}{=}\Gamma(E)\delta_{nm}$, where n and m are molecular orbital labels. In general, the coupling between a single-mode lead is characterized by a Hermitian Γ-matrix of rank one. We wish to study the dependence of the transmission eigenvalue distribution on the number of bonds formed with each electrode.

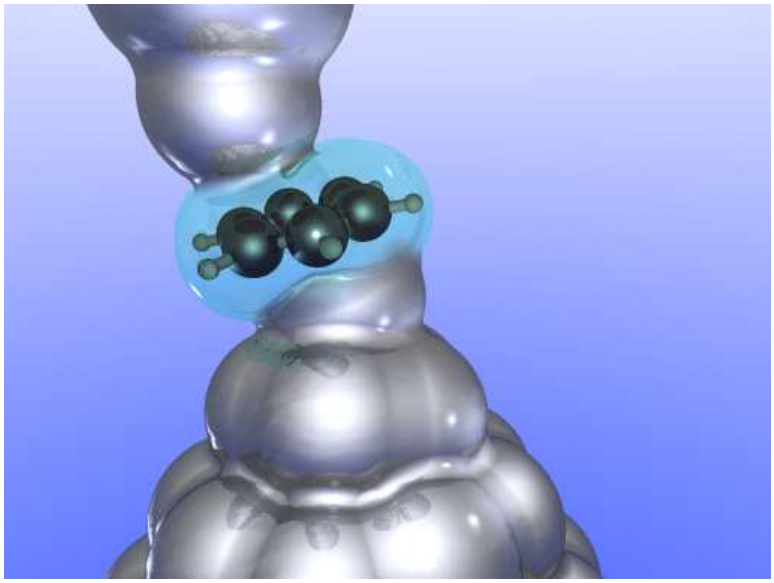

Figure 4.4: A schematic representation of the Pt-benzene-Pt junction

For M covalent bonds between a macroscopic lead and a molecule with P atomic orbitals, Γ is a rank-M matrix, which can be represented as

$$\Gamma = \sum_{m=1}^{M} \gamma_m^\dagger \gamma_m, \tag{4.14}$$

where γ_m are linearly-independent real row vectors of dimension P, representing linear combinations of the atomic orbitals of the molecule [1]. While Eq. (4.14) is certainly the form of a rank M matrix, it doesn't lend much insight into what constraints are placed on the tunneling-width amplitudes. Ideally, we'd like a prescription for how to calculate γ_m.

Our approach is to populate the elements of γ_m from a uniform random distribution on the interval [-A,A]. Recall that any non-zero element a of γ_m indicates a bond between the m^{th} mode of the lead and orbital a of the molecule. By sampling from a uniform distribution we refrain from making any assumptions about the distribution of bond strengths. Because bonding is local and there are large uncertainties in the distributions of angle, distance and coupling strength of the molecule, this seems to be a valid approximation.

[1] Γ is a real symmetric matrix for systems with time-reversal invariance.

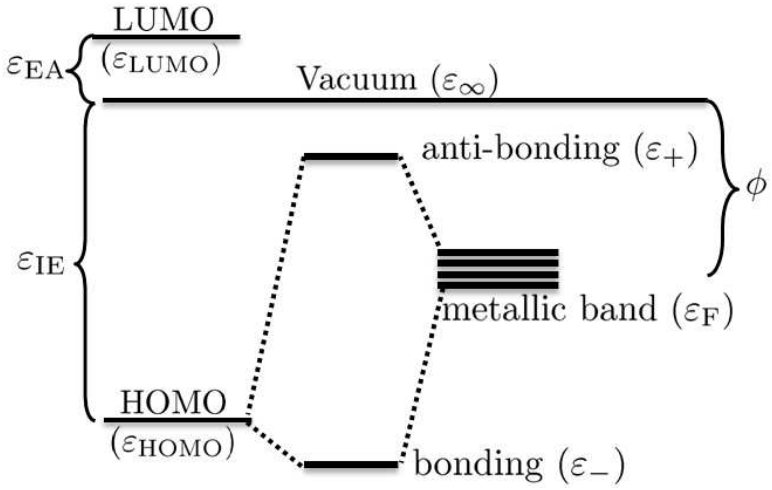

Figure 4.5: A characteristic level structure diagram of a molecule bound to a metallic surface. The vacuum energy ε_∞, which is taken as our zero energy, is within the HOMO-LUMO gap meaning that the unbound molecule is charge neutral. The ionization energy $\varepsilon_{\rm IE}$ is the energy required to remove an electron and $\varepsilon_{\rm EA}$ is the energy required to add an electron. The metallic work function ϕ is the energy required to promote a metal electron at the Fermi energy to become a free electron in vacuum. When the molecule and metal are brought close to one another the energy levels of both shift and hybridize, forming bonding and anti-bonding states with energies ε_+ and ε_-, respectively.

In order to proceed, it is useful to consider a few details of the lead-molecule bond. As indicated schematically in Fig. 4.5, when a molecule bonds with a metallic lead the relevant energy levels shift and hybridize forming bonding and anti-bonding states. Applying many-body perturbation theory up to second order gives two contributions to the binding energy $\Delta E_{\rm b}$

$$\Delta E_{\rm b} = \varepsilon_{\rm HOMO} - \varepsilon_- = \Delta E_{\rm vdW} + \Delta E_{\rm hybrid}, \tag{4.15}$$

where the van der Waals energy shift $-\Delta E_{\rm vdW}$=$\langle \tilde{H}_{\rm mol}\rangle$-$\langle H_{\rm mol}\rangle$. $\tilde{H}_{\rm mol}$ and $H_{\rm mol}$ are the Hamiltonians for the bonded and gas phase molecules, respectively. As we shall see, $\Delta E_{\rm vdW}$ can be quite large since the equilibrium height of a molecule bonded to a metallic surface is often sufficiently small that image charge effects can strongly screen intramolecular interactions.

The hybridization energy may be found using second order perturbation theory.

For the moment, let us only consider the effect arising from the HOMO level alone

$$-\Delta E_{\text{hybrid}} = \sum_{\nu}\sum_{k,\sigma} \frac{\langle \text{FG}, 0_N|H_{\text{T}}|\nu, k\sigma\rangle\langle k\sigma, \nu|H_{\text{T}}|0_N, \text{FG}\rangle}{E_{\text{N}}^{(0)} - E_{\text{N}-1}^{\nu} - \varepsilon_{k\sigma}}, \tag{4.16}$$

where ν is a molecular state index, k and σ are lead state indices, $|0_{\text{N}}\rangle$ is the N particle ground state of the (neutral) molecule, $|\text{FG}\rangle$ is the Fermi gas state of the lead, and H_{T} is the tunneling Hamiltonian, first given in Eq. (2.6). The matrix elements in the numerator of Eq. (4.16) can be evaluated directly as

$$\begin{aligned} \langle k\sigma, \nu|H_{\text{T}}|0_N, \text{FG}\rangle &= \sum_n V_{nk}^* \langle \nu|d_{n\sigma}|0_N\rangle\langle k\sigma|c_{k\sigma}^\dagger|\text{FG}\rangle \\ &= [1 - f(\varepsilon_{k\sigma})] \sum_n V_{nk}^* \langle \nu|d_{n\sigma}|0_N\rangle, \end{aligned} \tag{4.17}$$

where n is a site index and the matrix element $\langle k\sigma|c_{k\sigma}^\dagger|\text{FG}\rangle$ corresponds to the likelihood that a lead state has an electronic vacancy (i.e. a hole). Taking the modulus squared of Eq. (4.17) and rephrasing the result in terms of $\Gamma(E)$ we find

$$-\Delta E_{\text{hybrid}} = \sum_{\nu} \int_{\mu}^{\infty} \frac{dE}{2\pi} \frac{\text{Tr}\left\{\Gamma(E) C^{\nu,0_{\text{N}}}\right\}}{E_{\text{N}}^{(0)} - E_{\text{N}-1}^{\nu} - E} \tag{4.18}$$

where ν is the N-1 particle space index, μ is the metal-specific Fermi energy, Γ is the matrix of Eq. (4.14), and the many-body term is given by Eq. (2.27)

$$[C^{\nu\nu'}]_{n\sigma,m\sigma'} = \langle \nu|d_{n\sigma}|\nu'\rangle\langle \nu'|d_{m\sigma'}^\dagger|\nu\rangle. \tag{4.19}$$

The trace in Eq. (4.18) is over all molecular sites but only one spin species. Repeating a nearly identical analysis for the LUMO level we find that the full hybridization term of the binding energy is given by

$$-\Delta E_{\text{hybrid}} = \sum_{\nu} \int_{\mu}^{\infty} \frac{dE}{2\pi} \frac{\text{Tr}\left\{\Gamma(E) C^{\nu,0_{\text{N}}}\right\}}{E_{\text{N}}^{(0)} - E_{\text{N}-1}^{\nu} - E} + \sum_{\nu'} \int_{\mu}^{\infty} \frac{dE}{2\pi} \frac{\text{Tr}\left\{\Gamma(E) C^{0_{\text{N}},\nu'}\right\}}{E + E_{\text{N}}^{(0)} - E_{\text{N}+1}^{\nu}} \tag{4.20}$$

where the ν (ν') sum is over all N-1 (N+1) particle states.

4.2.2 Benzene on platinum

With the theoretical formalism in place, we now turn to the specifics of the Pt-benzene-Pt junction. Our choice of this junction is motivated by the experimental

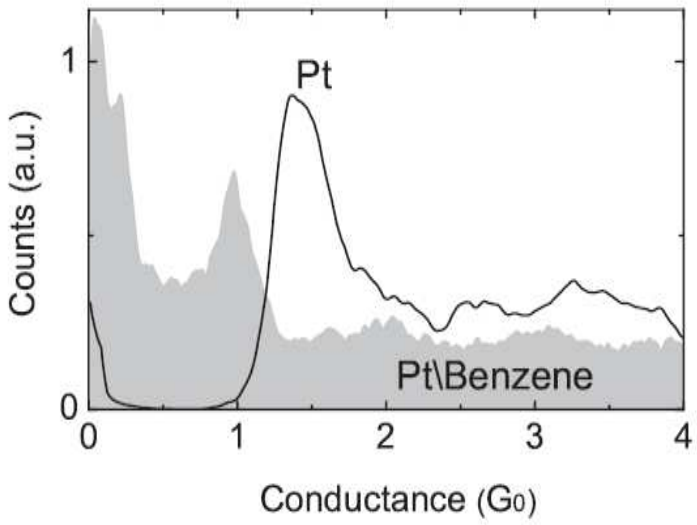

Figure 4.6: Normalized conductance histograms for a Pt junction (black), and for Pt after introducing benzene (filled). A conductance near $1G_0$=$2e^2/h$ is found for the Pt-benzene-Pt junction while the conductance of platinum alone was found to be $1.5G_0$. Each conductance histogram is constructed from more than 3000 conductance traces recorded with a bias of 0.1 V during repeated breaking of the contact. Figure is taken from Ref. 90.

work of Kiguchi et al. [90] on the same system. In their work, Kiguchi et al. found that benzene forms a strong direct bond with the platinum surface. As indicated in Fig. 4.6, the conductance of the Pt-benzene-Pt junction is nearly $1G_0$, an order of magnitude larger than for the Au-benzenedithiol-Au junction [203].

Kiguchi et al. also measure the shot noise of the Pt-benzene-Pt molecular junction which they used to calculate the channel transmission probabilities. As we discussed previously, the number of channels is limited by the number of bonds. Although benzene has six π-orbitals the mismatch between the center of the HOMO-LUMO gap and the Fermi level of Pt means that only one resonance, in this case the HOMO , contributes appreciably to the bonding. For an aromatic ring like benzene, this resonance has an orbital degeneracy and so we predict that there should be just two dominant channels in the transport. Interestingly, in one of the three shot noise measurements a small (10%) contribution to the transmission is found for

a third channel. The reason for this will become apparent after we examine some of the specifics of the Pt-benzene-Pt junction.

At room temperature, the density of states (DOS) of platinum is very sharply peaked around the Fermi energy, implying that the metal is not very free-electron-like [96]. One method of extracting the DOS at this energy is from the low-temperature specific heat

$$g(\varepsilon_{\rm F}) = \frac{3\gamma}{\pi^2 k_{\rm B}^2}, \tag{4.21}$$

where γ is the coefficient of specific heat which is linear in T and $k_{\rm B}$ is Boltzmann's constant. For platinum, $\gamma_{\rm Pt}$=6.8mJ/molK^2 so that $g_{\rm Pt}(\varepsilon_{\rm F})$=2.88/eV, a value nearly 10$\times$ that of Gold at the Fermi energy [95]. With such a sharply peaked DOS $\Gamma(E) \approx \Gamma(\varepsilon_F) Z\delta(E-\varepsilon_F)/g(\varepsilon_F)$ and we may approximate Eq. (4.20) as follows

$$-\Delta E_{\rm hybrid} \approx \frac{Z}{2\pi g(\varepsilon_{\rm F})}\left[\sum_{\nu}\frac{{\rm Tr}\left\{\Gamma(\varepsilon_{\rm F})C^{\nu,0_6}\right\}}{E_6^{(0)}-E_5^{\nu}-\mu_{\rm Pt}}+\sum_{\nu'}\frac{{\rm Tr}\left\{\Gamma(\varepsilon_{\rm F})C^{0_6,\nu'}\right\}}{\mu_{\rm Pt}+E_6^{(0)}-E_7^{\nu}}\right] \leq \Delta E_{\rm b}^{\rm max}, \tag{4.22}$$

where neutral benzene has N=6 and Z is the metal's valence. Although neutral platinum is in the $5d^9 6s^1$ configuration, the strong influence of the d-orbitals give a valence $Z_{\rm Pt}$=4. From Eq. (4.22) we see that in general, for a fixed hybridization energy, a large DOS requires a commensurately large $\Gamma(\varepsilon_{\rm F})$ which in turn results in a large junction conductance.

The Platinum (111) surface

In order to determine the range of tunneling-width amplitude matrix elements, we'll examine the details of the adsorption of benzene on the (111) plane of platinum. In addition to being thermodynamically the most stable face of platinum, the close-packed (111) plane is also highly symmetric and has been the subject of numerous adsorption studies involving benzene [39, 159, 134].

The observed binding energy of benzene on a Pt(111) surface ranges between 21 kcal/mol (0.911 eV/atom) to 29 kcal/mol (1.26 eV/atom) corresponding to the atop(0) and bridge(30) bonding configurations, respectively [39, 134]. All possible binding sites for benzene on Pt are shown in Fig. 4.7. Using an effective field theory

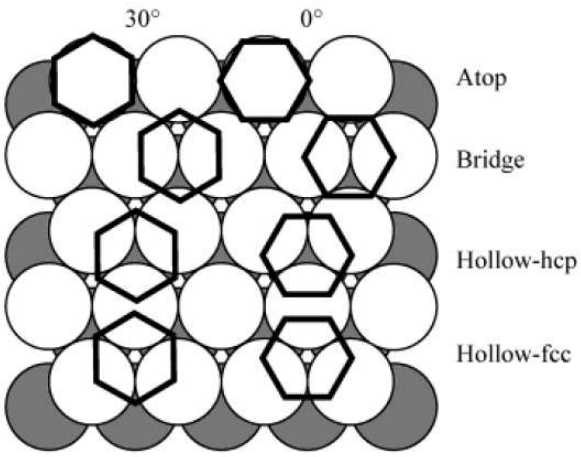

Figure 4.7: Schematic of possible benzene adsorption sites on at Pt(111) surface. Image is taken from Ref. 159.

of interacting π-electrons to model the electronic degrees of freedom most relevant for transport and assuming that the screening is dominated by the nearest Pt atom 2.25Å from the benzene ring, we find [16] that the HOMO-LUMO gap of benzene reduces from 10.05eV in the gas-phase to 7.52eV on Pt(111) and $\Delta E_{\rm vdW} = 0.49$eV. This implies

$$\Delta E_{\rm hybrid} \leq 0.77\text{eV}. \tag{4.23}$$

We have used the fact that the work function for the (111) plane of Pt is $\phi_{\rm Pt(111)}$=5.93eV [118].

The only remaining parameter needed to characterize the lead-molecule coupling distribution is the percentile of the maximal binding energy. The leads in a break junction are formed by pulling a metal nanowire apart until an atomically sharp edge is formed. Since the most favourable binding of benzene on the closest-packed Pt(111) surface gives $\Delta E_{\rm hybrid}$=0.77eV, we assume this is essentially an upper bound on hybridization in a SMJ, where the bonding is more random. The distributions of $\Delta E_{\rm hybrid}$ and $\mathrm{Tr}\{\Gamma_\alpha\}$ shown in Fig. 4.8 have long Gaussian tails, so the value $A = 0.82$eV was chosen to fix the $99^{\rm th}$-percentile of $\Delta E_{\rm hybrid}$ at 0.77eV [179]. The $99^{\rm th}$-percentile of $\mathrm{Tr}\{\Gamma_\alpha\}$ is 10.82eV which, per orbital, is nearly 3× the coupling found for a Au-BDT-Au junction [23].

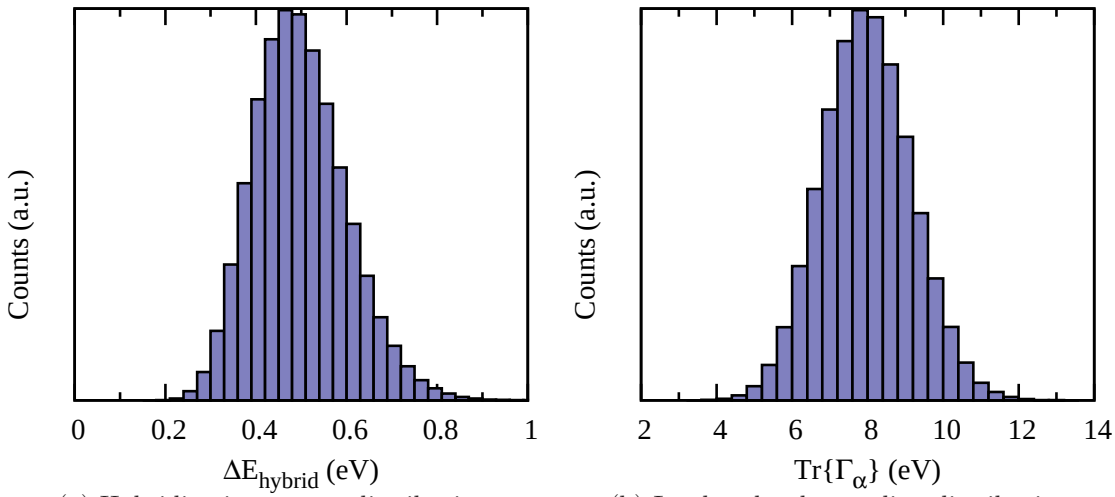

(a) Hybridization energy distribution (b) Lead-molecule coupling distribution

Figure 4.8: Distributions of the hybridization energy (a) and lead-molecule coupling (b) with 99$^{\text{th}}$-percentile values of 0.77eV and 10.82eV, respectively. The lead-molecule coupling distribution is for one lead only since the experimental binding energy was measured for benzene adsorbed on a Pt(111) surface. Here α=1,2 labels the lead-molecule contacts.

Transmission eigenchannel distribution

The Pt-benzene-Pt junctions are formed using mechanically controlled break junctions and so sample an ensemble of crystal planes as well as bonding configuration. The work function of platinum ranges from 5.93eV to 5.12eV for the (111) and (331) crystal faces, respectively [118]. Referring back to Fig. 4.5, the center of the HOMO-LUMO gap μ_0 is given by

$$\mu_0 = \frac{\varepsilon_{\text{IE}} + \varepsilon_{\text{EA}}}{2} = \frac{-9.25\text{eV} + (1.14\text{eV})}{2} = -4.055\text{eV}. \tag{4.24}$$

With a single Pt lead, the HOMO-LUMO gap is found to be 7.52eV, a reduction of 2.53eV compared with the measured gas-phase gap of 10.05eV. This reduction in the transport gap is symmetric about μ_0, so the screened HOMO energy is

$$\tilde{\varepsilon}_{\text{HOMO}} = \mu_0 - \frac{7.52}{2}\text{eV} = -7.815\text{eV} \tag{4.25}$$

relative to ε_∞=0 and

$$-1.875\text{eV} \leq \mu_{\text{Pt}} - \mu_0 \leq -1.065\text{eV}, \tag{4.26}$$

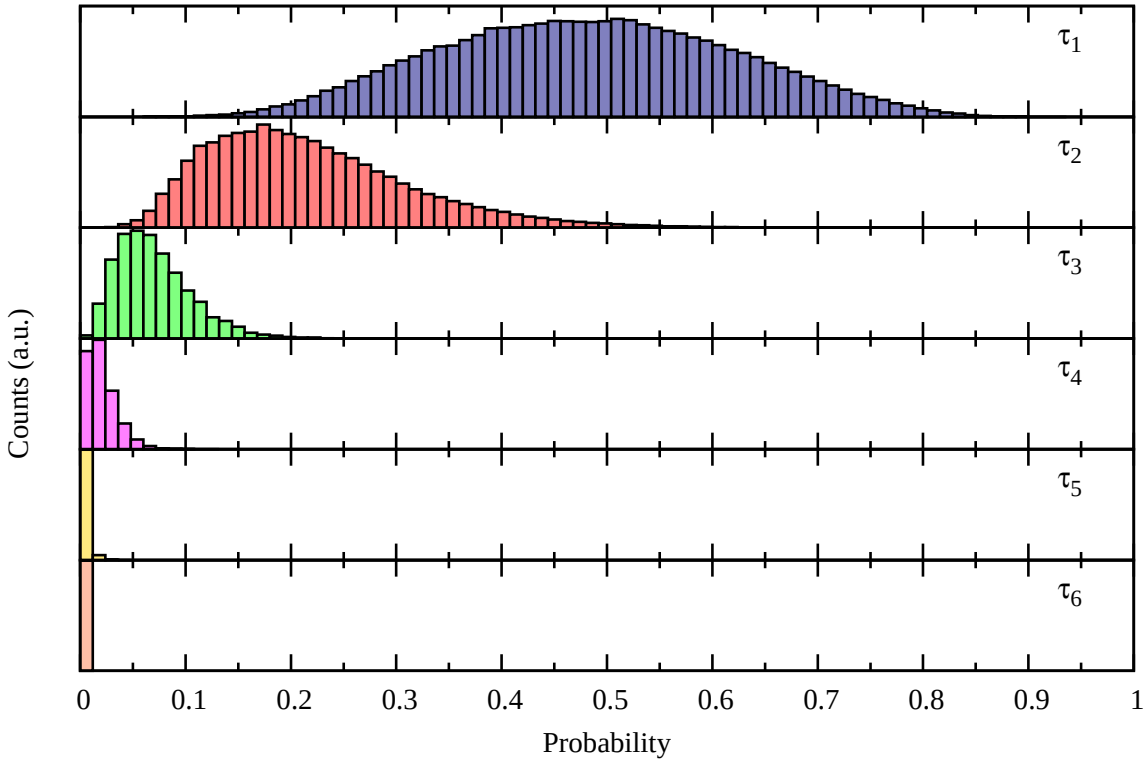

Figure 4.9: Calculated transmission eigenvalue distributions for an ensemble of 24×10^4 Pt–benzene–Pt junctions. 3,000 bonding configurations $\times$ 80 Pt surfaces were included. Each lead was assumed to form M=6 bonds with the molecule. There are two dominant transmission channels arising from the two-fold degenerate HOMO resonance closest to the Pt Fermi level, with a small but experimentally resolvable third channel arising from further off-resonant tunneling.

where μ_{Pt} is the chemical potential of the Pt lead.

The transmission eigenvalue distributions are shown in Fig. 4.9 for an ensemble of 24×10^4 Pt–benzene–Pt junctions, where τ_n are eigenvalues of the elastic transmission matrix given by Eq. (4.7). Each lead was assumed to form $M = 6$ bonds with the molecule. Despite the existence of six covalent bonds between the molecule and each lead, there are only two dominant transmission channels, which arise from the two-fold degenerate HOMO resonance closest to the Pt Fermi level. There is also a small but experimentally resolvable third channel arising from further off-resonant tunneling. This channel is non-negligible because of the very large lead-molecule coupling Γ in the Pt-benzene junction. Explicit calculations with smaller values

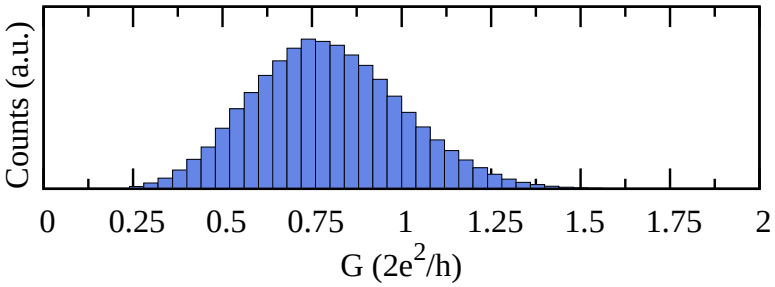

Figure 4.10: Calculated conductance histogram for the same ensemble of Pt–benzene–Pt junctions discussed in Fig. 4.9, where $G = (2e^2/h)\sum_n \tau_n$.

of $\mathrm{Tr}\{\Gamma\}$ yielded only two non-negligible transmission eigenvalues. Thus, for metals with a smaller DOS at the Fermi level, such as Cu, Ag, or Au, junctions with benzene would be expected to exhibit only two measurable transmission channels.

The calculated transmission eigenvalue distribution shown in Fig. 4.9 is consistent with the experiment [90], which determined the transmission eigenvalues for three particular junctions: $\{\tau_n\}$=$\{0.68, 0.40\}$, $\{0.36, 0.25, 0.10\}$, $\{0.20\}$, where a third channel was observable only once. The conductance histogram for the same ensemble of junctions is shown in Fig. 4.10. The peak conductance value is some 20% less than that reported experimentally [90]. This discrepancy might be attributable, in part, to the inclusion of a small fraction of Pt–Pt junctions in the experimental histogram.

In addition to the ensemble of junctions shown in Fig. 4.9, we also investigated ensembles of junctions with $M_\alpha = 1, \ldots, 6$, including the case $M_1 \neq M_2$. Consistent with the discussion in Refs. [173, 90], we find that the total number of nonzero transmission eigenvalues is $M_{\min} = \min\{M_1, M_2\}$. However, whenever $M_{\min} \geq 2$ there are always two dominant transmission channels, and the total transmission probability does not increase appreciably beyond $M_{\min} = 2$.

The above analysis demonstrates that the two dominant transmission channels evolve from the two-fold degenerate HOMO resonance in the molecular Green's function G_{mol} (2.29) as the lead-molecule coupling Σ_{T} is turned on. For finite Σ_{T}, the poles of G_{mol} are mixed by Dyson's equation (4.2), making it problematic to decompose the transmission *eigenvalues* into separate contributions from each molecular

resonance [173]. Alternatively, the projections of the transmission *eigenvectors* onto the molecular resonances can be computed [77]. Because an "extended molecule" is often used in density-functional calculations to account for charge transfer between the molecule and electrodes, it is difficult if not impossible to interpret these contributions in terms of the resonances of the molecule itself [77]. Since charging effects in SMJs are well-described in our many-body theory [23], there is no need to utilize an "extended molecule," so the projections of the transmission eigenvectors onto the molecular resonances can be determined unambiguously (see appendix A). We find that the mean-square projections of the first and second transmission channels in Fig. 4.9 onto the benzene HOMO resonance are 87% and 71%, respectively, confirming the conclusion that these eigenchannels correspond to tunneling primarily through the HOMO resonance.

4.2.3 Butadiene on platinum

To test our hypothesis that the number of dominant transmission channels is limited by the degeneracy of the most relevant molecular orbital, we have investigated transmission eigenvalue distributions for Pt–butadiene–Pt junctions. Butadiene (C_4H_6) is a linear conjugated polymer, lacking the discrete (six-fold) rotational symmetry of benzene. Since the molecular orbitals of butadiene are nondegenerate, we anticipate a single dominant transmission channel. Using the same per-orbital hybridization as for benzene gives $\mathrm{Tr}\,\Gamma_\alpha \leq 7.21\mathrm{eV}$. The image charge method gives $\Delta E_{\mathrm{vdW}} = 0.52\mathrm{eV}$ and we find $\Delta E_{\mathrm{hybrid}} \leq 0.59\mathrm{eV}$, so that $\Delta E_{\mathrm{b}} \leq 1.12\mathrm{eV} \equiv 107.7\mathrm{kJ/mol}$, in line with existing values reported in the literature [192]. The distributions of binding energy and Γ are shown in Fig. 4.11. The range of Pt work functions for all possible Pt surfaces gives a chemical potential range of

$$-1.70\mathrm{eV} \leq \mu_{\mathrm{Pt}} - \mu_0 \leq -0.89\mathrm{eV}. \tag{4.27}$$

The conductance channel histrograms for 24×10^4 Pt-butadiene-Pt junctions are shown in Fig. 4.12. Despite forming four bonds with each electrode, it is evident from the figure that the Pt–butadiene–Pt junction has a single dominant transmission

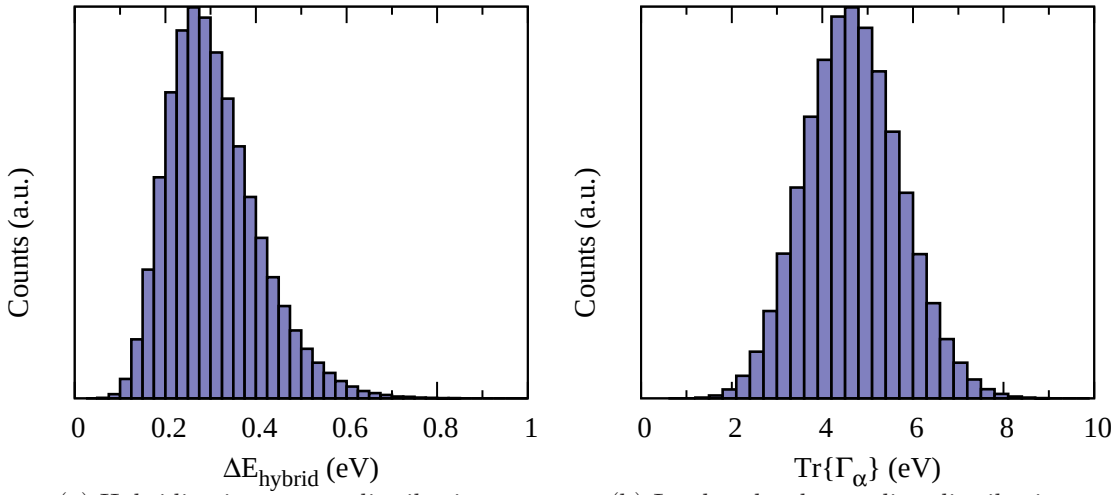

(a) Hybridization energy distribution (b) Lead-molecule coupling distribution

Figure 4.11: The distributions of hybridization energy (a) and lead-molecule coupling (b) with 99^{th}-percentile values of 0.59eV and 7.21eV, respectively. These distributions were found using A=0.937. Just as in the Pt-benzene-Pt junction, the total Γ in a junction would be twice that shown above.

channel. The mean-square projection of this transmission channel onto the non-degenerate butadiene HOMO resonance is 80% (see appendix A).

We have seen that the number of dominant transmission channels in a SMJ is equal to the degeneracy of the molecular orbital closest to the metal Fermi level. Transmission eigenvalue distributions were calculated for Pt-benzene-Pt and Pt-butadiene-Pt junctions using realistic state-of-the-art many-body techniques. In both cases, transmission occurs primarily through the HOMO resonance, which lies closest to the Pt Fermi level, resulting in two dominant transmission channels for benzene (2-fold degenerate HOMO) and a single dominant transmission channel for butadiene (non-degenerate HOMO). Our results for the transmission channel distributions of Pt-benzene-Pt junctions are in quantitative agreement with experiment [90].

Despite the larger number of states available for tunneling transport in SMJs, we predict that the number of transmission channels is typically more limited than in single-atom contacts because molecules are less symmetrical than atoms. Nonetheless, certain highly-symmetric molecules exist that should permit several dominant

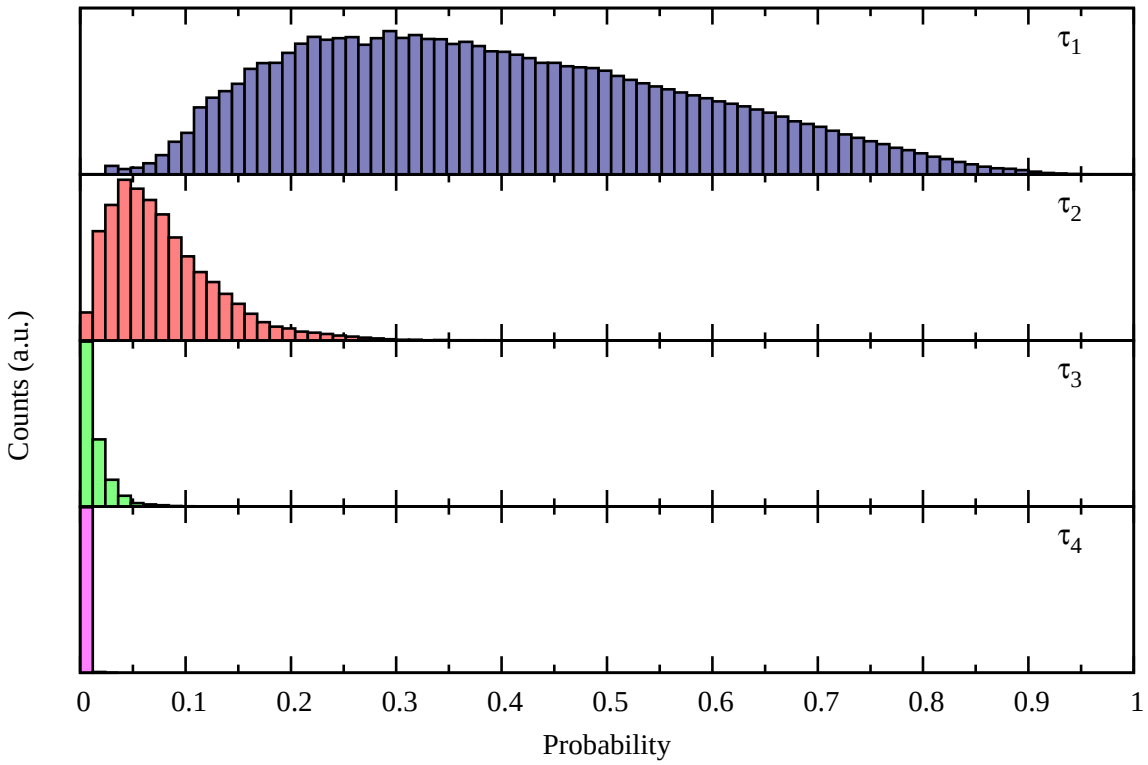

Figure 4.12: Transmission eigenvalue distributions for an ensemble of 24×10^4 Pt–butadiene–Pt junctions. 3,000 bonding configurations $\times$ 80 Pt surfaces were included. Each lead was assumed to form $M = 4$ bonds with the molecule. The linear butadiene (C_4H_6) molecule lacks the orbital degeneracy of the benzene ring and consequently exhibits only 1 dominant channel. A second channel due to further off-resonant tunneling may be experimentally resolvable. The total conductance distribution peaks around $\sim 0.4 G_0$.

transmission channels. For example, the C_{60} molecule possesses icosahedral symmetry, and has a 5-fold degenerate HOMO resonance and 3-fold degenerate LUMO resonance [80]. C_{60}-based SMJs with gold electrodes have been fabricated, and shown to exhibit fascinating electromechanical [145] and spin-dependent [207] transport properties. For Pt-C_{60}-Pt junctions, we predict *five dominant transmission channels* stemming from the C_{60} HOMO resonance, which lies closest to the Pt Fermi level [117, 100].

4.3 Friedel Oscillations

Thus far, we have viewed the molecular junction in a distinctly molecule-centric perspective, wherein the leads are included as self-energy corrections to the bare molecule's Green's functions. A major mathematical advantage of this perspective is that the self-energies compactly encapsulate the effect of coupling macroscopic leads to a microscopic molecule so that junction transport can be phrased in terms of the modified molecule rather than the entire junction.

In this section, we consider the molecular junction from the lead's perspective. In analogy with the aforementioned viewpoint, a finite lead-molecule coupling will give rise to a self-energy which will modify the pole structure of the lead's Green's function. While it is conceptually straightforward to shift the problem from a molecule-centric to a lead-centric one, the reader may wonder what motivates our doing so, since the leads are macroscopic and generally pose an intractable quantum mechanical many-body problem. Though it is true that a general solution to the electronic problem of macroscopic leads is not known, it is known for certain models such as the 1D tight-binding chain considered in this section. Moreover, measurements on macroscopic leads are much easier to perform than on single molecules, so if some measurable property of the lead is affected by a molecule in a known way then the lead can be used to effectively measure properties about the molecule.

To begin with, we derive expressions for the lead's Green's functions. The lesser Green's function is related to the charge density which exhibits so-called Friedel oscillations [59] as a function of distance from the molecule. Friedel oscillations arise because the incoming and scattered electronic waves interfere with one another, giving rise to charge density oscillations with a wavevector $2k_{\mathrm{F}}$ where k_{F} is the Fermi wavevector.

4.3.1 The lead's Green's functions

In analogy with the junction's Green's function discussed in chapter 2, we can express the retarded Green's function of lead α as

$$\tilde{g}^{(\alpha)}_{k\sigma,k'\sigma'}(t,t') = -\frac{i}{\hbar}\theta(t-t')\left\langle\left\{c_{k\sigma}(t), c^{\dagger}_{k'\sigma'}(t')\right\}\right\rangle, \tag{4.28}$$

where $\theta(t)$ is the Heaviside function and $c_{k\sigma}$ ($c^{\dagger}_{k\sigma}$) annihilates (creates) an electron with spin σ in mode k of lead α. Equation (4.28) is the probability amplitude that lead α will be found in a state with a particle (electron or hole) of spin σ in mode k at time t when a particle of spin σ' was added in mode k' at an earlier time t'. The junction's Green's functions, first given in Eq. (2.7), only had a single time variable since we were interested in stead-state phenomena and therefore assumed that the system was time-shift invariant. In the following derivation we find that the algebra is simplified if we include both time variables until the end. Once a closed set of equations is found, we proceed by transforming them into the Fourier domain where time-shift invariance will again be assumed.

In Sec. 2.1.2, we derived an expression for the junction Green's function G in terms of the molecular Green's function $G_{\rm mol}$ and a self-energy Σ=$\Sigma_{\rm T}$+$\Delta\Sigma_{\rm C}$, where $\Sigma_{\rm T}$ and $\Delta\Sigma_{\rm C}$ are the tunneling self-energy and the correction to the Coulomb self-energy, respectively. Presently, we would like to derive an expression for $\tilde{g}$ in terms of some 'free propagator' $\tilde{g}^0$ and self-energy $\tilde{\Sigma}$.

Equations-of-motion method

We begin the equations-of-motion (EOM) procedure by taking the derivative of Eq. (4.28) with respect to t'

$$\begin{aligned}
i\frac{\partial}{\partial t'}\tilde{g}^{(\alpha)}_{k\sigma,k'\sigma'}(t,t') &= -\delta(t-t')\,\delta_{kk'}\delta_{\sigma\sigma'} + \theta(t-t')\left\langle\left\{c_{k\sigma}(t), \frac{d}{dt}\left[c^{\dagger}_{k'\sigma'}(t')\right]\right\}\right\rangle \\
&= -\delta(t-t')\delta_{kk'}\delta_{\sigma\sigma'} - i\theta(t-t')\left\langle\left\{c_{k\sigma}(t), \left[c^{\dagger}_{k'\sigma'}(t'), H_{\rm junction}(t')\right]\right\}\right\rangle \\
&= -\delta(t-t')\delta_{kk'}\delta_{\sigma\sigma'} - i\theta(t-t') \\
&\qquad \left\langle\left\{c_{k\sigma}(t), \left[c^{\dagger}_{k'\sigma'}(t'), H_{\rm leads}(t')\right] + \left[c^{\dagger}_{k'\sigma'}(t'), H_{\rm T}(t')\right]\right\}\right\rangle
\end{aligned} \tag{4.29}$$

where we have applied Heisenberg's equation of motion $dA/dt = i[H(t), A(t)]$ and, in the final step, we have also taken advantage of the fact that the lead creation and annihilation operators commute with those of the molecule. We have also taken $\hbar$=1. The lead and tunneling Hamiltonians $H_{\rm T} = \sum_{\alpha=1}^{M} H_{\rm T}^{(\alpha)}$ and $H_{\rm leads}$=$\sum_{\alpha} H_{\rm lead}^{(\alpha)}$ were introduced in Sec. 2.1.1, where

$$H_{\rm T}^{(\alpha)} = \sum_{\substack{k\in\alpha \\ n,\sigma}} \left[V_{nk} d_{n\sigma}^{\dagger} c_{k\sigma} + V_{nk}^{*} c_{k\sigma}^{\dagger} d_{n\sigma} \right] \tag{4.30}$$

and

$$H_{\rm lead}^{(\alpha)} = \sum_{\substack{k\in\alpha \\ \sigma}} \varepsilon_{k\sigma} c_{k\sigma}^{\dagger} c_{k\sigma}. \tag{4.31}$$

Since the Hilbert spaces of separate leads are independent, their electronic creation and annihilation operators commute. The commutators involving $c_{k'\sigma'}^{\dagger}$ in Eq. (4.29) are therefore non-zero only for $H_{\rm leads}^{(\alpha)}$ and $H_{\rm T}^{(\alpha)}$, since all other lead Hamiltonians commute. We proceed by directly evaluating these commutators. For the lead part we find

$$\begin{aligned} \left[c_{k'\sigma'}^{\dagger}(t'), H_{\rm leads}(t') \right] &= \left[c_{k'\sigma'}^{\dagger}(t'), H_{\rm leads}^{(\alpha)}(t') \right] \\ &= \sum_{k''\in\alpha,\sigma''} \varepsilon_{k''\sigma''} \left[c_{k'\sigma'}^{\dagger}(t'), c_{k''\sigma''}^{\dagger}(t') c_{k''\sigma''}(t') \right] \\ &= -\varepsilon_{k'\sigma'} c_{k'\sigma'}^{\dagger}(t'), \end{aligned} \tag{4.32}$$

where we have used the fact that $\left[c_{k'\sigma'}^{\dagger}, c_{k''\sigma''}^{\dagger} c_{k''\sigma''} \right] = -c_{k''\sigma''}^{\dagger} \delta_{k'k''} \delta_{\sigma'\sigma''}$ via the more general relation

$$[A, BC] = \{B, A\} C - B \{C, A\}. \tag{4.33}$$

The commutator with the tunneling Hamiltonian is slightly more complicated but

can also be evaluated directly as

$$\begin{aligned}\left[c^{\dagger}_{k'\sigma'}(t'),H_{\rm T}(t')\right] &= \left[c^{\dagger}_{k'\sigma'}(t'),H^{(\alpha)}_{\rm T}(t')\right]\\ &= \sum_{\substack{k''\in\alpha\\ n'',\sigma''}} V_{n''k''}\underbrace{\left[c^{\dagger}_{k'\sigma'}(t'),d^{\dagger}_{n''\sigma''}(t')c_{k''\sigma''}(t')\right]}_{=\left\{d^{\dagger}_{n''\sigma''},c^{\dagger}_{k'\sigma'}\right\}c_{k''\sigma''}-d^{\dagger}_{n''\sigma''}\delta_{\sigma'\sigma''}\delta_{k'k''}} +\\ &\qquad V^{*}_{n'k''}\underbrace{\left[c^{\dagger}_{k'\sigma'}(t'),c^{\dagger}_{k''\sigma''}(t')d_{n''\sigma''}(t')\right]}_{=-c^{\dagger}_{k''\sigma''}\left\{d_{n''\sigma''},c^{\dagger}_{k'\sigma'}\right\}=0}\\ &= -\sum_{n''}V_{n''k'}d^{\dagger}_{n''\sigma'} \end{aligned} \tag{4.34}$$

where the $d_{n\sigma}$ and $c_{k\sigma}$ operators anti-commute for equal times. We should mention that $c_{k\sigma}$ and $c^{\dagger}_{k\sigma}$ are Fermionic operators and, as such, obey the usual equal-time *anti-commutation* relations (e.g. $\{c_{k\sigma}(t),c^{\dagger}_{k'\sigma'}(t)\}=\delta_{kk'}\delta_{\sigma\sigma'}$). One must therefore be careful when deriving commutation relations for these operators. Inserting Eqs. (4.32) and (4.34) into Eq. (4.29) we find

$$\begin{aligned} i\frac{\partial}{\partial t'}\tilde{g}_{k\sigma,k'\sigma'}(t,t') &= -\delta(t-t')\,\delta_{kk'}\delta_{\sigma\sigma'}\\ &\quad +i\theta(t-t')\left\langle\left\{c_{k\sigma}(t),\varepsilon_{k'\sigma'}c^{\dagger}_{k'\sigma'}(t')+\sum_{n'}V_{n'k'}d^{\dagger}_{n'\sigma'}(t')\right\}\right\rangle\\ &= -\delta(t-t')\,\delta_{kk'}\delta_{\sigma\sigma'}-\varepsilon_{k'\sigma'}\tilde{g}_{k\sigma,k'\sigma'}(t,t')-\sum_{n'}V_{n'k'}g_{k\sigma,n'\sigma'}(t,t'), \end{aligned} \tag{4.35}$$

where the lead-molecule Green's function was given by Eq. (2.11)

$$g_{k\sigma,n'\sigma'}(t,t')=-i\theta(t)\left\langle\left\{c_{k\sigma}(t),d^{\dagger}_{n'\sigma'}(t')\right\}\right\rangle. \tag{4.36}$$

In order to form a closed set of equations we consider the time derivative of g which may be written as

$$i\frac{\partial}{\partial t}g_{k\sigma,n'\sigma'}(t,t')=-i\theta(t-t')\left\langle\left\{\left[c_{k\sigma}(t),H_{\rm leads}+H_{\rm T}\right],d^{\dagger}_{n'\sigma'}(t')\right\}\right\rangle. \tag{4.37}$$

The commutators may be found by following the same procedures as outlined above

and replacing $c^{\dagger}_{k'\sigma'}$ by $c_{k'\sigma'}$. We find the commutators are given as follows

$$\begin{aligned}
\left[c_{k\sigma}\left(t\right), H_{\text{leads}}(t)\right] &= \varepsilon_{k\sigma}c_{k\sigma}\left(t\right) \qquad (4.38)\\
\left[c_{k\sigma}(t), H_{\text{T}}(t)\right] &= \sum_{\substack{k''\in\alpha\\ n'',\sigma''}} V_{n''k''}\underbrace{\left[c_{k\sigma}(t), d^{\dagger}_{n''\sigma''}(t)c_{k''\sigma''}(t)\right]}_{=\left\{d^{\dagger}_{n''\sigma''},c_{k\sigma}\right\}c_{k''\sigma''}=0} + \\
&\qquad V^{*}_{n'k''}\underbrace{\left[c_{k\sigma}(t), c^{\dagger}_{k''\sigma''}(t)d_{n''\sigma''}(t)\right]}_{=d^{\dagger}_{n''\sigma''}\delta_{\sigma\sigma''}\delta_{kk''}}\\
&= \sum_{n''} V_{n''k}d_{n''\sigma}(t) \qquad (4.39)
\end{aligned}$$

where we have used the identity $\left[c_{k\sigma}, c^{\dagger}_{k''\sigma''}c_{k''\sigma''}\right] = c_{k\sigma}\delta_{\sigma\sigma''}\delta_{kk''}$. Plugging these back into Eq. (4.37) we find

$$\begin{aligned}
i\frac{\partial}{\partial t}g_{k\sigma,n'\sigma'}(t,t') &= -i\theta(t-t')\left\langle\left\{\varepsilon_{k\sigma}c_{k\sigma}\left(t\right) + \left(\sum_{n''} V^{*}_{n''k}d_{n''\sigma}(t)\right), d^{\dagger}_{n'\sigma'}(t')\right\}\right\rangle\\
&= \varepsilon_{k\sigma}g_{k\sigma,n'\sigma'}\left(t,t'\right) + \sum_{n''} V^{*}_{n''k}G_{n''\sigma,n'\sigma'}(t,t'), \qquad (4.40)
\end{aligned}$$

where G is the junction Green's function.

Equations (4.35) and (4.40) constitute a closed set of differential equations relating $\tilde{g}$, g and G to one another. In order to proceed we transform these equations into the Fourier domain, wherein differential equations become algebraic equations. The Fourier operator is defined as

$$G\left(E\right) = \mathscr{F}\{g(t)\} \equiv \int_{-\infty}^{\infty} dt e^{iEt} g\left(t\right). \qquad (4.41)$$

We should note that the differential in Eq. (4.35) is taken with respect to t' while that in Eq. (4.40) is with respect to t such that:

$$\begin{aligned}
\mathscr{F}\left\{\frac{\partial}{\partial t}g_{k\sigma,n\sigma'}(t-t')\right\} &\equiv \frac{\partial(t-t')}{\partial t}\mathscr{F}\left\{\frac{\partial g_{k\sigma,n\sigma'}(t'')}{\partial t''}\right\} = -iEg_{k\sigma,n\sigma'}(E)\\
\mathscr{F}\left\{\frac{\partial}{\partial t'}\tilde{g}_{k\sigma,k'\sigma'}(t-t')\right\} &\equiv +iE\tilde{g}_{k\sigma,k'\sigma'}(E). \qquad (4.42)
\end{aligned}$$

With this in mind, the transformed equations are given by

$$(E - \varepsilon_{k'\sigma'})\,\tilde{g}_{k\sigma,k'\sigma'}(E) = \delta_{kk'}\delta_{\sigma\sigma'} + \sum_{n'} V_{n'k'} g_{k\sigma,n'\sigma'}(E) \tag{4.43}$$

$$g_{k\sigma,n'\sigma'}(E) = \frac{1}{E - \varepsilon_{k\sigma}} \sum_{n''} V^*_{n''k} G_{n''\sigma,n'\sigma'}(E). \tag{4.44}$$

All that remains is to combine Eqs. (4.43) and (4.44) and rearrange the resulting expression into meaningful terms. For completeness we include the details of that derivation here

$$\begin{aligned}
\tilde{g}_{k\sigma,k'\sigma'}(E) &= \tilde{g}^{(0)}_{k\sigma,k'\sigma'}(E) + \left(\frac{1}{E - \varepsilon_{k\sigma}}\right) \sum_{n',n''} V_{n'k'} V^*_{n''k} G_{n''\sigma,n'\sigma'}(E) \left(\frac{1}{E - \varepsilon_{k'\sigma'}}\right) \\
&= \tilde{g}^{(0)}_{k\sigma,k'\sigma'}(E) + \left(\frac{1}{E - \varepsilon_{k\sigma}}\right) \left[\tilde{\Sigma}_{\mathrm{T}}(E)\right]_{k\sigma,k'\sigma'} \left(\frac{1}{E - \varepsilon_{k'\sigma'}}\right) \\
&= \tilde{g}^{(0)}_{k\sigma,k'\sigma'}(E) + \sum_{k'',\sigma''} \sum_{k''',\sigma'''} \tilde{g}^{(0)}_{k\sigma,k''\sigma''}(E) \left[\tilde{\Sigma}_{\mathrm{T}}(E)\right]_{k''\sigma'',k'''\sigma'''} \tilde{g}^{(0)}_{k'''\sigma''',k\sigma}(E),
\end{aligned} \tag{4.45}$$

where

$$\frac{1}{E - \varepsilon_{k\sigma}} \equiv \sum_{k'',\sigma''} \frac{\delta_{k''k}\delta_{\sigma''\sigma}}{E - \varepsilon_{k''\sigma''}} \equiv \sum_{k'',\sigma''} \tilde{g}^{(0)}_{k''\sigma'',k\sigma}(E) \tag{4.46}$$

and we have set

$$\left[\tilde{\Sigma}_{\mathrm{T}}(E)\right]_{k\sigma,k'\sigma'} = \sum_{n',n'} V_{n'k'} V^*_{n''k} G_{n''\sigma,n'\sigma'}(E). \tag{4.47}$$

Equation Eq. (4.45) may be equivalently expressed in matrix form as

$$\tilde{g}(E) = \tilde{g}^{(0)}(E) + \tilde{g}^{(0)}(E)\tilde{\Sigma}_{\mathrm{T}}(E)\tilde{g}^{(0)}(E), \tag{4.48}$$

which is *not* stated as a Dyson's equation since $\tilde{g}$ is not recursively defined. In order to make connection to existing Keldysh theory [89, 38, 81] it is advantageous to transform Eq. (4.48) into a Dyson's equation. If we substitute $\tilde{\Sigma}_{\mathrm{T}}(E)\tilde{g}^{(0)}(E)$=$\tilde{\Sigma}^{(0)}_{\mathrm{T}}(E)\tilde{g}(E)$ then

$$\tilde{g}(E) = \tilde{g}^{(0)}(E) + \tilde{g}^{(0)}(E)\tilde{\Sigma}^{(0)}_{\mathrm{T}}(E)\tilde{g}(E), \tag{4.49}$$

where following some algebra we find $\tilde{\Sigma}_{\mathrm{T}} = \tilde{\Sigma}^{(0)}_{\mathrm{T}} \left(\mathbf{1} - \tilde{g}^{(0)}\tilde{\Sigma}^{(0)}_{\mathrm{T}}\right)^{-1}$.

The 'lesser' lead Green's function

Friedel oscillations are a modulation of the electronic density seen as a function of distance from an impurity, which in our case is a molecule. Moreover, the electronic density is proportional to the integral of the equal-time Keldysh Green's function

$$n\left(x\right) = -\frac{i}{2\pi}\int_{-\infty}^{\infty} dE\ \tilde{g}^{<}(x,x,E), \tag{4.50}$$

where x is a coordinate in a spatial basis and $\tilde{g}^{<}(x,x,E)$ is the lead's lesser Green's function in that same basis. As discussed in chapter 1, the Keldysh equation is a general result stemming from the mathematics of converting functions on complex time contour variables into real time variables. The lesser Keldysh Green's function for the lead is given by

$$\begin{aligned}\tilde{g}^{<}(E) &= \left(1+\tilde{g}(E)\tilde{\Sigma}^{(0)}(E)\right)\tilde{g}_0^{<}(E)\left(1+\tilde{\Sigma}^{(0),\dagger}(E)\tilde{g}^{\dagger}(E)\right) \\ &\quad + \tilde{g}(E)\tilde{\Sigma}^{(0),<}(E)\tilde{g}^{\dagger}(E),\end{aligned} \tag{4.51}$$

where in the present context $\tilde{\Sigma}$=$\tilde{\Sigma}_{\mathrm{T}}$ and

$$\tilde{\Sigma}^{(0),<} = \lim_{H_{\mathrm{T}}\to 0} H_{\mathrm{T}} G^{<}_{\mathrm{mol}} H_{\mathrm{T}} \tag{4.52}$$

Following some algebraic manipulation Eq. (4.51) can be equivalently expressed in terms of $\tilde{\Sigma}$ and $\tilde{g}^{(0)}$ instead

$$\begin{aligned}\tilde{g}^{<}(E) &= \tilde{g}^{(0),<}(E) + \tilde{g}^{(0)}(E)\tilde{\Sigma}(E)\tilde{g}^{(0),<}(E) + \\ &\quad \tilde{g}^{(0),<}(E)\tilde{\Sigma}^{\dagger}(E)\tilde{g}^{(0),\dagger}(E) + \\ &\quad \tilde{g}^{(0)}(E)\tilde{\Sigma}^{<}(E)\tilde{g}^{(0),\dagger}(E)\end{aligned} \tag{4.53}$$

where each term is an energy dependent matrix and $\tilde{\Sigma}$ is given by Eq. (4.47).

4.3.2 1-D tight-binding leads

In order to calculate the charge density, Eq. (4.53) must be evaluated explicitly. Although the *exact* Green's functions of a macroscopic object such as a lead are not generally known, the energy dispersion of several systems are known exactly. Presently, we consider a junction composed of a semi-infinite 1-D chain coupled to a molecule, shown schematically in Fig. 4.13.

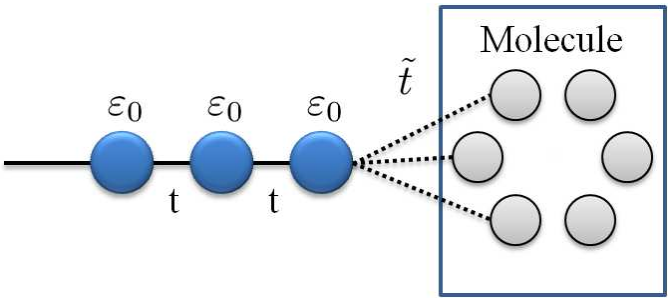

Figure 4.13: A semi-infinite 1-D lead coupled to a molecule. The inter-chain nearest neighbor hopping is t and the lead-molecule coupling is characterized by $\tilde{t}$.

The retarded Green's function

The retarded Green's function of the lead is diagonal in the momentum basis, but the bonding between the lead and the molecule is local, suggesting that the problem is most simply formulated in configuration space. Performing the change of basis we find

$$\begin{aligned} \tilde{g}^{(0)}(x,x';E) &= \left\langle x\left|\tilde{g}^{(0)}(E)\right|x'\right\rangle = \sum_k \frac{\langle x|k\rangle\langle k|x'\rangle}{E-E_k+i0^+} \\ &\Rightarrow \frac{L}{2\pi}\int_{-\pi/a}^{\pi/a} dk \frac{\Psi_k(x)\Psi_k^*(x')}{E-E_k+i0^+} = \frac{1}{\pi a}\int_{-\pi}^{\pi} dp \frac{\sin(pn)\sin(pn')}{E+2t\cos(p)+i0^+}, \end{aligned} \tag{4.54}$$

where we consider only a single spin species, $\langle x|k\rangle = \Psi_k(x_n)=\sqrt{\frac{2}{L}}\sin(kx_n)$ are the eigenfunctions of a 1-D chain of length L, and $E_k=\varepsilon_0-2t\cos(ka)$. The final step in Eq. (4.54) involves taking the limit such that the sum on k becomes an integral (i.e. $\sum_k \to \frac{L}{2\pi}\int dk$). One should also keep in mind that the lead's x coordinate must be an integer multiple of the atom-to-atom spacing a (i.e $x=na$). Following a lengthy derivation, Eq. (4.54) may be solved giving

$$\tilde{g}^{(0)}(x,x';E) = \frac{e^{ik_{\rm E}|x-x'|}-e^{ik_{\rm E}|x+x'|}}{ia\sqrt{4t^2-E^2}}, \tag{4.55}$$

where $k_{\rm E}a = \cos^{-1}\left(\left(\varepsilon_0-E_k\right)/2t\right)$ and we assume that $x>x'$.

The lesser Green's function

In k-space the lesser Green's function is also diagonal

$$\tilde{g}_0^<(k,k';E) = i2\pi\delta_{kk'}\sum_k \delta(E-\varepsilon_k)f(E) \tag{4.56}$$

which in configuration space becomes

$$\begin{aligned}
\tilde{g}_0^<(n,n';E) &= i2\pi\sum_k \langle n|k\rangle\langle k|n'\rangle\delta(E-\varepsilon_k)f(E) \\
&= iL\int_{-\pi/a}^{\pi/a} dk\langle n|k\rangle\langle k|n'\rangle\delta(E-\varepsilon_k)f(E) \\
&= i\frac{2}{a}\int_{-\pi}^{\pi} dp\sin(pn)\sin(pn')\delta(E+2t\cos(p))f(-2t\cos(p)) \\
&= i\frac{2}{a}\int_{-\pi}^{\pi} dp\sin(pn)\sin(pn')\delta\left(p-\cos^{-1}\left(-E/2t\right)\right)f(-2t\cos(p)) \\
&= i4f(E)\frac{\sin(k_E an)\sin(k_E an')}{a\sqrt{4t^2-E^2}},
\end{aligned} \tag{4.57}$$

where again we have used that $\langle x|k\rangle = \sqrt{2/L}\sin(kan)$ with a as the 1-D lead's lattice constant and n an integer. Using Eq. (4.50) with Eq. (4.57) we can calculate the charge density as a function of distance in a 1-D lead

$$\begin{aligned}
n(x) &= \frac{-i}{2\pi}\int_{-\infty}^{\infty} dE\tilde{g}^<(na,na;E) \\
&\equiv \frac{1}{\pi}\int_{-2t}^{2t} dE f(E)\frac{1-\cos(2k_E x)}{a\sqrt{4t^2-E^2}},
\end{aligned} \tag{4.58}$$

where

$$\tilde{g}^<(x,x;E) = \tilde{g}_0^<(n,n;E) = i2f(E)\frac{1-\cos(2k_E x)}{a\sqrt{4t^2-E^2}}. \tag{4.59}$$

As shown in Fig. 4.14, at half-filling the density oscillates but is 0.5 for all integer multiples of a. The filling of a 1-D tight-binding lead $\langle n\rangle = \frac{2a}{\pi}k_{\rm F}$, where $k_{\rm F}$ is the lead's Fermi wavevector. At half-filling $2k_{\rm F}=2(\pi/2a)$ and Eq. (4.59) is 0.5 for all integer values of x/a in agreement with the figure.

Connecting the molecule

Finally we have all the parts needed to consider a junction composed of a 1-D chain coupled to a single molecule. In order to simplify our present discussion, we'll focus

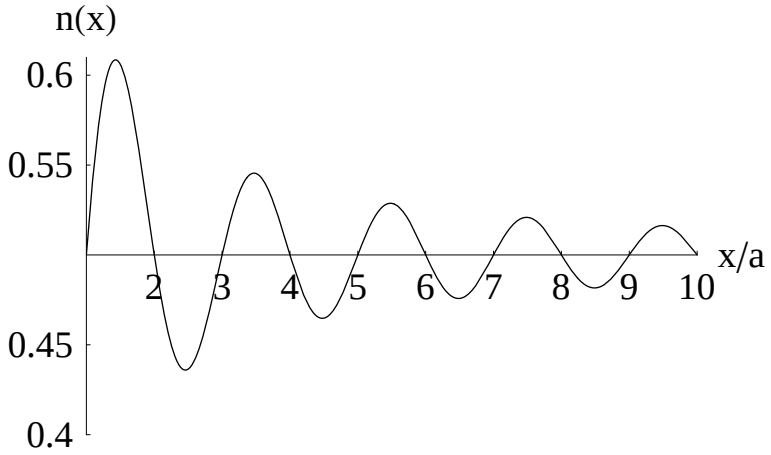

Figure 4.14: The lead charge accumulation for a semi-infinite 1-D lead showing that at half-filling the charge density is zero on each lattice site. The lattice sites are at coordinates corresponding to integer multiples x/a. The inter-chain hopping matrix element t=2eV.

on leads which only couple to a single atomic orbital j of the molecule. In such a junction, Eq. (4.53) becomes

$$\begin{aligned}\tilde{g}^{<}(x,x;E) &= \tilde{g}_0^{<}(x,x';E) + \\ &\quad \tilde{g}_0(x,j;E)\tilde{\Sigma}_{jj}(E)\tilde{g}_0^{<}(j,x;E) + \\ &\quad \tilde{g}_0^{<}(x,j;E)\tilde{\Sigma}_{jj}^{\dagger}(E)\tilde{g}_0^{\dagger}(j,x;E) + \\ &\quad \tilde{g}_0(x,j;E)\tilde{\Sigma}_{jj}^{<}(E)\tilde{g}_0^{\dagger}(j,x;E),\end{aligned} \tag{4.60}$$

where $\tilde{\Sigma}^{<}(E)= H_{\mathrm{T}}G_0^{<}(E)H_{\mathrm{T}}$ and therefore

$$\tilde{\Sigma}_{jj}^{<}(E) = \tilde{t}^2 G_{jj}^{<}(E), \tag{4.61}$$

where $\tilde{t}$ is the hopping matrix element between the site j of the molecule and the end of the lead. Similarly, the retarded self-energy is given by

$$\tilde{\Sigma}_{jj}(E) = \tilde{t}^2 G_{jj}(E). \tag{4.62}$$

Finally, the tunneling self-energy $\Sigma_{\rm T}$ of the molecular Green's function must be consistent with those of the leads, namely

$$[\Sigma_{\rm T}(E)]_{n\sigma,n'\sigma'} = \delta_{nj}\delta_{n'j}\delta_{\sigma\sigma'}\tilde{t}^2\tilde{g}_0(j,j;E) \tag{4.63}$$

and

$$\begin{aligned}[\Sigma^<_{\rm T}(E)]_{n\sigma,n'\sigma'} &= \delta_{nj}\delta_{n'j}\delta_{\sigma\sigma'}\tilde{t}^2\tilde{g}^<_0(j,j;E) \\ &= i2\tilde{t}^2 f(E)\frac{1-\cos(2k_E aj)}{a\sqrt{4t^2-E^2}}.\end{aligned} \tag{4.64}$$

Together Eqs. (4.60)-(4.64) constitute an important theoretical result, since they relate the molecular pole structure of $G(E)$ to the Keldysh Green's function of the lead $\tilde{g}^<(x,x';E)$, which in turn is used to calculate the charge density. In this way a direct link between the molecular state and the charged density of the leads is established.

4.4 Summary

The importance of the lead-molecule interface in molecular electronics cannot be overemphasized. Transport is a property of a molecular junction—molecule plus leads—and as such depends critically on the nature of their coupling. It is only with an accurate model of the lead's electrical response that any meaningful information can be gleaned about the electronic transport through the molecule.

In the first and second sections of this chapter we extended the framework of our many-body theory to include multi-orbital bonding configurations and multi-channel leads, respectively. In molecular junctions where a single-channel lead couples to all orbitals, the phase accumulated by an electron tunneling through the junction is a coherent superposition of the transmission amplitude of all possible junction connectivities. By virtue of the nodal structure of the many-body wavefunction we found that many of these amplitudes cancel, or nearly cancel, strongly suppressing the Coulomb-blockade peaks while leaving the charge state unaffected. When multi-channel leads are coupled to multiple orbitals we discovered that the maxi-

mum number of transport channels is given by the degeneracy of the most relevant molecular orbital, rather than the number of orbitals or lead channels.

For the final topic of this chapter, we derived the lead Green's functions needed to calculate the charge distribution in a macroscopic lead. In a departure from the perspective we have adopted up to this point, the effect of the molecule was included as a self-energy correction to the lead's Green's functions. We investigated a junction composed of a single semi-infinite 1-D quantum chain attached to a single molecule and found that the lead's lesser Green's functions were directly related to the Green's functions of the molecule. This exciting result explicitly shows how the Friedel oscillations in the lead's charge density relate to the molecular spectrum.

CHAPTER 5

Dynamic screening self-energy: Optoelectronic response

In the self-consistent Hartree-Fock approximation for the Coulomb self-energy, discussed in chapter 2, the Coulomb self-energy $\Sigma_{\rm C}$=$\Sigma_{\rm C}^{(0)}$+$\Delta\Sigma_{\rm C}^{\rm HF}$ and the transport is completely elastic (i.e. $\Sigma_{\rm C}^{<}$=0). In bulk metallic systems at low temperatures, however, inelastic electron-electron scattering is the dominant mechanism of decoherence, so it is of fundamental interest to understand inelastic Coulomb interactions in single-molecule junctions (SMJs).

In this chapter we develop a systematic theoretical framework to treat the optoelectronic response of a SMJ far from equilibrium. To that end, we generate a theory to evaluate $\Delta\Sigma_{\rm C}$ in the random-phase (or GW) approximation and investigate the effect of higher-order tunneling corrections to the Coulomb self-energy. The GW approximation is known to provide a realistic description of collective charge excitations, including inelastic electron-electron scattering and the optoelectric response. Our approach includes electron correlations beyond the mean-field level, which is essential for an accurate description of excited states and the highest occupied molecular orbital (HOMO) to lowest unoccupied molecular orbital (LUMO) gap. As a first application of our theory, we have obtained results for rectification and electroabsorption in an asymmetric SMJ, indicating that this system is promising for further photovoltaic studies.

5.1 Theoretical framework

In general, the Coulomb self-energy matrix $\Sigma_{\rm C} = \Sigma_{\rm C}^{(0)} + \Delta\Sigma_{\rm C}$, where $\Delta\Sigma_{\rm C}$ describes the change of the Coulomb self-energy due to lead-molecule coherence emerging at temperatures $k_BT \lesssim {\rm Tr}\{\Gamma^\alpha\}$. Using this decomposition of the Coulomb self-energy,

the junction Green's function can be written as a molecular Dyson's equation

$$G^{-1}(E) = G^{-1}_{\rm mol}(E) - \Sigma_{\rm T} - \Delta\Sigma_{\rm C}, \tag{5.1}$$

where G is the Green's function of the molecular junction, $G_{\rm mol}$ is the molecular Green's function taken in the sequential tunneling limit, and the self-energy terms $\Sigma_{\rm T} + \Delta\Sigma_{\rm C}$ describe the effects of finite tunneling width. Here we point out that $\Delta\Sigma_{\rm C}$—unlike $\Sigma^{(0)}_{\rm C}$—can be evaluated perturbatively using diagrammatic techniques on the Keldysh time-contour (see Sec. 1.3.3). Such a perturbative approach is valid, in principle, at temperatures/bias voltages satisfying $\max\{T, eV/k_B\} > T_K$, where T_K is the Kondo temperature[151]—or when there is no unpaired electron on the molecule (such as within the HOMO-LUMO gap of conjugated organic molecules).

As was discussed in chapter 2, a subtlety of our perturbative approach is that the diagrams determining $\Delta\Sigma_{\rm C}$, which are typically formulated [124] in terms of the Green's functions of the noninteracting system, are instead calculated by reformulating the terms in the perturbative expansion in terms of the full Green's function $G(E)$ via appropriate resummations. This procedure is in general nontrivial. However, as we showed in Sec. 2.1.4 the use of the interacting Green's functions G and $G_{\rm mol}$ in the evaluation of the Hartree self-energy is clearly justified on physical grounds, since this yields the classical electrostatic potential due to the actual nonequilibrium charge distribution on the molecule. The direct (Hartree) and exchange (Fock) contributions to $\Delta\Sigma_{\rm C}$ must be treated on an equal footing in order to cancel the unphysical self-interaction, justifying the use of the same interacting Green's functions in the evaluation of the exchange self-energy.

Higher-order self-energy diagrams (e.g., GW correction [185]) can be included in a similar fashion and are discussed in the next section. Treatment of $\Delta\Sigma_{\rm C}$ at the level of the GW approximation allows for the inclusion of inelastic processes due to electron-electron interactions, the dominant mechanism of decoherence in bulk systems at low temperatures, and allows us to investigate the optical response of SMJs.

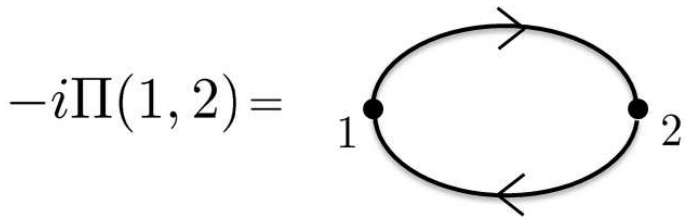

Figure 5.1: Diagrammatic representation of the polarizability matrix.

5.1.1 The GW Approximation

In the GW approximation, the bare interaction matrix U is replaced by the screened interaction $\tilde{U}$ that obeys Dyson's equation on the Keldysh time contour

$$\tilde{U}(\tau_1, \tau_2) = U\delta(\tau_1 - \tau_2) + \int \tau_3 U\Pi(\tau_1, \tau_3)\tilde{U}(\tau_3, \tau_2). \tag{5.2}$$

The retarded interaction in the frequency domain is

$$\tilde{U}(\omega) = \left[\mathbf{1} - U\Pi(\omega)\right]^{-1} U. \tag{5.3}$$

The polarizability matrix Π can be found by evaluating the diagram shown in Fig. 5.1 using the Feynman rules discussed in Sec. 1.3.2, where on the Keldysh contour

$$\Pi(1,2) = -iG(1,2)G(2,1). \tag{5.4}$$

Using Langreth's rules (Table 1.1) to transform Eq. (5.4) into the time domain and then taking the Fourier transform of the result we find

$$\Pi^r_{nm}(\omega) = -i\sum_\sigma \int_{-\infty}^{\infty} \frac{dE}{2\pi} \left[G^r_{n\sigma,m\sigma}(E)G^<_{m\sigma,n\sigma}(E-\omega) + G^<_{n\sigma,m\sigma}(E)G^a_{m\sigma,n\sigma}(E-\omega)\right]. \tag{5.5}$$

The 'lesser' screened interaction obeys a Keldysh equation

$$\tilde{U}^<(\omega) = \tilde{U}(\omega)\Pi(\omega)\tilde{U}^a(\omega) \tag{5.6}$$

where $\tilde{U}^a_{nm}(\omega)$=$\tilde{U}_{mn}(-\omega)$ and

$$\Pi^<_{nm}(\omega) = -i\sum_\sigma \int_{-\infty}^{\infty} \frac{dE}{2\pi} G^<_{n\sigma,m\sigma}(E)G^>_{m\sigma,n\sigma}(E-\omega). \tag{5.7}$$

The lesser Coulomb self-energy in the GW approximation can be found using Eq. (1.64) with $U^< \to \tilde{U}^<$ such that the exchange self-energy becomes

$$[\Sigma_{\rm C}^<(E)]_{n\sigma,m\sigma} = i(1-\delta_{nm})\int_{-\infty}^{\infty}\frac{d\omega}{2\pi}\tilde{U}^<_{nm}(\omega)G^<_{n\sigma,m\sigma}(E-\omega). \tag{5.8}$$

The inelastic scattering rate is determined by $\Gamma^{\rm in}{=}i(\Sigma_{\rm C}{-}\Sigma_{\rm C}^\dagger){=}i(\Sigma_{\rm C}^>{-}\Sigma_{\rm C}^<)$. Evaluating the scattering rate when the Fermi energy μ is far from a transmission resonance ε we find

$$\Gamma^{\rm in}(\mu) \sim \frac{(k_{\rm B}T)^2U^2\Gamma^3}{4\pi^2(\mu-\varepsilon)^6}, \tag{5.9}$$

while on resonance $\Gamma^{\rm in} \sim (k_{\rm B}T)^2/\Gamma$. The smallness of these terms at room temperature supports our use of a perturbative method in evaluating $\Delta\Sigma_{\rm C}$.

5.1.2 Electroabsorption

The linear optical response of the junction is determined by the dielectric matrix

$$\varepsilon(\omega) = \mathbf{1} - \Pi(\omega)U, \tag{5.10}$$

where the polarizability matrix, including the effects of lead-molecule coupling and finite DC bias, is given by Eq. (5.5). In non-magnetic systems such as those considered here, the real part of ε is related to the index of refraction while the imaginary part is related to the optical absorption. This formalism can be used to determine the photovoltaic effect in a SMJ by calculating the absorption spectrum of the junction as a function of the DC bias (electroabsorption). The maximum reverse bias for which absorption occurs (over the frequency range of interest) is the open-circuit photovoltage of the junction. Similarly, the photoemission spectrum in translationally-invariant bulk systems [104] is determined by $\Pi^<(\omega)$.

5.2 Single-molecule photovoltaics

Organic π-conjugated molecular and polymeric systems are under extensive investigation as active components of various kinds of optoelectronic devices. Research

on large area flat-panel displays has already led to huge success and commercialization. The fundamental physical process in such light-emitting devices is field-driven electron-hole recombination leading to the emission of light. The opposite process of photoinduced charge generation lies at the heart of solar energy conversion, and organic photovoltaics has been a highly active research area in recent years.

In spite of the intense research in many laboratories over the past fifteen years, the maximum power-conversion efficiency reached to date with organic and polymeric solar cells under AM1.5 radiation remains $\sim 5\%$ [123, 158, 113, 93]. This limited efficiency has prevented commercialization of organic solar cells. The low power-conversion efficiencies are due to a variety of factors, including (i) large exciton binding energy in the organics (~ 0.5 eV), (ii) loss of photogenerated carriers due to geminate recombination, and (iii) low exciton and carrier diffusion lengths. Current emphasis in this area is on so-called bulk heterojunction materials, with donor and acceptor molecules and polymers. These systems have shown evidence for charge-transfer states at the interface of the donor and acceptor which prevents efficient charge-transfer [20, 68, 26, 50].

In order to overcome the above difficulties, we propose to investigate a new concept, involving single-molecule photovoltaics. In collaboration with the experimental nanotechnology group at Arizona State University led by Professor Nongjian Tao, our proposed device is simply an organic molecule between two electrodes as shown in Fig. 5.2. The molecule has a "donor end" and an "acceptor end," which are constructed by chemical substitution, and can be (somewhat simplistically) thought of as a molecular p-n junction. The aim of this design is to overcome the difficulties associated with small exciton and carrier mobilities, and to be able to influence charge separation by proper chemical substitution. Thus for example, in molecules with sufficiently large ground state dipole moments, it is expected that the tendency toward charge separation is even larger in the photoexcited state.

We recognize that the absorption spectrum of a finite molecule, even when broadened due to coupling with metal electrodes, may have less than optimal overlap with the solar power spectrum which reaches a broad maximum in the near-infrared

wavelength region. We emphasize, however, that our current goal is to demonstrate a proof-of-concept in single-molecule junctions, following which further chemical modifications of the molecules can be implemented. Junctions containing several different molecules in parallel (or in series [92]) can then be designed provide an optimal absorption spectrum. The photovoltaic (PV) studies at the single-molecule level will allow us to understand directed charge and energy transfer and provide fundamental insight on the photovoltaic effect in organic semiconducting materials [206, 92].

5.2.1 Molecular diodes

Molecular diodes are so-called because they contain two blocks, a donor and an acceptor block, resembling a p-n junction [133, 82, 110, 141] (see Fig. 5.2). Previous studies of the effects of chemical modification of phenyl rings on charge transport in a SMJ found that by inducing an intrinsic electric dipole in a molecule, two molecules with similar structure can have drastically different transport properties [48]. As is shown in Fig. 5.2a, a SMJ consisting of a dipyrimidinyl-diphenyl diblock molecule shows significant rectification at high biases. Such results are interesting because the electron-rich and electron-deficient areas in the molecule are analogous to the space charge region in a p-n junction, and also have similar effects on the transport behavior. Diodes are extremely important in bulk semiconducting devices, as the basic structure of this system is used in both Light-Emitting-Diodes and photovoltaic cells.

The optoelectronic mechanisms in a single-molecule diode should be completely different than the mechanisms in bulk semiconductors, and therefore constitute an extremely interesting area to study. Currently, Tao's group is developing a Mechanically Controlled Break Junction (MCBJ) system integrated with a Renishaw μRaman microscope for studying the optoelectronic properties of SMJs. Using this system they have already demonstrated that it is possible to measure photoemission from a molecular junction using a Photomultiplier Tube (PMT) as in Fig. 5.2b. Furthermore, with the Raman system it will be possible to focus a laser on the

molecular junction to measure the induced photocurrent. With a tunable laser system it should be possible to study the excitation dependence of the photoinduced current. Such an experiment can give precise information on many-body effects, including exciton binding, and their role in photovoltaics.

Although it is apparent that this system provides an optical pathway capable of extracting, and therefore introducing, photons into a molecular junction, there are several potential difficulties in leveraging this system for studying the photovoltaic properties of a single molecule junction. For instance, the plasmon modes in the gold electrodes used in most SMJ studies may quench the excited state of the molecule via energy transfer before the charge carriers are separated by the built-in field of the molecule [74]. To overcome this issue, transparent electrodes can be utilized [34]. Indium-Tin-Oxide (ITO) electrodes are both transparent and conductive, and are capable of binding to carboxylic acid groups on a molecule; by using this scheme in an AFM system it was possible to measure the conductance of single molecule junctions.

This material can be incorporated with the break junction system currently under development coupled to an optical pathway as a way of alleviating the issue of excited state quenching. Another major issue with performing photovoltaic measurements on the diode molecule shown in Fig. 5.2a is that the bandgap of this molecule is approximately 3.6eV, as determined from absorbance spectroscopy. This bandgap requires the use of a high-energy laser to create an excited state in the molecule and will be difficult to use with the current system. As such, the molecule in Fig. 5.2d, which has a bandgap of 1.6eV, will also be studied. This bandgap is in the near-IR region of the electromagnetic spectrum and will allow us to study photovoltaic effects with the MCBJ system currently under development. Finally, with a high intensity light source focused on the gap region, the temperature increase may reduce the stability of the molecular junction, and this effect will have to be minimized by controlling exposure times and light intensity.

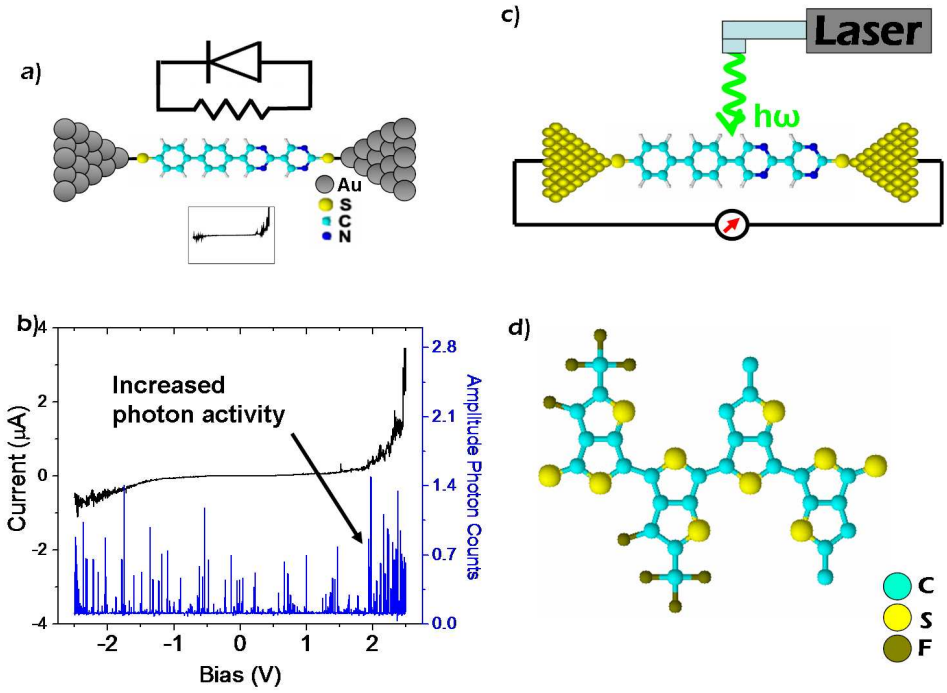

Figure 5.2: Single-molecule photovoltaics. a) Diode behavior can be achieved in an asymmetric dipyrimidinyl-diphenyl diblock molecule composed of a donor block and an acceptor block [133]. Here the light blue atoms are Carbon, dark blue atoms are Nitrogen, and large yellow atoms are Sulfur. b) Under high bias conditions increased photon activity can be observed in the forward bias direction. (Preliminary results courtesy of NJ Tao.) c) Schematic of the proposed photovoltaic experiment with the diode molecule from (a). d) Structure of an additional molecule for single molecule optoelectronic studies, where the yellow-grey atoms are Fluorine.

5.2.2 Simulated response

The measured current-voltage (I-V) spectra of tetraphenyl and dipyrimidinyl-diphenyl-based single-molecule heterojunctions are shown in the central portion of Fig. 5.4. The substitution of four carbon atoms in the tetraphenyl with four nitrogen atoms gives rise to a rectification in the current, a result of the induced molecular dipole caused by the charge imbalance between the donor and acceptor blocks.

The junction's electrical response, shown in Fig. 5.4, was calculated using a simplified four state molecular model (see Fig. 5.3) in which we include the LUMO and HOMO of the donor and acceptor blocks. At low-bias and away from any

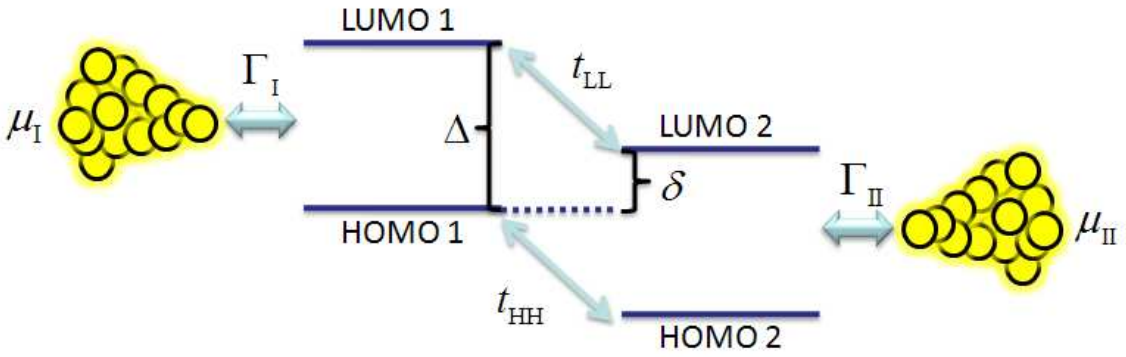

Figure 5.3: A four-state molecular model representing the HOMO and LUMO levels of the donor and acceptor blocks of tetraphenyl and dipyrimidinyl-diphenyl. Δ is the HOMO-LUMO gap. δ is the offset between the donor and acceptor which will give rise to rectification. $\Gamma_{\rm I}$ and $\Gamma_{\rm II}$ are the energy-independent tunneling widths characterizing the lead-molecule coupling and $\mu_{\rm I}$ and $\mu_{\rm II}$ are those lead's chemical potentials. $t_{\rm HH}$ and $t_{\rm LL}$ are the hopping matrix elements between HOMO and LUMO levels, respectively.

resonances the current is linearly related to the bias voltage by the conductance G. From the current formula (cf. Sec. 2.1.5) we can determine the approximate values of $\Gamma_{\rm I}$ and $\Gamma_{\rm II}$. t=$t_{\rm HH}$=$t_{\rm LL}$ was taken to be 1.5eV. The effective interaction energies U were chosen to be in accordance with the measured HOMO-LUMO gap of $\approx$3.6eV and the measured $\approx$1eV exciton binding energy in these molecules. The final two parameters, the mismatch between the HOMO-LUMO gap and the leads' chemical potentials and δ, were adjusted until the simulated I-V spectra closely matched the experimental spectra. The resulting spectra are shown in the bottom portion of Fig. 5.4.

The degree of charge polarization between the donor and acceptor portions of the molecule is related to the dielectric matrix ϵ by Eq. (5.10). In non-magnetic materials such as those considered here, the real part of ϵ is related to the index of refraction while the imaginary part is related to the optical absorption. In a PV experiment, light with energy $\hbar\omega$ would induce charge separation and generate a photovoltage across the junction. By considering this scenario in reverse and calculating the optical absorption as a function of bias voltage one can reconstruct

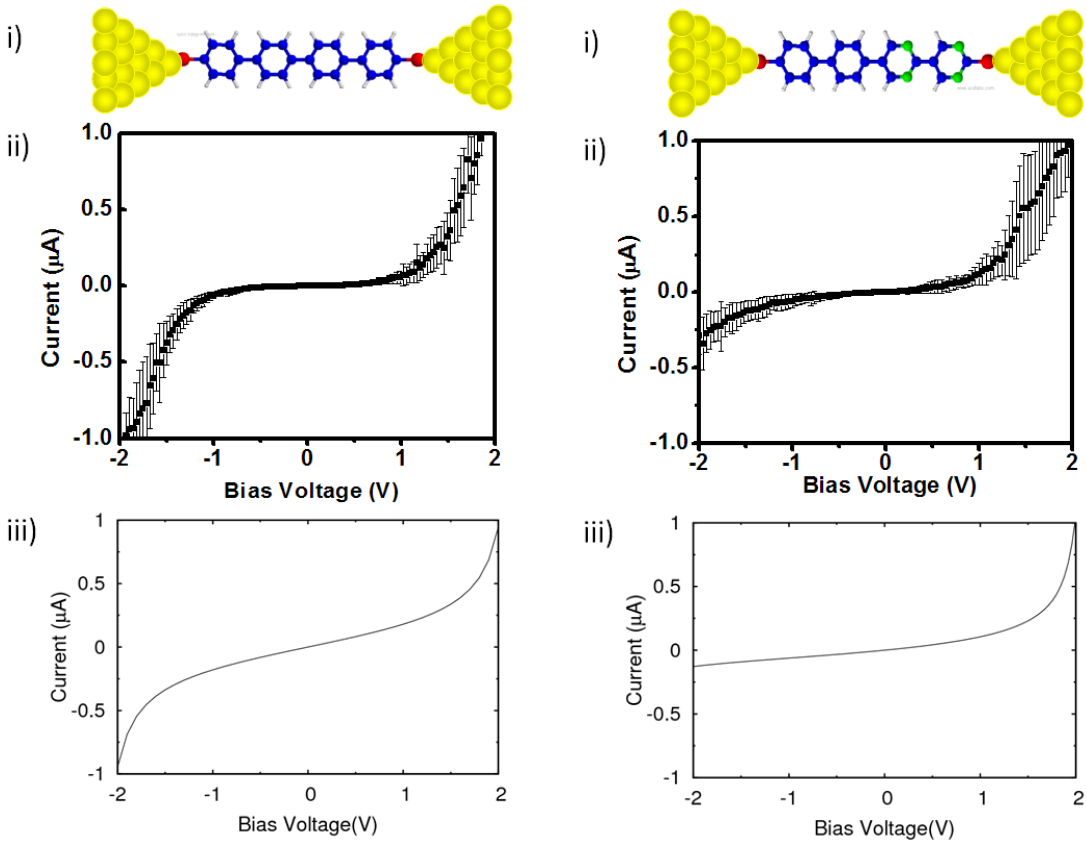

(a) tetraphenyl (b) dipyrimidinyl-diphenyl

Figure 5.4: The I-V spectra for two single-molecule junctions. i) Schematics of each molecule where red spheres represent Sulfur atoms, green spheres are Nitrogen atoms and blue spheres are Carbon atoms. Each molecule is ≈10Å in length. ii) Measured I-V spectrum. iii) Calculated I-V spectrum. Measured data are from Ref. 47.

the open-circuit photovoltage for a given spectrum of irradiation.

The simulated optical response of these two molecules is shown in Fig. 5.5. From the figure it is clear that the large 2V bias has little effect on the absorption peak positions and heights of tetraphenyl. This means that illumination will not induce an appreciable photovoltage in this molecule, a result which we could have predicted from its lack of inbuilt field and rectification. In contrast, the absorption spectrum of dipyrimidinyl-diphenyl shows a strong dependence on bias voltage, indicating that this is a promising system for investigating photovoltaic effects.

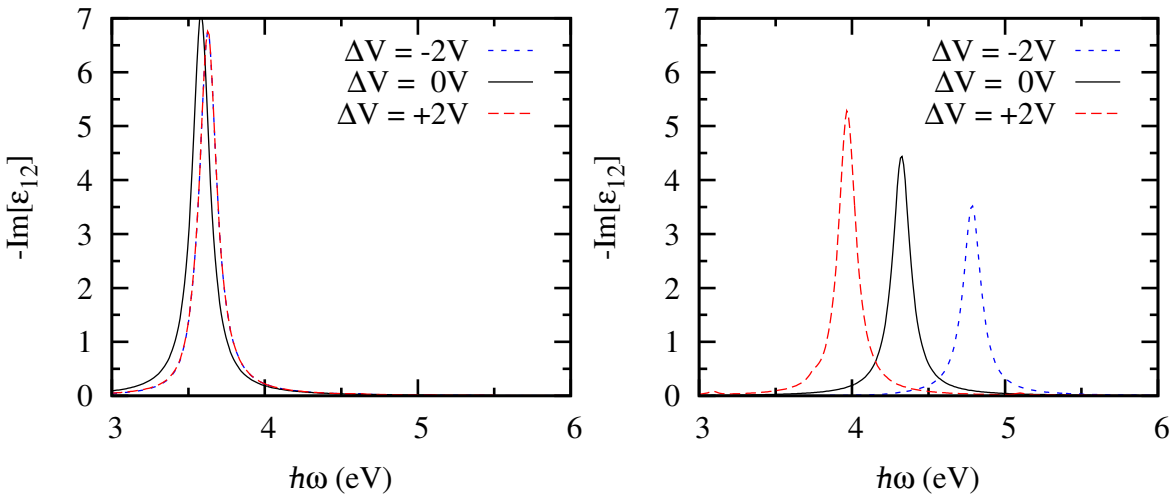

(a) tetraphenyl (b) dipyrimidinyl-diphenyl

Figure 5.5: The imaginary portion of ϵ as a function of bias voltage ΔV. $\mathrm{Im}\{\varepsilon\}$ is related to the optical absorption. a) The symmetric tetraphenyl molecule shows very little shift even with $\pm$2V bias applied indicating that there is little to no charge separation. b) The dipyrimidinyl-diphenyl molecule's optical absorption peak position and height shows a strong dependence on bias voltage showing a pronounced red-shift with increased forward bias.

5.3 Summary

In this chapter, we extended our NEGF many-body theory to include optical response, thereby allowing us to calculate the dielectric matrix far out of equilibrium. We studied two similar molecules: tetraphenyl and dipyrimidinyl-diphenyl. The latter differs in that four carbon atoms are replaced with nitrogen atoms, inducing an inbuilt molecular dipole moment. Using a simple four-orbital model we were able to fit all parameters and reconstruct the measured nonlinear I-V curves. For each molecular model, we then calculated the optical response and found a negligible electroabsorption for tetraphenyl and a very large electroabsorption for dipyrimidinyl-diphenyl, indicating that this system is a good candidate for investigating photovoltaic effects in single-molecule junctions.

APPENDIX A

Molecular resonance decomposition of transmission channels

In order to understand how transport in a SMJ is determined by the chemical properties of the molecule, it would be desirable to express the transmission eigenchannels in terms of molecular resonances [77, 173]. The transmission eigenvalues τ_n and eigenvectors $|n\rangle$ are solutions of the equation

$$T|n\rangle = \tau_n|n\rangle, \tag{A.1}$$

where T is the transmission matrix given by Eq. (2.41). By definition, $|n\rangle$ is a linear combination of the atomic orbitals of the molecule. In an effective single-particle model [77], $|n\rangle$ may also be expressed as a linear combination of *molecular orbitals* $|\phi_j\rangle$

$$|n\rangle = \sum_j \alpha_n^j |\phi_j\rangle. \tag{A.2}$$

Here $|\alpha_n^j|^2$ can be identified as the contribution of the jth molecular orbital to the nth transmission channel [77], which can be conveniently expressed in terms of the projection operator $\hat{P}_j = |\phi_j\rangle\langle\phi_j|$ as $|\alpha_n^j|^2 = \langle n|\hat{P}_j|n\rangle$.

In the many-body problem, there is no orthonormal set of "molecular orbitals"; rather each molecular resonance of energy $E_{\nu'} - E_\nu$ corresponds to a transition $\nu \to \nu'$ between an N-body and an $(N+1)$-body molecular eigenstate [see Eqs. (2.27) and (2.29)]. The projection operator onto a molecular resonance is

$$\hat{P}_{\nu\to\nu'} \equiv \frac{C(\nu,\nu')}{\mathrm{Tr}\{C(\nu,\nu')\}}, \tag{A.3}$$

where $C(\nu,\nu')$ is the many-body matrix element given by Eq. (2.27). The absolute square projection of the nth transmission eigenvector onto the resonance $\nu \to \nu'$ is given by

$$|\alpha_n^{\nu\to\nu'}|^2 = \langle n|\hat{P}_{\nu\to\nu'}|n\rangle. \tag{A.4}$$

A *necessary condition* to identify an eigenchannel $|n\rangle$ with transmission through a particular molecular resonance is $|\alpha_n^{\nu\to\nu'}|^2 \approx 1$.

The above procedure is in principle straightforward to implement in an effective single-particle model based on density functional theory (DFT)[77]. However, in practice, an "extended molecule" must be used in DFT calculations to account for charge transfer between the molecule and electrodes. This is because current implementations of DFT fail to account for the *particle aspect* of the electron [188, 97, 136, 63], i.e., the strong tendency for the electric charge on the molecule within the junction to be quantized in integer multiples of the electron charge e. Analyzing transport in terms of extended molecular orbitals has unfortunately proven problematic. For example, the resonances of the extended molecule in Ref. 77 apparently accounted for less than 9% of the current through the junction.

Since charging effects in SMJs are well-described in our many-body theory [23], there is no need to utilize an "extended molecule," so the projections of the transmission eigenvectors onto the molecular resonances can be determined directly from A.4.

A.1 Benzene resonances

The neutral ground state of benzene is nondegenerate, while the HOMO and LUMO resonances are both doubly degenerate due to the (six-fold) rotational symmetry of the molecule. To be consistent with the discussion of Ref. 90, the additional two-fold spin degeneracy of each resonance is considered implicit.

We define the following projection operators:

$$\hat{P}_{\mathrm{HOMO}} \equiv \sum_{\nu\in 0_5} \hat{P}_{\nu\to 0_6}, \tag{A.5}$$

$$\hat{P}_{\mathrm{LUMO}} \equiv \sum_{\nu'\in 0_7} \hat{P}_{0_6\to\nu'}, \tag{A.6}$$

$$\hat{P}_{\perp} \equiv \mathbf{1} - \hat{P}_{\mathrm{HOMO}} - \hat{P}_{\mathrm{LUMO}}, \tag{A.7}$$

where 0_N is the ground state with N π-electrons and $\mathbf{1}$ is the six-dimensional unit

matrix in the space of π-orbitals. $\hat{P}_{\mathrm{HOMO}}$ and $\hat{P}_{\mathrm{LUMO}}$ are projection operators onto the two-dimensional subspaces spanned by the HOMO and LUMO resonances, respectively. Equations (A.5–A.7) define a complete, orthogonal set of projection operators in six-dimensions with the properties

$$\sum_j \hat{P}_j = \mathbf{1}, \tag{A.8}$$

$$\hat{P}_i \hat{P}_j = \hat{P}_i \delta_{ij}. \tag{A.9}$$

In particular, Eq. (A.9) implies that the HOMO and LUMO subspaces of benzene are orthogonal. The absolute square of the projection of the n$^{\mathrm{th}}$ transmission eigenvector onto the subspace spanned by $\hat{P}_j$ is

$$|\alpha_n^j|^2 = \langle n|\hat{P}_j|n\rangle. \tag{A.10}$$

These coefficients satisfy the condition

$$\sum_j |\alpha_n^j|^2 = 1, \tag{A.11}$$

where the sum runs over j=HOMO, LUMO, $\perp$.

Figure A.1 shows the mean-square projections $\langle|\alpha_n^j|^2\rangle$ of the transmission eigenvectors onto (a) the benzene HOMO resonance; (b) the benzene LUMO resonance; and (c) the two-dimensional subspace orthogonal to both the HOMO and LUMO resonances, as a function of electrode chemical potential for the same ensemble of Pt–benzene–Pt junctions discussed in Sec. 4.2.2. We find that the mean-square projections of the first and second transmission channels onto the benzene HOMO resonance are 87% and 71%, respectively, confirming the conclusion that these eigenchannels correspond to tunneling primarily through the HOMO resonance.

Midway between the HOMO and LUMO resonances at $\mu = \mu_0$, the first two transmission channels have mean-square projections of ≈ 0.5 onto both the HOMO and LUMO resonances, consistent with the expectation that the HOMO and LUMO resonances should contribute equally to transmission. The remaining channels do not have negligible overlap with the HOMO resonance, but instead

cluster around $\langle|\alpha_n^{\rm HOMO}|^2\rangle \sim 0.3$. The transmission channels with $\langle\tau_n\rangle \ll 1$ correspond to contributions from several far off-resonant poles, each of which has some overlap with the HOMO resonance due to the overcompleteness of the projectors $\hat{P}_{\nu\to\nu'}$ [1].

They are essentially random unit vectors in the six-dimensional space of benzene π-orbitals, whose mean-square overlap with the two-dimensional HOMO subspace should be $\langle|\alpha_n^{\rm HOMO}|^2\rangle = 2/6 = 1/3$.

The first two transmission channels only have an appreciable overlap with the subspace orthogonal to the HOMO and LUMO resonances in the vicinity of a pronounced dip in the transmission spectrum at $\mu - \mu_0 \approx \pm 3.5$eV.

A.2 Butadiene resonances

The neutral ground state of butadiene is nondegenerate, and the HOMO and LUMO resonances have no orbital degeneracy. The projection operators onto the HOMO and LUMO resonances of butadiene are

$$\hat{P}_{\rm HOMO} \equiv \hat{P}_{0_3\to 0_4}, \tag{A.12}$$

$$\hat{P}_{\rm LUMO} \equiv \hat{P}_{0_4\to 0_5}, \tag{A.13}$$

respectively. A.2 shows the mean-square projections of the transmission eigenvectors onto the nondegenerate butadiene HOMO and LUMO resonances as a function of electrode chemical potential for the same ensemble of Pt–butadiene–Pt junctions discussed in Sec. (4.2.3). In this case, the single dominant channel has a strong overlap with the nondegenerate HOMO resonance: $\langle|\alpha_1^{\rm HOMO}|^2\rangle = 0.80$ when averaged over the range -1.70eV$\leq \mu_{\rm Pt} - \mu_0 \leq$ -0.89eV, while the far off-resonant channels with $\langle\tau_n\rangle \ll 1$ have $\langle|\alpha_n^{\rm HOMO}|^2\rangle \sim 1/4$, as expected based on the arguments given above.

[1] Note that there are 600 poles of the molecular Green's function for a neutral benzene molecule, consistent with particle-number and S_z selection rules (although some of these transitions are forbidden by the S^2 selection rule), vastly more than the six atomic orbitals in the basis set.

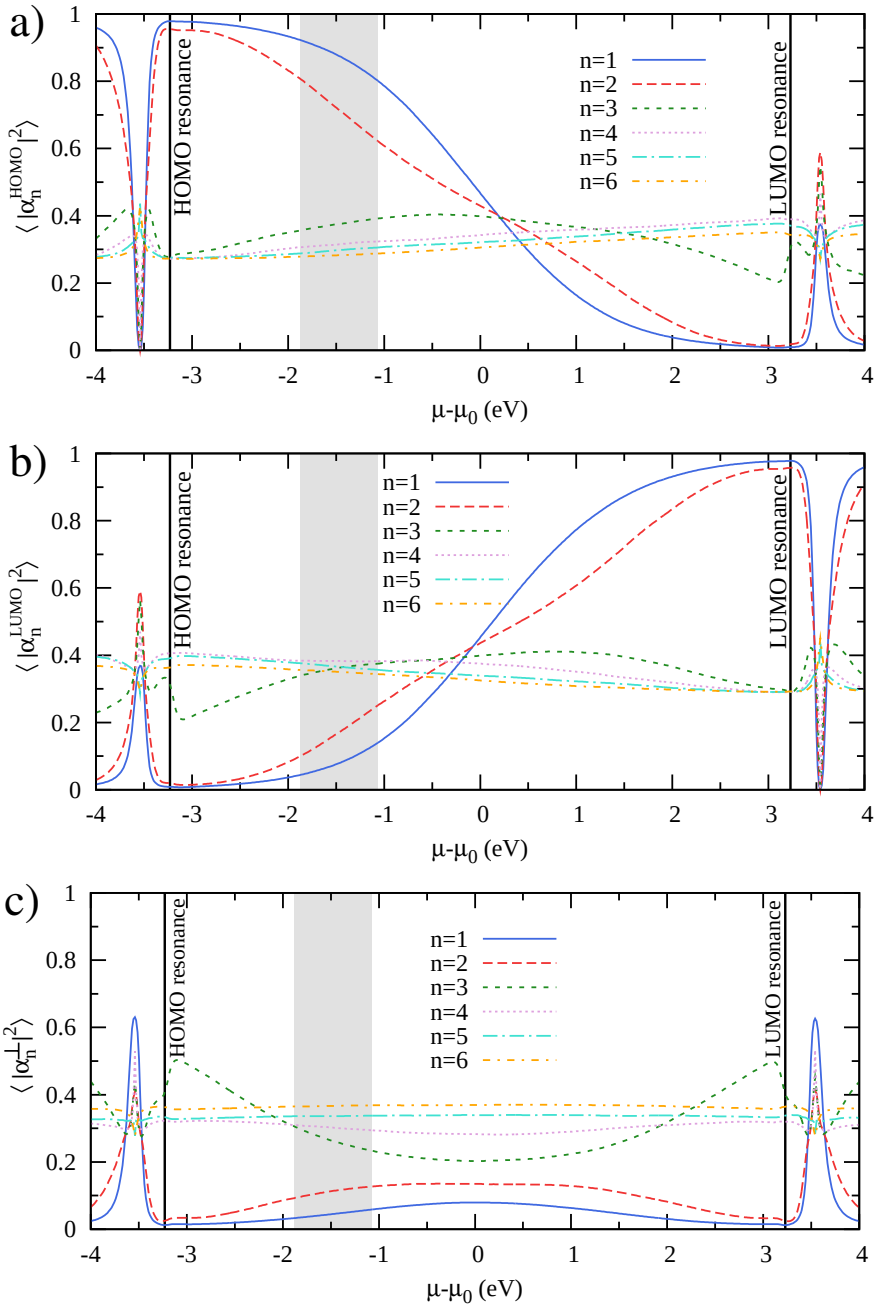

Figure A.1: The mean-square projections $|\alpha_n^j|^2 = \langle n|\hat{P}_j|n\rangle$ of the transmission eigenvectors onto the two-dimensional subspaces (a) spanned by the benzene HOMO resonance; (b) spanned by the benzene LUMO resonance; and (c) orthogonal to the HOMO and LUMO subspaces, for the same ensemble of Pt–benzene–Pt junctions discussed in Sec. 4.2.2. For the range of possible chemical potentials of Pt electrodes, -1.88eV$\leq \mu_{\rm Pt} - \mu_0 \leq$ -1.07eV indicated by the grey boxes in each subfigure, the first two channels have very strong overlap with the HOMO resonance: 87% and 71%, respectively.

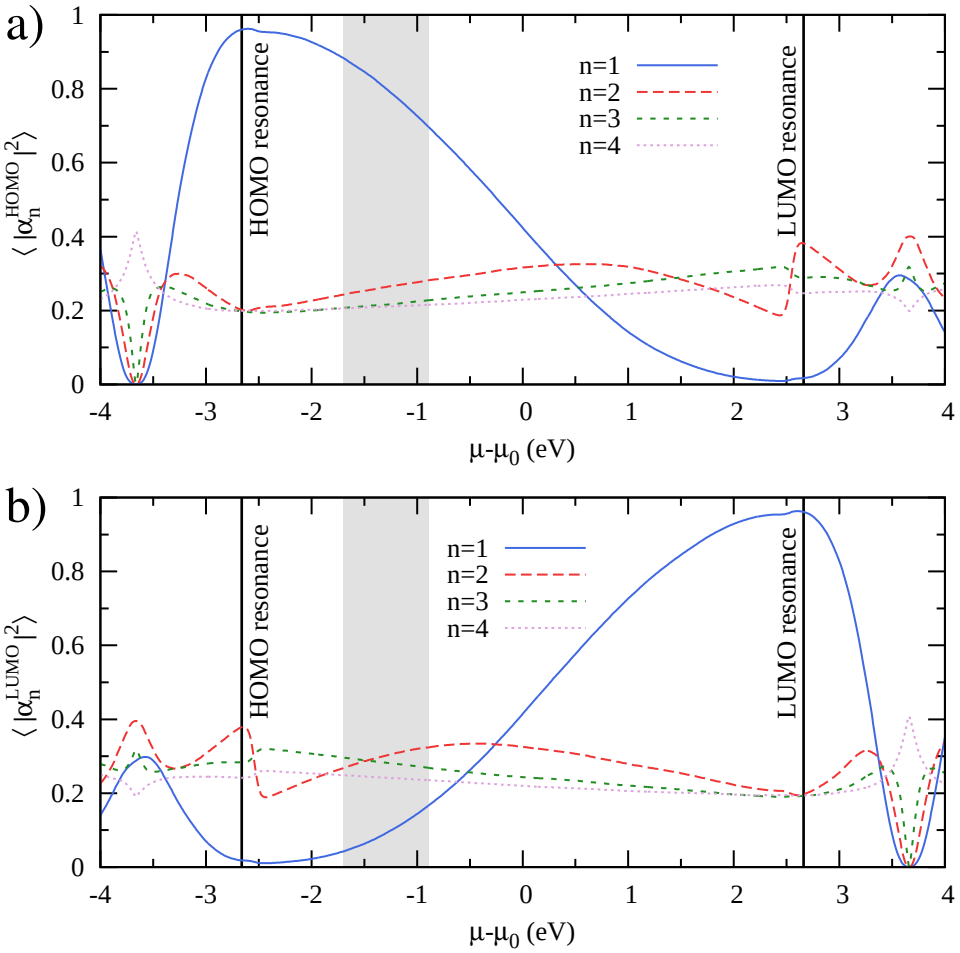

Figure A.2: The mean-square projections $|\alpha_n^j|^2 = \langle n|\hat{P}_j|n\rangle$ of the transmission eigenvectors onto (a) the butadiene HOMO resonance; and (b) the butadiene LUMO resonance, for the same ensemble of Pt–butadiene–Pt junctions discussed in Sec. 4.2.3. The dominant channel has a strong overlap (80% mean-square) with the HOMO resonance for the range of possible chemical potentials of Pt electrodes, -1.70eV$\leq \mu_{\rm Pt} - \mu_0 \leq$ -0.89eV, indicated on each subfigure by a solid grey box.

REFERENCES

[1] A.A. Abrikosov, L. G. and I. Dzyaloshinski (1975). *Methods of Quantum Field Theory in Statistical Physics*. Dover, Mineola, New York.

[2] Agraït, N., A. Levy Yeyati, and J. M. van Ruitenbeek (2003, and references therein). Quantum properties of atomic-sized conductors. *Phys. Rep.*, **377**, pp. 81–279.

[3] Agraït, N., C. Untiedt, G. Rubio-Bollinger, and S. Vieira (2002). Onset of Energy Dissipation in Ballistic Atomic Wires. *Phys. Rev. Lett.*, **88**, p. 216803.

[4] Aleiner, I. L., P. W. Brouwer, and L. I. Glazman (2002). Quantum effects in Coulomb blockade. *Phys. Rep.*, **358**(5-6), pp. 309–440.

[5] Alhassid, Y. (2000). The statistical theory of quantum dots. *Rev. Mod. Phys.*, **72**(4), pp. 895–968.

[6] Anderson, P. W. (1961). Localized Magnetic States in Metals. *Phys. Rev.*, **124**(1), pp. 41–53. doi:10.1103/PhysRev.124.41.

[7] Anderson, P. W. (1967). Infrared Catastrophe in Fermi Gases with Local Scattering Potentials. *Phys. Rev. Lett.*, **18**(24), pp. 1049–1051. doi:10.1103/PhysRevLett.18.1049.

[8] Andres, R. P., T. Bein, M. Dorogi, S. Feng, J. I. Henderson, C. P. Kubiak, W. Mahoney, R. G. Osifchin, and R. Reifenberger (1996). "Coulomb Staircase" at Room Temperature in a Self-Assembled Molecular Nanostructure. *Science*, **272**, pp. 1323–1325.

[9] Ashcroft, N. W. and N. D. Mermin (1976). *Solid State Physics*. Brooks/Cole - Thomson Learning.

[10] Averin, D. V. and Y. V. Nazarov (1990). Virtual Electron Diffusion during Quantum Tunneling of the Electric Charge. *Phys. Rev. Lett.*, **65**, p. 2446.

[11] Avinun-Kalish, M., M. Heiblum, O. Zarchin, D. Mahalu, and V. Umansky (2005). Crossover from /'mesoscopic/' to /'universal/' phase for electron transmission in quantum dots. *Nature*, **436**(7050), pp. 529–533. ISSN 0028-0836.

[12] Aviram, A. and M. A. Ratner (1974). *Chem. Phys. Lett.*, **29**, p. 277.

[13] Bachtold, A., C. Strunk, J.-P. Salvetat, J.-M. Bonard, L. Forró, T. Nussbaumer, and C. Schönenberger (1999). Aharonov-Bohm oscillations in carbon nanotubes. *nat*, **397**, pp. 673–675.

[14] Baeriswyl, D., D. K. Campbell, and S. Mazumdar (1992). In Kiess, H. (ed.) *Conjugated Conducting Polymers*. Springer-Verlag, Berlin.

[15] Baheti, K., J. Malen, P. Doak, P. Reddy, S.-Y. Jang, T. Tilley, A. Majumdar, and R. Segalman (2008). Probing the Chemistry of Molecular Heterojunctions Using Thermoelectricity. *Nano Letters*, **8**, pp. 715–719.

[16] Barr, J. D., J. P. Bergfield, and C. A. Stafford (????). unpublished.

[17] Beenakker, C. W. J. (1991). Theory of Coulomb-blockade oscillations in the conductance of a quantum dot. *Phys. Rev. B*, **44**, pp. 1646–1656.

[18] Begemann, G., D. Darau, A. Donarini, and M. Grifoni (2008). Symmetry fingerprints of a benzene single-electron transistor: Interplay between Coulomb interaction and orbital symmetry. *Phys. Rev. B*, **77**, p. 201406.

[19] Bell, L. E. (2008). Cooling, Heating, Generating Power, and Recovering Waste Heat with Thermoelectric Systems. *Science*, **321**(5895), pp. 1457–1461.

[20] Benson-Smith, J. J., L. Goris, K. Vandewal, K. Haenen, J. V. Manca, D. Vanderzande, D. D. C. Bradley, and J. Nelson (2007). Formation of a ground-state charge-transfer complex in Polyfluorene/[6,6]-Phenyl-C_{61} butyric acid methyl ester (PCBM) blend films and its role in the function of polymer/PCBM solar cells. *Adv. Funct. Mater.*, **17**, pp. 451–457.

[21] Bergfield, J. P., P. Jacquod, and C. A. Stafford (2010). Coherent destruction of Coulomb blockade peaks in molecular junctions. *Phys. Rev. B*, **82**(20), p. 205405.

[22] Bergfield, J. P., M. A. Solis, and C. A. Stafford (2010). Giant Thermoelectric Effect from Transmission Supernodes. *ACS Nano*, **4**(9), pp. 5314–5320.

[23] Bergfield, J. P. and C. A. Stafford (2009). Many-body theory of electronic transport in single-molecule heterojunctions. *Phys. Rev. B*, **79**(24), p. 245125.

[24] Bergfield, J. P. and C. A. Stafford (2009). Thermoelectric Signatures of Coherent Transport in Single-Molecule Heterojunctions. *Nano Letters*, **9**, pp. 3072–3076.

[25] Binnig, G. and H. Rohrer (1987). Scanning Tunneling Microscopy-from Birth to Adolescence (Nobel Lecture). *Angewandte Chemie International Edition in English*, **26**(7), pp. 606–614.

[26] Bruevich, V. V., T. S. Makhmutov, S. G. Elizarov, E. M. Nechvolodova, and D. Y. Paraschuk (2007). Raman spectroscopy of intermolecular charge-transfer complex between a conjugated polymer and an organic acceptor molecule. *J. Chem. Phys.*, **127**, p. 104905.

[27] Bürki, J., C. A. Stafford, and D. L. Stein (2006). Comment on 'Nonlinear current-voltage curves of gold quantum point contacts'. *Applied Physics Letters*, **88**, p. 166101.

[28] Büttiker, M. (1986). 4-TERMINAL PHASE-COHERENT CONDUCTANCE. *Phys. Rev. Lett.*, **57**, p. 1761.

[29] Cardamone, D. M., C. A. Stafford, and S. Mazumdar (2006). Controlling quantum transport through a single molecule. *Nano Letters*, **6**(11), p. 2422.

[30] Castleton, C. W. M. and W. Barford (2002). Screening and the quantitative pi-model description of the optical spectra and polarizations of phenyl based oligomers. *J. Chem. Phys.*, **117**, pp. 3570–3582.

[31] Chaikin, P. M. and G. Beni (1976). Thermopower in the correlated hopping regime. *Phys. Rev. B*, **13**, pp. 647–651.

[32] Chakrabarti, A. and S. Mazumdar (1999). Theory of even-parity states in polyphenylenes. *Phys. Rev. B*, **59**, pp. 4839–4848.

[33] Chandross, M., S. Mazumdar, M. Liess, P. A. Lane, Z. V. Vardeny, M. Hamaguchi, and K. Yoshino (1997). Optical absorption in the substituted phenylene-based conjugated polymers: Theory and experiment. *Phys. Rev. B*, **55**, p. 1486.

[34] Chen, F., Z. Huang, and N. Tao (2007). Forming single molecular junctions between indium tin oxide electrodes. *Applied Physics Letters*, **91**(16). ISSN 0003-6951. doi:{10.1063/1.2800303}.

[35] Chen, F., X. Li, J. Hihath, Z. Huang, and N. Tao (2006). Effect of Anchoring Groups on Single-Molecule Conductance: Comparative Study of Thiol-, Amine-, and Carboxylic-Acid-Terminated Molecules. *Journal of the American Chemical Society*, **128**(49), pp. 15874–15881. ISSN 0002-7863.

[36] Clerk, A. A., X. Waintal, and P. W. Brouwer (2001). Fano Resonances as a Probe of Phase Coherence in Quantum Dots. *Phys. Rev. Lett.*, **86**, pp. 4636–4639.

[37] Cohen, A. J., P. Mori-Sánchez, and W. Yang (2008). Insights into Current Limitations of Density Functional Theory. *Science*, **321**, pp. 792–794.

[38] Craig, R. A. (1968). Perturbation Expansion for Real-Time Green's Functions. *Journal of Mathematical Physics*, **9**(4), pp. 605–611. doi:10.1063/1.1664616.

[39] Cruz, M. T. d. M., J. W. d. M. Carneiro, D. A. G. Aranda, and M. Bhl (2007). Density Functional Theory Study of Benzene Adsorption on Small Pd and Pt Clusters. *The Journal of Physical Chemistry C*, **111**(29), pp. 11068–11076. ISSN 1932-7447.

[40] Dadosh, T., Y. Gordin, R. Krahne, I. Khivrich, D. Mahalu, V. Frydman, J. Sperling, A. Yacoby, and I. Bar-Joseph (2005). Measurement of the conductance of single conjugated molecules. *Nature*, **436**, pp. 677–680.

[41] Danilov, A., S. Kubatkin, S. Kafanov, P. Hedegard, N. Stuhr-Hansen, K. Moth-Poulsen, and T. Bjornholm (2008). Electronic Transport in Single Molecule Junctions: Control of the Molecule-Electrode Coupling through Intramolecular Tunneling Barriers. *Nano Letters*, **8**(1), pp. 1–5.

[42] Datta, S. (1995). *Electronic Transport in Mesoscopic Systems*. Cambridge University Press.

[43] Datta, S. (1995). *Electronic Transport in Mesoscopic Systems*, pp. 117–174. Cambridge University Press, Cambridge, UK.

[44] De Franceschi, S., S. Sasaki, J. M. Elzerman, W. G. van der Wiel, S. Tarucha, and L. P. Kouwenhoven (2001). Electron Cotunneling in a Semiconductor Quantum Dot. *Phys. Rev. Lett.*, **86**(5), pp. 878–881.

[45] de la Vega, L., A. Martín-Rodero, N. Agraït, and A. Levy Yeyati (2006). Universal features of electron-phonon initeractions in atomic wires. *Phys. Rev. B*, **73**, p. 075428.

[46] Di Ventra, M. and N. D. Lang (2001). Transport in nanoscale conductors from first principles. *Phys. Rev. B*, **65**, p. 045402.

[47] Díez-Pérez, I., J. Hihath, Y. Lee, L. Yu, L. Adamska, M. A. Kozhushner, I. I. Oleynik, and N. Tao (2009). Rectification and stability of a single molecular diode with controlled orientation. *Nature Chemistry*, **1**, pp. 635–641. doi: 10.1038/nchem.392.

[48] Díez-Pérez, I., J. Hihath, Y. Lee, L. Yu, L. Adamska, M. A. Kozhushner, I. I. Oleynik, and N. Tao (2009). Rectification and stability of a single molecular diode with controlled orientation. *Nat. Chem.*, **1**, pp. 635–641.

[49] DiSalvo, F. J. (1999). Thermoelectric Cooling and Power Generation. *Science*, **285**(5428), pp. 703–706.

[50] Drori, T., C.-X. Sheng, A. Ndobe, S. Singh, J. Holt, and Z. V. Vardeny (2008). Below-Gap Excitation of π-Conjugated Polymer-Fullerene Blends: Implications for Bulk Organic Heterojunction Solar Cells. *Phys. Rev. Lett.*, **101**, p. 037401.

[51] Dyson, F. J. (1949). The Radiation Theories of Tomonaga, Schwinger, and Feynman. *Phys. Rev.*, **75**(3), pp. 486–502.

[52] Dyson, F. J. (1949). The S Matrix in Quantum Electrodynamics. *Phys. Rev.*, **75**(11), pp. 1736–1755.

[53] Elbing, M., R. Ochs, M. Koentopp, M. Fischer, C. von Hnisch, F. Weigend, F. Evers, H. B. Weber, and M. Mayor (2005). A single-molecule diode. *Proceedings of the National Academy of Sciences of the United States of America*, **102**(25), pp. 8815–8820.

[54] Emberly, E. G. and G. Kirczenow (2003). The Smallest Molecular Switch. *Phys. Rev. Lett.*, **91**, p. 188301.

[55] Fetter, A. L. and J. D. Walecka (2003). *Quantum Theory of Many-Particle Systems*. Dover, Mineola, New York.

[56] Feynman, R. P. (1949). Space-Time Approach to Quantum Electrodynamics. *Phys. Rev.*, **76**(6), pp. 769–789.

[57] Finch, C. M., V. M. García-Suárez, and C. J. Lambert (2009). Giant thermopower and figure of merit in single-molecule devices. *Phys. Rev. B*, **79**(3), p. 033405.

[58] Fisher, D. S. and P. A. Lee (1981). Relation between conductivity and transmission matrix. *Phys. Rev. B*, **23**(12), pp. 6851–6854.

[59] Friedel, J. (1958). Metallic alloys. *Nuovo Cimento Suppl.*, **7**, p. 287.

[60] Galperin, M., A. Nitzan, and M. A. Ratner (2008). Inelastic transport in the Coulomb blockade regime within a nonequilibrium atomic limit. *Phys. Rev. B*, **78**, p. 125320.

[61] Galperin, M., M. A. Ratner, and A. Nitzan (2004). Inelastic electron tunneling spectroscopy in molecular junctions: Peaks and dips. *J. Chem. Phys.*, **121**, p. 11965.

[62] Gell-Mann, M. and F. Low (1951). Bound States in Quantum Field Theory. *Phys. Rev.*, **84**(2), pp. 350–354.

[63] Geskin, V., R. Stadler, and J. Cornil (2009). Multideterminant assessment of mean-field methods for the description of electron transfer in the weak-coupling regime. *Phys. Rev. B*, **80**, p. 085411.

[64] Golubev, D. S. and A. D. Zaikin (1994). Quantum fluctuations of the charge near the Coulomb-blockade threshold. *Phys. Rev. B*, **50**, pp. 8736–8745.

[65] Göppert, G. and H. Grabert (2001, and references therein). Charge fluctuations in the single-electron box. *Phys. Rev. B*, **63**, p. 125307.

[66] Groshev, A., T. Ivanov, and V. Valtchinov (1991). Charging Effects in a Single Quantum Level in a Box. *Phys. Rev. Lett.*, **66**, pp. 1082–1085.

[67] Hackenbroich, G. (2001, and references therein). Phase coherent transmission through interacting mesoscopic systems. *Phys. Rep.*, **343**, pp. 463–538.

[68] Hallermann, M., S. Hanedar, and E. D. Como (2008). Charge-transfer states in conjugated polymer/fullerene blends: Below-gap weakly bound excitons for polymer photovoltaics. *Appl. Phys. Lett.*, **93**, p. 053307.

[69] Harbola, U. and S. Mukamel (2008). Superoperator nonequilibrium Green's function theory of many-body systems; applications to charge transfer and transport in open junctions. *Physics Reports*, **465**(5), pp. 191 – 222.

[70] Harman, T. C., P. J. Taylor, M. P. Walsh, and B. E. LaForge (2002). Quantum Dot Superlattice Thermoelectric Materials and Devices. *Science*, **297**(5590), pp. 2229–2232.

[71] Haug, H. and A.-P. Jauho (1996). *Quantum Kinetics in Transport and Optics of Semiconductors*, volume 123 of *Solid-State Sciences*. Springer.

[72] Haug, H. and A.-P. Jauho (1996). *Quantum Kinetics in Transport and Optics of Semiconductors*, volume 123 of *Solid-State Sciences*. Springer.

[73] Haule, K. (2002). *Diagrammatic Theory of Strongly Correlated Electron Systems*. Ph.D. thesis, University of Ljubljana.

[74] He, J., F. Chen, P. Liddell, J. Andreasson, S. Straight, D. Gust, T. Moore, A. Moore, J. Li, O. Sankey, and S. Lindsay (2005). Switching of a photochromic molecule on gold electrodes: single-molecule measurements. *Nanotechnology*, **16**(6), pp. 695–702. ISSN 0957-4484. doi:{10.1088/0957-4484/16/6/012}.

[75] Herrmann, C., G. C. Solomon, and M. A. Ratner (2010). Organic Radicals As Spin Filters. *Journal of the American Chemical Society*, **132**(11), pp. 3682–3684.

[76] Hettler, M. H., W. Wenzel, M. R. Wegewijs, and H. Schoeller (2003). Current Collapse in Tunneling Transport through Benzene. *Phys. Rev. Lett.*, **90**, p. 076805.

[77] Heurich, J., J. C. Cuevas, W. Wenzel, and G. Schön (2002). Electrical Transport through Single-Molecule Junctions: From Molecular Orbitals to Conduction Channels. *Phys. Rev. Lett.*, **88**, p. 256803.

[78] Hihath, J., C. R. Arroyo, G. Rubio-Bollinger, N. Tao, and N. Agrait (2008, and references therein). Study of electron-phonon interactions in a single molecule covalently connected to two electrodes. *Nano Letters*, **8**, pp. 1673–1678.

[79] Hochbaum, A. I., R. Chen, R. D. Delgado, W. Liang, E. C. Garnett, M. Najarian, A. Majumdar, and P. Yang (2008). Enhanced thermoelectric performance of rough silicon nanowires. *Nature*, **451**(7175), pp. 163–167.

[80] Iwasa, Y. and T. Takenobu (2003). Superconductivity, MottHubbard states, and molecular orbital order in intercalated fullerides. *J. Phys.: Condens. Matter*, **15**(13), p. R495.

[81] Jauho, A.-P., N. S. Wingreen, and Y. Meir (1994). TIME-DEPENDENT TRANSPORT IN INTERACTING AND NONINTERACTING RESONANT-TUNNELING SYSTEMS. *Phys. Rev. B*, **50**, p. 5528.

[82] Jiang, P., G. Morales, W. You, and L. Yu (2004). Synthesis of diode molecules and their sequential assembly to control electron transport. *Angewandte Chemie-International Edition*, **43**(34), pp. 4471–4475. ISSN 1433-7851. doi: {10.1002/anie.200460110}.

[83] Kadanoff, L. P. and G. Baym (1962). *Quantum Statistical Mechanics: Green's Function Methods in Equilibrium and Non-Equilibrium Problems.* New York: W.A. Benjamin.

[84] Karrasch, C., T. Hecht, A. Weichselbaum, Y. Oreg, J. von Delft, and V. Meden (2007). Mesoscopic to Universal Crossover of the Transmission Phase of Multilevel Quantum Dots. *Phys. Rev. Lett.*, **98**(18), p. 186802.

[85] Kassubek, F., C. A. Stafford, and H. Grabert (1999). Force, charge, and conductance of an ideal metallic nanowire. *Phys. Rev. B*, **59**, pp. 7560–7574.

[86] Ke, S.-H., H. U. Baranger, and W. Yang (2005). Models of electrodes and contacts in molecular electronics. *J. Chem. Phys.*, **123**, p. 114701.

[87] Ke, S.-H., H. U. Baranger, and W. Yang (2007). Role of the exchange-correlation potential in *ab initio* electron transport calculations. *J. Chem. Phys.*, **126**, p. 201102.

[88] Ke, S.-H., W. Yang, and H. U. Baranger (2008). Quantum Interference Controlled Molecular Electronics. *Nano Letters*, **8**, p. 3257.

[89] Keldysh, L. V. (1964). Diagram technique for nonequilibrium processes. *Zh. Eksp. Teor. Fiz.*, **47**, pp. 1515–1527.

[90] Kiguchi, M., O. Tal, S. Wohlthat, F. Pauly, M. Krieger, D. Djukic, J. C. Cuevas, and J. M. van Ruitenbeek (2008). Highly conductive molecular junctions based on direct binding of benzene to platinum electrodes. *Phys. Rev. Lett.*, **101**, p. 046801.

[91] Kiguchi, M., O. Tal, S. Wohlthat, F. Pauly, M. Krieger, D. Djukic, J. C. Cuevas, and J. M. van Ruitenbeek (2008). Highly Conductive Molecular Junctions Based on Direct Binding of Benzene to Platinum Electrodes. *Phys. Rev. Lett.*, **101**(4), p. 046801.

[92] Kim, J. Y., K. Lee, N. E. Coates, D. Moses, T.-Q. Nguyen, M. Dante, and A. J. Heeger (2007). Efficient Tandem Polymer Solar Cells Fabricated by All-Solution Processing. *Science*, **317**, pp. 222–225.

[93] Kim, Y., S. Cook, S. M. Tuladhar, S. A. Choulis, J. Nelson, J. R. Durrant, D. D. C. Bradley, M. Giles, I. McCulloch, C.-S. Ha, and M. Ree (2005). A strong regioregularity effect in self-organizing conjugated polymer films and high-efficiency polythiophene:fullerene solar cells. *Nat. Mater.*, **5**, pp. 197–203.

[94] Kinaret, J. M., Y. Meir, N. S. Wingreen, P. A. Lee, and X.-G. Wen (1992). Many-body coherence effects in conduction through a quantum dot in the fractional quantum Hall regime. *Phys. Rev. B*, **46**, pp. 4681–4692.

[95] Kittel, C. (1976). *Introduction to solid state physics*. John Wiley and Sons, Inc.

[96] Kleber, R. (1973). On the electronic density of states of the transition metals. *Zeitschrift fr Physik A Hadrons and Nuclei*, **264**(4), pp. 301–308.

[97] Koentopp, M., K. Burke, and F. Evers (2006). Zero-bias molecular electronics: Exchange-correlation corrections to Landauer's formula. *Phys. Rev. B*, **73**, p. 121403.

[98] König, J., H. Schoeller, and G. Schön (1997). Cotunneling at Resonance for the Single-Electron Transistor. *Phys. Rev. Lett.*, **78**, pp. 4482–4485.

[99] Kriplani, N. M., D. P. Nackashi, C. J. Amsinck, N. H. Di Spigna, M. B. Steer, P. D. Franzon, R. L. Rick, G. C. Solomon, and J. R. Reimers (2006). Physically based molecular device model in a transient circuit simulator. *Chemical Physics*, **326**, pp. 188–196.

[100] Kroto, H. W., A. W. Allaf, and S. P. Balm (1991). C60: Buckminsterfullerene. *Chem. Rev.*, **91**(6), pp. 1213–1235.

[101] Kubatkin, S., A. Danilov, M. Hjort, J. Cornil, J.-L. Brédas, N. Stuhr-Hansen, P. Hedegard, and T. Bjornholm (2003). Single-electron transistor of a single organic molecule with access to several redox states. *Nature*, **425**, pp. 698–701.

[102] Kushmerick, J. G., J. Lazorcik, C. H. Patterson, and R. Shashidhar (2004). Vibronic Contributions to Charge Transport Across Molecular Junctions. *Nano Letters*, **4**, pp. 639–642.

[103] Kuznetso, A. M. and J. Ulstrup (eds.) (1999). *Electron Transfer in Chemistry: An Introduction to the Theory*. Chichester:Wiley.

[104] Kwong, N. H., G. Rupper, and R. Binder (2009). Self-consistent T-matrix theory of semiconductor light-absorption and luminescence. *Phys. Rev. B*, **79**(15), p. 155205. doi:10.1103/PhysRevB.79.155205.

[105] Lafferentz, L., F. Ample, H. Yu, S. Hecht, C. Joachim, and L. Grill (2009). Conductance of a Single Conjugated Polymer as a Continuous Function of Its Length. *Science*, **323**, pp. 1193–. doi:10.1126/science.1168255.

[106] Landau, L. D., E. M. Lifshitz, and L. P. Pitaevskii (1984). *Electrodynamics of Continuous Media*. Pergamon Press, 2nd edition.

[107] Landauer, R. (1957). Spatial Variation of Currents and Fields Due to Localized Scatterers in Metallic Conduction. *IBM J. Res. Dev.*, **1**, p. 223.

[108] Langreth, D. C. (1966). Friedel Sum Rule for Anderson's Model of Localized Impurity States. *Phys. Rev.*, **150**(2), pp. 516–518.

[109] Lee, H.-W. (1999). Generic Transmission Zeros and In-Phase Resonances in Time-Reversal Symmetric Single Channel Transport. *Phys. Rev. Lett.*, **82**(11), pp. 2358–2361.

[110] Lee, Y., S. Yuan, A. Sanchez, and L. Yu (2008). Charge transport mediated by d-orbitals in transition metal complexes. *Chemical Communications*, (2), pp. 247–249. ISSN 1359-7345. doi:{10.1039/b712978e}.

[111] Levy Yeyati, A. and M. Büttiker (2000). Scattering phases in quantum dots: An analysis based on lattice models. *Phys. Rev. B*, **62**(11), pp. 7307–7315.

[112] Li, C. Z., H. X. He, and N. J. Tao (2000). Quantized tunneling current in the metallic nanogaps formed by electrodeposition and etching. *Applied Physics Letters*, **77**(24), pp. 3995–3997.

[113] Li, G., V. Shrotriya, J. Huang, Y. Yao, T. Moriarty, K. Emery, and Y. Yang (2005). High-efficiency solution processable polymer photovoltaic cells by self-organization of polymer blends. *Nat. Mater.*, **4**, pp. 864–868.

[114] Li, X., J. He, J. Hihath, B. Xu, S. M. Lindsay, and N. Tao (2006). Conductance of Single Alkanedithiols: Conduction Mechanism and Effect of Molecule-Electrode Contacts. *J. Am. Chem. Soc.*, **128**, pp. 2135–2141.

[115] Liang, W., M. P. Shores, M. Bockrath, J. R. Long, and H. Park (2002). Kondo resonance in a single-molecule transistor. *Nature*, **417**, pp. 725–729.

[116] Liang, W., M. P. Shores, M. Bockrath, J. R. Long, and H. Park (2002). Kondo resonance in a single-molecule transistor. *Nature*, **417**, pp. 725–729.

[117] Lichtenberger, D. L., K. W. Nebesny, C. D. Ray, D. R. Huffman, and L. D. Lamb (1991). Valence and core photoelectron spectroscopy of C60, buckminsterfullerene. *Chem. Phys. Lett.*, **176**(2), pp. 203 – 208.

[118] Lide *et al.*, D. R. (ed.) (2005). *CRC Handbook of Chemistry and Physics*. CRC Press, Boca Raton, Fla.

[119] Lindsay, S. (2005). Single-Molecule Electronic Measurements with Metal Electrodes. *Journal of Chemical Education*, **82**(5), pp. 727–.

[120] Lindsay, S. M. and M. A. Ratner (2007, and references therein). Molecular Transport Junctions: Clearing Mists. *Adv. Mater.*, **19**, pp. 23–31.

[121] Liu, Y.-S., Y.-R. Chen, and Y.-C. Chen (2009). Thermoelectric Efficiency in Nanojunctions: A Comparison between Atomic Junctions and Molecular Junctions. *ACS Nano*, **3**(11), pp. 3497–3504.

[122] Luttinger, J. M. (1960). Fermi Surface and Some Simple Equilibrium Properties of a System of Interacting Fermions. *Phys. Rev.*, **119**(4), pp. 1153–1163.

[123] Ma, W., C. Y. Yang, X. Gong, K. Lee, and A. J. Heeger (2005). Thermally Stable, Efficient Polymer Solar Cells with Nanoscale Control of the Interpenetrating Network Morphology. *Adv. Funct. Mater.*, **15**, p. 1617.

[124] Mahan, G. D. (1990). *Many-Particle Physics*. Plenum Press, New York.

[125] Majumdar, A. (2004). MATERIALS SCIENCE: Enhanced: Thermoelectricity in Semiconductor Nanostructures. *Science*, **303**(5659), pp. 777–778.

[126] Martin, A. S., J. R. Sambles, and G. J. Ashwell (1993). Molecular rectifier. *Phys. Rev. Lett.*, **70**(2), pp. 218–221. doi:10.1103/PhysRevLett.70.218.

[127] Mattuck, D., Richard (1992). *A Guide to Feynman Diagrams in the Many-Body Problem*. Dover Publications, Inc., New York.

[128] Matveev, K. A. (1995). Coulomb blockade at almost perfect transmission. *Phys. Rev. B*, **51**, pp. 1743–1751.

[129] Mayor, M., H. B. Weber, J. Reichert, M. Elbing, C. von Hänisch, D. Beckmann, and M. Fischer (2003). Electric Current throuhg a Molecular Rod—Relevance of the Position of the Anchor Groups. *Angew. Chem. Int. Ed.*, **42**, pp. 5834–5838.

[130] Meir, Y. and N. S. Wingreen (1992). Landauer Formula for the Current through an Interacting Electron Region. *Phys. Rev. Lett.*, **68**, pp. 2512–2515.

[131] Meir, Y., N. S. Wingreen, and P. A. Lee (1991). Transport through a Strongly Interacting Electron System: Theory of Periodic Conductance Oscillations. *Phys. Rev. Lett.*, **66**, pp. 3048–3051.

[132] Mitra, A., I. Aleiner, and A. J. Millis (2004). Phonon effects in molecular transistors: Quantal and classical treatment. *Phys. Rev. B*, **69**, p. 245302.

[133] Morales, G., P. Jiang, S. Yuan, Y. Lee, A. Sanchez, W. You, and L. Yu (2005). Inversion of the rectifying effect in diblock molecular diodes by protonation. *Journal of the American Chemical Society*, **127**(30), pp. 10456–10457. ISSN 0002-7863. doi:{10.1021/ja051332c}.

[134] Morin, C., D. Simon, and P. Sautet (2003). Density-Functional Study of the Adsorption and Vibration Spectra of Benzene Molecules on Pt(111). *The Journal of Physical Chemistry B*, **107**(13), pp. 2995–3002.

[135] Mujica, V., M. Kemp, and M. A. Ratner (1994). ELECTRON CONDUCTION IN MOLECULAR WIRES 1. A SCATTERING FORMALISM. *J. Chem. Phys.*, **101**, p. 6849.

[136] Muralidharan, B., A. W. Ghosh, and S. Datta (2006). Probing electronic excitations in molecular conduction. *Phys. Rev. B*, **73**, p. 155410.

[137] Muralidharan, B., A. W. Ghosh, and S. Datta (2006). Probing electronic excitations in molecular conduction. *Phys. Rev. B*, **73**, p. 155410.

[138] Myohanen, P., A. Stan, G. Stefanucci, and R. van Leeuwen (2008). A many-body approach to quantum transport dynamics: Initial correlations and memory effects. *Europhysics Letters*, **84**(6), p. 67001 (5pp).

[139] Nakanishi, T. and T. Kato (2007). Thermopower of a Quantum Dot in a Coherent Regime. *Journal of the Physical Society of Japan*, **76**(3), p. 034715.

[140] Natelson, D., L. H. Yu, J. W. Ciszek, Z. K. Keane, and J. M. Tour (2006, and references therein). Single-molecule transistors: Electron transfer in the solid state. *Chem. Phys.*, **324**, pp. 267–275.

[141] Ng, M., D. Lee, and L. Yu (2002). Molecular diodes based on conjugated diblock co-oligomers. *Journal of the American Chemical Society*, **124**(40), pp. 11862–11863. ISSN 0002-7863. doi:{10.1021/ja026808w}.

[142] Nitzan, A. (2001). Electron transmission through molecules and molecular interfaces. *Annu. Rev. Phys. Chem.*, **52**, pp. 681–750.

[143] Nitzan, A. and M. A. Ratner (2003, and references therein). Electron Transport in Molecular Wire Junctions. *Science*, **300**, pp. 1384–1389.

[144] Park, H., A. K. L. Lim, A. P. Alivisatos, J. Park, and P. L. McEuen (1999). Fabrication of metallic electrodes with nanometer separation by electromigration. *Applied Physics Letters*, **75**(2), pp. 301–303. doi:10.1063/1.124354.

[145] Park, H., J. Park, A. K. L. Lim, E. H. Anderson, A. P. Alivisatos, and P. L. McEuen (2000). Nanomechanical oscillations in a single-C_{60} transistor. *Nature*, **407**, pp. 57–60.

[146] Paulsson, M. and S. Datta (2003). Thermoelectric effect in molecular electronics. *Phys. Rev. B*, **67**, p. 241403.

[147] Paulsson, M., T. Frederiksen, and M. Brandbyge (2005). Modeling inelastic phonon scattering in atomic- and molecular-wire junctions. *Phys. Rev. B*, **72**, p. 201101(R).

[148] Pedersen, J. N. and A. Wacker (2005). Tunneling through nanosystems: Combining broadening with many-particle states. *Phys. Rev. B*, **72**, p. 195330.

[149] Poot, M., E. Osorio, K. O'Neill, J. M. Thijssen, D. Vanmaekelbergh, C. A. van Walree, L. W. Jenneskens, and S. J. van der Zant (2006). Temperature Dependence of Three-Terminal Molecular Junctions with Sulfur End-Functionalized Tercyclohexylidenes. *Nano Letters*, **6**, pp. 1031–1035.

[150] Porath, D., Y. Levi, M. Tarabiah, and O. Millo (1997). Tunneling spectroscopy of isolated C_{60} molecules in the presence of charging effects. *Phys. Rev. B*, **56**(15), pp. 9829–9833.

[151] Pustilnik, M. and L. Glazman (2004, and references therein). Kondo effect in quantum dots. *J. Phys. Condens. Matter*, **16**, pp. R513–R537.

[152] Reddy, P., S.-Y. Jang, R. A. Segalman, and A. Majumdar (2007). Thermoelectricity in Molecular Junctions. *Science*, **315**, pp. 1568–1571.

[153] Reed, M. A., C. Zhou, C. J. Muller, T. P. Burgin, and J. M. Tour (1997). Conductance of a molecular junction. *Science*, **278**, pp. 252–254.

[154] Rego, L. G. C. and G. Kirczenow (1999). Fractional exclusion statistics and the universal quantum of thermal conductance: A unifying approach. *Phys. Rev. B*, **59**(20), pp. 13080–13086.

[155] Reichert, J., H. B. Weber, M. Mayor, and H. v. Löhneysen (2003). Low-temperature conductance measurements on single molecules. *Applied Physics Letters*, **82**, pp. 4137–4139.

[156] Repp, J., G. Meyer, S. Paavilainen, F. E. Olsson, and M. Persson (2006). Imaging Bond Formation Between a Gold Atom and Pentacene on an Insulating Surface. *Science*, **312**(5777), pp. 1196–1199.

[157] Repp, J., G. Meyer, S. M. Stojković, A. Gourdon, and C. Joachim (2005). Molecules on Insulating Films: Scanning-Tunneling Microscopy Imaging of Individual Molecular Orbitals. *Phys. Rev. Lett.*, **94**(2), p. 026803.

[158] Reyes-Reyes, M., K. Kim, and D. L. Caroll (2005). High-efficiency photovoltaic devices based on annealed poly(3-hexylthiophene) and 1-(3-methoxycarbonyl)-propyl-1- phenyl-(6,6)C61 blends. *Appl. Phys. Lett*, **87**, p. 083506.

[159] Saeys, M., M.-F. Reyniers, G. B. Marin, and M. Neurock (2002). Density Functional Study of Benzene Adsorption on Pt(111). *The Journal of Physical Chemistry B*, **106**(30), pp. 7489–7498.

[160] Sapmaz, S., P. Jarillo-Herrero, Y. M. Blanter, C. Dekker, and H. S. J. van der Zant (2006). Tunneling in Suspended Carbon Nanotubes Assisted by Longitudinal Phonons. *Phys. Rev. Lett.*, **96**(2), p. 026801.

[161] Schoeller, H. and J. König (2000). Real-Time Renormalization Group and Charge Fluctuations in Quantum Dots. *Phys. Rev. Lett.*, **84**, pp. 3686–3689.

[162] Schreiber, S. L. (2005). Small molecules: the missing link in the central dogma. *Nat. Chem. Biol.*, **1**, pp. 64–66.

[163] Schuster, R., E. Buks, M. Heiblum, D. Mahalu, V. Umansky, and H. Shtrikman (1997). Phase measurement in a quantum dot via a double slit interference experiment. *Nature*, **385**, pp. 417–420.

[164] Schwinger, J. (1961). Brownian Motion of a Quantum Oscillator. *Journal of Mathematical Physics*, **2**(3), pp. 407–432.

[165] Segal, D., A. Nitzan, and P. Hänggi (2003). Thermal conductance through molecular wires. *jcp*, **119**, pp. 6840–6855.

[166] Silva, A., Y. Oreg, and Y. Gefen (2002). Signs of quantum dot˘lead matrix elements: The effect on transport versus spectral properties. *Phys. Rev. B*, **66**(19), p. 195316.

[167] Silvestrov, P. G. and Y. Imry (2000). Towards an Explanation of the Mesoscopic Double-Slit Experiment: A New Model for Charging of a Quantum Dot. *Phys. Rev. Lett.*, **85**(12), pp. 2565–2568.

[168] Sivan, U. and Y. Imry (1986). Multichannel Landauer formula for thermoelectric transport with application to thermopower near the mobility edge. *Phys. Rev. B*, **33**, pp. 551–558.

[169] Snyder, G. J. and E. S. Toberer (2008). Complex thermoelectric materials. *Nat Mater*, **7**(2), pp. 105–114.

[170] Solomon, G. C., D. Q. Andrews, R. H. Goldsmith, T. Hansen, M. R. Wasielewski, R. P. Van Duyne, and M. A. Ratner (2008). Quantum Interference in Acyclic Systems: Conductance of Cross-Conjugated Molecules. *J. Am. Chem. Soc.*, **130**(51), pp. 17301–17308.

[171] Solomon, G. C., D. Q. Andrews, T. Hansen, M. R. Goldsmith, Randall H.and Wasielewski, R. P. Van Duyne, and M. A. Ratner (2008). Understanding quantum interference in coherent molecular conduction. *J. Chem. Phys.*, **129**, p. 054701.

[172] Solomon, G. C., D. Q. Andrews, R. P. Van Duyne, and M. A. Ratner (2008). When things are not as they seem: Quantum interference turns molecular electron transfer "Rules" upside down. *J. Am. Chem. Soc.*, **130**, p. 7788.

[173] Solomon, G. C., A. Gagliardi, A. Pecchia, T. Frauenheim, A. di Carlo, J. R. Reimers, and N. S. Hush (2006). Molecular Origins of Conduction Channels Observed in Shot-Noise Measurements. *Nano Letters*, **6**, pp. 2431–2437.

[174] Solomon, G. C., A. Gagliardi, A. Pecchia, T. Frauenheim, A. Di Carlo, J. R. Reimers, and N. S. Hush (2006). Understanding the inelastic electron-tunneling spectra of alkanedithiols on gold. *J. Chem. Phys.*, **124**, p. 094704.

[175] Song, H., Y. Kim, Y. H. Jang, H. Jeong, M. A. Reed, and T. Lee (2009). Observation of molecular orbital gating. *Nature*, **462**(7276), pp. 1039–1043.

[176] Stafford, C. A. (1993). Unusual low-temperature thermopower in the one-dimensional Hubbard model. *Phys. Rev. B*, **48**, p. 8430.

[177] Stafford, C. A. (1996). Nonlinear conductance in resonant tunneling. *Phys. Rev. Lett.*, **77**, pp. 2770–2773.

[178] Stafford, C. A., D. M. Cardamone, and S. Mazumdar (2007). The Quantum Interference Effect Transistor. *Nanotechnology*, **18**, p. 424014.

[179] Stafford, C. A., F. Kassubek, J. Bürki, and H. Grabert (1999). Universality in Metallic Nanocohesion: A Quantum Chaos Approach. *Phys. Rev. Lett.*, **83**, pp. 4836–4839.

[180] Stafford, C. A., R. Kotlyar, and S. Das Sarma (1998). Coherent resonant tunneling through an artificial molecule. *Phys. Rev. B*, **58**, p. 7091.

[181] Stefanucci, G. (2007). Bound states in ab initio approaches to quantum transport: A time-dependent formulation. *Phys. Rev. B*, **75**, p. 195115.

[182] Tao, N. J. (2006, and references therein). Electron transport in molecular junctions. *Nature Nanotechnology*, **1**, pp. 173–181.

[183] Taylor, J., H. Guo, and J. Wang (2001). Ab initio modeling of quantum transport properties of molecular electronic devices. *Phys. Rev. B*, **63**, p. 245407.

[184] Terrier, C., C. Strunk, T. Nussbaumer, D. Babić, and C. Schönenberger (1999). Amplitude of Aharonov-Bohm Oscillations in Mesoscopic Metallic Rings as a Function of the DC Bias Voltage. *Fizika A*, **8**, pp. 157–164.

[185] Thygesen, K. S. and A. Rubio (2008). Conserving *GW* scheme for nonequilibrium quantum transport in molecular contacts. *Phys. Rev. B*, **77**(11), p. 115333.

[186] Tian, W., S. Datta, S. Hong, R. Reifenberger, J. I. Henderson, and C. P. Kubiak (1998). Conductance spectra of molecular wires. *J. Chem. Phys.*, **109**, pp. 2874–2882.

[187] Todorov, T. N., J. Hoekstra, and A. P. Sutton (2000). Current-induced forces in atomic-scale conductors. *Philosophical Magazine B*, **80**, p. 421.

[188] Toher, C., A. Filippetti, S. Sanvito, and K. Burke (2005). Self-Interaction Errors in Density-Functional Calculations of Electronic Transport. *Phys. Rev. Lett.*, **95**, p. 146402.

[189] Toher, C. and S. Sanvito (2007). Efficient Atomic Self-Interaction Correction Scheme for Nonequilibrium Quantum Transport. *Phys. Rev. Lett.*, **99**, p. 056801.

[190] Tomfohr, J. K. and O. F. Sankey (2004). Theoretical analysis of electron transport through organic molecules. *J. Chem. Phys.*, **120**, pp. 1542–1554.

[191] Tran, M.-T. (2008). Initial correlations in a nonequilibrium Falicov-Kimball model. *Phys. Rev. B*, **78**, p. 125103.

[192] Valcarcel, A., A. Clotet, J. M. Ricart, F. Delbecq, and P. Sautet (2004). Comparative DFT study of the adsorption of 1,3-butadiene, 1-butene and 2-cis/trans-butenes on the Pt(111) and Pd(111) surfaces. *Surface Science*, **549**, pp. 121–133. doi:10.1016/j.susc.2003.11.036.

[193] van Houten, H., L. W. Molenkamp, C. W. J. Beenakker, and C. T. Foxon (1992). Thermo-electric properties of quantum point contacts. *Semicond. Sci. Technol.*, **7**, pp. B215–B221.

[194] van Wees, B. J., H. van Houten, C. W. J. Beenakker, J. G. Williamson, L. P. Kouwenhoven, D. van der Marel, and C. T. Foxon (1988). Quantized conductance of point contacts in a two-dimensional electron gas. *Phys. Rev. Lett.*, **60**(9), pp. 848–850.

[195] Venkataraman, L., J. E. Klare, I. W. Tam, C. Nuckolls, M. S. Hybertsen, and M. L. Steigerwald (2006). Single-Molecule Circuits with Well-Defined Molecular Conductance. *Nano Letters*, **6**(3), pp. 458–462. ISSN 1530-6984.

[196] Verdozzi, C. (2008). Time-Dependent Density-Functional Theory and Strongly-Correlated Systems: Insight from Numerical Studies. *Phys. Rev. Lett.*, **101**, p. 166401.

[197] Viljas, J. K., J. C. Cuevas, F. Pauly, and M. Häfner (2005). Electron-vibration interaction in transport through atomic gold wires. *Phys. Rev. B*, **72**, p. 245415.

[198] von Delft, J. and D. C. Ralph (2001). Spectroscopy of discrete energy levels in ultrasmall metallic grains. *Phys. Rep.*, **345**(2-3), pp. 61–173.

[199] Wang, Z., J. A. Carter, A. Lagutchev, Y. K. Koh, N. Seong, D. G. Cahill, and D. D. Dlott (2007). Ultrafast Flash Thermal Conductance of Molecular Chains. *Science*, **317**, pp. 787–.

[200] Ward, D. R., N. J. Halas, J. W. Ciszek, J. M. Tour, Y. Wu, P. Nordiander, and D. Natelson (2008). Simultaneous measurements of electronic conduction and Raman response in molecular junctions. *Nano Letters*, **8**, pp. 919–924.

[201] Weis, J., R. J. Haug, K. v. Klitzing, and K. Ploog (1993). Competing channels in single-electron tunneling through a quantum dot. *Phys. Rev. Lett.*, **71**(24), pp. 4019–4022.

[202] Wheeler, J. A. (1937). On the Mathematical Description of Light Nuclei by the Method of Resonating Group Structure. *Phys. Rev.*, **52**(11), pp. 1107–1122. doi:10.1103/PhysRev.52.1107.

[203] Xiao, X., B. Xu, and N. J. Tao (2004). Measurement of Single Molecule Conductance: Benzenedithiol and Benzenedimethanethiol. *Nano Letters*, **4**, pp. 267–271.

[204] Xu, B. Q. and N. J. Tao (2003). Measurement of Single Molecule Conductance by Repeated Formation of Molecular Junctions. *Science*, **301**, pp. 1221–1223.

[205] Yacoby, A., M. Heiblum, D. Mahalu, and H. Shtrikman (1995). Coherence and Phase Sensitive Measurements in a Quantum Dot. *Phys. Rev. Lett.*, **74**(20), pp. 4047–4050.

[206] Yu, G., J. Gao, J. Hummelen, F. Wudl, and A. Heeger (1995). Polymer Photovoltaic Cells: Enhanced Efficiencies via a Network of Internal Donor-Acceptor Heterojunctions. *Science*, **270**(5243), pp. 1789–1791. ISSN 0036-8075.

[207] Yu, L. and D. Natelson (2004). The Kondo effect in C-60 single-molecule transistors. *Nano Letters*, **4**(1), pp. 79–83.

[208] Yu, L. H., Z. K. Keane, J. W. Ciszek, L. Cheng, M. P. Stewart, J. M. Tour, and D. Natelson (2004). Inelastic electron tunneling via molecular vibrations in single-molecule transistors. *Phys. Rev. Lett.*, **93**, p. 266802.

[209] Zangmeister, C. D., S. W. Robey, R. D. van Zee, Y. Yao, and J. M. Tour (2004). Fermi Level Alignment and Electronic Levels in Molecular Wire? Self-Assembled Monolayers on Au. *The Journal of Physical Chemistry B*, **108**(41), pp. 16187–16193.

[210] Zimbovskaya, N. A. (2008). Electron transport through a quantum dot in the Coulomb blockade regime: Nonequilibrium Green's function based model. *Phys. Rev. B*, **78**(3), p. 035331. doi:10.1103/PhysRevB.78.035331.